2003

DIAGONAL AND OFF-DIAGONAL MAGNETO-IMPEDANCE IN FERROMAGNETIC MICROWIRES AND THIN FILMS

Makhnovskiy, Dmitriy

DIAGONAL AND OFF–DIAGONAL MAGNETO-IMPEDANCE IN FERROMAGNETIC MICROWIRES AND THIN FILMS

by

Dmitriy Makhnovskiy

A thesis submitted to the University of Plymouth
in partial fulfilment for the degree of

Doctor of Philosophy

Summer 2003

ABSTRACT

DIAGONAL AND OFF–DIAGONAL MAGNETO-IMPEDANCE IN FERROMAGNETIC MICROWIRES AND THIN FILMS

The discovery of the giant magneto-impedance (GMI) effect in 1994 had a strong impact on the development of micro magnetic sensors. In certain soft magnetic materials, such as composites of amorphous thin wires, the magneto-impedance change (MI ratio) is in the range of 50-100% in the MHz frequency band for external magnetic fields of few Oe. Special thin-film structures have been proposed to provide the MI effect in miniature elements.

In the present work, the concept of the magneto-impedance matrix has been elaborated, which enables the explanation of variety of MI field characteristics in wires and films from the common point of view. The fabrication technologies of the narrow thin film MI samples with different structures also were developed, including layered films and films integrated with a helical planar microcoil. The experimental technique employed in the work allowed us to measure all components of the total magneto-impedance matrix that came as the first verification of the matrix concept of the magneto-impedance. Different methods of getting the asymmetrical and antisymmetrical magneto-impedance behaviours were proposed demonstrating a great success of the impedance matrix concept. In the case of a simple transverse magnetic anisotropy, the diagonal components of the magneto-impedance matrix are symmetric and the off-diagonal components are antisymmetrical with respect to the dc longitudinal magnetic field. The asymmetry in MI behaviour can be related to either a certain asymmetric arrangement of the dc magnetic configuration or a contribution to the measured voltage due to the ac cross-magnetisation process, represented by the off-diagonal component. The first case is realised in the wire and film having the helical or crossed anisotropies respectively, which are subjected to an ac current superposed with a dc bias current. In the other approach, the asymmetric voltage response can be obtained by applying the ac current in series through the MI element (wire or film) and the small coil surrounded it. No helical anisotropy is required in this case. These kinds of asymmetrical MI are especially important for developing auto-biased linear MI sensors. The thin film with the integrated planar microcoil allowed us to measure the off-diagonal impedance in the sandwiched film. Results obtained for MI in thin films open up the perspective directions for the integrated MI sensors.

The applications of the MI effect are not limited only by magnetic sensor technology. In this work, a new type of tuneable composite materials was proposed, the effective microwave permittivity (dielectric constant) of which depends on the dc external magnetic field applied to the composite as a whole. The composite consists of the short pieces of ferromagnetic wires embedded into a dielectric matrix. The composite sample can be fabricated in the form of thin slab with thickness less than 1 millimetre. The short wire inclusions play the role of "the elementary scatterers", when the electromagnetic wave irradiates the composite and induces an electrical dipole moment in each inclusion. These induced dipole moments form the dipole response of the composite, which can be characterised by some effective permittivity. The field dependence of the effective permittivity arises from a high field sensitivity of the ac surface impedance of a ferromagnetic wire. In the vicinity of the antenna resonance (related with the short wire inclusions) any variations in the magneto-impedance of wires result in large changes of the effective permittivity. Therefore, this composite demonstrates both the tuneable and resonance properties (selective absorption). Thus, we have demonstrated a possibility of using the MI effect to design field-controlled composites and band-gap structures. A number of applications can be proposed, including selective microwave coatings with the field-dependent reflection/transmission coefficients and selective tuneable waveguides where the composite material may be used as an additional field-dependent coating. In addition, in the final chapter of future work we will take a quick look at tuneable composites with other microstructures and methods of the excitation.

AUTHOR'S DECLARATION

Author's study and research were financed with the aid of a studentship from the University of Plymouth during the period of 02/99 – 03/2001 and from the EPSRC grant starting with 03/2001, when the author obtained the work permit as a Research Assistant in Electrodynamics at the School of Computing, Communications and Electronics of the University of Plymouth.

The work contained in this thesis was partly presented at several international conferences and workshops. The research output includes: 1 book chapter, 2 invited presentations, 1 patent application, 11 regular refereed journal papers, 8 conference refereed papers (in journals and proceedings).

Author's signature..16/01/2004.....

Date..Max.....

Book chapter:

L. V. Panina and **D. P. Makhnovskiy**, *"Magneto-impedance in Multilayered Films for Miniature Magnetic Sensors"*, **Book chapter** in The Introduction to Complex Mediums for Optics and Electromagnetics, Editors: Werner S. Weiglhofer and Akhlesh Lakhtakia, SPIE Optical Engineering Press, 2003.

Invited presentations:

1. L. V. Panina and **D. P. Makhnovskiy**, *"Giant magneto-impedance in structured materials"*, The International Symposium on Optical Science and Technology, Complex Mediums III: Beyond Linear Isotropic Dielectrics; Seattle, July 2002. Published in The Proceedings SPIE International Society for Optical Engineering, vol. 4806, pp. 18-31, 2002.

2. L. V. Panina and **D. P. Makhnovskiy, Key lecture:** *"Magneto-impedance in amorphous wires and multifunctional applications: from miniature magnetic sensors to tuneable microwave metamaterials"*, The International Conference on Magnetism (ICM), Rome, Italy, July 2003. Accepted for publication in J. Magn. Magn. Mater, 2003.

Patent application:

A. N. Grigorenko, L. V. Panina, S. I. Sandacci, **D. P. Makhnovskiy**, D. J. Mapps, I. Y. Khrushchev, M. V. Dubov, *"Laser method of local annealing of amorphous microwires for fabrication of continuous magnetic coding"*, 2002, Great Britain patent application.

Other publications:

1. D. P. Makhnovskiy, A. S. Antonov, A. N. Lagarkov, and L. V. Panina, *"Field–dependent surface impedance of a bilayer film with an antisymmetric bias magnetization"*, Journal of Applied Physics **84**, p. 5698 (1998).

2. A. P. Vinogradov, **D. P. Makhnovskiy**, and K. N. Rozanov, Journal of Communications Technology and Electronics **44**, p. 317 (1999).

3. L. V. Panina, **D. P. Makhnovskiy**, and K. Mohri, *"Analisis of magneto-impedance in multilayers with crossed anisotropy"*, J. Magn. Soc. Japan **23**, p. 925 (1999).

4. L. V. Panina, **D. P. Makhnovskiy**, and K. Mohri, *"Mechanism of asymmetrical magneto-impedance in amorphous wires"*, Journal of Applied Physics **85**, p. 5444 (1999).

5. D. P. Makhnovskiy and L. V. Panina, *"Size effect on magneto–impedance in sandwich films"*, Sensor and Actuators **A81**, p. 91 (2000).

6. D. P. Makhnovskiy, A. N. Lagarkov, L. V. Panina, and K. Mohri, *"Effect of antisymmetric bias field on magneto-impedance in multilayers with crossed anisotropy"*, Sensor and Actuators **A81**, p. 106 (2000).

7. D. P. Makhnovskiy, L. V. Panina, and D. J. Mapps, *"Measurement of field-dependent surface impedance tensor in amorphous wires with circumferential anisotropy"*, Journal of Applied Physics **87**, p. 4804 (2000).

8. D. P. Makhnovskiy, L. V. Panina, and D. J. Mapps, *"Asymmetrical magneto–impedance in a sandwich film with a transverse anisotropy using an ac bias"*, Journal of Magnetism and Magnetic Materials **215-216**, p. 629 (2000).

9. D. P. Makhnovskiy, L. V. Panina, and D. J. Mapps, *"Asymmetrical magneto-impedance in as-cast CoFeSiB amorphous wires due to ac bias"*, Applied Physics Letters **77**, p. 121 (2000).

10. L. V. Panina, **D. P. Makhnovskiy**, D. J. Mapps, K. Mohri, and P. I. Nikitin, *"Effect of frequency and dc current on ac-biased asymmetrical magneto-impedance in wires"*, Materials Science Forum **373/376**, p. 741 (2001).

11. D. P. Makhnovskiy, L. V. Panina, and D. J. Mapps, *"Surface impedance tensor in amorphous wires with helical anisotropy: magnetic hysteresis and asymmetry"*, Journal of Applied Physics **89**, p. 7224 (2001).

12. L. V. Panina, **D. P. Makhnovskiy**, D. J. Mapps, and D. S. Zarechnyuk, *"2-D analysis of magneto-impedance in magnetic/metallic multilayers"*, Journal of Applied Physics **89**, p. 7221 (2001).

13. D. P. Makhnovskiy, L. V. Panina, and D. J. Mapps, *"Field-dependent surface impedance tensor in amorphous wires with two types of magnetic anisotropy: helical and circumferential"*, Physical Review **B 63**, p. 144424 (2001).

14. D. P. Makhnovskiy, L. V. Panina, D. J. Mapps, and A. K. Sarychev, *"Effect of transition layers on the electromagnetic properties of composites containing conducting fibres"*, Physical Review **B 64**, p. 134205 (2001).

15. V. A. Zhukova, A. B. Chizhik, J. Gonzalez, **D. P. Makhnovskiy**, L. V. Panina, D. J. Mapps, and A. P. Zhukov, *"Effect of annealing under torsion stress on the field dependence of the impedance tensor in amorphous wires"*, J. Magn. Magn. Mater. **249**, p. 324 (2002).

16. L. V. Panina, A. N. Grigorenko, and **D. P. Makhnovskiy**, *"Optomagnetic composite medium with conducting nanoelements"*, Physical Review **B 66**, p. 155411 (2002).

17. D. P. Makhnovskiy and L. V. Panina, *"Field dependent permittivity of composite materials containing ferromagnetic wires"*, Journal of Applied Physics (accepted, the 15 April, issue 2003).

18. N. Fry, **D. P. Makhnovskiy**, L. V. Panina, S. I. Sandacci, M. Akhter, and D. J. Mapps, *"Field dependence of the off-diagonal impedance in NiFe/Au/NiFe layered film with a planar microcoil"*, IEEE Trans. Magn. (submitted, 2002).

19. S. I. Sandacci, **D. P. Makhnovskiy**, L. V. Panina, K. Mohri, and Y. Honkura, *"Off-diagonal impedance in amorphous wires and application to linear magnetic sensors"*, IEEE Trans. Magn. (submitted, 2002).

INTERNATIONAL CONFERENSES, SYMPOSIUMS, AND WORKSHOPS:

1. (Key lecture) The International Conference on Magnetism (ICM), Rome, Italy, July 2003.

2. The Physics Congress, Heriot-Watt University, Edinburgh, Scotland, 23-27 March 2003.

3. (Invited lecture) The International Symposium on Optical Science and Technology, Complex Mediums III: Beyond Linear Isotropic Dielectrics; Seattle, July 2002.

4. International Workshop on Magnetic Wires (IWMW), The University of San Sebastian, San Sebastian, Spain, June 2001.

5. Joint International Conference on Magnetics, Magnetism and Magnetic Materials (Intermag/MMM), San Antonio, USA, January 2001.

6. 4th Joint UK Magnetic Workshop, University of Cardiff, Cardiff, Wales, July 2001.

7. European Magnetic Materials and Application Conference (EMMA), Kiev, Ukraine, June 2000.

8. 44th Annual Conference on Magnetism and Magnetic Materials (MMM), San Jose, USA, November 1999.

9. European Conference on Sensors and Actuators (EMSA), Sheffield, Scotland, July 1998.

10. International Conference and Workshop on Electromagnetics of Complex Media (BIANISOTROPICS'97), University of Glasgow, Glasgow, Scotland, June 1997.

QUALITY OF RESEARCH:

Scientific papers are published in refereed international journals, such as: Physical Review B, Journal of Applied Physics, Applied Physics Letters, Journal of Magnetism and Magnetic Materials, Sensors and Actuators, IEEE Transactions on Magnetics.

ACKNOWLEDGEMENTS

I would like to express my sincerest thank to all of the following people for their help and support during my research work on this thesis, in particular,

My wise teacher Professor Larissa Panina, who formulated the scientific problem of the thesis and vectored my research. All results obtained in this thesis are in the course of ideas intended by pioneering works of Professor Panina on the GMI effect. Each of us knows how difficult it is to begin creative work especially in such an area of science where the ocean of problems appears so unapproachable. The first successful results fill one with enthusiasm to over come the difficulties. Professor Panina introduced me into science and gave me the self-believe to fulfil my own research potential. Larissa is my reliable friend, who was always there to understand and help.

My co-supervisors, Professor Desmond Mapps and Dr Mazafar Akhter for their constructive supervision and guidance. Their wide life and scientific experience was very useful for me.

Mr Nick Fry, who taught me thin film technology and helped in all questions related with experiments and writing the papers. Nick's great experience in any technological aspects gave us the opportunity to realise many interesting MI behaviours in thin films and tuneable composite materials.

Our craftsman, Mr Phillip Brown. Phil can make everything from a bicycle to a steam locomotive. All accessories in our clean room have been made by Phil's hands. Furthermore, he is nice and kindhearted man.

Our Captain, Mr Stewart Warner. Stewart is an expert in electronics and a living picture of a genuine Englishman. His Navy bearing and punctuality made for a good-style of work in the laboratory. Stewart has developed several electronic circuits for the MI sensors, which allow us to appreciate the advantages of the MI effect. What is more important, he is a dreamer in a good sense of this word. Such people make discoveries!

Mr Serghei Sandacci, for the friendship and collaboration.

CONTENTS

Appendixes to Chapter 5 (papers):

FIGURE LIST

Chapter 1 Introduction and background research

No figures

Chapter 2 Magneto-impedance matrix in ferromagnetic wires

Chapter 3 Magneto-impedance matrix in thin films

Chapter 4 Magneto-impedance sensors

Chapter 5 Tuneable composites

Chapter 6 Future work

In loving memory of my father

Peter Makhnovskiy…

[15.07.1927 – 20.02.2003]

Chapter 1 Introduction and background research

1.0 Actuality and eccentricity of the investigation

Since the discovery of the magneto-impedance effect (MI) in 1994,[1,2] it has received much attention due to its importance for developing micro-magnetic sensors of high performance.[3-10] The variety of MI materials has increased significantly. These materials include thin metallic ferromagnetic wires (which can be coated by glass), ribbons and thin films made of amorphous or nanocrystalline ferromagnetic alloys. In simple terms, the MI effect is understood as a change of the complex resistance (impedance) of a ferromagnetic sample subjected to a high frequency current and a dc external magnetic field. Strong field effect, which makes the MI effect attractive for sensor applications, became possible because of discovery of new materials with specific magnetic structures, in the first place, amorphous ferromagnetic wires with circumferential or helical anisotropy. At present, the MI effect is considered wider as the generalisation of Ohm's law, which includes the off-diagonal components originating from the gyrotropic properties of ferromagnetic media. A manifestation of the off-diagonal effect is generation of coil voltage by an ac longitudinal current flowing in MI element.

The MI effect, which accumulates many peculiar physical principles used in other sensors, provides a wide variety of the field characteristics along with simplicity of the sensor circuit design. In turn, it requires the detailed analysis of many factors determining the MI effect. However, most of the theoretical work is restricted to specific conditions not always consistent with the experiment. In certain cases, conflicting experimental results on MI in materials with similar magnetic structures have been reported. This may occur, for example, when different types of excitation are used. In particular, this is related to the case of a complicated magnetic configuration, as the case of a helical magnetisation in a ferromagnetic wire. Therefore, rigorous theoretical and experimental research of the MI effect accounting for specific magnetic structures and excitation methods remains to be of a considerable interest and importance.

In the present work, the concept of the magneto-impedance matrix has been elaborated, which enables the explanation of variety of MI field characteristics in wires and films from the common point of view.[11-14] The experimental technique employed in the work allowed us to measure all components of the total magneto-impedance matrix that came as the first verification of the matrix concept of the magneto-impedance.[12]

The fabrication technologies of the narrow thin film MI samples with different structures also were developed, including sandwiched films and films integrated with a helical planar microcoil.[15] This opens up possibilities of creation of the integrated MI sensors.

The applications of the MI effect are not limited only by magnetic sensor technology. In this work, a new type of tuneable composite materials was proposed, the effective microwave permittivity (dielectric constant) of which depends on the dc external magnetic field applied to the composite as a whole.[16] The composite consists of the short pieces of ferromagnetic wires embedded into a dielectric matrix. It can be fabricated in the form of thin slab with thickness less than 1 millimetre. The wire inclusions have random orientations in the plane of the composite slab. The field dependence of the effective permittivity arises from a high field sensitivity of the ac surface impedance of a ferromagnetic wire. A number of applications can be proposed, including selective microwave coatings with the field-dependent reflection/transmission coefficients and selective tuneable waveguides where the composite material may be used as an additional field-dependent coating.

The work is organised as follows. In Chapter 1, we will consider general physical principles of the MI effect. The equation of motion of the magnetisation under the action of an external magnetic field plays a key role in MI study. In spite of the fact that this equation is excepted without any revisions, the MI structures required new electrodynamics problem settings. Considering a weak alternating excitation in the microwave range, the equation of motion of magnetisation allows us to calculate the ac permeability matrix of a linear local response. This matrix is used to solve the Maxwell equations in the magneto-anisotropic medium, where the solution has to satisfy specific boundary conditions. The measurable quantity calculated is the surface impedance matrix, which is expressed through the components of the permeability matrix. After the consideration of the essential aspects of ferromagnetism in Section 1.1, we proceed to the main subject concerning the response of a ferromagnetic system to an external magnetic field. In Section 1.2, we begin our analysis with the equation of motion of an elementary magnetic moment. This equation prompts the general form, which is used in Section 1.3 to obtain the equation of motion of the magnetisation in an isotropic and unbounded ferromagnetic medium considered as a strongly correlated system of elementary magnetic moments. In addition, in Section 1.3 we introduce a phenomenological approach to the dissipative processes in the ferromagnetic system. The modifications of the equation of motion for shaped and anisotropic samples are considered in Sections 1.4 and 1.5.

In Sections 1.6 and 1.7 we introduce the magnetostatic model used in the present work and discuss the role of the exchange effect on the ac response.

1.1 Essential aspects of ferromagnetism

This Section is undertaken as a comprehensive review of the physical principles of ferromagnetism since this magnetic state constitutes the basis of any MI element. Three 3d-metal crystals are ferromagnetic at room temperature: iron, nickel, and cobalt, as well as, their alloys. The ferromagnetic state also can be established in some amorphous ferromagnetic alloys, therefore it is not a specific crystalline property. Note that Co-based amorphous alloys form the basis of the MI materials [4,7].

In general, there are five main magnetic states: (a) diamagnetism, (b) paramagnetism, (c) ferromagnetism, (d) antiferromagnetism and (e) ferrimagnetism.[17] The first two magnetic states (a) and (b) are not related with magnetic ordering in material, whereas the last three (c)-(e) grow out of a certain magnetic ordering. The magnetic moment per unit volume of a magnetic material is the magnetisation M. The relationship between M and the external magnetic field H can be expressed by $M = M_{rm} + \chi H$, where M_{rm} is the residual magnetisation (remanence), $\chi(M)$ is the magnetic susceptibility. This general relationship between M and H takes into account a possible hysteretic behaviour, when $\chi(M)$ becomes a two-valued function having different values for two branches of the hysteresis loop. The observed value of susceptibility ranges from 10^{-5} up to 10^{6} and higher. In some cases, it takes a negative value. Sometimes the relationship between M and H is not linear, so χ depends on the intensity of H. All magnetic states can be characterised through the properties of χ.

Diamagnetism is a weak magnetic effect in which the magnetisation is exhibited opposite to the direction of the applied field. The susceptibility is negative and is usually about 10^{-5}. The origin of this magnetism is an orbital rotation of electrons about the nuclei induced electromagnetically by the application of an external field. The induced current produces a magnetic flux, which is opposite to the external field. Paramagnetism is observed in materials possessing atomic magnetic moments. The application of a weak magnetic field results in partial ordering, having a negligible effect on the value of elementary magnetic moments. The order of χ is $10^{-5} - 10^{-3}$.

In most cases, paramagnetic materials contain magnetic atoms or ions whose spins are isolated from their magnetic environment and can more or less freely change their directions. Therefore, the small effect is caused by thermal agitation, which acts to oppose the ordering influence of the applied magnetic field. The susceptibility in such paramagnetics is inversely proportional to the absolute temperature (the Curie law). Conduction electrons, which form an energy band in metallic crystals, also exhibit paramagnetism. In this case, most conduction electrons have zero probability to align along the applied field since the energy states with parallel states are occupied. Only a fraction of electrons near the Fermi level contribute to the permeability, which is independent of temperature. (the so-called Pauli paramagnetism)

A ferromagnetic substance has a characteristic property of the spontaneous parallel orientation of elementary magnetic moments, which results in a larger magnetisation of the whole sample even for a weak external field, if the temperature does not exceed the Curie temperature T_c. On the other hand, it is possible for the magnetisation of the same sample to be zero in zero (or nearly zero) applied field. *These two experimental facts define the essential aspects of ferromagnetism.*[17,18] Thus, the ferromagnetic sample is to be characterised as a system of strongly ordered magnetic moments. As it was pointed out by Weiss,[19] the thermal agitation could be largely circumvented if one postulated in ferromagnetic materials the existence of a strong internal *effective field* or the so-called *"molecular" field* H_Λ. The effective field gives an approximate representation of the quantum-mechanical *exchange interaction*, which is mutual electrostatic interactions between electrons.[17,18,20] The electrostatic energy of electrons depends on the relative orientation of their spins: the difference in energy defines the exchange energy. This interaction tends to line up the magnetic moments parallel to one another. The required magnitude for the Weiss effective field may be estimated as follows. At the Curie temperature T_c the thermal energy κT_c of an electron spin is of the same order of magnitude as the interaction energy $\mu_B H_\Lambda$ of the magnetic moment μ_B of electron acted on by the effective field H_Λ, so that:[18]

$$H_\Lambda = \frac{\kappa T_c}{\mu_B}, \qquad (1)$$

where κ is the Boltzmann constant and μ_B is the Bohr magneton. For typical ferromagnetic materials as Fe $T_c \sim 10^3 K$, which gives the value of H_Λ of the order of 10^7 Oe.

At temperatures below T_c the effect of the effective field outweighs the thermal fluctuation energy and substance becomes ferromagnetic.

The dipole magnetic moment interaction between electrons is much weaker to account for the effective field. The dipole field is evaluated as:[18]

$$H_m \sim \frac{\mu_B}{r^3}, \tag{2}$$

where r is the atomic distance. Taking $r \propto 10^{-8}$ cm, $H_m \sim 10^4$ Oe, which is much smaller than the Weiss field H_Λ. The magnetic moment interaction by itself would lead to the Curie temperature of about of 0.1^0K. The exchange interaction will be dealt with later in Section 1.7.

However, the important property of a ferromagnetic substance, namely, that the magnetisation may be much smaller than the saturation one, can not be explained in the assumption of the existence of the effective field H_Λ only. This behaviour can be explained by assuming that actual samples are composed of a number of small regions called domains, within each of which the local magnetisation is saturated. The same effects are observed in polycrystalline samples, for which the resultant magnetic moment becomes zero by virtue of a random distribution of the local magnetic moments in different granules. The increase of the resultant magnetic moment of the whole sample under the action of an applied magnetic field arises from two mechanisms: (i) an increase in the volume of domains which are favourably oriented with respect to the field at the expense of unfavourably oriented domains, and (ii) rotation of the directions of magnetisations towards the direction of the field.[17,18] In weak fields the resultant magnetisation changes mostly due to the domain wall motion, whereas in strong fields it is by means of the rotation of magnetic moments.

Antiferromagnets assume a kind of the magnetic ordering in which the magnetic moments completely compensate for each other and this causes zero spontaneous magnetisation of the whole sample. In simplest case, this ordering may be realised in the so-called "chessboard structure" in which each magnetic moment is surrounded by the moments with opposite direction. Some more complicated orderings are also possible. Antiferromagnetism exists within the limits of a certain temperature range until the Neel temperature T_N. The origin of antiferromagnetism also lies in the negative exchange interaction between electrons, in contrary to the positive one in the case of ferromagnetism.

Since at low temperature the ordering of opposite moments becomes more pronounced, the susceptibility decreases with a decrease in temperature, as opposed to the paramagnetic or ferromagnetic behaviour. Above the Neel temperature the moment arrangement becomes random, so that the susceptibility also decreases with an increase of temperature and the antiferromagnet passes into the paramagnetic state.

In a ferrimagnet the magnetic moments with opposite directions occupy two (or more) sublattices, the number of magnetic moments and their magnitude are different in each lattice and that gives rise to a resultant spontaneous magnetisation of the whole sample. Therefore, ferrimagnetism can be characterised as "uncompenseted" antiferromagnetism.

1.2 Equation of motion of an elementary magnetic moment

We begin our study of the basic theory with the classical description of the motion of an elementary magnetic moment $\mathbf{m}$ in an external magnetic field $\mathbf{H}$, assuming that $\mathbf{H}$ may possibly vary with time.[17,21-23] $\mathbf{H}$ will produce a torque on the magnetic moment of amount $(\mathbf{m}\times\mathbf{H})$, where the multiplication symbol inside the brackets denotes the vector multiplication. If the magnetic moment could turn, it would attempt to line up along $\mathbf{H}$. Under the conditions that $\mathbf{H}$ is constant in time and there are no losses related with $\mathbf{m}$ ("frictionless" moment), $\mathbf{m}$ would actually oscillate about the equilibrium direction. If there are some losses, the oscillations would die out until eventually $\mathbf{m}$ would be lined up along $\mathbf{H}$.

When the magnetic moment $\mathbf{m}$ also possesses angular momentum $\mathbf{J}$, the situation is modified, since it now acts like a gyroscope. In the absence of losses, $\mathbf{m}$ would remain at a fixed angle with respect to $\mathbf{H}$ (providing $\mathbf{H}$ is constant in time), but would precess about it. The conversion of energy back and forth between the potential and kinetic energies would not occur. It would still be true, however, that if there are some losses, $\mathbf{m}$ would eventually become parallel to a static field $\mathbf{H}$. The losses correspond to the relaxation processes with a characteristic time t associated with the approach to thermal equilibrium. t is called the "spin-lattice relaxation time". Phenomenological treatment of the losses in the system of magnetic moments will be considered later in Section 1.3. Here, we would like to write the equation of motion of the magnetic moment without losses, which is found by equating the torque with the rate of change of angular moment, $\mathbf{J}$:[17,21]

$$\frac{d\mathbf{J}}{dt} = -(\mathbf{m}\times\mathbf{H}). \qquad (3)$$

Since $\mathbf{m}=\gamma\mathbf{J}$, we may eliminate $\mathbf{J}$, getting:

$$\frac{d\mathbf{m}}{dt}=-\gamma(\mathbf{m}\times\mathbf{H}), \tag{4}$$

where γ is a scalar called *the gyromagnetic ratio.* This equation, which holds regardless of whether or not $\mathbf{H}$ is time dependent, tells us that at any instant the changes in m are perpendicular to both m and $\mathbf{H}$.

A simple classical picture will enable us to make a correct order-of-magnitude estimate of γ. Let us calculate the magnetic moment and angular moment of a particle of mass m and charge e moving in a circular path of radius r with period T. The angular momentum is then:

$$J=m\frac{2\pi r^2}{T} \tag{5}$$

while the magnetic moment (treating the system as a current loop) is:

$$\mathrm{m}=\frac{e}{c}\frac{\pi r^2}{T}. \tag{6}$$

Comparison of the expressions for m and J therefore gives us $\gamma=e/2mc$. The important result of this formula is that large masses have low γ's. We expect about a factor of 1000 lower γ for nuclei than for electrons.

In the quantum theory, $\mathbf{m}$ and $\mathbf{J}$ are treated as operators $\hat{\mathrm{m}}$ and $\hat{\mathrm{J}}$, respectively. We define a dimensionless angular moment operator, $\hat{\mathrm{I}}$, by the equation:[24,17]

$$\hat{\mathrm{J}}=\hbar\hat{\mathrm{I}}, \tag{7}$$

where $\hat{\mathrm{I}}^2$ has eigenvalues $L(L+1)$, where L is either integer or half-integer. Any component of $\hat{\mathrm{I}}$ (for example, $\hat{\mathrm{I}}_z$) commutes with $\hat{\mathrm{I}}^2$, so that we may specify simultaneously eigenvalues of both $\hat{\mathrm{I}}^2$ and $\hat{\mathrm{I}}_z$. The eigenvalues m of $\hat{\mathrm{I}}_z$ may be any of the $2L+1$ values: $L, L-1, \ldots, -L$.

The application of a magnetic field $\mathbf{H}$ produces an interaction energy of amount $-(\mathbf{m}\cdot\mathbf{H})$, where the multiplication symbol denotes the scalar multiplication. We have, therefore, a very simple Hamiltonian (Zeeman energy):

$$\hat{\mathrm{H}}=-\mathbf{m}\cdot\mathbf{H}. \tag{8}$$

Taking the field to be H_0 along the z-direction, we find:

$$\hat{\mathrm{H}} = -\gamma\hbar H_0 \hat{\mathrm{I}}_z . \tag{9}$$

The eigenvalues of this Hamiltonian are simple, being only multiplies ($\gamma\hbar H_0$) of the eigenvalues of $\hat{\mathrm{I}}_z$. Therefore the allowed energies are:

$$\mathrm{E} = \gamma\hbar H_0 m,\ m = L,\ L-1,\ \ldots,\ -L . \tag{10}$$

One should hope to be able to detect the presence of such a set of energy levels by some form of spectral absorption. The coupling most commonly used to produce magnetic resonances is an alternating magnetic field applied perpendicular to the static field H_0. To satisfy the conservation of energy, an angular frequency ω must be that:

$$\hbar\omega = \Delta\mathrm{E} = \gamma\hbar H_0 \text{ or } \omega = \gamma H_0 . \tag{11}$$

Note that Planck's constant has disappeared from the resonance equation. This fact suggests that the result is closely related to a classical picture. From Eq. (11) we can calculate the frequency needed to observe a resonance: $\omega_{res} = \gamma H_0$.

The close correspondence of the classical and quantum mechanical treatments is made particularly clear by examination of a differential equation relating the time variations of the expectation values m_x, m_y, and m_z. The equation is based on a well-known formula whose derivation we sketch.[21,24]

Suppose we have a pair of wave functions $\Psi(t)$ and $\Phi(t)$, both of which are solutions of the same Schrödinger equation with an Hermitian operator of energy $\hat{\mathrm{H}}$:

$$-\frac{\hbar}{i}\frac{\partial\Psi}{\partial t} = \hat{\mathrm{H}}\Psi , \qquad -\frac{\hbar}{i}\frac{\partial\Phi}{\partial t} = \hat{\mathrm{H}}\Phi . \tag{12}$$

Let us have some operator $\hat{\mathrm{F}}$ that has no explicit time dependence. Then:

$$\frac{d}{dt}\int\Phi^*\hat{\mathrm{F}}\Psi\,\mathbf{dx} = \frac{i}{\hbar}\int\Phi^*(\hat{\mathrm{H}}\hat{\mathrm{F}} - \hat{\mathrm{F}}\hat{\mathrm{H}})\Psi\,\mathbf{dx} , \tag{13}$$

where $\mathbf{x}$ is the vector of the three rectangular coordinate and the symbol "*" designates the complex conjugation.

We define the operator "$d\hat{\mathrm{F}}/dt$" by the equation:

$$\int\Phi^*\frac{d\hat{\mathrm{F}}}{dt}\Psi\,\mathbf{dx} = \frac{d}{dt}\int\Phi^*\hat{\mathrm{F}}\Psi\,\mathbf{dx} . \tag{14}$$

By using $d\hat{\mathrm{F}}/dt$ in this symbolic sense, we have:[24]

$$\frac{d\hat{\mathrm{F}}}{dt}=\frac{i}{\hbar}[\hat{\mathrm{H}},\hat{\mathrm{F}}], \tag{15}$$

where $[\hat{\mathrm{H}},\hat{\mathrm{F}}]$ is the usual commutator $\hat{\mathrm{H}}\,\hat{\mathrm{F}}-\hat{\mathrm{F}}\hat{\mathrm{H}}$. We may use this formalism to calculate the time derivative of the expectation values of m_{X}, m_{y}, and m_{Z}. We shall wish to use the commutation relations for the components of angular momentum, all of which may be obtained by cyclic permutation from $[\hat{\mathrm{I}}_x,\hat{\mathrm{I}}_y]=i\hat{\mathrm{I}}_z$. Then:

$$\frac{d\hat{\mathrm{I}}_x}{dt}=\frac{i}{\hbar}[\hat{\mathrm{H}},\hat{\mathrm{I}}_x]=\gamma H_0\hat{\mathrm{I}}_y,$$

$$\frac{d\hat{\mathrm{I}}_y}{dt}=\frac{i}{\hbar}[\hat{\mathrm{H}},\hat{\mathrm{I}}_x]=-\gamma H_0\hat{\mathrm{I}}_x, \tag{16}$$

$$\frac{d\hat{\mathrm{I}}_z}{dt}=0.$$

These equations are the component equations of the vector operator equation:

$$\frac{d\hat{\mathrm{I}}}{dt}=-\gamma(\hat{\mathrm{I}}\times\mathbf{H}). \tag{17}$$

Since $\hat{\mathrm{m}}=\gamma\hbar\hat{\mathrm{I}}$, using Eq. (14) we obtain the equation for the expectation value of magnetisation $\mathbf{m}=<\hat{\mathrm{m}}>$: $d\mathbf{m}/dt=-\gamma(\mathbf{m}\times\mathbf{H})$, which is just the classical equation (4). *Therefore, the classical equation correctly describes the dynamics of the magnetisation.*

1.3 Equation of motion of the magnetisation in isotropic ferromagnetic medium

The exchange interaction, which strongly ties together the elementary magnetic moments in the magneto-ordered materials, allows a continual macroscopic approach [22] for the description of the motion of magnetisation $\mathbf{M}$. The same continual approach was used in the Weiss theory of ferromagnetism,[17-19] where the exchange interaction ("molecular field") was postulated. Since $\mathbf{M}$ is the magnetic moment per unit volume, using Eq. (4) we can immediately write the equation of motion of $\mathbf{M}$ in an isotropic and unbounded ferromagnetic medium:[17,21-24]

$$\frac{d\mathbf{M}}{dt}=-\gamma(\mathbf{M}\times\mathbf{H}), \tag{18}$$

where $\mathbf{M} = \frac{1}{\Delta V}\sum_{\Delta V}\mathbf{m}$ and ΔV is a small macroscopic volume containing magnetic moments, $\gamma = ge/2mc$, and g is the Lande factor. Note that the g-factor is assumed, subject to experimental verification, to be a constant independent of field orientation, sample shape, etc.

In the frame of this phenomenological approach, the losses in the magnetic system can be taken into account by means of a small dissipative term $\mathbf{R}$ added in Eq. (18):[17, 21-25]

$$\frac{d\mathbf{M}}{dt} = -\gamma(\mathbf{M}\times\mathbf{H}) + \mathbf{R}, \tag{19}$$

where $\mathbf{R}$ describes a dissipation of energy due to the spin-lattice relaxation.

There are several different notations of the dissipative term in Eq. (19). The simplest and natural assumption is that the magnetisation is exposed to an additional effective field (in spite of $\mathbf{H}$) proportionate to the velocity of the magnetisation change $\partial\mathbf{M}/\partial t$, in other words "friction" proportionate to the velocity of change. This assumption is quite typical for many dynamic systems, and not only for mechanical ones. Then, introducing the dimensionless spin-relaxation (damping) parameter τ, we obtain the following equation:

$$\frac{d\mathbf{M}}{dt} = -\gamma(\mathbf{M}\times\mathbf{H}) + \frac{\tau}{M}\left(\mathbf{M}\times\frac{\partial\mathbf{M}}{\partial t}\right), \tag{20}$$

which is known as *the Gilbert equation*.[26,27] This equation was first obtained in a slightly different form by Landau and Lifshitz in 1935 and used for the study of domain wall motion:[28]

$$\frac{d\mathbf{M}}{dt} = -\gamma(\mathbf{M}\times\mathbf{H}) - \frac{\omega_d}{M^2}(\mathbf{M}\times(\mathbf{M}\times\mathbf{H})), \tag{21}$$

where ω_d is the characteristic damping frequency. Both Eqs. (20) and (21) are equal since Eq. (21) can be transformed into the form (20) by means the replacements $\gamma \to \gamma/(1+\tau^2)$ and $\omega_d \to \tau\gamma M/(1+\tau^2)$. However, because of physical meaning of γ, Eqs. (20) and (21) are similar only the limit of a small relaxation ($\tau << 1$). For $\tau \sim 1$, Eq. (20) has to be used. Equations (20) and (21) are characterised by a single dissipative parameter and will be collectively called *the Landau-Lifshitz-Gilbert equation.*

The main property of Eqs. (20) and (21) is that the dissipative terms are perpendicular to $\mathbf{M}$, hence $|\mathbf{M}|$ is a constant: $\partial|\mathbf{M}|/\partial t \equiv 0$. In some cases, the processes, which give rise to a dissipation, do not provide the constancy of $|\mathbf{M}|$.

In the presence of these processes, Eqs. (20) and (21) are not fully valid, but since damping is usually found experimentally to be small, $|\mathbf{M}|$ still remains nearly time-independent.

Many attempts have been undertaken to write the equations of motion of $\mathbf{M}$ with a great number of the dissipative parameters, which would provide a possibility to a change of the magnetisation magnitude. In particular, the following so-called *Bloch equation* was proposed, containing two dissipative parameters $\tau_{1,2}$:[22,23]

$$\frac{d\mathbf{M}}{dt} = -\gamma(\mathbf{M}\times\mathbf{H}) + \frac{(\mathbf{M}_0 - \mathbf{M}_z)}{\tau_1} - \frac{(\mathbf{M} - \mathbf{M}_z)}{\tau_2}, \tag{22}$$

where the z-axis is directed along the equilibrium magnetisation $\mathbf{M}_0$ and $\mathbf{M}_z$ is the direct-axis magnetisation. The dissipative parameters in Eq. (22) differ for the transverse $(\mathbf{M} - \mathbf{M}_z)$ and longitudinal $(\mathbf{M}_0 - \mathbf{M}_z)$ magnetisations. This equation is used for the description of the magnetic resonance in the magneto-disordered systems, such as: the nuclear magnetic resonance and electronic paramagnetic resonance.[21]

The study of damped magnetisation dynamics remains important in modern research due to its significance for the development of nanomagnetic devices and high-density magnetic recording. As was recently shown by Smith and Arnett [29], thermally generated magnetisation fluctuations in very thin (1–3 nm) soft magnetic sensing layers (CoFe and/or NiFe) of thin-film magneto-resistive devices may be observed as broadband resistance-noise using simple electrical measurements. Thermally induced magnetic noise at lower frequencies < 1–2 GHz in particular has potentially serious practical implications, as it will serve as a fundamental limit of the signal/noise ratio of these devices when used as sensors. For this reason, the study of this phenomenon has received significant recent attention.[30,31]

The Landau–Lifshitz and Gilbert equations obtained above conserve the absolute value of magnetisation ($|\mathbf{M}| = const$) in a single domain region due to the strong exchange interaction approximation. The value of magnetisation depending on temperature remains constant during any dynamical process, which is described by a special type of the relaxation term. Recently a new theoretical approach was proposed by Safonov and Bertram to correct the limitations of the Landau–Lifshitz–Gilbert (LLG) theory. This new theoretical approach was developed in the series of papers [32-36]. The main idea consists of the representation of the magnetisation dynamics as the motion of damped non-linear oscillators with random forces of thermal fluctuations. Nonlinearity in the relaxation process appears with the increase of magnetisation deviation from equilibrium.[35]

Depending on the situation, the non-linear magnetisation damping either increases or decreases the total relaxation rate. According to this approach, for a uniform magnetisation motion the crystal symmetry should influence the form of the relaxation terms and therefore the phenomenological damping term should contain a damping tensor with several damping parameters (''hierarchy of dissipative terms'') instead of one (isotropic) damping term.[33,36] However, the general problem of magnetisation damping cannot be solved using just symmetry considerations. The magnetisation relaxation process appears as a result of microscopic interactions of spins with each other and with phonons, conduction electrons, and so on. In other words, a direct connection with microscopic physics must be made to clarify the nature of the damping terms.[35]

The approach proposed by Safonov and Bertram was criticised by Smith in [37]. Smith has shown that the fluctuation-dissipation theorem (FDT) can be used to quantitatively describe the relation between the measured resistance-noise power and the dissipative properties of the constituent magnetic films, the latter typically is characterised by a Gilbert phenomenological damping term with a scalar parameter τ. The FDT was used to argue that the phenomenological Gilbert approximation, implicitly assuming a spatially (and temporally) local damping mechanism, provides a physically plausible model for damping in ferromagnetic materials that is quite analogous to well understood resistive damping in simple metallic conductors. The FDT does not prove that Gilbert damping is physically correct. Rather, it simply argues that the Gilbert term is physically consistent with more basic theoretical considerations of intrinsic physical damping mechanisms in real ferromagnetic films and does not lead to physically nonsensical results under examination with the FDT in the naturally general case of spatially nonuniform magnetisation fluctuations. Similarly, the FDT analysis here does not disprove the possibility of some form of ''nonlocal'' phenomenological damping model. Rather, it would more modestly argue that any nonlocal components of such a model should have a physical basis that is related to an *actual damping mechanism* in real ferromagnetic materials, such as discussed elsewhere recently rather than rely on broad generalizations based on faulty physics/mathematics or on simple, heuristically appealing but otherwise not physically justified, approximations.

There is no doubt that thermal fluctuations will restrict the signal/noise resolution in a real MI sensor. Nevertheless, this factor does not change the general concept of the investigation using the LLG theory and it can be taken into account by means of the FDT, as it has been fairly noted by Smith.

As it will be seen throughout this work, the LLG theory is a suitable model which allows us to describe the main features of the MI field behaviour for all components of the impedance matrix. Also, it is important to note that MI elements never reach nanoscale dimensions (see the discussion on the size effect in Section 3.8), when the thermal effects become especially critical. Moreover, in the MI theory we always consider only a small excitation magnetic field (*the so-called "linear response theory"*), which does not result in magnetic reversal, and hence there is no need to consider possible non-linear relaxation processes, which the Safonov-Bertram theory appeals to.

1.4 Equation of motion of the magnetisation in the shaped sample

Previous consideration in Section 1.3 assumed that $\mathbf{M}$ was exposed to the applied field $\mathbf{H}$. This assumption is no longer valid for a shaped sample, where the internal magnetic field $\mathbf{H}_i$ does not coincide with $\mathbf{H}$ by the direction and magnitude due to the demagnetising field. Therefore, we have to modify Eqs. (20) and (21) to take into account this effect. In Section 1.5, the methods developed here will be generalised for the anisotropic sample.

The ac linear response from a small isotropic ferromagnetic ellipsoid was first investigated by Kittel.[38] It was a significant advance after the work of Landau and Lifshitz.[28] The Kittel method of the demagnetising factors developed for an isotropic ellipsoid was further generalised by MacDonald [39] for the anisotropic one.

We begin our study with the isotropic and nonconductive ferromagnetic ellipsoid. The ellipsoid is subjected to an external magnetic field $\mathbf{H}$, which consists of a larger constant field (dc) $\mathbf{H}_{ex}$ and small alternating field (ac) $\mathbf{h}$: $\mathbf{H} = \mathbf{H}_{ex} + \mathbf{h}$. The ellipsoid dimension is assumed to be much smaller than the wavelength inside the material, the so-called quasistatic approximation. This allows us to use only magnetostatic equations to determine the internal magnetic field $\mathbf{H}_i$, which also can be decomposed into the dc and ac fields: $\mathbf{H}_i = \mathbf{H}_i^0 + \mathbf{h}_i$. As it is well known from the magnetostatic theory,[40] the field $\mathbf{H}_i$ inside the nonconductive magnetic ellipsoid is homogeneous and can be represented through $\mathbf{H}$ and $\mathbf{M}$ by means of the demagnetising matrix $\hat{\mathbf{N}}$:

$$\mathbf{H}_i = \mathbf{H} - \hat{\mathbf{N}}\mathbf{M}, \tag{23}$$

where $\mathbf{M}$ may depend on $\mathbf{H}_i$. The field $\mathbf{H}_{DM} = -\hat{\mathbf{N}}\mathbf{M}$ is called the demagnetising field.

At the quasistatic approximation, we can neglect the retarding effect inside the ellipsoid so that the momentary value of $\mathbf{H}$, $\mathbf{H}_i$ and $\mathbf{M}$ are related by the same equations and boundary conditions as the static ones. In this case, the relation (23) can be written separately for the dc and ac fields:

$$\mathbf{H}_i^0 = \mathbf{H}_{ex} - \hat{\mathbf{N}}\mathbf{M}_0, \tag{24}$$

$$\mathbf{h}_i = \mathbf{h} - \hat{\mathbf{N}}\mathbf{m}, \tag{25}$$

where $\mathbf{M} = \mathbf{M}_0 + \mathbf{m}$, $\mathbf{M}_0$ is the equilibrium magnetisation, and $\mathbf{m}$ is the ac (small) magnetisation induced by $\mathbf{h}$. The equilibrium direction of $\mathbf{M}_0$ is found from Eq. (24):

$$(\mathbf{M}_0 \times \mathbf{H}_i^0) = (\mathbf{M}_0 \times (\mathbf{H}_{ex} - \hat{\mathbf{N}}\mathbf{M}_0)) \equiv 0, \tag{26}$$

where $|\mathbf{M}_0|$ is considered to be field-independent.

The Kittel method of the effective demagnetising factors [38] lies in the fact that using Eqs. (24) and (25), the unknown internal field $\mathbf{H}_i$ can be left out from the equation of motion. Since we intend to study a linear response, the ac excitation has to be quite small to provide the strong inequality $|\mathbf{m}| << |\mathbf{M}_0|$. Because of this, the demagnetising matrix $\hat{\mathbf{N}}$ is a function of $\mathbf{M}_0$ only:

$$\mathbf{h}_i = \mathbf{h} - \hat{\mathbf{N}}(\mathbf{M}_0)\mathbf{m} \tag{27}$$

This is the main equation of the Kittel method.

Substituting $\mathbf{H}_i$ instead of $\mathbf{H}$ in Eqs. (20) and (21), we obtain new equations with the account of the demagnetising effects:

$$\frac{d\mathbf{m}}{dt} = -\gamma(\mathbf{M} \times \mathbf{H}_i) + \frac{\tau}{M}\left(\mathbf{M} \times \frac{\partial \mathbf{m}}{\partial t}\right), \tag{28}$$

$$\frac{d\mathbf{m}}{dt} = -\gamma(\mathbf{M} \times \mathbf{H}_i) - \frac{\omega_d}{M^2}(\mathbf{M} \times (\mathbf{M} \times \mathbf{H}_i)), \tag{29}$$

where the equality $\partial \mathbf{M}_0 / \partial t \equiv 0$ was used.

The linearisation method of solution consists in the representation of all quantities as the sum of a larger dc constituent and small ac addition: $\mathbf{M} = \mathbf{M}_0 + \mathbf{m}$ and $\mathbf{H}_i = \mathbf{H}_i^0 + \mathbf{h}_i$, where $|\mathbf{m}| << |\mathbf{M}_0|$ and $|\mathbf{h}_i| << |\mathbf{H}_i^0|$.

Using these inequalities and Eqs. (24), (27), (28), we obtain at the single-mode excitation $\sim \exp(-i\omega t)$ the following linearised equation in the first approximation by the complex amplitude $\mathbf{m}$ and $\mathbf{h}$:

$$-i\omega\,\mathbf{m}+(\omega_H - i\tau\omega)(\mathbf{m}\times\mathbf{n}_{z'})+\gamma M_0((\hat{\mathbf{N}}\mathbf{m})\times\mathbf{n}_{z'})=\gamma M_0(\mathbf{h}\times\mathbf{n}_{z'}), \qquad (30)$$

where $\hat{\mathbf{N}}=\hat{\mathbf{N}}(\mathbf{M}_0)$, $\omega_H=\gamma H_i^0$, $H_i^0=\mid \mathbf{H}_{ex}-\hat{\mathbf{N}}\mathbf{M}_0\mid_{z'}$, and $\mathbf{n}_{z'}$ is the unit vector directed along $\mathbf{M}_0$.

If the ellipsoid is conductive, the relations (25) and (27) are no longer valid since the ac magnetic field $\mathbf{h}_i$ is not homogenous inside the sample due to the skin effect. In this case, to calculate a linear response the equation of motion (20) or (21) has to be solved together with the Maxwell equations. This task is extraordinarily difficult. Nevertheless, if the skin depth is of the order of the characteristic size of the sample or larger, the relations (25) and (27) are still true. Thus, for the weak skin effect the Kittel method may be employed for a conductive sample. Another approach to solving electrodynamic problems in ferromagnetic conductive sample is to find the so-called "internal" ac permeability parameter without account of shape effects for alternating field and magnetisation, and then to solve the Maxwell equations with local permeability tensor. In our work, we will use this approach. This is possible, if the demagnetising effect is significantly reduced, when the sample magnetic structure and applied fields do not tolerate strong magnetic poles on its surface. This condition would be provided, for example, by the closure domains in thin film and the dc in-plane external field, or helical magnetisation in wire and the dc longitudinal external field.

1.5 General equation of motion of the magnetisation

In this Section, we would like to generalise the Kittel method of the effective demagnetising factors (see Eq. (27)) for the ferromagnetic sample the state of which is defined by the overall magnetic energy. To conduct this program, we need some additional analysis of the internal field $\mathbf{H}_i$ with relation to the energy accumulated in the sample.

As it can be noted from Eq. (23), the field $\mathbf{H}_i$ in the isotropic ferromagnetic ellipsoid can be calculated as the derivative $-\partial/\partial\mathbf{M}$ from a magnetic energy density U, which is the sum of the Zeeman energy density U_H and the magnetic self-energy density U_M associated with the sample shape:

$$\mathbf{H}_i = -\frac{\partial U}{\partial \mathbf{M}} = \mathbf{H} - \hat{\mathbf{N}}\mathbf{M}, \tag{31}$$

where

$U = U_H + U_M$,

$$U_H = -(\mathbf{M}\cdot\mathbf{H}), \tag{32}$$

$$U_M = \frac{1}{2}(\mathbf{M}\cdot(\hat{\mathbf{N}}\mathbf{M})). \tag{33}$$

The form of Eq. (31) prompts us that $\mathbf{H}_i$ can be considered as an effective field arising from an effective magnetic energy density U. In general, along with U_H and U_M, there are other contributions to the total magnetic energy density, such as: Weiss exchange energy U_e, magnetocrystalline anisotropy energy U_a, the magnetoelastic energy U_{ma} connected with magnetostriction, and domain wall energy U_w. The sum all of these energy densities is called *the magnetic enthalpy density* U_E:

$$U_E = U_H + U_M + U_e + U_a + U_{ma} + U_w. \tag{34}$$

This energy density defines the state of the ferromagnetic sample at given $\mathbf{H}$ and zero absolute temperature $T = 0^0 K$. For $T > 0^0 K$ the same role plays *the so-called free energy density* U_F:

$$U_F = U_H + U_M + U_e + U_a + U_{ma} + U_w - ST, \tag{35}$$

where S is the entropy density. The entropy term $(-ST)$ in this equation becomes very important at high temperatures. It is because of this term, at $T > T_C$ the magneto-disordered state becomes more preferable than the ferromagnetic one due to its larger entropy. However, for our aim of the study of the magneto-ordered system the entropy term can be omitted.

The free energy density U_F is a function of the variables $\mathbf{M}$ and $\partial\mathbf{M}/\partial\mathbf{x}$. Hence, the total energy H of the sample is given by the integral over its volume:

$$\mathrm{H} = \int_V U_F(\mathbf{M}, \partial\mathbf{M}/\partial\mathbf{x})d\mathbf{x}. \tag{36}$$

Applying the condition that the total energy H must be stationary with respect to small variations of $\mathbf{M}$, we obtain:[22,23,39]

$$\delta\int_V U_F(\mathbf{M}, \partial\mathbf{M}/\partial\mathbf{x})d\mathbf{x} = \int_V \left(\left\{ \frac{\partial U_F}{\partial \mathbf{M}} - \sum_{i=1}^{3} \frac{\partial}{\partial x_i} \left(\frac{\partial U_F}{\partial(\partial\mathbf{M}/\partial x_i)} \right) \right\} \cdot \delta\mathbf{M} \right) d\mathbf{x}, \tag{37}$$

where

$$\frac{\delta}{\delta \mathbf{M}} = \frac{\partial}{\partial \mathbf{M}} - \sum_{i=1}^{3} \frac{\partial}{\partial x_i}\left(\frac{\partial}{\partial(\partial \mathbf{M}/\partial x_i)}\right) \tag{38}$$

is the variational derivative (see any description of the calculus of variations, for example, Morse and Feshbach [40]). Since the magnitude of $\mathbf{M}$ has been assumed to be a constant (see explanation in connection with Eqs. (20) and (21)), the variation $\delta \mathbf{M}$ is not completely arbitrary but must lie in the plane perpendicular to the equilibrium magnetisation $\mathbf{M}_0$. Because of this, the stationarity of the functional (37) will be provided if the following condition holds true:

$$\frac{\delta}{\delta \mathbf{M}}\left[U_F + \lambda \mathbf{M}^2\right] = \frac{\delta U_F}{\delta \mathbf{M}} + 2\lambda \mathbf{M} = 0, \tag{39}$$

where λ is the Lagrange constant.

The magnetisation $\mathbf{M}$ inside the sample must be directed along an effective field $\mathbf{H}_{eff}$. By analogy with $\mathbf{H}_i$ in Eq. (31), we can define $\mathbf{H}_{eff}$ as the variational derivative from U_F:

$$\mathbf{H}_{eff} = -\frac{\delta U_F}{\delta \mathbf{M}}. \tag{40}$$

Using Eq. (39), we make sure that the required complanarity condition between $\mathbf{H}_{eff}$ and $\mathbf{M}$ holds true: $(\mathbf{H}_{eff} \times \mathbf{M}) \equiv 0$.

Substituting $\mathbf{H}_{eff}$ instead of $\mathbf{H}$ in Eqs. (20) and (21), we obtain the most general equations of motion:

$$\frac{d\mathbf{m}}{dt} = -\gamma(\mathbf{M} \times \mathbf{H}_{eff}) + \frac{\tau}{M}\left(\mathbf{M} \times \frac{\partial \mathbf{m}}{\partial t}\right), \tag{41}$$

$$\frac{d\mathbf{m}}{dt} = -\gamma(\mathbf{M} \times \mathbf{H}_{eff}) - \frac{\omega_d}{M^2}\left(\mathbf{M} \times \left(\mathbf{M} \times \mathbf{H}_{eff}\right)\right), \tag{42}$$

where the effective field $\mathbf{H}_{eff}$ is given by Eq. (40).

MacDonald has shown in [39] that the effective field $\mathbf{H}_{eff} = \mathbf{H}_{eff}^0 + \mathbf{h}_{eff}$ can be represented in the same forms as the internal field $\mathbf{H}_i$ in Eqs. (23)-(25):

$$\mathbf{H}_{eff} = \mathbf{H} - \hat{\mathbf{N}}_{eff}\mathbf{M}, \tag{43}$$

$$\mathbf{H}_{eff}^{0} = \mathbf{H}_{ex} - \hat{\mathbf{N}}_{eff}\,\mathbf{M}_0, \tag{44}$$

$$\mathbf{h}_{eff} = \mathbf{h} - \hat{\mathbf{N}}_{eff}\,\mathbf{m}, \tag{45}$$

where $\hat{\mathbf{N}}_{eff} = \hat{\mathbf{N}}_{eff}(\mathbf{M}_0)$ is the matrix of effective factors and $\mathbf{h}$ is the external ac magnetic field. Equation (45) is the exact Kittel equation (27).

Using the linearisation method and Eqs. (41), (43)-(45), by analogy with Eq. (30) we obtain the following equation for the complex amplitude $\mathbf{m}$ and $\mathbf{h}$:

$$-i\omega\,\mathbf{m} + (\omega_H - i\tau\omega)(\mathbf{m}\times\mathbf{n}_{z'}) + \gamma M_0((\hat{\mathbf{N}}_{eff}\,\mathbf{m})\times\mathbf{n}_{z'}) = \gamma M_0(\mathbf{h}\times\mathbf{n}_{z'}), \tag{46}$$

where $\hat{\mathbf{N}}_{eff} = \hat{\mathbf{N}}_{eff}(\mathbf{M}_0)$, $\omega_H = \gamma\left(\partial U_F/\partial \mathbf{M}_0\right)_{z'}$ is a scalar, which is understood as the value at the z'-component of the gradient $\left(\partial U_F/\partial \mathbf{M}_0\right)$, and U_F is given by Eq. (35).

Let us indicate the general properties of the susceptibility matrix $\hat{\chi}$, which is found from Eqs. (30) or (46). These properties are more convenient to be formulated in the coordinate system concerned with some preferential direction. So, in an isotropic ferromagnetic medium there is only one preferential direction, which coincides with the direction of the dc external field $\mathbf{H}_{ex}$. In this case, $\hat{\chi}$ must be invariant with respect to the rotations around this axis that gives rise to the off-diagonal and non-symmetric matrix form:[17,22,23]

$$\hat{\chi} = \begin{pmatrix} \chi & -i\chi_a & 0 \\ i\chi_a & \chi & 0 \\ 0 & 0 & \chi_{z'} \end{pmatrix}, \tag{47}$$

where $\chi_{z'}$ is equal to zero in the saturated state (without domains). In general case of a shaped or an anisotropic ferromagnetic sample, the simplest form of $\hat{\chi}$ can be obtained in the coordinate system, where the z'-axis is directed along the equilibrium magnetisation $\mathbf{M}_0$ at the fixed $\mathbf{H}_{ex}$. Then, $\hat{\chi}$ has the off-diagonal form similar to Eq. (47), but the diagonal components χ_{11} and χ_{22} are not equal. Absent a dissipation ($\tau = 0$) in the ferromagnetic system, all components of $\hat{\chi}$ are at resonance at a certain frequency called the ferromagnetic resonance (FMR). A dissipation ($\tau \neq 0$) results in the resonance dispersion curves with a limited amplitude and a finite width.

1.6 Anisotropy energy density

In this and next Sections we would like to continue the discussion of the contributions to the free energy density U_F, which may occur in the MI samples. The most important of them is the anisotropy energy. It is necessary to distinguish between the magnetocrystalline U_a and magnetoelastic U_{ma} anisotropy densities. The latter defines the anisotropy with respect to the directions of the internal or external elastic stresses. For example, in such popular MI material as glass-covered CoFeSiB amorphous wire [42-44] the high quenching rates involved in the fabrication process [45] along with the presence of the glass coating are responsible for a large tension stress induced during fabrication. In turn, these tension stresses and negative magnetostriction (typical for Co-based amorphous alloys) result in a circumferential anisotropy, which play a principal role in the MI effect in wires. The same result can be achieved in glassless CoFeSiB wires by means of a wire drawing of an as-prepared sample.[4,46] A Co-based amorphous alloy is generally used as the material for MI applications, although other materials with a crystalline and polycrystalline (nanocrystalline) structure can be utilised as well.

In the MI thin film samples the required in-plane easy axis anisotropy (transverse, crossed or longitudinal) can be established during the sputtering process in the presence of a strong magnetic field or annealing of an as-prepared film in the presence of magnetic field. But for all that the coupling stress between the final film and substrate may significantly change the easy axis direction from the predetermined one by a strong magnetic field during the sputtering process. In this case, even "a sparing thermal treatment" may restress the whole sample and restore the easy axis to the original direction along the operating field.

Above we took a quick look at main origins of the strain anisotropy encountered in the MI samples. Akulov has shown [18] that regardless of the nature of an anisotropy the anisotropy energy density can be expanded into the power series in the direction cosines of the equilibrium magnetisation $\mathbf{M}_0$. The coefficients at the terms of such series are the phenomenological constants defining the magnetic anisotropy. Below we will designate the anisotropy energy density as U_a regardless its origin.

In magnetic materials characterised by single magnetic axis (easy axis) the anisotropy energy can be approximated by the following expression:[17,47]

$$U_a = -K\cos^2\phi, \tag{48}$$

where K is the anisotropy constant, ϕ is the angle between the easy axis and $\mathbf{M}_0$. When the sample represents single domain, change of its magnetic state under the action of a dc external magnetic field H_{ex} can take place only by rotation of $\mathbf{M}_0$. The character of the magnetisation process $\mathbf{M}_0(H_{ex})$ is defined by the total magnetostatic energy U_0, which is in this case the sum of U_a and the Zeeman energy U_H. In next Chapters it will be shown that a wide variety of the MI field behaviours can be provided by a combination of the anisotropy and crossed dc fields, which include the drive external field $\mathbf{H}_{ex}$ and fixed bias field $\mathbf{H}_b$ applied perpendicularly to $\mathbf{H}_{ex}$. Using Eq. (32), the Zeeman energy in the presence of crossed fields can be written in the following form:

$$U_H = -(\mathbf{M}_0 \cdot (\mathbf{H}_{ex}+\mathbf{H}_b)) = -M_0 H_{ex}\cos\theta - M_0 H_b \sin\theta, \tag{49}$$

where $\mathbf{H}_b \perp \mathbf{H}_{ex}$ and θ is the angle between $\mathbf{M}_0$ and $\mathbf{H}_{ex}$. If α designates the angle between the easy axis and $\mathbf{H}_{ex}$, then using Eq. (48) $U_0 = U_a + U_H$ can be written as the following:[14]

$$U_0 = -K\cos^2(\alpha-\theta) - M_0 H_{ex}\cos\theta - M_0 H_b \sin\theta. \tag{50}$$

The single domain magnetostatic model expressed by Eq. (50) is called *the Stoner-Wohlfarth model.*[47] A real MI sample, if only it is not saturated, is usually in the multidomain state. Nevertheless, for the model calculation we will use only the single domain approximation. There are some reasons for such approach. Firstly, the MI materials are magnetosoft and have sufficiently small coercivity, therefore applying a moderate bias field $\mathbf{H}_b$ we can obtain single domain state, and hence Eq. (50) becomes quite true. Secondly, considering mainly high frequency properties, a local ac response from the sample also can be calculated in the single domain approximation since the domain walls do not have time to follow the ac field and hence their motion is strongly damped. Nevertheless, the domain structure of an unsaturated sample is essential for the magnetostatic properties and in principle can be accounted in the modified joint magnetostatic model, where the magnetisation jumps are defined by the domain coercivity and approaching to the saturation state is describe by rotation of magnetisation.

Furthermore, the ac response of the sample as a whole may differ completely from the local ac response, as it takes place for the off-diagonal impedance in a wire with a circumferential anisotropy and "bamboo-like" domain structure.[12,14] Thus, in the present work the local ac response will be calculated in single domain approximation but the conclusion concerning the total ac response will be always made on basis of averaging over the whole domain structure.

Along with the multidomain structure, dispersion of the magnetic anisotropy may take place. This weak dispersion of the anisotropy is called *magnetisation ripple*. Up to now, this effect has been studied only in thin films (see, for example, [48-51] and references herein) since ferromagnetic wires (amorphous and polycrystalline) are quite new materials. Based on micromagnetics, the ripple theory [52-56] relates the measurable magnetic properties of a magnetic thin film to its real structural characteristics, such as grain size, stress, texture, etc., and explains the deviation from the ideal uniaxial properties described by the Stoner-Wohlfarth theory. Even though weak, the magnetisation ripple may significantly change some measured quantities, such as the ac permeability or impedance (in our case). For example, in [49] the analytical calculation of the permeability frequency spectra using Landau–Lifshitz theory was compared with the experimental results obtained in thin amorphous ferromagnetic films in the vicinity of the ferromagnetic resonance (FMR). It was shown that the initial disagreement between theory and experiment can be attributed to magnetic ripples in the film. In our case, the influence of the anisotropy dispersion on the impedance components can be taken into account by means of their averaging by the anisotropy angle around its direction. In practical situations, it will be enough to introduce a small angle deviation from the perfect direction, as we do in the case of the circumferential and transverse anisotropies.

Also it is necessary to take into account the following conditions. *First, we believe that the size effect in narrow MI films, which has an electrodynamic nature and is discussed in Chapter 3, will reduce the MI effect much more than any "micromagnetic causes" related to the size decrease. Second, the MI effect does not relate to FMR (ferromagnetic resonance), where on account of the resonance behaviour any "irregularities" will change dramatically the measured response. Therefore, the magnetisation ripple effect may not be significant for practical MI elements.*

1.7 Exchange energy density

In this Section we clarify the role of the exchange effect on the ac response in ferromagnetic materials. As it has been mentioned in Section 1.1, the exchange interaction gives rise to the internal exchange energy of magnetic moments subjected to the "effective molecule field" $\mathbf{H}_\Lambda$ (Weiss field). The field $\mathbf{H}_\Lambda$ is proportional to the magnetisation $\mathbf{M}$. In the most general case, the energy U_Λ, related with $\mathbf{H}_\Lambda$, can be represented in the following form:[22,23]

$$U_\Lambda = -\frac{1}{2}\mathbf{M}\hat{\Lambda}\mathbf{M}, \tag{51}$$

where $\mathbf{H}_\Lambda = \hat{\Lambda}\mathbf{M}$ and $\hat{\Lambda}$ is the exchange matrix determined by the anisotropy properties of the material. In many practical cases, relation (51) can be approximated by a simpler functional dependence:

$$U_\Lambda = -\frac{1}{2}\Lambda\mathbf{M}^2, \tag{52}$$

where Λ is a constant. However, the energy U_Λ is insufficient for the full account of the exchange interaction. The fact is that the exchange energy must increase when the adjacent magnetic moments are unparallel that may take place at a rapid spatial changing of $\mathbf{M}$. This circumstance can be taken into account by *the inhomogeneous exchange energy* U_q, which can be represented in the general case as a quadratic form of the magnetisation derivatives:[22,23]

$$U_q = \frac{1}{2}\sum_{i=1}^{3}\sum_{j=1}^{3} q_{ij}\left(\frac{\partial\mathbf{M}}{\partial x_i}\cdot\frac{\partial\mathbf{M}}{\partial x_j}\right), \tag{53}$$

where the scalar multiplication is inside the brackets and q_{ij} is a matrix of the inhomogeneous exchange interaction. A scalar approximation of this equation is of the form:

$$U_q = \frac{1}{2}q\sum_{i=1}^{3}\left(\frac{\partial\mathbf{M}}{\partial x_i}\right)^2, \tag{54}$$

where q is the exchange constant. Therefore, the total exchange energy U_e is expressed by the sum $U_e = U_\Lambda + U_q$.

The principal moment is to clear up a question how the exchange interaction influences the dispersion behaviour of the susceptibility matrix $\hat{\chi}$. Let us consider "the scalar exchange" described by Eqs. (52) and (54). In this case, the contribution from the exchange effect to H_{eff} has to be calculated by means of the variational derivative (40) from U_e:

$$H^e_{eff} = -\frac{\delta U_e}{\delta \mathbf{M}} = \Lambda \mathbf{M} + q\sum_{i=1}^{3}\frac{\partial^2 \mathbf{M}}{\partial x_i^2}. \qquad (55)$$

As it follows from Eqs. (41) and (42), the contribution from H^e_{eff} to the equations of motion for $\mathbf{m}$ is defined by the vector multiplication $(\mathbf{M}\times\mathbf{H}^e_{eff})$. Therefore, the first term in Eq. (55) has no effect on the dynamics of $\mathbf{m}$. The second term may be important in conducting ferromagnetic materials because of the skin effect, in particular, when the skin depth is comparable with the characteristic exchange length. The equation of motion for $\mathbf{m}$ will contain then the term $\partial^2 \mathbf{m}/\partial x_i^2$ and will have to be solved in conjunction with the Maxwell equations. This is a lengthy complicated process. The results of such a solution, reported in works of MacDonald,[39] Kittel and Herring,[56] indicated no appreciable resonance shift $\Delta H/H$, where H is the external dc field at which the ferromagnetic resonance takes place, and ΔH is the resonance shifting in the field scale with respect to the case when the exchange is a negligible quantity. The resonance interval is most sensitive in the dispersion curve, therefore the exchange effect outside of the resonance should be even smaller.

Nevertheless, as it was shown by Rado et al.,[57,58] under suitable conditions the effect of the exchange interaction on the ferromagnetic resonance in metals can be observed experimentally. The ideas underlying these experiments were the following. To increase $\Delta H/H$, the resonance field H should be made rather small and ΔH reasonably large, the latter was accomplished by producing a fairly small skin depth. Because of the relatively low frequency necessitated by the small H, a small skin depth requires a very large effective permeability at resonance. A resonance and large permeability were obtained despite the small H in a polycrystal with a magnetocrystalline anisotropy, K, of about zero. The calculations carried in works [57,58] under conditions of $K \approx 0$ and weak spin-lattice relaxation predicted the resonance shifting $\Delta H/H$ of about 20-30% that had good agreement with experimental data obtained for the specially prepared $Ni_{66}Fe_{34}$ rod with longitudinal magnetisation.[57] In this case, the line width and shape are essentially determined by the conductivity and exchange.

It is important to make few general comments. Any small contributions in the vicinity of a resonance (of an arbitrary nature) add small parameters in the resonance denominator. Therefore, the resonance value is determined by the biggest parameter in the denominator, such as anisotropy and field. Then, the requirement $K \approx 0$ seems to be very important to observe the exchange effect since in the presence of anisotropy the contribution from the dispersion of the anisotropy direction should prevail over the contribution from the exchange effect. In fact, this situation is applied to real MI samples, where the dispersion of anisotropy always takes place. Furthermore, the MI effect is usually considered outside of the ferromagnetic resonance, and therefore the exchange effect is of little importance. Nevertheless, in some resent works [59-61] it was proposed that the exchange interaction may significantly influence the MI field characteristics. However, the idealised models considered in those works with perfectly established anisotropy in a single domain are never observed in practice, whereas exactly this "model idealities" make possible "an exarticulation" of the exchange effect. The early experiments by Rado and Weertman [57] clearly demonstrated that for the observation of the exchange effect, very specific conditions and sample preparations are required. Thus, the conditions required for the observation of the exchange effect in MI are difficult-to-realise, therefore this effect will be neglected throughout the present work.

1.8 References

[1] L. V. Panina and K. Mohri, Appl. Phys. Lett. **65**, 1189 (1994).

[2] R. S. Beach and A. E. Berkowitz, J. Appl. Phys. **76**, 6209 (1994).

[3] L. V. Panina, K. Mohri, K. Bushida, and M. Noda, J. Appl. Phys. **76**, 6198 (1994).

[4] K. Mohri, L. V. Panina, T. Uchiyama, K. Bushida, and M. Noda, IEEE Trans. Magn. **31**, 1266 (1995).

[5] K. Mohri, T. Uchiyama, and L. V. Panina, Sensor and Actuators **A 59**, 1 (1997).

[6] N. Kawajiri, M. Nakabayashi, C. M. Cai, K. Mohri, and T. Uchiyama, IEEE Trans. Magn. **35**, 3667 (1999).

[7] L. V. Panina and K. Mohri, Sensors and Actuators **A 81**, 71 (2000).

[8] D. P. Makhnovskiy, L. V. Panina, and D. J. Mapps, Appl. Phys. Letters **77**, 121 (2000).

[9] K. Mohri, T. Uchiyama, L. P. Shen, C. M. Cai, and L. V. Panina, Sensors and Actuators **A 91**, 85 (2001).

[10] K. Mohri, T. Uchiyama, L. P. Shen, C. M. Cai, and L. V. Panina, J. Magn. Magn. Mater **249**, 351 (2002).

[11] D. P. Makhnovskiy, A. S. Antonov, A. N. Lagarkov, and L. V. Panina, J. Appl. Phys **84**, 5698 (1998).

[12] D. P. Makhnovskiy, L. V. Panina, and D. J. Mapps, J. Appl. Phys. **87**, 4804 (2000).

[13] D. P. Makhnovskiy, A. N. Lagarkov, L. V. Panina, and K. Mohri, Sensor and Actuators **A 81**, 106 (2000).

[14] D. P. Makhnovskiy, L. V. Panina, and D. J. Mapps, Phys. Rev. **B 63**, 144424 (2001).

[15] N. Fry, D. P. Makhnovskiy, L. V. Panina, S. I. Sandacci, M. Akhter, and D. J. Mapps, submitted to IEEE Trans. Magn. (2002).

[16] D. P. Makhnovskiy and L. V. Panina, J. Appl. Phys. **93**, 4120 (2003).

[17] S. Chikazumi, *Physics of Magnetism*, (John Wily&Sons Inc., New York, London, Sydney 1964).

[18] C. Kittel, Rev. Mod. Phys. **21**, 541 (1949).

[19] P. Weiss, J. de Phys. **6**, 661 (1907).

[20] J. H. Van Vleck, Rev. Mod. Phys. 17, 27 (1945).

[21] C. P. Slichter, *Principles of Magnetic Resonance*, (Happer&Row publishers; New York, Evanston, London, 1963).

[22] A. G. Gurevich, *Ferrites at Microwave Frequencies*, (New York: Consultants Bureau, 1963).

[23] A. G. Gurevich and G. A. Melkov, *Magnetic oscillations and waves*, (Boca Ratton: CRC Press, 1996).

[24] L. D. Landau, E. M. Lifshitz and L. P. Pitaevskii, *Quantum Mechanics - Non-Relativistic Theory, Vol. 3*, (Edition: 3d, Elsevier Science, 1977)

[25] M. J. Hurben and C. E. Patton, J. Appl. Phys. 83, 4344 (1998).

[26] T. L. Gilbert, Phys. Rev. **100**, 1243 (1955).

[27] R. Kikuchi, J. Appl. Phys. **27**, 1352 (1956).

[28] L. Landau and E. Lifshitz, Phys. Z. Sowjetunion **8**, 153 (1935).

[29] N. Smith and P. Arnett, Appl. Phys. Letters **78**, 1448 (2001).

[30] N. Smith, V. Synogatch, D. Mauri, J. A. Katine, and M.-C. Cyrille, J. Appl. Phys. **91**, 7454 (2002).

[31] V. Synogatch, N. Smith, and J. R. Childress, J. Appl. Phys. **93**, 8570 (2003).

[32] V. L. Safonov, J. Appl. Phys. **85**, 4370 (1999).

[33] V. L. Safonov, J. Appl. Phys. **91**, 8653 (2002).

[34] W. Xiaobin, H. N. Bertram, V. L. Safonov, J. Appl. Phys. **92**, 2064 (2002).

[35] V. L. Safonov and H. N. Bertram, J. Appl. Phys. **93**, 6912 (2003).

[36] V. L. Safonov and H. N. Bertram, J. Appl. Phys. **94**, 529 (2003).

[37] N. Smith, J. Appl. Phys. **92**, 3877 (2002).

[38] C. Kittel, Phys. Rev. **73**, 155 (1948).

[39] J. R. MacDonald, Proc. Phys. Soc. **A 64**, 968 (1951).

[40] L. D. Landau and E. M. Lifshitz, *Electrodynamics of Continuous Media*, (Pergamon Press, 1975).

[41] F. Morse and H. Feshbach, *Methods of Theoretical Physics*, (New York: McGraw-Hill, 1953).

[42] H. Chiriac and T. A. Ovari, Progress in Mat. Sci. **40**, 333 (1996).

[43] A. P. Zhukov, J. Gonzalez, J. M. Blanco, M. Vazquez, and V. S. Larin, J. Mat. Res. **15**, 2107 (2000).

[44] H. Chiriac and T. A. Ovari, J. Magn. Magn. Mater **249**, 46 (2002).

[45] V. S. Larin, A. V. Torcunov, A. Zhukov, J. Gonzalez, M. Vazquez, L. V. Panina, J. Magn. Magn. Mater **249**, 39 (2002).

[46] I. Ogasawara and S. Ueno, IEEE Trans. Magn. **31**, 1219 (1995).

[47] E. C. Stoner and E. P. Wohlfarth, Phil. Trans. Roy. Soc. **A 240**, 599 (1948).

[48] D. Spenato, A. Fessant, J. Gieraltowski, H. Le Gall, and C. Tannous, J. Appl. Phys. **85**, 6010 (1999).

[49] T. J. Klemmer, K. A. Ellis, and B. van Dover, J. Appl. Phys. **87**, 5846 (2000).

[50] N. X. Sun and S. X. Wang, J. Appl. Phys. **92**, 1477 (2002).

[51] H. S. Jung, W. D. Doyle, J. E. Wittig, J. F. Al-Sharab, and J. Bentley, Appl. Phys. Letters **81**, 2415 (2002).

[52] H. Hoffman, Phys. Status Solidi **33**, 175 (1969).

[53] K. Kemiter and H. Hoffman, Phys. Status Solidi **33**, 237 (1969).

[54] H. Hoffman, Thin Solid Films **373**, 107 (2000).

[55] H. Hoffman, IEEE Trans. Magn. **4**, 32 (1968).

[56] C. Kittel and C. Herring, Phys. Rev. **77**, 725 (1950).

[57] G. T. Rado and J. R. Weertman, Phys. Rev. **94**, 1386 (1954).

[58] W. S. Ament and G. T. Rado, Phys. Rev. **94**, 1558 (1955).

[59] L. Kraus, J. Magn. Magn. Mater. **195**, 764 (1999).

[60] L. Kraus, J. Magn. Magn. Mater. **196/197**, 354 (1999).

[61] D. Menard and A. Yelon, J. Appl. Phys. **88**, 379 (2000).

Chapter 2 Magneto-impedance matrix in ferromagnetic wires

2.0 Generalised Ohm's law

This Chapter concerns the theoretical and experimental investigations of the magneto-impedance effect (MI) in amorphous wires in terms of the surface impedance matrix $\hat{\varsigma}$.[1] In certain cases [2,3], the MI effect can be understood as the field dependence of a high frequency impedance $Z(a/\delta_m,\sigma)$ (complex resistance) in ferromagnetic samples:

$$V_z(H_{ex}) = j \cdot Z(a/\delta_m,\sigma), \qquad (1)$$

where V_z is the field-dependent voltage measured across the wire, H_{ex} is the dc external magnetic field applied along the axis, j is the ac excitation current with a constant amplitude, $2a$ is the sample cross-section dimension, $\delta_m = c/\sqrt{2\pi\sigma\omega\mu_t(H_{ex})}$ is the magnetic skin-depth, σ is the sample conductivity, $\mu_t(H_{ex})$ is the ac effective circumferential permeability with respect to the ac current flow (axial), c is the velocity of light, and ω is the circular frequency. Here the impedance $Z(a/\delta_m,\sigma)$ is a function of the ratio a/δ_m and conductivity σ. However, in a general case, the MI effect requires the account of a specific matrix form of the ac permeability ($\hat{\mu}$) and impedance ($\hat{\varsigma}$), then Z is expressed using the components of impedance matrix $\hat{\varsigma}$.[1] In this case, a simple form (1) of Ohm's law for the MI response is no longer valid. Numerous experimental results on MI require a more realistic theory taking into account a specific matrix form of the ac permeability and impedance. Although the permeability of a wire always is a matrix-type quantity, the off-diagonal terms have often been ignored due, in part, to the analytic complexity of handling such expressions and the difficulty in measuring them. However, many applications of magnetic materials require very accurate knowledge of the permeability and impedance matrix, therefore the off-diagonal components can not always be ignored. Various excitation and measurement methods are required to reveal the matrix forms. An ac response can be measured not only across the sample ends, but also by means of an additional pick-up coil surrounding the sample. This technique is similar to that, which is used for measurements of the off-diagonal components of the permeability matrix.[4] If the equilibrium direction of the magnetisation is deflected to some angle away from the circular one, the ac current j induces both the longitudinal voltage V_z and the coil voltage V_c, as shown in Fig. 2.1(a). This is because the current flow gives rise to an ac antisymmetric circulatory magnetisation and a non–zero total longitudinal magnetisation.

In contrast, if the wire is placed in an ac longitudinal magnetic field h_z induced by the ac current j_b in the primary coil (so-called "ac bias"), the generated longitudinal and circulatory magnetisation contribute to V_c and V_z respectively, as shown in Fig. 2.1(b). The crossed magnetisation processes that relate to the voltages V_z and V_c are known as the inverse Wiedemann and Matteucci effects.[5] Both cases can be described in terms of the surface impedance matrix $\hat{\varsigma}$ containing the off-diagonal components, which are directly proportional to the corresponding voltages. *The concept of the impedance matrix allows the conductive and inductive effects to be considered from a common view point.*[1]

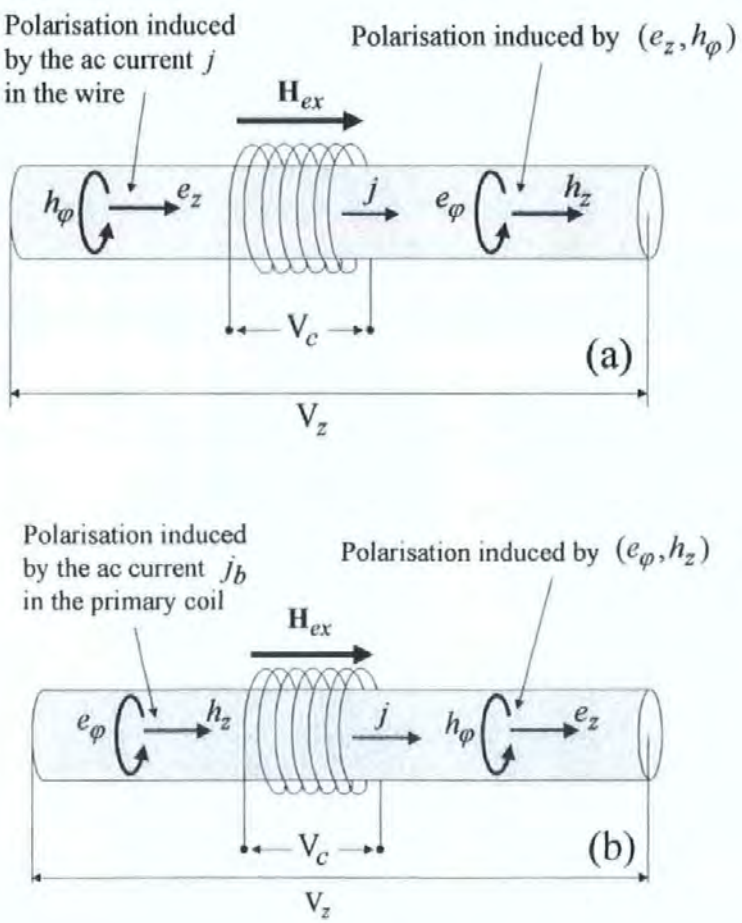

Fig. 2.1 *Various excitation and measurement methods. The wire is subjected to an ac current j in (a) and an ac longitudinal magnetic field h_z in (b). The static magnetic structure in a wire can be changed by a dc longitudinal magnetic field H_{ex}.*

The off-diagonal components should be formally interpreted as *the off-diagonal impedances* in a generalised approach. Thus, the total surface impedance matrix $\hat{\varsigma}$ represents the generalised Ohms law (matrix form), where the voltage vector (V_z, V_c) is related through the surface impedance matrix $\hat{\varsigma}$ with the excitation current vector (j, j_b) (see Section 2.2):

$$\begin{pmatrix} V_z/l \\ V_c/2\pi aN \end{pmatrix} = \begin{pmatrix} \varsigma_{zz} & -\varsigma_{z\varphi} \\ \varsigma_{\varphi z} & -\varsigma_{\varphi\varphi} \end{pmatrix} \otimes \begin{pmatrix} A\cdot j \\ B\cdot j_b \end{pmatrix}, \quad \hat{\varsigma} = \begin{pmatrix} \varsigma_{zz} & \varsigma_{z\varphi} \\ \varsigma_{\varphi z} & \varsigma_{\varphi\varphi} \end{pmatrix}. \tag{2}$$

Here l is the wire length, $2\pi aN$ is the total length of turns in the pick-up coil, N is the number of turns, the constants A and B relate the ac excitation currents with the corresponding ac magnetic fields at the wire surface: $\bar{h}_\varphi = A\cdot j$ and $\bar{h}_z = B\cdot j_b$.

The magnetic structure-dependent impedance matrix $\hat{\varsigma}$ will be calculated for any frequency and external magnetic field, and is not restricted to the case when only the strong skin-effect is present.[1] A general approach to solving the electrodynamic problems is based on the expansion of Maxwell's equations in asymptotic series. The characteristic parameter of the asymptotic expansions can be chosen to be the ratio $\beta = a/\delta$ where $\delta = c/\sqrt{2\pi\sigma\omega}$ is the non-magnetic penetration depth. Constructing the asymptotic serious for two limiting cases $\beta >> 1$ and $\beta << 1$ and matching them in the intermediate region, the solution for ac field distribution becomes valid in the entire frequency (or dc magnetic field) range. For obtaining the asymptotic series in the case $\beta >> 1$, a singular perturbation method is used, which is needed to describe the field distribution in the surface layer. For $\beta << 1$, a standard regular perturbation method can be employed. The ac magnetisation is assumed to be related to the rotational process and is described by a matrix of a general form having 6 different components. To demonstrate consistency between theory and experiment, measurements of the impedance matrix in amorphous wires with both types of anisotropy have been made under proper excitation conditions.

Before we proceed with the impedance analysis, the properties of the amorphous magnetic wires have to be addressed.

2.1 Typical materials

In the last two decades the level of interest in glass-forming metallic alloy, which vitrify at relatively low cooling rates from the molten state (compared with conventional rapidly quenched metallic glasses), has grown.[6] Owing to their resistance to crystallisation, these easy glass-forming alloys can be cast in bulk shape with very small dimensions down to microns. Magnetic glassy alloys can be classified into two groups: Fe- and Co-based bulk alloys with soft magnetic properties, and Ln–Fe-based (Ln=Nd or Pr) bulk amorphous alloys with hard ferromagnetism at room temperature. At present, the mechanisms determining soft magnetic behaviour of Fe- and Co-based alloys, on one hand, large values of the coercive field for Ln-based bulk amorphous alloys on the other hand, are not well understood. These new ferromagnetic bulk amorphous alloys are very attractive for both fundamental science and engineering applications.

Thin amorphous ferromagnetic wires having a negative magnetostriction can be considered to be one of the best materials for the MI applications.[2,3] The general composition of alloy is F_xM_y with Fe and/or Co as F and metalloid like Si and B as M.[7-11] The content "x" ranges typically between 70 and 80%. The alloys may also contain small amounts of other elements such as Cr, Mn, Al, Cu, and Nb in order to improve mechanical, corrosion or magnetic properties. In particular, FeSiBCuNb microwires can even improve their ultrasoft magnetic behaviour by suitable thermal treatments. Partial diversification may result in a stable and homogeneous "nanocrystalline" structure with balanced magnetocrystalline and magnetoelastic anisotropies. The magnetostriction plays the main role to determine the magnetic behaviour (i.e. domain structure and hysteresis loop).[7,8,10] The sign and value of the magnetostriction, λ, are decisive. Positive and negative magnetostrictions result respectively in radial and circumferential easy axis in the shell, whereas the inner core always has the longitudinal magnetisation (although it can be very small). The domain models for $\lambda > 0$ and $\lambda < 0$ are shown in Fig. 2.2(a) and Fig. 2.2(b), respectively.[7,8] The wire sample with circumferential anisotropy is divided into a "bamboo" domain structure, where adjacent domains have opposite directions of magnetisation, as shown in Fig. 2.2(b).

The magnetostriction constant λ is correlated to the alloy composition. In the $(Co_{1-x}Fe_x)_{75}Si_{15}B_{10}$ series, λ is positive for $x > 0.06$, and it becomes negative when the Fe-content drops below down this value. Therefore, the negative magnetostriction is typical for Co-rich alloys. For example, a wire of a composition $Fe_{4.35}Co_{68.15}Si_{12.5}B_{15}$ exhibits excellent soft magnetic properties having almost zero (but still negative) magnetostriction of $\lambda = -10^{-7}$. *This composition is most popular for the MI applications.* The Co-rich microwires with $\lambda < 0$ present an almost nonhysteretic magnetisation curve. In contrast, Fe-rich microwires with $\lambda > 0$ are characterised by a large Barkhausen jump that results in square-shaped hysteresis loops.

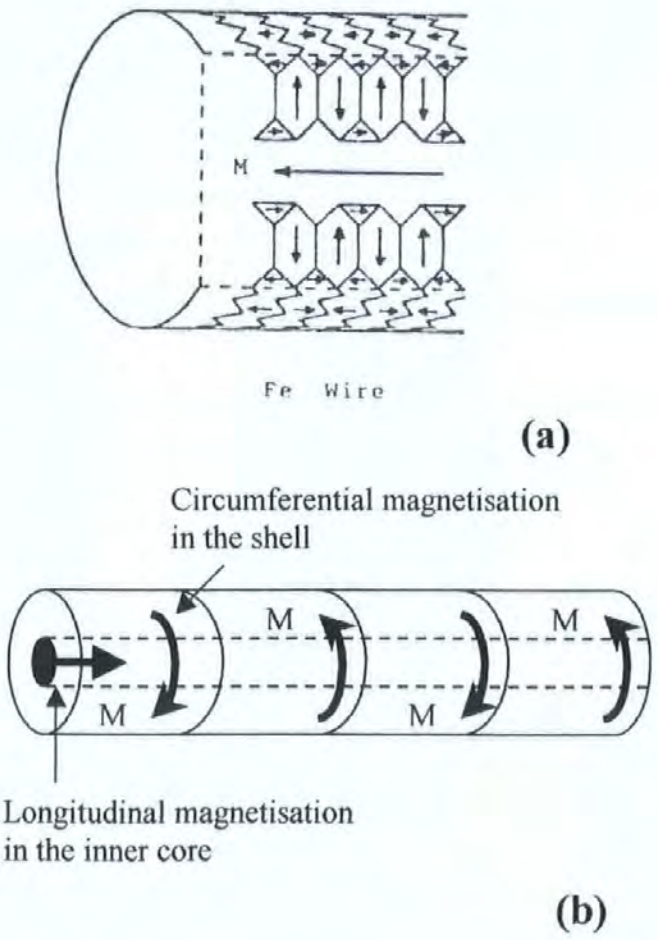

Fig. 2.2 *Domain structures of wires with positive $\lambda > 0$ in (a) and negative $\lambda < 0$ in (b) magnetostrictions. The positive magnetostriction is typical for Fe-rich alloys, whereas the negative for Co-rich alloys (bamboo-like domain structure). The wire sample with circumferential anisotropy is divided into a "bamboo" domain structure (b).*

Currently, there are two main techniques of wire fabrication:

i) Amorphous wires are made by **UNITIKA LTD**. R&D (Kyoto, Japan) using the in-water spinning method, and then cold drawn from a diameter of about 125 μm of the as-cast wire to diameters of 20–30 μm. The fabrication method is shown in Fig. 2.3.[8] The final sample undergoes annealing with a tension stress to build up a certain magnetic structure. This method requires very careful control of the annealing process to obtain repeatable magnetic parameters.

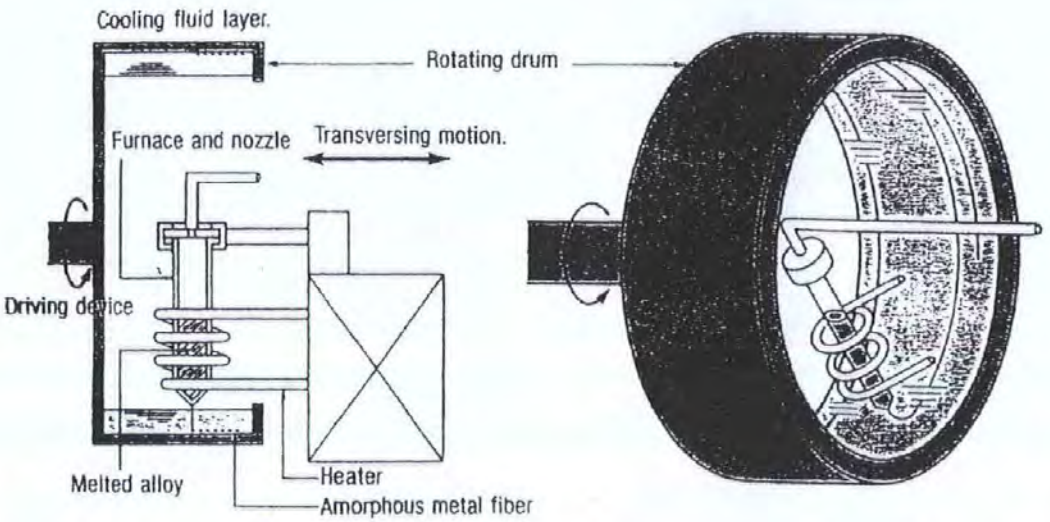

Fig. 2.3 *Schematic illustration of the in-rotating-liquid-spinning process for the fabrication of amorphous wires.*

ii) Some commercial companies and research laboratories produce amorphous wires with a glass coating, by a modified Taylor-Ulitovskiy method.[9,11] The fabrication method is shown in Fig. 2.4. One end of the glass tube with the alloy of a needed composition is sealed. Then, it is heated to the temperature at which glass is soften and alloy is in a melting state. Drawing the heated end creates a very thin glass capillary (ranging between 10–60 microns) where the molten metal streams, as demonstrated in Fig. 2.4(a). The final fibre structure shown in Fig. 2.5 is formed by the water cooling (water stream in Fig. 2.4(a,b)) to obtain a metallic core (in amorphous state). The core has a diameter d_m, while the total diameter of the micro wire, i.e. core and the coating, is D_w.

(a)

(b)

Fig. 2.4 *Fabrication method of the glass-covered microwires. Drawing the heated end (see (a)) creates very thin glass capillary where the molten metal streams. The final fibber structure is formed by the water cooling (water stream in (a,b)) to obtain a metallic core in an amorphous or microcrystalline state.*

The metallic core (ranging between 5-50 microns) has an amorphous and/or microcrystalline microstructure in order to achieve the desired magnetic properties, such as magnetic anisotropy and coercivity. The ratio of the metal core and glass coating thickness also affects the magnetic properties.[10] The fabrication method of glass-covered microwires introduces a quite large internal stress mainly arising from the difference in thermal expansion coefficients of metal (nucleus) and glass (sheath). The value of this internal stress, which has the tensor nature, can be easily controlled by the ratio of diameters of the glass cover and the metal core.[10,12]

The direction of the easy magnetoelastic anisotropy axis associated with this stress is determined by the sign of the magnetostriction constant λ. *In context of cost and simplicity of the technological process, the glass-covered wires have great advantage over those produced by in-water spinning method.*

Fig. 2.5 *Final structure of the glass covered wires. The core has a diameter d_m, while the total diameter of the micro wire, i.e. core and the glass coating, is D_w.*

2.2 Voltage response and surface impedance matrix

The MI effect deals with a voltage response in a thin metallic magnetic material subjected to a high frequency excitation and dc bias current I_b, as shown in Fig. 2.6.

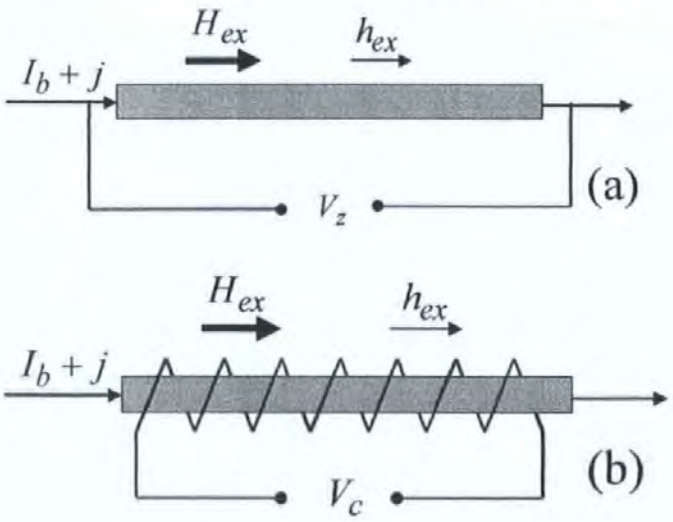

Fig. 2.6 *Voltage response due to the ac excitation using current j and field h_{ex}, measured across the wire in (a) and in the coil in (b).*

An ac current j and/or an ac axial field h_{ex} are used as a source of excitation. The time dependence $\exp(-i\omega t)$ and Gaussian units are chosen. The voltage is measured either across the wire (V_z) or in the coil (V_c) mounted on it. The value of V_z is determined by considering the energy consumption in the wire:

$$jV_z = \frac{c}{4\pi}\int_S (\mathbf{e}\times\mathbf{h})\mathbf{ds}, \tag{3}$$

where the integration is performed along the wire surface, **e** and **h** are the ac electric and magnetic fields, c is the velocity of light. The voltage V_c is found by integrating **e** along the coil turns:

$$V_c = \oint \mathbf{edl}. \tag{4}$$

As it follows from (3),(4), the induced voltage can be found by calculating the tangential components of the fields $\bar{\mathbf{e}}_t$, $\bar{\mathbf{h}}_t$ at the wire surface. Since it is assumed that the wavelength is larger than the sample size, the field distribution outside the sample corresponds to the static case. Then, the excitation method imposes the boundary conditions for the magnetic field $\bar{\mathbf{h}}_t$. Using the cylindrical co-ordinates (r,φ,z) with the axis z along the wire, as shown in Fig. 2.7, the boundary conditions can be written as:

$$h_\varphi(a) = \bar{h}_\varphi = 2j/ca, \quad \bar{h}_z(a) = h_{ex}, \tag{5}$$

where a is the wire radius. The electric field $\bar{\mathbf{e}}_t$ is related to the magnetic field $\bar{\mathbf{h}}_t$ via the surface impedance matrix $\hat{\varsigma}$:[13]

$$\bar{\mathbf{e}}_t = \hat{\varsigma}(\bar{\mathbf{h}}_t \times \mathbf{n}), \tag{6}$$

where **n** is a unit radial vector directed inside the wire. Comparing (3)-(6) it is seen that the impedance $\hat{\varsigma}$ is the only characteristic describing the voltage response in the system excited by the external magnetic field **h** (of any origin). In ferromagnetic conductors, $\hat{\varsigma}$ is a two-dimensional matrix even for the electrically isotropic case.

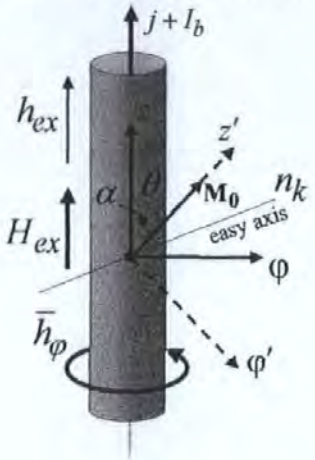

Fig. 2.7 *Principle directions and quantities used.*

The present analysis is concerned with the calculation of the surface impedance matrix for a wire with a uniform static magnetisation having a helical orientation. In this case, the matrix $\hat{\varsigma}$ is constant on the surface. Writing vector equation (6) in the co-ordinate representation, the components of $\hat{\varsigma}$ can be determined as:

$$\begin{aligned} \bar{e}_\varphi &= -\varsigma_{\varphi\varphi}\bar{h}_z + \varsigma_{\varphi z}\bar{h}_\varphi, \\ \bar{e}_z &= -\varsigma_{z\varphi}\bar{h}_z + \varsigma_{zz}\bar{h}_\varphi, \end{aligned} \tag{7}$$

where $\varsigma_{z\varphi} = \varsigma_{\varphi z}$ because of symmetry. Substituting (7) to (3) and (4) gives the voltage responses:

$$V_z = \bar{e}_z l = (\varsigma_{zz}\frac{2j}{ca} - \varsigma_{z\varphi}\, h_{ex})l, \tag{8}$$

$$V_c = \bar{e}_\varphi 2\pi a n l = (-\varsigma_{\varphi\varphi}\, h_{ex} + \varsigma_{\varphi z}\frac{2j}{ca})2\pi a n l, \tag{9}$$

where l is the wire length and n is the number of coil turns per unit length.

2.3 Basic equations and model assumptions

The calculation of $\hat{\varsigma}$ is based on the solution of the Maxwell equations for the fields **e** and **h** together with the equation of motion for the magnetisation vector **M**. An analytical treatment is possible in a linear approximation with respect to the time-variable parameters **e**, **h**, $\mathbf{m} = \mathbf{M} - \mathbf{M}_0$, where $\mathbf{M}_0$ is the static magnetisation. Assuming a local relationship between **m** and **h**: $\mathbf{m} = \hat{\chi}\mathbf{h}$, the problem is simplified to finding the solutions of the Maxwell equations with a given ac permeability matrix $\hat{\mu} = \hat{\mathbf{I}} + 4\pi\hat{\chi}$:

$$\text{rot}\,\mathbf{e} = i\omega(\hat{\mu}\mathbf{h})/c, \qquad \text{rot}\,\mathbf{h} = 4\pi\sigma\mathbf{e}/c \tag{10}$$

satisfying the boundary conditions (5). Here σ is the conductivity.

Introducing the local permeability matrix $\hat{\mu}$ *corresponds to neglecting the exchange effects. This approximation is reasonable for not very high frequencies, such that the skin depth is still larger than the exchange length. Further assumptions about* $\hat{\mu}$ *are needed.*

The ac permeability depends on many factors, including the domain configuration, anisotropy and stress distribution, and the mode of magnetisation (domain wall motion or magnetisation rotation). These factors can be complex in real materials, making modelling very difficult. In this analysis, the domain structure is not considered, it can be eliminated by a proper dc bias. It is assumed that $\mathbf{M}_0$ is aligned in a helical direction having a constant angle θ with the wire axis. This assumption is true for the central part of a wire piece (i.e. not very near the wire ends), the length of which is larger than 1-2 mm. Variation from a constant helical direction will take place at the wire ends. Nevertheless, if the wire is long enough (a few millimetres) the contribution to the impedance response from the central part, where the anisotropy is well established, will prevail over the end effects and so we will not consider them. In this case, $\hat{\mu}$ is determined by the magnetic moment rotation and is independent of the position. This is approximation even for an ideal material, since a circumferential magnetisation near the wire centre results in an infinite exchange energy. Then, there is always a radial distribution in permeability, which is stronger in the case of a helical anisotropy due to a stress distribution. Because of this, a wire with circumferential or helical anisotropy has always the inner core with the longitudinal magnetisation, as it shown in Fig. 2.2(b). Nevertheless, direct measurements of the longitudinal B-H loops show that the outer shell (with circumferential or helical anisotropy) gives the main contribution to the measured flux. It follows that the inner core diameter is strongly reduced. Since the magnetic paths are always closed in the outer shell during the magnetisation process, there are no magnetic poles on the wire surface and ends. Thus, in our case the demagnetising effect is absent if the wire is long enough. When we consider the high frequency case, the permeability is predominantly a surface permeability, and hence the influence of the inner core effect on the ac response can be completely ignored. In the low frequency case, where the radial change in permeability becomes important, the magneto-impedance effect is relatively small. In fact, an averaged value of the permeability can be used for a low frequency approximation. Thus, in both cases a permeability matrix can be introduced. The comparison between the theory and experiment is good proving that this approach is reasonable and a radial distribution in permeability is not significant for the MI effects.

The matrix $\hat{\boldsymbol{\mu}}$ has a general form with: $\mu_{\varphi r} = -\mu_{r\varphi}$, $\mu_{rz} = -\mu_{zr}$, $\mu_{\varphi z} = \mu_{z\varphi}$ due to the magnetic symmetry. Considering that the time dependence is given by $\exp(-i\omega t)$ and utilising the cylindrical symmetry ($\mathbf{e} = (e_\varphi, e_z)$, $\mathbf{b} = (b_\varphi, b_z)$), the Maxwell equations can be reduced to:

$$\frac{\partial e_z}{\partial r} = -\frac{i\omega}{c} b_\varphi, \quad \frac{1}{r}\frac{\partial (r e_\varphi)}{\partial r} = \frac{i\omega}{c} b_z, \tag{11}$$

$$\frac{\partial h_z}{\partial r} = -\frac{4\pi\sigma}{c} e_\varphi, \quad \frac{1}{r}\frac{\partial (r h_\varphi)}{\partial r} = \frac{4\pi\sigma}{c} e_z, \tag{12}$$

where $\mathbf{b} = \hat{\boldsymbol{\mu}}\,\mathbf{h}$ is the vector of magnetic induction. Since $b_r = 0$ (which satisfies the boundary conditions at the wire surface), the material equations are of the form:

$$\begin{aligned} b_\varphi &= \mu_1 h_\varphi + \mu_3 h_z \\ b_z &= \mu_3 h_\varphi + \mu_2 h_z \end{aligned} \tag{13}$$

The magnetic parameters are given by:

$$\mu_1 = \mu_{\varphi\varphi} + \mu_{\varphi r}^2 / \mu_{rr}, \qquad \mu_2 = \mu_{zz} + \mu_{rz}^2 / \mu_{rr}, \qquad \mu_3 = \mu_{\varphi z} - (\mu_{\varphi r}\mu_{rz})/\mu_{rr}. \tag{14}$$

Substituting (13) to (11), (12) and eliminating the electric field $\mathbf{e}$ gives the equations for the magnetic field components h_z and h_φ:

$$\begin{aligned} r^2\frac{\partial^2 h_\varphi}{\partial r^2} + r\frac{\partial h_\varphi}{\partial r} + \left(k_1^2 r^2 - 1\right) h_\varphi &= -k_3^2 r^2 h_z, \\ r^2\frac{\partial^2 h_z}{\partial r^2} + r\frac{\partial h_z}{\partial r} + k_2^2 r^2 h_z &= -k_3^2 r^2 h_\varphi, \end{aligned} \tag{15}$$

where $k_n^2 = \mu_n \left(4\pi i\omega\sigma/c^2\right)$ and $n = 1, 2, 3$. Equations (15) are solved imposing boundary conditions (5) at the wire surface. The boundary conditions at $r = 0$ must exclude the infinite solutions, requiring:

$$h_\varphi(r \le a) < \infty, \qquad h_z(r \le a) < \infty. \tag{16}$$

Then, the coupled equations (15) with conditions (5) and (16) are completely determined.

In the present analysis, asymptotic solutions of equations (15) are found in two limiting cases: $\delta << a$ and $\delta >> a$, where $\delta = c/\sqrt{2\pi\sigma\omega}$ is the skin depth in a non-magnetic material ($\hat{\boldsymbol{\mu}} = \hat{\mathbf{I}}$), as power series in a corresponding small parameter (δ/a or a/δ).

On the other hand, no condition is imposed on the value of the magnetic skin depth $\delta_n = c/\sqrt{2\pi\sigma\omega\mu_n}$, where μ_n is a corresponding magnetic parameter defined by (14). The series representation for the electric field $\mathbf{e} = (e_z, e_\varphi)$ is then deduced from equations (12). If the surface values $\bar{e}_\varphi, \bar{e}_z$ are written in the form linear with respect to the boundary values $\bar{h}_\varphi$ and h_{ex}, the surface impedance matrix can be calculated from equations (7).

To simplify the further analysis, it is useful to write the matrix $\hat{\boldsymbol{\mu}}$ in the co-ordinate system with the axis $z' \| \mathbf{M}_0$ where it has the simplest form. In the case of a uniform precession of the total magnetisation vector $\mathbf{M}$ around $\mathbf{M}_0$, the susceptibility matrix in the prime co-ordinates (r, φ', z') related with the equilibrium magnetisation $\mathbf{M}_0$ (see Fig. 2.7) is of the form:

$$\hat{\chi} = \begin{pmatrix} \chi_1 & -i\chi_a & 0 \\ i\chi_a & \chi_2 & 0 \\ 0 & 0 & 0 \end{pmatrix}. \tag{17}$$

This form can be easily obtained from the linearised Landau-Lifshitz equation. The expressions for χ_1, χ_2, χ_a depend on a given magnetic configuration and will be determined later. The susceptibility matrix can be converted to the original co-ordinate representation (r, φ, z) by rotating the prime system by an angle θ which determines the direction of $\mathbf{M}_0$ with respect to the wire axis z:

$$\hat{\chi} = \begin{pmatrix} \chi_1 & -i\chi_a\cos(\theta) & i\chi_a\sin(\theta) \\ i\chi_a\cos(\theta) & \chi_2\cos^2(\theta) & -\chi_2\sin(\theta)\cos(\theta) \\ -i\chi_a\sin(\theta) & -\chi_2\sin(\theta)\cos(\theta) & \chi_2\sin^2(\theta) \end{pmatrix}. \tag{18}$$

Using (18) gives:

$$\mu_1 = 1 + 4\pi\cos^2(\theta)\tilde{\chi}, \qquad \mu_2 = 1 + 4\pi\sin^2(\theta)\tilde{\chi}, \tag{19}$$

$$\mu_3 = -4\pi\sin(\theta)\cos(\theta)\tilde{\chi}, \qquad \tilde{\chi} = \chi_2 - \frac{4\pi\chi_a^2}{1 + 4\pi\chi_1}.$$

2.4 High frequency approximation

The singular perturbation method constructed with respect to a small parameter $\beta = \delta/a << 1$ is used to obtain asymptotic solutions of equations (15) in the case of high frequencies. Customarily, this case is treated by considering the plane geometry. However, such an approach allows the zero-order terms only to be found. For the purpose of building a general asymptotic solution valid in a wide frequency range, the higher-order terms in the series expansion are also important.

Introducing a new variable $x = r/a$ and multiplying equations (15) by β^2 gives:

$$\begin{aligned} &\beta^2 x^2 \frac{\partial^2 h_\varphi}{\partial x^2} + \beta^2 x \frac{\partial h_\varphi}{\partial x} + \left(\beta_1^2 x^2 - \beta^2\right) h_\varphi = -\beta_3^2 x^2 h_z \\ &\beta^2 x^2 \frac{\partial^2 h_z}{\partial x^2} + \beta^2 x \frac{\partial h_z}{\partial x} + \beta_2^2 x^2 h_z = -\beta_3^2 x^2 h_\varphi \end{aligned} \tag{20}$$

The boundary conditions for equations (20) are:

$$\begin{aligned} &h_\varphi(1) = \bar{h}_\varphi, \quad h_z(1) = h_{ex}, \\ &h_\varphi(x) < \infty, \quad h_z(x) < \infty, \quad 0 \le x \le 1. \end{aligned} \tag{21}$$

Here $\beta_n^2 = 2i\mu_n$. Equations (20) have a small parameter at the second-order derivative and are related to so-called singular perturbed equations.[14-16] The solution of such an equation can be represented as the sum of two (regular and singular) asymptotic series of powers of the small parameter. The regular part approximates the solution within a certain internal area whereas the singular series is related to the boundary layer (near $x = 1$) where the solution undergoes rapid changes. Such a layer is named as a frontier layer. In our case it corresponds to the skin depth. In the internal area $0 < x < 1$, the singular part decays exponentially and the regular series has a smooth behaviour.

Following the singular perturbation method, the solution of (20) is written in the form:

$$h_\varphi(x,\eta) = \sum_{n\ge 0} \beta^n R_{\varphi n}(x) + \sum_{n\ge 0} \beta^n S_{\varphi n}(\eta), \tag{22}$$

$$h_z(x,\eta) = \sum_{n\ge 0} \beta^n R_{z n}(x) + \sum_{n\ge 0} \beta^n S_{z n}(\eta), \tag{23}$$

where $R_{\varphi n}$, R_{zn} and $S_{\varphi n}$, S_{zn} represent regular and singular terms, respectively, and $\eta = (x-1)/\beta$ is "the fast" variable.

Equations (20),(21) written in terms of the fast variable η become:

$$
\begin{aligned}
&(\eta\beta+1)^2\frac{\partial^2 h_\varphi}{\partial\eta^2}+\beta(\eta\beta+1)\frac{\partial h_\varphi}{\partial\eta}+\left(\beta_1^2(\eta\beta+1)^2-\beta^2\right)h_\varphi=-\beta_3^2(\eta\beta+1)^2 h_z\\
&(\eta\beta+1)^2\frac{\partial^2 h_z}{\partial\eta^2}+\beta(\eta\beta+1)\frac{\partial h_z}{\partial\eta}+\beta_2^2(\eta\beta+1)^2 h_z=-\beta_3^2(\eta\beta+1)^2 h_\varphi \qquad (24)\\
&h_\varphi(0)=\bar{h}_\varphi,\quad h_z(0)=h_{ex}\\
&h_\varphi(\eta)<\infty,\quad h_z(\eta)<\infty,\quad -1/\beta\le\eta\le 0
\end{aligned}
$$

Substituting the regular series into (20) and the singular series into (24), and grouping together terms of the same power n of β, the asymptotic solution of degree n is constructed. In the case of the regular series, the zero-order ($n=0$) approximation gives:

$$
\begin{aligned}
&\beta_2^2 R_{z0}(x)=-\beta_3^2 R_{\varphi 0}(x)\\
&\beta_1^2 R_{\varphi 0}(x)=-\beta_3^2 R_{z0}(x)
\end{aligned}
\qquad (25)
$$

Equations (25) are satisfied only if $R_{z0}(x)=R_{\varphi 0}(x)=0$. Proceeding in a similar way, it can be shown that all higher-order terms turn out to be zero as well. Therefore, in the present case the solution does not have a regular part, which could be expected as a consequence of the skin-effect. The existence of the regular solution would result in the deep "diffusion" of the electromagnetic field inside the wire at high frequencies. According to the general property of singular equations, the singular part decays exponentially as $\exp(-a(1-x)/\delta)$, therefore the frontier layer corresponds to the skin depth δ.

Considering the singular series, the zero-order terms are found by solving the following equations:

$$
\begin{aligned}
&\frac{\partial^2 S_{\varphi 0}}{\partial\eta^2}+\beta_1^2 S_{\varphi 0}=-\beta_3^2 S_{z0},\quad S_{\varphi 0}(0)=\bar{h}_\varphi\\
&\frac{\partial^2 S_{z0}}{\partial\eta^2}+\beta_2^2 S_{z0}=-\beta_3^2 S_{\varphi 0},\quad S_{z0}(0)=h_{ex}
\end{aligned}
\qquad (26)
$$

To choose a physically reasonable solution, the following condition has to be imposed:

$$
\lim_{\substack{\beta\to 0\\ x<1}} S((x-1)/\beta)=\lim_{\eta\to-\infty} S(\eta)=0. \qquad (27)
$$

The solution of (26) is taken in the form $C\,\mathbf{y}\exp(\xi\eta)$ where $\mathbf{y}$ is the intrinsic vector of coupled equations, C is a constant, and ξ satisfies to:

$$\xi^4+\xi^2\left(\beta_1^2+\beta_2^2\right)+\left(\beta_1^2\beta_2^2-\beta_3^4\right)=0. \tag{28}$$

Using $\beta_n^2=2i\mu_n$, where μ_n are determined by (19), we obtain:

$$\begin{aligned}&\xi_1=\pm(1-i),\quad \xi_2=\pm(1-i)\sqrt{\tilde{\mu}}\\&\tilde{\mu}=1+4\pi\tilde{\chi}\end{aligned} \tag{29}$$

In (29), only the sign "+" has to be taken to be consistent with condition (27) since in this case the exponent $\exp(\xi\eta)$ is limited for any $\eta<0$. Finally, the general solution of (26) is represented as:

$$\begin{pmatrix}h_\varphi\\h_z\end{pmatrix}=C^{(1)}\begin{pmatrix}y_1^{(1)}\\y_2^{(1)}\end{pmatrix}\exp\left(\frac{(1-i)a}{\delta}(x-1)\right)+C^{(2)}\begin{pmatrix}y_1^{(2)}\\y_2^{(2)}\end{pmatrix}\exp\left(\frac{(1-i)a}{\delta}\sqrt{\tilde{\mu}}(x-1)\right). \tag{30}$$

There are two decay lengths in Eq. (30): δ and $\delta_m=\delta/\sqrt{\tilde{\mu}}$. The former δ is related to a non magnetic but electrically conducting case describing the distribution of the electromagnetic field having the local polarisation with the magnetic field parallel to the dc magnetisation $\mathbf{M}_0$. The latter δ_m is a magnetic skin depth corresponding to the mode with $\mathbf{h}$ perpendicular to $\mathbf{M}_0$. In the case under consideration, the vector $\mathbf{M}_0$ is directed along a helical path, resulting in the existence of both polarisations and the solution involving the two characteristic decay lengths.

Defining $C^{(1,2)}$ from boundary conditions in Eqs. (24), the zero-order estimate for the magnetic field h_φ, h_z is completed. Substituting Eq. (30) into (12) yields the solution for the electric field $\mathbf{e}$. Then, from Eqs. (7) the surface impedance matrix is deduced:

$$\hat{\varsigma}=\begin{pmatrix}\varsigma_{zz}&\varsigma_{z\varphi}\\\varsigma_{\varphi z}&\varsigma_{\varphi\varphi}\end{pmatrix}=\frac{c(1-i)}{4\pi\sigma\delta}\begin{pmatrix}\sqrt{\tilde{\mu}}\cos^2(\theta)+\sin^2(\theta)&\left(\sqrt{\tilde{\mu}}-1\right)\sin(\theta)\cos(\theta)\\\left(\sqrt{\tilde{\mu}}-1\right)\sin(\theta)\cos(\theta)&\cos^2(\theta)+\sqrt{\tilde{\mu}}\sin^2(\theta)\end{pmatrix}. \tag{31}$$

The high-frequency limit equation (31) for the surface impedance matrix (or its certain components) has been obtained in a number of papers,[17-20] regarding small regions at the wire surface as flat surfaces, and imposing the boundary conditions similar to Eq. (5). However, this method restricts to a zero-order approximation only.

The higher-order terms can be important to determine more accurately the validity conditions. For example, it has been considered that a strong skin-effect approximation yielding (31) requires $\delta/a<<1$ which is much stronger than that involving the magnetic skin-depth $\delta_m/a<<1$. This opinion is based on the field distribution as in Eq. (30) depending on the both decay parameters. For an amorphous wire ($\sigma=10^{16}$ s^{-1}) of 30 μm diameter the non-magnetic skin depth becomes of the order of a at GHz frequencies. On the other hand, numerous experimental results on MI are concerned with frequencies of 1−100 MHz, and it seems that the high frequency case has a very limited use. Within the proposed method, the full asymptotic series can be found. Considering the first-order approximation is important in context to prove that the condition $\delta_m/a<<1$ is sufficient to justify the use of Eq. (31).

The first-order equations for S_{z1} and $S_{\varphi 1}$ are of the form:

$$\begin{aligned}&\frac{\partial^2 S_{z1}}{\partial\eta^2}+\beta_2^2 S_{z1}=-\beta_3^2 S_{\varphi 1}-\frac{\partial S_{z0}}{\partial\eta}, \qquad S_{z1}(0)=0\\ &\frac{\partial^2 S_{\varphi 1}}{\partial\eta^2}+\beta_1^2 S_{\varphi 1}=-\beta_3^2 S_{z1}-\frac{\partial S_{\varphi 0}}{\partial\eta}, \qquad S_{\varphi 1}(0)=0\end{aligned} \tag{32}$$

Since the functions $\partial S_{z0}/\partial\eta$ and $\partial S_{\varphi 0}/\partial\eta$ are represented in the exponential form, the particular solution of equation (32) is given by:

$$\begin{aligned}&\widetilde{S}_{z1}=(a_1\eta+b_1)e^{\xi_1\eta}+(a_2\eta+b_2)e^{\xi_2\eta},\\ &\widetilde{S}_{\varphi 1}=(c_1\eta+d_1)e^{\xi_1\eta}+(c_2\eta+d_2)e^{\xi_2\eta},\end{aligned} \tag{33}$$

where $\xi_{1,2}$ are determined by Eqs. (29). The general solution of coupled homogeneous equations (32) is of the form of (30) where the constants $C^{(1)}$ and $C^{(2)}$ are found from the zero boundary conditions in Eqs. (32). The calculation process is straight forward but time consuming and results in rather cumbersome expressions. However, substituting the values of β_n specific for the given problem, the result becomes as simple as:

$$\left.\frac{\partial S_{z1}}{\partial\eta}\right|_{\eta=0}=-\frac{1}{2}h_z, \qquad \left.\frac{\partial S_{\varphi 1}}{\partial\eta}\right|_{\eta=0}=\frac{1}{2}h_\varphi. \tag{34}$$

Then, the first-order term for the impedance matrix is:

$$\hat{\varsigma}_1 = \frac{c(1-i)}{4\pi\sigma\delta}\left(\frac{\delta}{a}\right)\begin{pmatrix}\frac{(1+i)}{4} & 0\\ 0 & -\frac{(1+i)}{4}\end{pmatrix}. \tag{35}$$

Comparing (35) and (31), it is seen that the ratio of $\hat{\varsigma}_1/\hat{\varsigma}_0$ is of the order $(\delta/a)/\sqrt{\tilde{\mu}}$ or δ_m/a. *Therefore, the actual parameter in the expansion for the impedance is* δ_m/a, *proving the validity of the high frequency results in a wider frequency region if* $\tilde{\mu}$ *is sufficiently large.*

2.5 Low frequency approximation

Let us now construct the solution for the impedance in the opposite limit $a/\delta << 1$. Having the high-frequency result (35), it can be expected that in this case the actual parameter of the expansion involves the magnetic skin depth as well. Then, it may be difficult to join the two asymptotes together. Therefore, we would like to build the low frequency asymptote such that it could be expanded to the case $a/\delta_m > 1$. The solution of (15) is taken in the form:

$$h_\varphi = \bar{h}_\varphi \frac{J_1(k_1 a x)}{J_1(k_1 a)} + \tilde{h}_\varphi(x), \qquad h_z = h_{ex}\frac{J_0(k_2 a x)}{J_0(k_2 a)} + \tilde{h}_z(x), \tag{36}$$

where $J_{0,1}$ are the Bessel functions of the first kind. In (36), the first terms give the exact solutions for the homogeneous forms of equations (15). This representation for fields h_φ, h_z is proving to be adequate to get almost a monotonic transition from one asymptote to the other, changing a frequency or an external magnetic field.

The functions $\tilde{h}_\varphi$ and $\tilde{h}_z$ determining the extent of coupling of equations (5) are found from:

$$\begin{aligned} x^2\frac{\partial^2\tilde{h}_\varphi}{\partial x^2} + x\frac{\partial\tilde{h}_\varphi}{\partial x} + \left(\beta_1^2\beta^2x^2 - 1\right)\tilde{h}_\varphi &= -h_{ex}\frac{\beta_3^2\beta^2x^2J_0(\beta_2\beta x)}{J_0(\beta_2\beta)} - \beta_3^2\beta^2x^2\tilde{h}_z \\ x^2\frac{\partial^2\tilde{h}_z}{\partial x^2} + x\frac{\partial\tilde{h}_z}{\partial x} + \beta_2^2\beta^2x^2\tilde{h}_z &= -\bar{h}_\varphi\frac{\beta_3^2\beta^2x^2J_1(\beta_1\beta x)}{J_1(\beta_1\beta)} - \beta_3^2\beta^2x^2\tilde{h}_\varphi \end{aligned} \tag{37}$$

satisfying the conditions

$\tilde{h}_\varphi(1)=0 \quad \tilde{h}_z(1)=0$

$\tilde{h}_\varphi(x)<\infty \quad \tilde{h}_z(x)<\infty$

Here we use the same notation $\beta = a/\delta$ for the small parameter though it is inverse to that used in Section 2.4. The solution of equation (37) is represented in terms of the asymptotic series of powers of β, using the regular perturbation method:

$$\tilde{h}_\varphi(x) = \sum_{n\geq 0} \beta^n \tilde{h}_{\varphi n}(x), \qquad \tilde{h}_z(x) = \sum_{n\geq 0} \beta^n \tilde{h}_{z\,n}(x),$$

$$\frac{J_1(\beta_1 \beta x)}{J_1(\beta_1 \beta)} = x\left[1 + \frac{\beta_1^2 \beta^2}{8}\left(1 - x^2\right)\right] + O\left(\beta^4\right), \tag{38}$$

$$\frac{J_0(\beta_2 \beta x)}{J_0(\beta_2 \beta)} = \left[1 + \frac{\beta_2^2 \beta^2}{4}\left(1 - x^2\right)\right] + O\left(\beta^4\right).$$

Substituting series (38) into equation (37) and grouping together terms having the same powers of β, the equations for the regular series $\tilde{h}_{\varphi n}(x)$ and $\tilde{h}_{z\,n}(x)$ are obtained. It turns out that the terms of the zero degree and of any (2n+1)-th degree are equal to zero. The second-degree terms are found from:

$$x^2 \frac{\partial^2 \tilde{h}_{\varphi 2}}{\partial x^2} + x \frac{\partial \tilde{h}_{\varphi 2}}{\partial x} - \tilde{h}_{\varphi 2} = -h_{ex}\, \beta_3^2\, x^2$$

$$x^2 \frac{\partial^2 \tilde{h}_{z2}}{\partial x^2} + x \frac{\partial \tilde{h}_{z\,2}}{\partial x} = -\bar{h}_\varphi\, \beta_3^2\, x^3 \tag{39}$$

$$\tilde{h}_{\varphi 2}(1) = 0 \quad \tilde{h}_{z2}(1) = 0$$

$$\tilde{h}_{\varphi 2}(x) < \infty \quad \tilde{h}_{z2}(x) < \infty$$

Solving equations (39) gives:

$$\tilde{h}_{\varphi 2} = \frac{h_{ex}\, \beta_3^2 \left(x - x^2\right)}{3}, \qquad \tilde{h}_{z2} = \frac{\bar{h}_\varphi\, \beta_3^2 \left(1 - x^3\right)}{9} \tag{40}$$

The equations for the fourth-degree terms are:

$$x^2 \frac{\partial^2 \tilde{h}_{\varphi 4}}{\partial x^2} + x \frac{\partial \tilde{h}_{\varphi 4}}{\partial x} - \tilde{h}_{\varphi 4} = -h_{ex} \frac{\beta_2^2\, \beta_3^2}{4} x^2 \left(1 - x^2\right) - x^2 \left(\beta_3^2\, \tilde{h}_{z\,2} + \beta_1^2\, \tilde{h}_{\varphi 2}\right)$$

$$x^2 \frac{\partial^2 \tilde{h}_{z\,4}}{\partial x^2} + x \frac{\partial \tilde{h}_{z\,4}}{\partial x} = -\bar{h}_\varphi \frac{\beta_1^2\, \beta_3^2}{8} x^3 \left(1 - x^2\right) - x^2 \left(\beta_2^2\, \tilde{h}_{z\,2} + \beta_3^2\, \tilde{h}_{\varphi 2}\right) \tag{41}$$

$$\tilde{h}_{\varphi 4}(1) = 0 \quad \tilde{h}_{z\,4}(1) = 0$$

$$\tilde{h}_{\varphi 4}(x) < \infty \quad \tilde{h}_{z\,4}(x) < \infty$$

Substituting (40) into (41) gives:

$$\tilde{h}_{\varphi 4} = -\bar{h}_{\varphi}\frac{\beta_3^4}{9}\left(\frac{x^2}{3}-\frac{x^5}{24}-\frac{21}{72}x\right)-h_{ex}\frac{\beta_2^2\beta_3^2}{4}\left(\frac{x^2}{3}-\frac{x^4}{15}-\frac{12}{45}x\right)- \\ -h_{ex}\frac{\beta_1^2\beta_3^2}{3}\left(\frac{x^3}{8}-\frac{x^4}{15}-\frac{7}{120}x\right),$$

$$\tilde{h}_{z4} = -\bar{h}_{\varphi}\frac{\beta_1^2\beta_3^2}{8}\left(\frac{x^3}{9}-\frac{x^5}{25}-\frac{16}{225}\right)-\bar{h}_{\varphi}\frac{\beta_3^2\beta_2^2}{9}\left(\frac{x^2}{4}-\frac{x^5}{25}-\frac{21}{100}\right)- \\ -h_{ex}\frac{\beta_3^4}{3}\left(\frac{x^3}{9}-\frac{x^4}{16}-\frac{7}{144}\right). \qquad (42)$$

Equations (36),(40) and (42) give the asymptotic series for the magnetic field, as far as the β^4-terms:

$$h_{\varphi} = \bar{h}_{\varphi}\frac{J_1(k_1 a\, x)}{J_1(k_1 a)}+\beta^2\tilde{h}_{\varphi 2}(x)+\beta^4\tilde{h}_{\varphi 4}(x), \qquad (43)$$

$$h_z = h_{ex}\frac{J_0(k_2 a\, x)}{J_0(k_2 a)}+\beta^2\tilde{h}_{z 2}(x)+\beta^4\tilde{h}_{z 4}(x).$$

Calculating the electric field from Eqs. (12) and representing it in the form linear in $\bar{h}_{\varphi}$ and h_{ex}, the components of the surface impedance matrix are obtained:

$$\varsigma_{zz} = \frac{k_1 c}{4\pi\sigma}\frac{J_0(k_1 a)}{J_1(k_1 a)}+\frac{1}{54}\left(\frac{a}{\delta}\right)^4\frac{c\mu_3^2}{\pi\sigma a}, \qquad (44)$$

$$\varsigma_{\varphi\varphi} = -\frac{k_2 c}{4\pi\sigma}\frac{J_1(k_2 a)}{J_0(k_2 a)}+\frac{1}{36}\left(\frac{a}{\delta}\right)^4\frac{c\mu_3^2}{\pi\sigma a}, \qquad (45)$$

$$\varsigma_{\varphi z} = \varsigma_{z\varphi} = i\frac{a\omega}{3c}\mu_3-\left(\frac{a}{\delta}\right)^4\left[\frac{\mu_1\mu_3}{60}+\frac{\mu_2\mu_3}{30}\right]\frac{c}{\pi\sigma a}. \qquad (46)$$

The second terms in Eqs. (44)–(46) depend on the corresponding magnetic parameters μ_n, demonstrating that the actual expansion parameter involves a sort of magnetic skin depth (but not exactly δ_m). For example, in equation (44) in the case of $k_1 a >> 1$ (but $a/\delta << 1$) the ratio of the second term to the first becomes $(1/54)(k_3 a)^4/k_1 a$. The values of k_n are of the same order, as it follows from Eqs. (15),(19).

Yet, the numerical analysis shows that the first terms in Eqs. (44)–(46) can give the main contribution to the impedance even in the case of $(k_n / a) \approx 1$, which is illustrated by a small numerical factor 1/54 in the above example. This helps joining the low frequency asymptote with the high frequency one. In the next Section, the asymptotic behaviour will be discussed in more detail for different magnetic configurations.

2.6 Analysis of the impedance behaviour for two types of anisotropy

Our approach can be applied to a wire having a circumferential or helical anisotropy. In general, the anisotropy axis $\mathbf{n}_K$ has an angle $45° < \alpha \leq 90°$ with the wire axis (z-axis), as shown in Fig. 2.7. The wire is assumed to be in a single domain state with the static magnetisation $\mathbf{M_0}$ directed in a helical way having an angle θ with the z-axis. As it has been discussed in Section 1.6, the local ac response will be calculated in single domain approximation but the conclusion concerning the total ac response will be always made on basis of averaging over the whole domain structure. The radial variation in θ is neglected as it is explained in Section 2.3. The magnetic configuration changes under the application of the external axial magnetic field H_{ex} and the dc bias current I_b inducing the circular magnetic field H_b. The stable direction of $\mathbf{M_0}$ is found by minimising the magnetostatic energy density $U_0 = U_H + U_a$ (see Section 1.6):[21]

$$\begin{aligned} &\partial U_0 / \partial \theta = 0, \\ &U_0 = -K \cos^2(\alpha - \theta) - M_0 H_{ex} \cos\theta - M_0 H_b \sin\theta, \end{aligned} \tag{47}$$

where H_b is the dc circular field induced by the dc bias current I_b. Equation (47) describes the rotational magnetisation process demonstrated in Fig. 2.8, where the magnetisation plots for two types of anisotropy and different values of the dc bias H_b are given. The domain processes may not be essential for the reversal of $\mathbf{M_0}$, since the magnetisation vector during its rotation is held parallel to the surface, without going through high-energy demagnetisation states. In the case of a circumferential anisotropy (Fig. 2.8(a)), a dc bias current (inducing H_b larger than the coercivity) eliminates the domain structure, without changing the magnetic symmetry.

The case of a helical anisotropy is more complicated. The dc bias causes the transition from a symmetric hysteresis curve to asymmetric anhysteretic one which happens at $H_b / H_K = \cos\alpha$ (see Fig. 2.8(b)). Therefore, in this case a much larger bias field is needed to realise a single domain state.

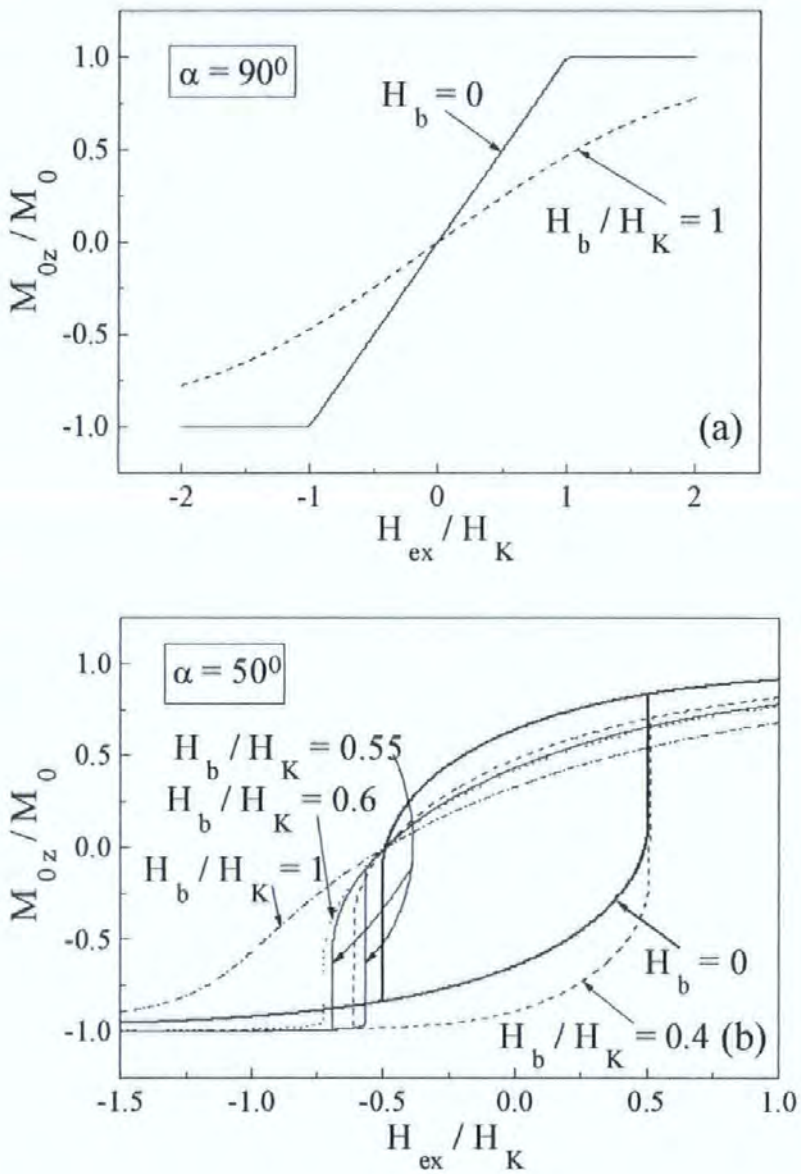

Fig. 2.8 *Magnetisation curves $M_{0z}(H_{ex})$ for different magnitudes of the dc bias field H_b. The cases related to a circumferential ($\alpha = 90°$) and helical ($\alpha = 50°$) anisotropy are shown in (a) and (b), respectively.*

The permeability matrix $\hat{\boldsymbol{\mu}} = \hat{\mathbf{I}} + 4\pi\hat{\boldsymbol{\chi}}$ is found from a linearised Landau-Lifshitz-Gilbert equation for $\mathbf{m} = \hat{\boldsymbol{\chi}}\,\mathbf{h}$ written in the co-ordinate system (r, φ', z') with the axis z' parallel to $\mathbf{M}_0$ (see Section 1.5):

$$-i\omega\,\mathbf{m} + (\omega_H - i\tau\omega)(\mathbf{m}\times\mathbf{n}_{z'}) + \gamma M_0((\hat{\mathbf{N}}_{eff}\,\mathbf{m})\times\mathbf{n}_{z'}) = \gamma M_0(\mathbf{h}\times\mathbf{n}_{z'}). \tag{48}$$

Here $\omega_H = \gamma(\partial U_F/\partial\mathbf{M}_0)_{z'}$, U_F is the free energy density, which coincides with U_0 in our case (see Sections 1.5 and 1.6), γ is the gyromagnetic constant, τ is the spin-relaxation parameter, $\hat{\mathbf{N}}_{eff}$ is the matrix of the effective factors in (r, φ', z')-system:

$$N_{z'z'} = -\frac{2K}{M_0^2}\cos^2(\theta-\alpha), \quad N_{\varphi'\varphi'} = -\frac{2K}{M_0^2}\sin^2(\theta-\alpha),$$

$$N_{z'\varphi'} = N_{\varphi'z'} = \frac{K}{M_0^2}\sin 2(\theta-\alpha). \tag{49}$$

Solving equation (48) determines the susceptibility matrix $\hat{\boldsymbol{\chi}}$ which has the form of Eq. (17) with:

$$\begin{aligned}
&\chi_1 = \omega_M(\omega_1 - i\tau\omega)/\Delta, \quad \chi_2 = \omega_M(\omega_2 - i\tau\omega)/\Delta, \quad \chi_a = \omega\,\omega_M/\Delta,\\
&\Delta = (\omega_2 - i\tau\omega)(\omega_1 - i\tau\omega) - \omega^2,\\
&\omega_1 = \gamma[H_{ex}\cos\theta + H_b\sin\theta + H_K\cos 2(\alpha-\theta)], \quad H_K = 2K/M_0\\
&\omega_2 = \gamma[H_{ex}\cos\theta + H_b\sin\theta + H_K\cos^2(\alpha-\theta)], \quad \omega_M = \gamma M_0.
\end{aligned} \tag{50}$$

The impedance matrix is determined via the permeability parameters μ_{tt} (low-frequency case) or the parameter $\tilde{\mu}$ (high-frequency case), all of them are determined by the apparent susceptibility $\tilde{\chi}$ in Eqs. (19). Substituting (50) into (19) gives:

$$\tilde{\chi} = \frac{\omega_M(\omega_2 - i\tau\omega) + 4\pi\omega_M^2}{(\omega_1 - i\tau\omega)(\omega_2 + 4\pi\omega_M - i\tau\omega) - \omega^2} \tag{51}$$

Figures 2.9(a-d) demonstrates the dispersion curves for the effective permeability parameter $\tilde{\mu} = 1 + 4\pi\tilde{\chi}$ (see Eqs. (19) and (29)), which enters the impedance matrix in combination with the magnetisation angle θ. The following magnetic parameters have been chosen: circumferential anisotropy ($\alpha = 90^0$), anisotropy field $H_K = 2$ Oe, saturation magnetisation $M_0 = 500$ G, gyromagnetic constant $\gamma = 2\times10^7$ (rad/s)/Oe. In calculations, a small dispersion of the anisotropy angle α with respect to 90^0 should be introduced to model a real sample and avoid zero ferromagnetic resonance frequency at $H_{ex} = H_K$.

The real part $\mathrm{Re}(\tilde{\mu}(\omega))$ approaches unity at the ferromagnetic resonance frequency $(\alpha = 90^0)$ $f_{FMR} = \gamma\sqrt{|H_{ex} - H_K|4\pi M_0}/2\pi$: $f_{FMR} = 365$ MHz at $H_{ex} = 0$ (see Fig. 2.9(a)) and $f_{FMR} = 725$ MHz at $H_{ex} = 10$ Oe (see Fig. 2.9(b)). In the gigahertz range, $\mathrm{Re}(\tilde{\mu}(\omega))$ is negative being in magnitude in the range of 10-20, and $\mathrm{Im}(\tilde{\mu}(\omega))$ is in the range of 10-40. Both of them become insensitive to the external magnetic field, as shown in Fig. 2.9(c). In this case, the field dependence of the impedance is entirely due to that for the static magnetisation orientation θ. Then, if θ is a sensitive function of H_{ex}, to insure high field sensitivity of the impedance it is important only that the condition $|\tilde{\mu}(\omega)| >> 1$ is held. This conclusion clearly demonstrates that the condition of the ferromagnetic resonance is not required for the MI effect, contrary to the widely expressed belief.[22,23]

A large difference between f_{FMR} and the frequency where the imaginary part reaches a maximum value is caused by the specific form of the effective susceptibility $\tilde{\chi}$ containing all the components of the susceptibility matrix $\hat{\chi}$. The dispersion curves, considered above, look very similar to a relaxation spectrum typical of polycrystalline multidomain ferrites. However, in our case, the "relaxation-like" dispersion is caused by a complicated form (18) of the effective susceptibility. Such kind of the dispersion is always observed in experiments with bulk ferromagnetic conductive samples, where the skin-effect is important and the effective susceptibility is composed of the components of the internal matrix $\hat{\chi}$. For example, in Ref. 24 the dispersion of the initial hard-axis permeability, which corresponds to the parameter $\mu_2 = 1 + 4\pi\sin^2(\theta)\tilde{\chi}$ in our designations (involving the same frequency-dependent parameter $\tilde{\chi}$), was measured in Co-rich and Fe-rich wires with 20 μm diameter at the megahertz and gigahertz ranges. The measured dispersion shown in Fig. 2.9(d) (solid line) has a qualitative agreement to that shown in Fig. 2.9(a). In Ref. 25 the initial hard axis permeability of NiFe and FeAlN films was investigated. For films with more than micron thickness, the permeability had a relaxation-like dispersion curve where f_{FMR} did not coincide with the frequency of the imaginary part peak. On the contrary, the dispersion curves in ultrathin layers had the resonance-like dispersion where the peak in the imaginary part corresponds to f_{FMR}.

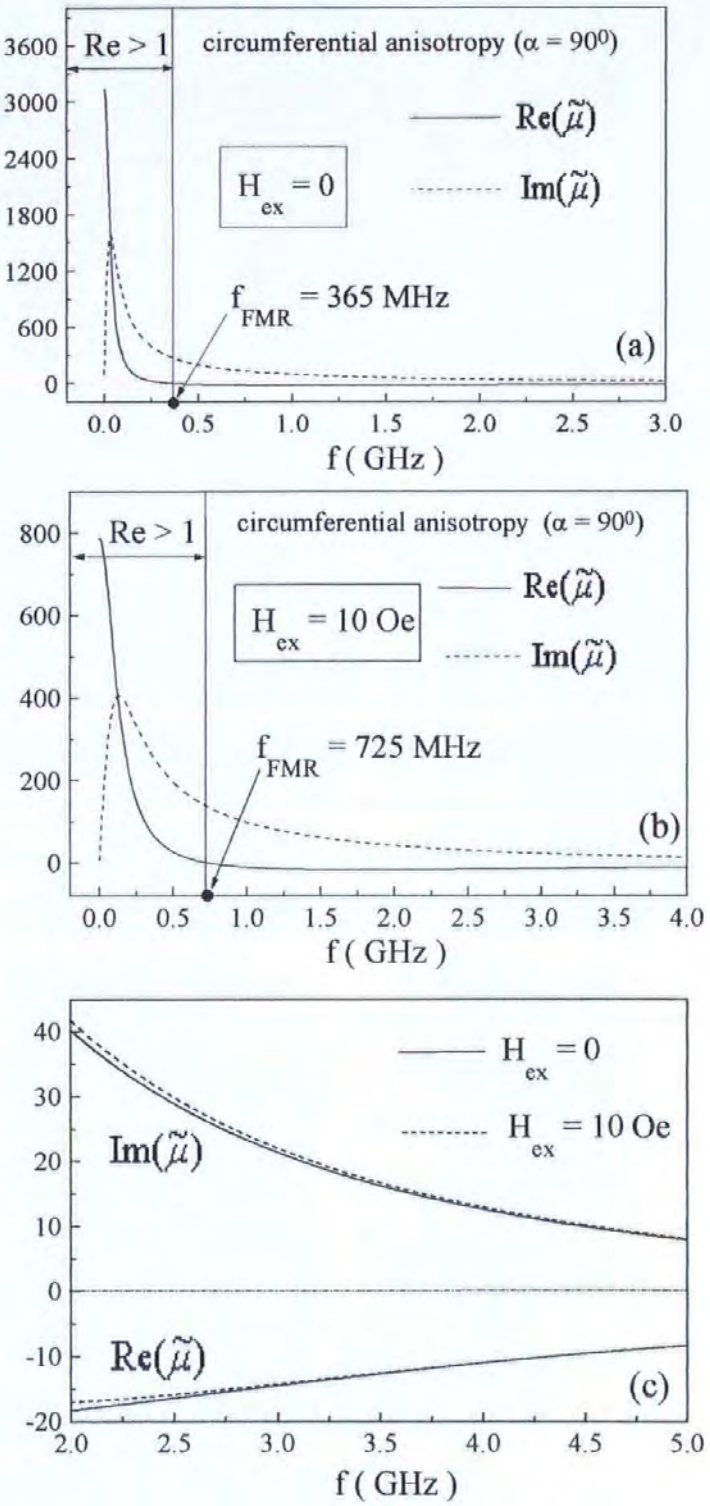

Fig. 2.9(a-c) *Dispersion curves of the effective permeability* $\tilde{\mu}$ *calculated for different* H_{ex}. *Magnetic parameters: anisotropy field* $H_K = 2$ *Oe, saturation magnetisation* $M_0 = 500$ *G, and gyromagnetic constant* $\gamma = 2\times10^7$ *(rad/s)/Oe. For frequencies much higher than* f_{FMR} *(gigahertz range)* $\tilde{\mu}$ *becomes insensitive to* H_{ex} *as shown in (c).*

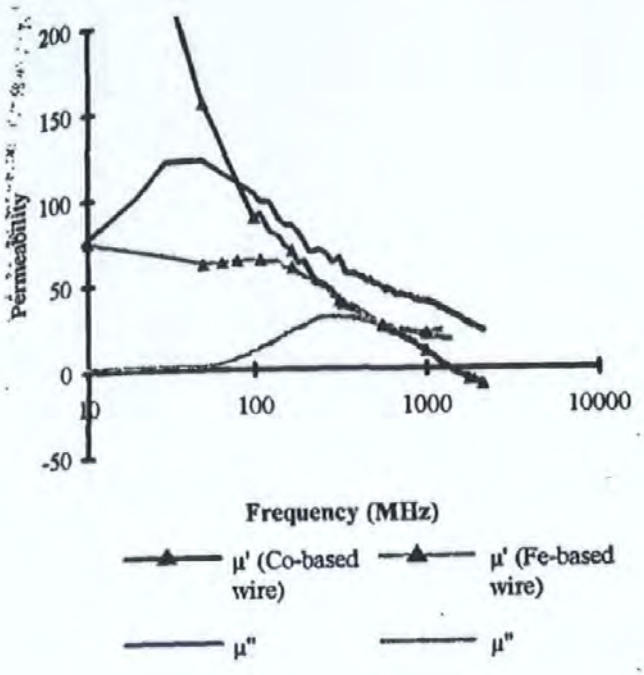

(d)

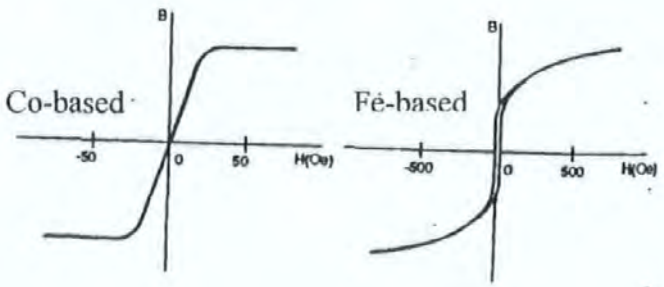

(e)

Fig. 2.9(d,e) *Experimental permeability dispersions (in (d)) and hysteresis loops along wire axis (in (e)) measured in Ref. [24] for Co-based and Fe-based wires with 20 μm diameter. Permeability levels are significantly higher for Co-based wire than for Fe-based, especially in the low frequency range. The real part of the permeability for Co-based wire is about 350 below 10 MHz. The measured dispersion of Co-based wire shown in Fig. 2.9(d) (solid line) has a qualitative agreement to that shown in Fig. 2.9(a). The hysteresis loop of Co-based wire has a low coercive force (less than 1 Oe) and a nearly linear response up to the saturation. This is a hard axis B-H loop (see Fig. 2.8(a)) corresponding to the circumferential magnetisation (see Fig. 2.2(b)). In contrast, Fe-based wire exhibits a coercive field larger than 10 Oe, and does not reach saturation before 800 Oe.*

The easy-axis permeability, which corresponds to the parameter $\mu_1 = 1 + 4\pi\cos^2(\theta)\tilde{\chi}$ in our designations, is related to a specific excitation method of the sample when the magnetic field is circular in the wire and transverse in the film. An indirect investigation of μ_1 in the wire can be carried out by means of the S-parameter measurements.[26,27]

Having specified the static magnetic configuration and the ac permeability matrix, we can proceed with the impedance analysis, using equations (44)–(46) for the low frequency case or equations (31),(35) for the opposite limit. Since both the approximations involve as an actual expansion parameter a certain magnetic skin depth, the choice between them depends not only on the value of frequency, but also on the value of H_{ex} determining the permeability parameters. Figure 2.10 shows the components of the impedance matrix as functions of the expansion parameter a/δ (or as functions of frequency) for $H_{ex} = 0.25H_K$ and two anisotropies: circumferential ($\alpha = 90°$) and helical ($\alpha = 60°$).

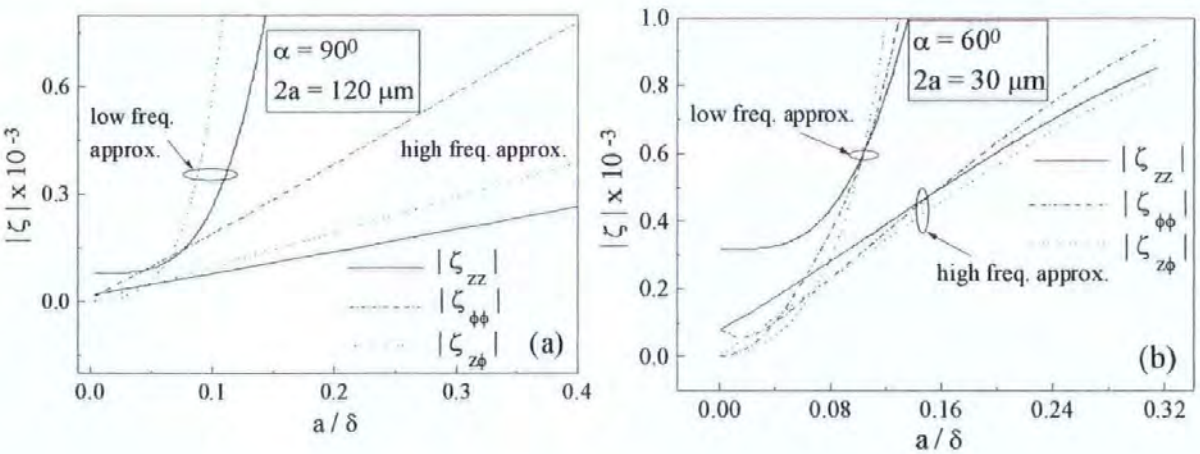

Fig. 2.10 *Frequency spectra of the components of matrix* $\hat{\varsigma}$ *calculated using the low and high frequency approximations for* $\alpha = 90°$ *in (a) and* $\alpha = 60°$ *in (b).* $H_{ex} = 0.25H_K$, $H_b = 0$. *For* $\alpha = 90°$ *in (a),* $\varsigma_{\varphi\varphi}$ *monotonically transits to the high frequency case, therefore only one line is shown for low and high frequency approximation. Parameters used:* $H_K = 5$ *Oe,* $\sigma = 10^{16}\,\mathrm{sec}^{-1}$, $M_0 = 500$ *G,* $\tau = 0.2$, $\gamma = 2\cdot 10^7$ *rad/s Oe.*

For these parameters, the values of the permeability are fairly large and the transition from the low-frequency case to the high-frequency one occurs at $a/\delta = 0.04 - 0.08$. For $\varsigma_{z\varphi}, \varsigma_{\varphi\varphi}$ components, the two asymptotes have an intersection regions (or even for $\alpha = 90°$, $\varsigma_{\varphi\varphi}$ monotonically transits to the high frequency case), for ς_{zz} there is a certain gap, actually rather small, but a sort of interpolation is needed. Considering the field dependences of the impedance matrix, a practical rule to replace a low frequency asymptote by the high frequency one may be the condition that the second term in expansions (44)–(46) has grown up to 10% of the first one.

The field characteristics of the impedance matrix are determined by the combined effect of $\tilde{\chi}(H_{ex})$ and $\theta(H_{ex})$, and are presented in Figs. 2.11-2.14 for the two types of anisotropy. The case of the circumferential anisotropy ($\alpha = 90°$) is given in Fig. 2.11. For this case, H_{ex} is a hard axis field, then both $M_{0z}(H_{ex})$ and $\tilde{\chi}(H_{ex})$ do not exhibit a hysteresis. The positions of maximums for ς_{zz}, $\varsigma_{\varphi\varphi}$, $\varsigma_{z\varphi}$ $(=\varsigma_{\varphi z})$ are closely related to those for $\cos^2\theta$, $\sin^2\theta$, $\sin 2\theta$, namely, $|H_{ex}| = H_K$, 0, $H_K/2$, respectively. With increasing frequency, the peaks for ς_{zz} and $\varsigma_{z\varphi}$ shift towards higher fields which is related to the permeability spectra. The application of the circular bias H_b makes the peaks smaller and broader, but does not lead to a characteristically different behaviour. The diagonal components ς_{zz} and $\varsigma_{\varphi\varphi}$ are symmetrical with respect to H_{ex}, whereas the off-diagonal components $\varsigma_{z\varphi}$ or $\varsigma_{\varphi z}$ are antisymmetrical that is demonstrated in Fig. 2.11(d) by plotting the real and imaginary parts of $\varsigma_{z\varphi}$.

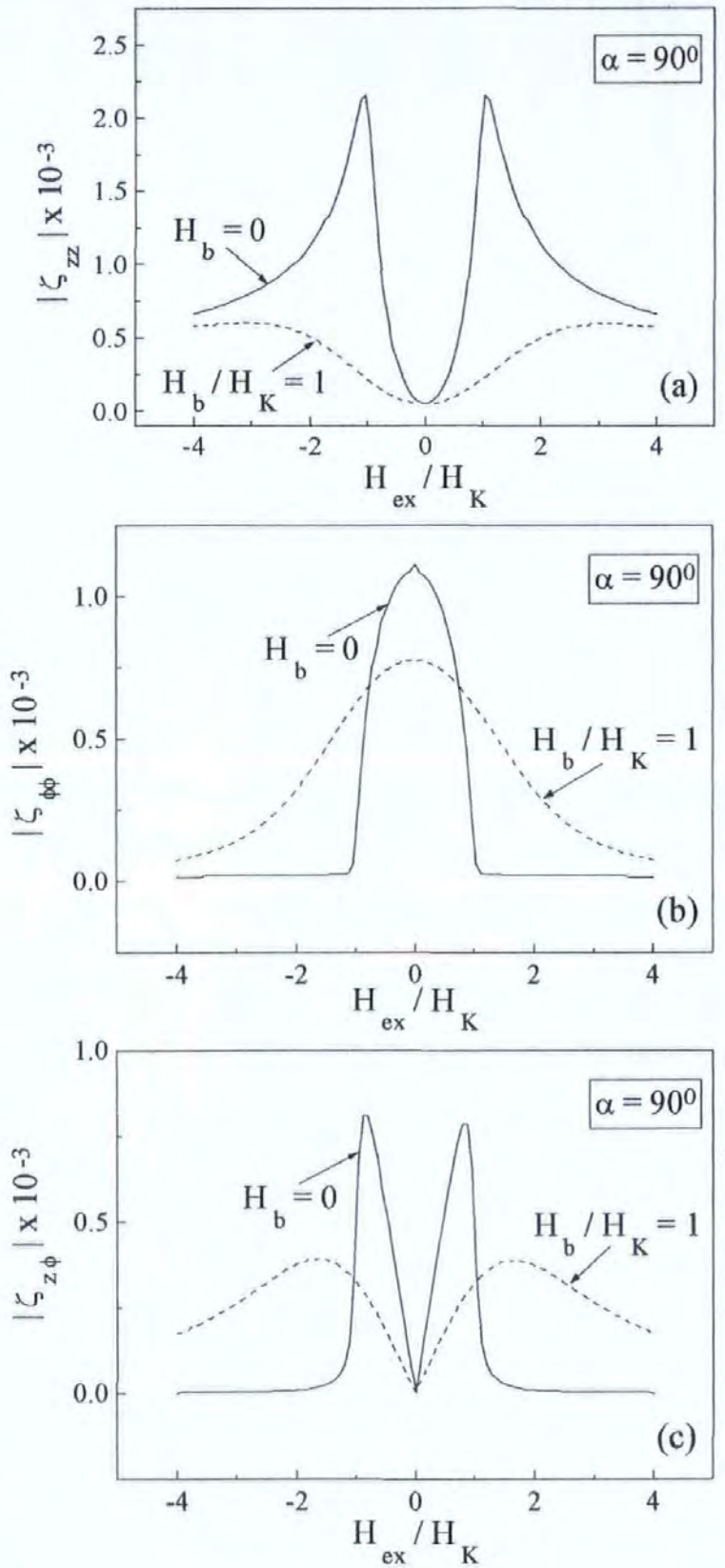
α = 90⁰
$|\zeta_{zz}|$ x 10⁻³
$H_b = 0$
$H_b / H_K = 1$
(a)
H_{ex} / H_K
α = 90⁰
$|\zeta_{\phi\phi}|$ x 10⁻³
$H_b = 0$
$H_b / H_K = 1$
(b)
H_{ex} / H_K
α = 90⁰
$|\zeta_{z\phi}|$ x 10⁻³
$H_b = 0$
$H_b / H_K = 1$
(c)
H_{ex} / H_K

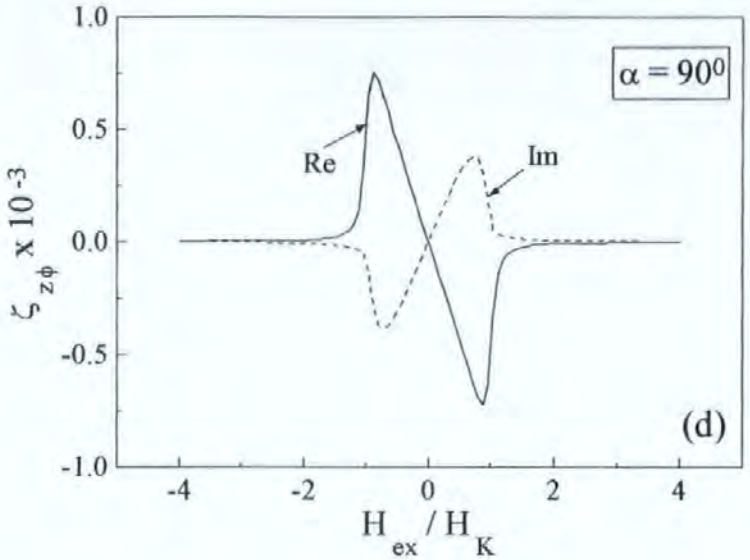

Fig. 2.11 *Field characteristics of the components of matrix* $\hat{\varsigma}$ *for a circumferential anisotropy. In (a)-(c) plots of magnitude of* ς_{zz}, $\varsigma_{\varphi\varphi}$ *and* $\varsigma_{z\varphi}$ *vs.* H_{ex}, *respectively, are given for* $H_b / H_K = 0$ *and 1. In (d), real and imaginary parts of* $\varsigma_{z\varphi}$ *vs.* H_{ex} *are plotted for* $H_b = 0$. $2a = 120\mu m$, $f = 20$ *MHz.*

The case of a helical anisotropy ($\alpha = 50°$) is more complicated involving hysteresis and considerable modifications under the effect of H_b. Analysing the behaviour of ς_{zz} vs. H_{ex}, shown in Fig. 2.12, we see that as the field decreases from positive value, ς_{zz} exhibits a broad flat peak, which occurs between 0 and H_K, depending on the anisotropy angle α. Upon reversing the field direction, the impedance rapidly drops down to its original low value, exhibiting the highest sensitivity. With further increase in H_{ex}, it jumps back to the level seen for positive fields, which is associated with irreversible rotational flip in $\mathbf{M}_0$. With increasing the dc bias H_b, considerable asymmetry appears in the impedance plots. Further increase in H_b results in a sudden shift of the hysteresis to negative fields with a simultaneous shrinkage of the hysteresis area, and $H_b > H_K \cos\alpha$ results in the disappearance of the hysteresis. For H_b slightly larger than $H_K \cos\alpha$, the field sensitivity of the impedance change is especially high: for negative fields the nominal change can be more than 100% when H_{ex} is changed by only $0.1\,H_K$.

The other components of the impedance matrix show characteristically similar behaviour under the effect of H_b, as demonstrated in Fig. 2.13 and Fig. 2.14.

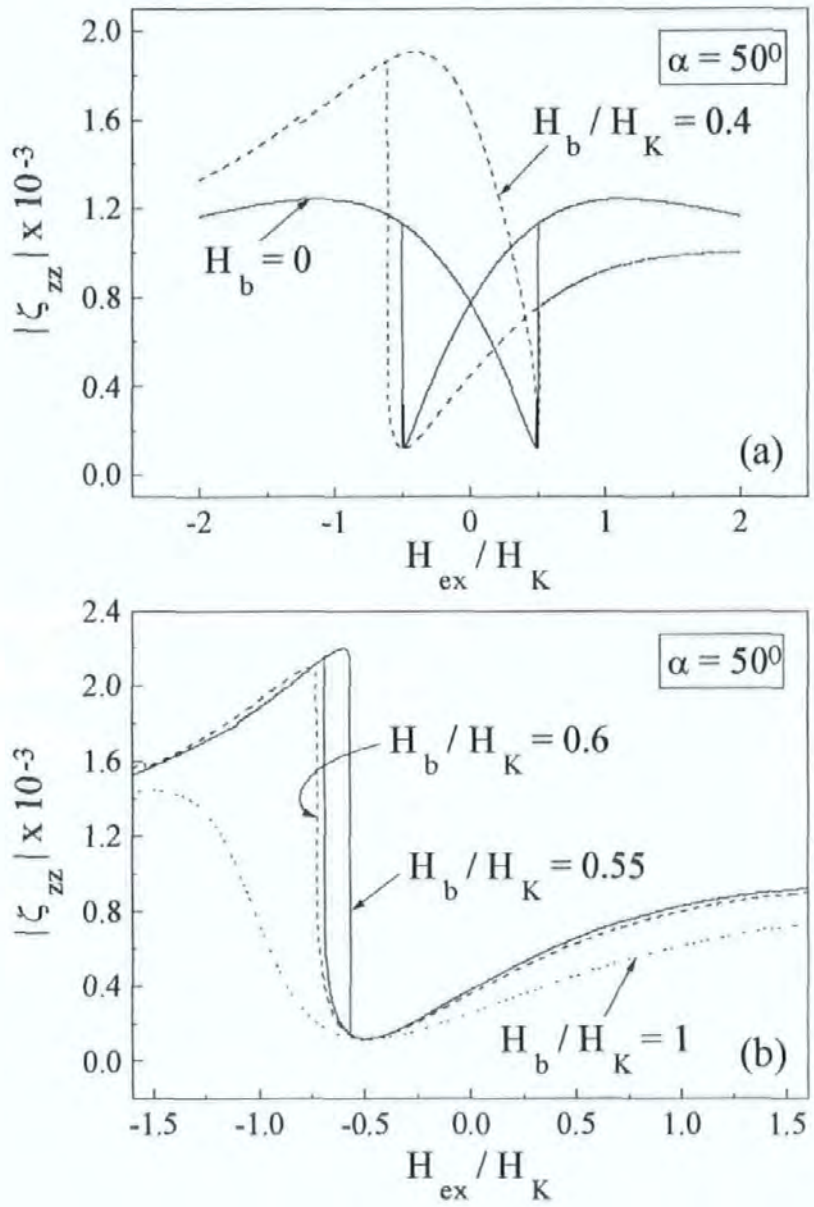

Fig. 2.12 *Modifications of the longitudinal impedance* ς_{zz} *vs.* H_{ex} *under the effect of the dc bias* $0 \le H_b / H_K \le 1$. $\alpha = 50°$. $2a = 120\mu m$, $f = 20$ *MHz.*

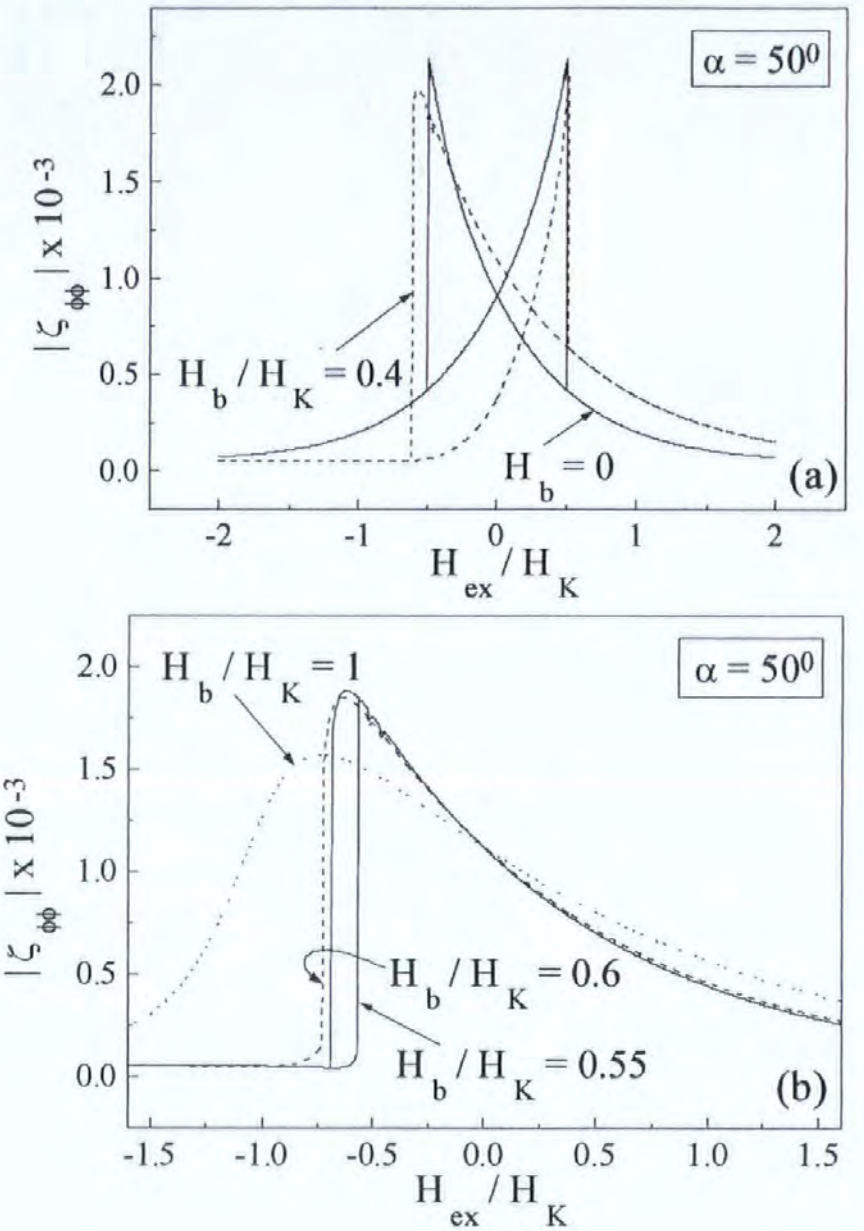

Fig. 2.13 *Modifications of the circumferential impedance* $\varsigma_{\varphi\varphi}$ *vs.* H_{ex} *under the effect of the dc bias* $0 \le H_b / H_K \le 1$. $\alpha = 50°$. $2a = 120\mu m$, $f = 20$ *MHz.*

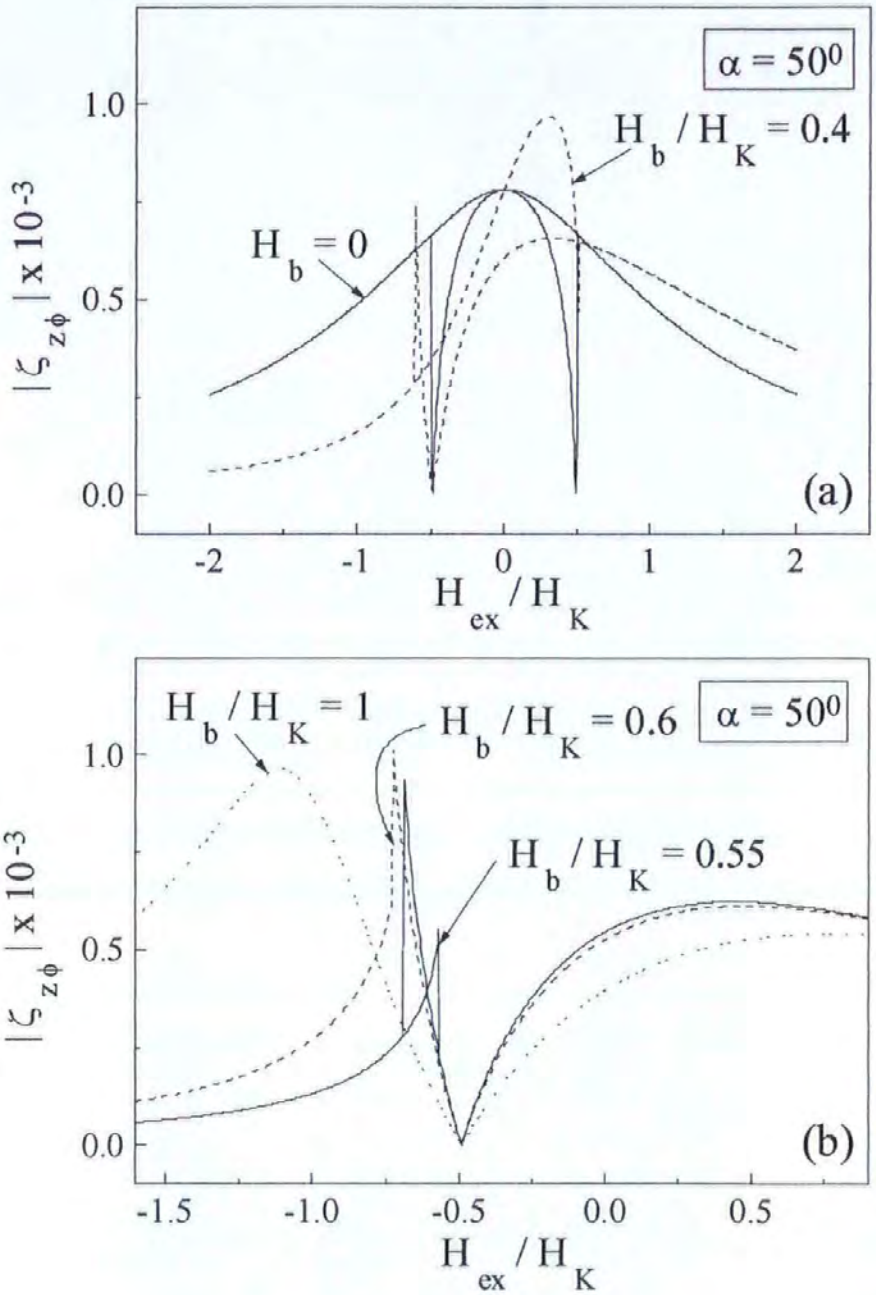

Fig. 2.14 *Modifications of the off-diagonal impedance* $\varsigma_{z\varphi}$ *vs.* H_{ex} *under the effect of the dc bias* $0 \le H_b / H_K \le 1$. $\alpha = 50°$. $2a = 120\mu m$, $f = 20$ *MHz.*

2.7 Experimental results and comparison with the theory

An important next step is to compare the theoretical impedance characteristics with those obtained experimentally. The experimental research on magneto-impedance in amorphous wires, although rather wide is mainly restricted to measurements of the voltage across the wire, which corresponds to measuring ς_{zz}. A number of results reported by different groups on $\varsigma_{zz}(H_{ex})$ seem to be in conflict. The field characteristics for same frequencies, obtained for similar wire samples, can exhibit completely different behaviour. This is a consequence of different ac excitations used, resulting in different magnetisation mechanisms involved in each case. For example, in the case of a circular or a helical domain structure, the ac current may cause the irreversible domain movement if its amplitude is larger than that corresponding to the circular coercivity. Such irreversible domain processes take place even at frequencies of few MHz. This process will mainly determine the field behaviour of the impedance: $\varsigma_{zz}(H_{ex})$ has a maximum at $H_{ex}=0$ and decreases rapidly with increasing the field.[3,28,29] This is due to the corresponding behaviour of the differential domain permeability under the effect of a hard axis field. If the current amplitude is small and irreversible domain displacements are not possible, the longitudinal impedance has two symmetrical maximums at $H_{ex}\approx H_K$, in agreement with that shown in Fig. 2.11.[1,30] Regarding the other components of the impedance matrix there are just few experimental works on field characteristics of $\varsigma_{z\varphi}$ and $\varsigma_{\varphi\varphi}$ for a wire with circumferential anisotropy.[20,30]

For the sake of accurate quantitative comparison, we have carried out measurements of the full surface impedance matrix as a function of H_{ex}, at conditions as close corresponding to the theoretical model as possible. Care has been taken to realise a linear ac excitation (the amplitudes of ac currents, magnetisation and fields are considerably smaller than such dc parameters as the coercivity, anisotropy, dc magnetisation). Another model restriction is considering a single domain state. In the experiment, the domain structure can be eliminated by a dc current, however, in the case of a helical anisotropy, the field produced by this current has to be larger than the anisotropy field (not coercivity). In the cases, where domain structure is inevitable, the effect of domain wall dynamics on impedance behaviour is less at higher frequencies due to damped wall motion.

Two kinds of wires have been used: as-cast 120 μm diameter CoFeSiB wire having a nearly zero magnetostrictive constant $\lambda < 0$ and a circumferential anisotropy (at least in the outer region), and tension-annealed 30 μm diameter CoSiB wire (magnetostriction $\lambda = -3 \cdot 10^{-6}$) having a spontaneous helical anisotropy due to a residual stress distribution.[31,32]

2.7.1 Experimental method

The impedance matrix is measured by means of the Hewlett-Packard 8753E Vector Network Analyser configured in the two-ports measuring option for the S_{21}-parameter (forward transmission): $S_{21} = V_{out} / V_{in}$, where V_{in} is the excitation sinusoidal signal from Port I and V_{out} is the output signal measured in Port II. The ac excitation current j and field h_{ex} in Eqs. 8,9 are determined by V_{in}, whereas V_{out} is equal to V_z or V_c in accordance of the excitation method. Thus, the S_{21}-parameter is directly proportional to the certain impedance component. Note that the S_{21}-parameter includes both the normalised amplitude $|V_{out} / V_{in}|$ and phase shifting $\mathrm{Arg}(V_{out} / V_{in})$ with respect to the excitation signal. The MI effect is assumed to be linear, therefore the excitation signal has to be quite small to exclude any non-linear effects. In this Chapter the linear MI effects are investigated using only a few milliamps of excitation, however, large amplitude excitations (tens of milliamps) can be useful for sensor applications where the improvement of the signal-to-noise is important. The general view of the measuring system is shown in Fig. 2.15.

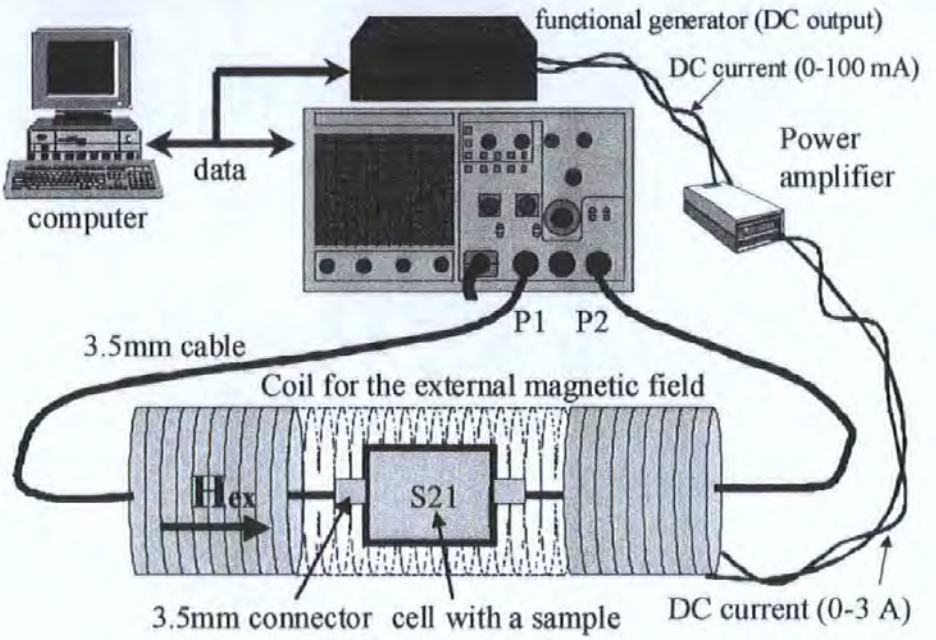

Fig. 2.15 *General view of the measuring system in the two port regime including: vector analyser, two measuring channels, functional generator, power amplifier, and coil. The magnetic field (H_{ex}) is produced from a coil driven by a functional generator and power amplifier. The operating processes of the Analyser and functional generator are synchronised by a computer program.*

Since the Analyser has an unequal sweep parameter — frequency, the field scanning has to be produced by an additional device. The magnetic field (H_{ex}) is produced from a coil driven by a functional generator and power amplifier. The operating processes of the Analyser and functional generator are synchronised by a computer program written using VEE software (Hewlett-Packard programming language). The frequency scanning ranged over several points (11 has been chosen). The magnetic field was incremented by a small value for each frequency range scanned. The field was driven in both positive and negative directions to produce the hysteresis plot. Thus, the functional generator is used as a programmable stepwise dc source to provide the field scans. The S_{21}-values, obtained within one frequency scan, are saved in the Analiser's memory in the form of a column (11 points). Therefore, each frequency scan gives a column of S_{21} taken at some fixed H_{ex}. The total value matrix $\{S_{21}\}_{f,H_{ex}}$ consists of columns of frequency coordinate points (f) and rows of field coordinate points (H_{ex}). The rows contain the field dependences at a fixed frequency.

The measured sample is placed onto an open-type cell made of copper-coated fibreglass printed circuit board (pcb), which has the following parameters: 1.8 mm thickness, average dielectric constant of $\varepsilon = 4.5$, 30 μm of copper on each side. The connection stripes were etched on one side of the pcb and the other was kept copper coated for the ground plane. All the connection stripes were made 2.8 mm wide to provide a wave impedance in the order of 50-Ohms over a wide range of frequencies. The electrical scheme of the cell for ς_{zz}, $\varsigma_{\varphi\varphi}$, $\varsigma_{z\varphi}$ and $\varsigma_{\varphi z}$ is shown in Fig. 2.16. Blocking capacitors (C) prevent the dc bias current I_b from entering the Analyser. The cell has input and output 3.5-mm connectors that are connected to the Analyser ports via 3.5-mm coaxial cables using 3.5-mm to type-N adapters. The microwave track including the cables and adapters was calibrated for the two-port measurements.

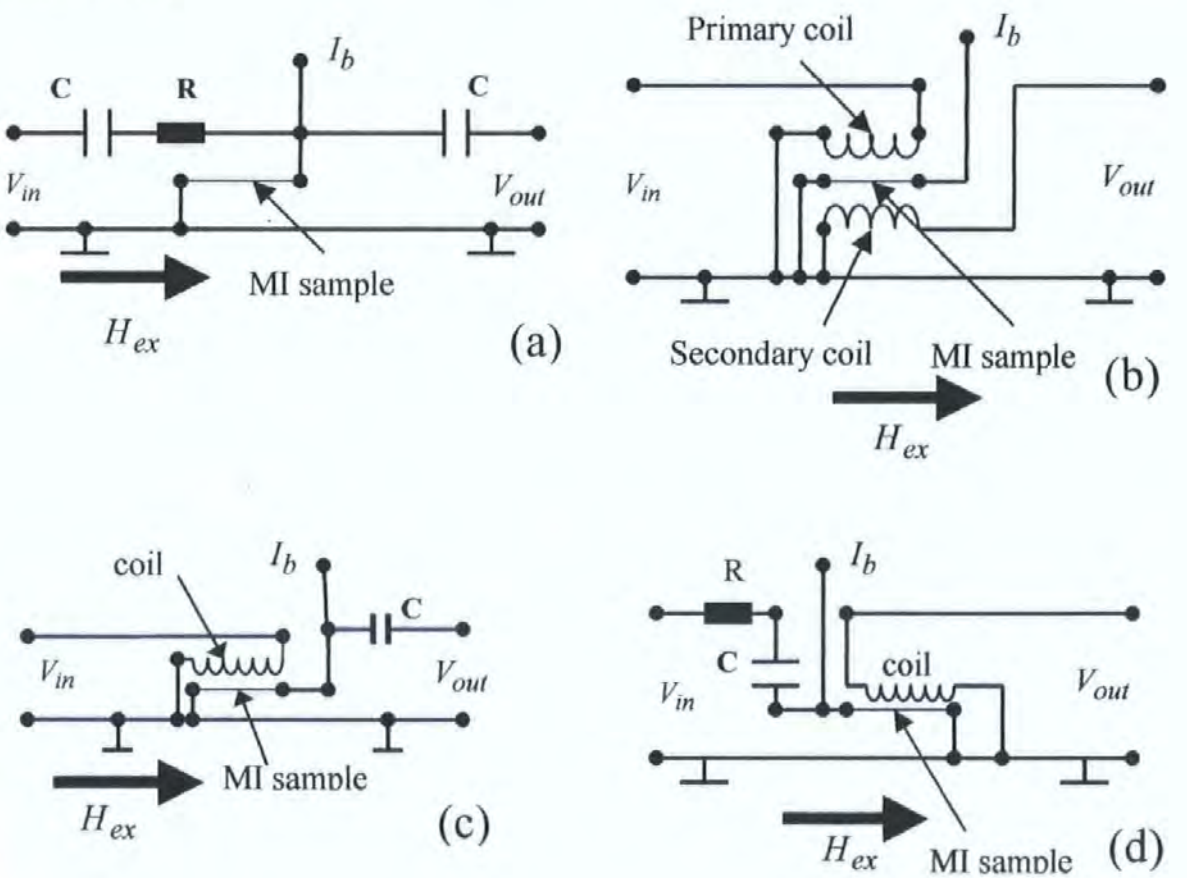

Fig. 2.16 *Electrical circuits of the cells for ς_{zz} in (a), $\varsigma_{\varphi\varphi}$ in (b), $\varsigma_{z\varphi}$ in (c), and $\varsigma_{\varphi z}$ in (d). The cells have input and output 3.5-mm connectors.*

The longitudinal diagonal component ς_{zz} (Fig. 2.16(a)) is determined by the usual way, measuring the wire voltage V_z when it is excited by the ac wire current ($h_{ex}=0$). In this case, in equation (8) $h_{ex}=0$, with the result that $S_{21}=V_z/V_{in}=\varsigma_{zz}(H_{ex})\left(\bar{h}_\varphi l/V_{in}\right)$. The circumferential diagonal component $\varsigma_{\varphi\varphi}$ (Fig. 2.16(b)) corresponds to the voltage V_c in the secondary coil mounted on the wire which is excited by the ac axial magnetic field induced in the primary coil ($j=0$). In this case:

$$V_c=i\omega n_2 l h_{ex}\pi\left(a_2^2-a^2\right)/c-2\pi a n_2 l h_{ex}\varsigma_{\varphi\varphi}. \qquad (52)$$

Here a_2 is the radius of the secondary coil and n_2 is a number of its turns per unit length. In equation (52), the first term represents the contribution from the flux (Faraday's law) between the wire and the secondary coil (the flux through the air gap), the second term corresponds to the coil voltage defined by equation (9) with $\bar{h}_\varphi=0$. For wires having sufficiently large diameter (few tens of microns) it is quite possible to wind the secondary coil directly on the wire. In this case, the flux through the air gap is nearly zero and there is no large signal insensitive to the dc external magnetic field. The off-diagonal components $\varsigma_{z\varphi}$ and $\varsigma_{\varphi z}$ (Fig. 2.16(c,d)) can be determined by measuring the coil voltage V_c when the wire is excited by the ac current j, or measuring the wire voltage V_z in the presence of the ac axial magnetic field h_{ex}. The latter is used here (Fig. 2.16(c), $j=0$). In this case, in equation (8) $h_\varphi=0$ with the result that $S_{21}=V_z/V_{in}=-\varsigma_{z\varphi}(H_{ex})\left(h_{ex}l/V_{in}\right)$.

The coil length in all the experiments is about 3 mm and the wire length is about 6 mm. The secondary coil is mounted directly on the wire: $a_2=a$. The primary coil is mounted on a glass tube with a diameter of 1 mm. The number of turns in both coils is 30. The amplitudes of the ac excitation current (in the wire or in the coil) are chosen to be less then 1 mA, then, the non-linear ac magnetisation processes like irreversible domain displacements are not possible. The experimental studies are made with the effect of the dc current which effectively governs the static magnetic structure, as discussed above.

2.7.2 Circumferential anisotropy

First we consider the impedance characteristics in a wire with a circumferential anisotropy $\alpha = 90^0$ and a circular domain structure in the outer region. These results have been reported in Refs. 1,30. The experimental field dependences for the ς_{zz} component and the comparison with the model calculations are shown in Fig. 2.17. The normalised impedance corresponds to the ratio V_z / V_{in}. The real and imaginary parts of this ratio are given in Fig. 2.17(a), showing two symmetrical peaks at H_{ex} nearly equal to the anisotropy field $H_K \approx 5$ Oe (the value of the anisotropy field has been checked by measuring the dc magnetisation loops). When the dc bias is applied, the impedance value at zero field becomes considerably smaller. The dc current eliminates the domain structure, resulting in the decrease in the overall permeability. For not very high I_b, the values of the impedance at the maximuma are almost constant since they are determined by the rotational processes only. However, if I_b is further increased, the value of the impedance at the maximuma becomes considerably smaller and the sensitivity drops, resulting from an increase in magnetic hardness by I_b. Figs. 2.17(b),(c) give the comparison of the experimental and theoretical results. The two curves are matched at positive (or negative) saturation, therefore the theoretical values are given in S_{21}-units. For $I_b = 0$, the main discrepancy between the theory and experiment is for fields H_{ex} smaller than the anisotropy field H_K, which is due to the contribution of the domain wall dynamics (which is essential even for frequency of 20 MHz) to the total permeability. The theoretical model considering a single-domain state ignores the domain dynamics completely. Applying a sufficiently large current $I_b = 100$ mA eliminates the bamboo domains in the outer shell and significantly decreases the diameter of the inner core magnetisation (see Fig. 2.2(b)). In this case, the theoretical curve becomes closer to the experimental one. Figure 2.18 presents the longitudinal impedance for higher frequency of 100 MHz, showing a much better agreement between the experiment and theory, since the domain walls are stronger damped and give considerably smaller contribution to the total permeability.

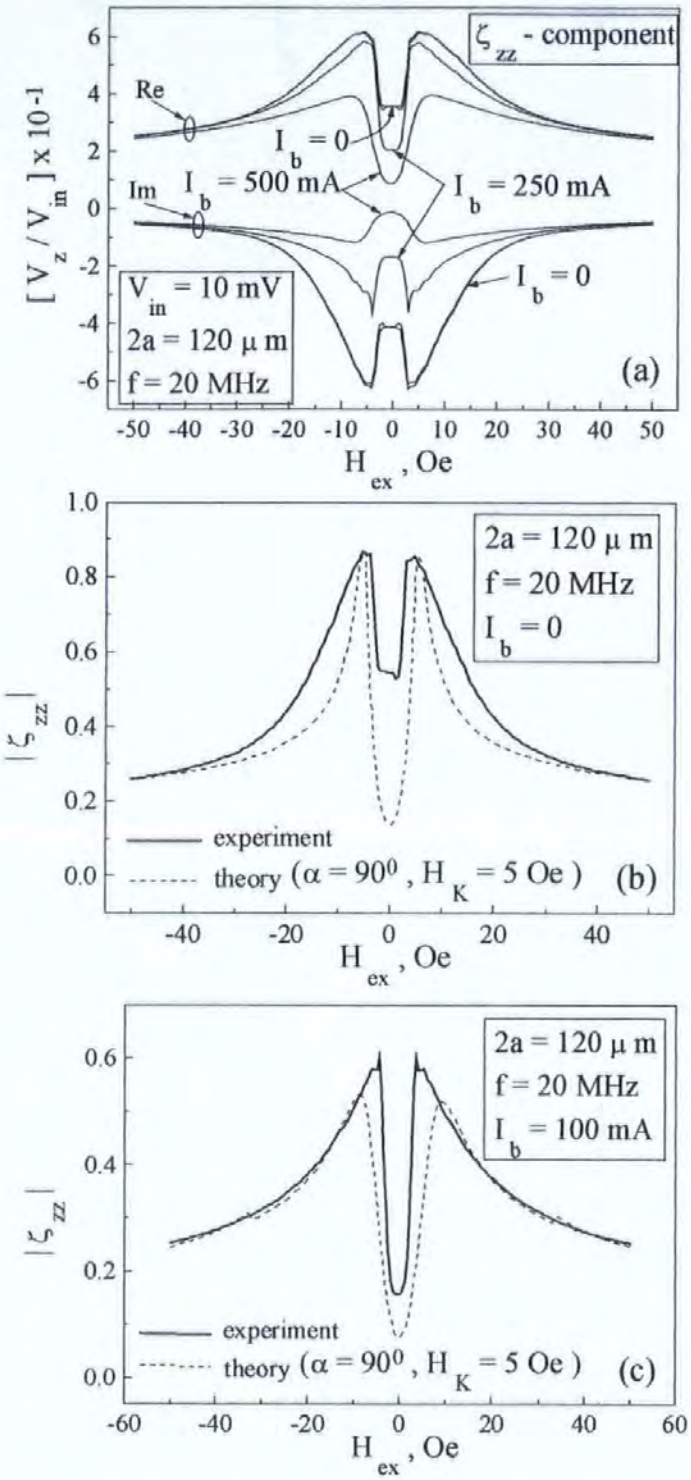

Fig. 2.17 *Experimental plots of the longitudinal impedance $\varsigma_{zz}(H_{ex})$ for different values of I_b and comparison with the theory (normalised curves). In (a), real and imaginary parts of the voltage ratio V_z/V_{in} (which is proportional to ς_{zz}) are given. In (b) and (c) the impedance magnitude $|\varsigma_{zz}|$ vs. H_{ex} (in values of $|V_z/V_{in}|$) is compared with the theoretical dependence for a frequency of 20 MHz.*

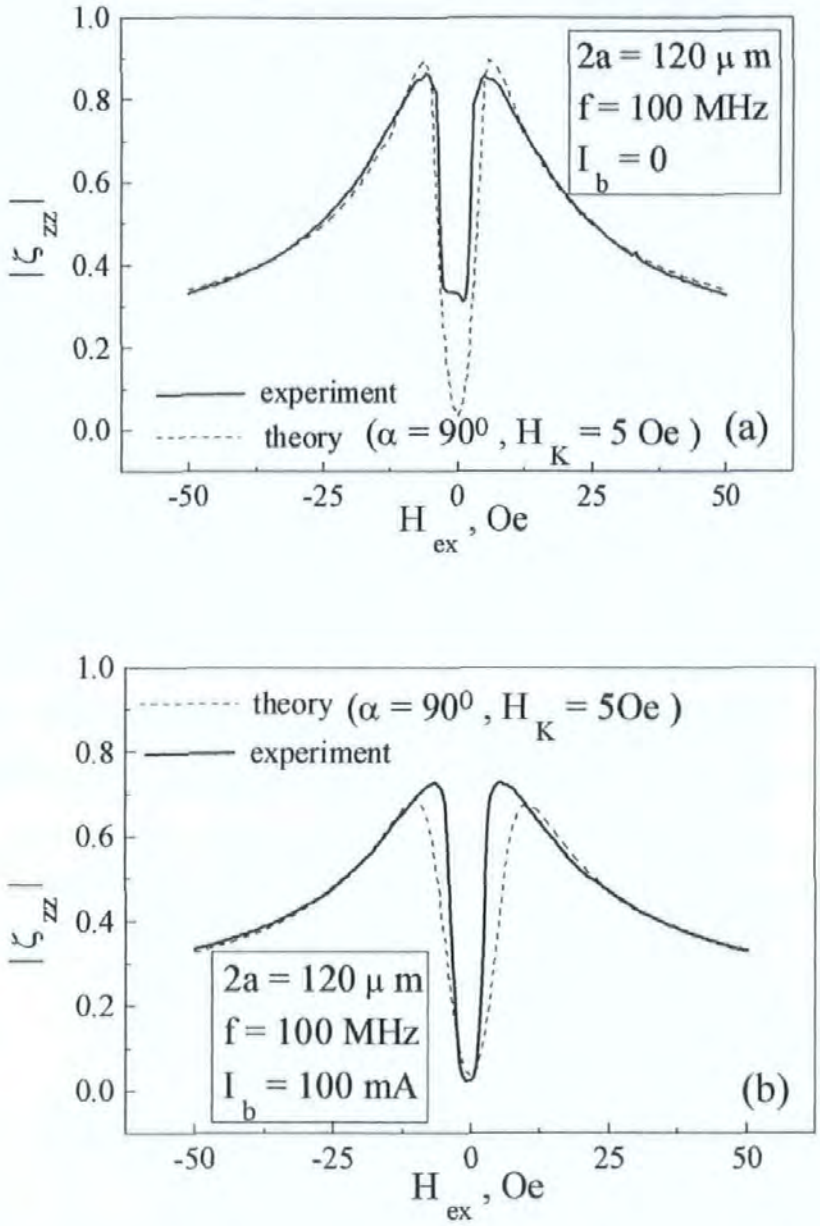

Fig. 2.18 *Theoretical (normalised) and experimental plots of* $|\varsigma_{zz}|$ *vs.* H_{ex} *(in values of* $|V_z/V_{in}|$*) for a frequency of 100 MHz, for* $I_b = 0$ *in (a) and* $I_b = 100$ *mA in (b).*

Figures 2.19 are related to the analysis of the circumferential diagonal impedance $\varsigma_{\varphi\varphi}$. Figure 2.19(a) presents the normalised voltage V_c/V_{in} in the secondary coil mounted directly on the wire which is excited by the ac axial magnetic field induced in the primary coil. This ratio is proportional to $\varsigma_{\varphi\varphi}$ which has a maximum at zero field and it decreases rapidly near the anisotropy field $H_K \approx 5$ Oe, whereas there is an insensitive wide region between $\pm H_K$, which is more pronounced for $I_b = 0$. It seems that this insensitive area is determined by the demagnetising factor since the sample has a rather small length (6 mm) comparing to the diameter (120 μm). However, we could not see this behaviour considering the field plots of ς_{zz}. More probably, it is related to the combined effect of the rotational permeability (which has a maximum at zero field and is decreasing with the field) and the domain wall permeability (which has a minimum at zero field and is increasing with the field). The theoretical curve does not have this flat portion, as shown in Fig. 2.19(b). The application of a relatively small current $I_b = 5.57$ mA increases the sensitivity of the impedance characteristics, which may be due to a better defined circumferential magnetisation induced by this current when θ is equal almost exactly to 90^0 without the anisotropy dispersion. The insensitive region becomes smaller under the effect of a larger I_b as the domain contribution is less essential, and this case is in a good agreement with the theoretical plot as demonstrated in Fig. 2.19(c).

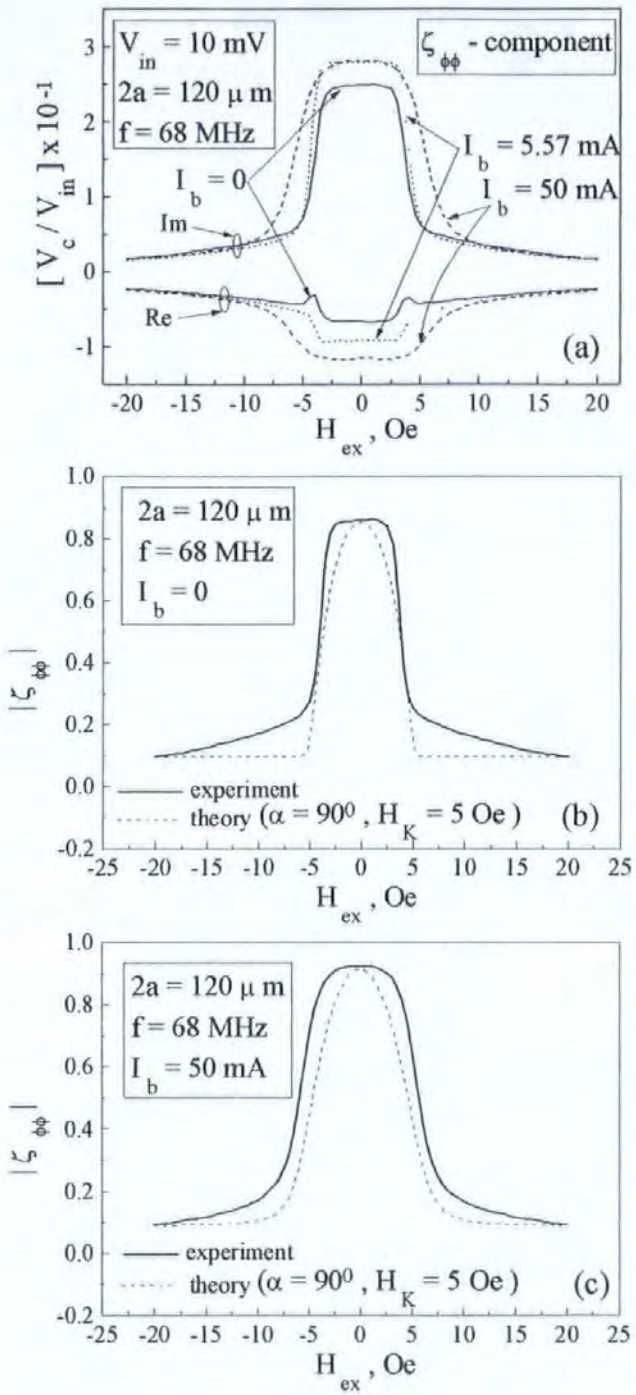

Fig. 2.19 *Experimental plots of the circumferential impedance* $\varsigma_{\varphi\varphi}(H_{ex})$ *for different values of* I_b *and comparison with the theory (normalised curves). In (a), real and imaginary parts of the voltage ratio* V_c/V_{in} *(which is proportional to* $\varsigma_{\varphi\varphi}$*) are given. In (b) and (c) the impedance magnitude* $|\varsigma_{\varphi\varphi}|$ *vs.* H_{ex} *(in values of* $|V_c/V_{in}|$*) is compared with the theoretical dependence for a frequency of 68 MHz.*

Figure 2.20 is related to the off-diagonal component $\varsigma_{z\varphi}$ ($\equiv \varsigma_{\varphi z}$). Figures 2.20(a),(b) show the normalised voltage V_z / V_{in} measured across the wire ends when the wire is excited by the external coil producing the ac longitudinal magnetic field (see Fig. 2.16(c)). Without the dc current I_b this characteristic is very small, but it increases substantially when the current is enough to eliminate circular domains (compare the characteristics with $I_b = 0$ and $I_b = 100$ mA). An actual wire sample with circumferential anisotropy is divided into a "bamboo" domain structure, where adjacent domains have opposite directions of magnetisation, as shown in Fig. 2.2(b). For this structure, the total off-diagonal response from the whole sample is formed by averaging over the domain structure, which will result in full annihilation, due to the antisymmetrical response from the off-diagonal impedance components in the adjacent domains: $<\varsigma_{z\varphi}>=<\varsigma_{\varphi z}>=0$ because $<\sin\theta\cos\theta>=0$. In reality, the system does not have a perfect "bamboo" domain structure and, therefore, the averaging does not produce zero, but the ac off diagonal response should be significantly decreased, as seen in Fig. 2.20 for $I_b = 0$. However, the situation will change in the presence of a bias field. At $H_b \neq 0$, domains with the same direction of the magnetisation as H_b will grow, resulting in an uncompensated averaging: $<\varsigma_{z\varphi}>=<\varsigma_{\varphi z}>\neq 0$. Finally, at a sufficient value of H_b the sample will become a single domain state (at least in the outer sheet). This results in the off-diagonal response increasing significantly. Therefore, in the case of a circumferential anisotropy and a circular domain structure, the presence of I_b is the necessary condition for the existence of the off-diagonal components of the impedance matrix. The off-diagonal component is antisymmetrical with respect to the field H_{ex}, which is demonstrated in Fig. 2.20(a) by presenting both the real and imaginary parts. Such behaviour is an agreement with the theory (compare with Fig. 2.11(d)). A considerable increase in I_b results in a decrease in sensitivity (see Fig. 2.20(b), $I_b = 500$ mA). In this case, two opposite effects of I_b are encountered: (i) the transition to a single-domain structure (that increases the off-diagonal components and its field sensitivity), and (ii) the increase in the magnetic hardness in the circular direction (that decreases the sensitivity). Thus, the bias field effect and the field dependence $\hat{\varsigma}(H_{ex})$ provide a useful information about the magnetic state of any given structure.

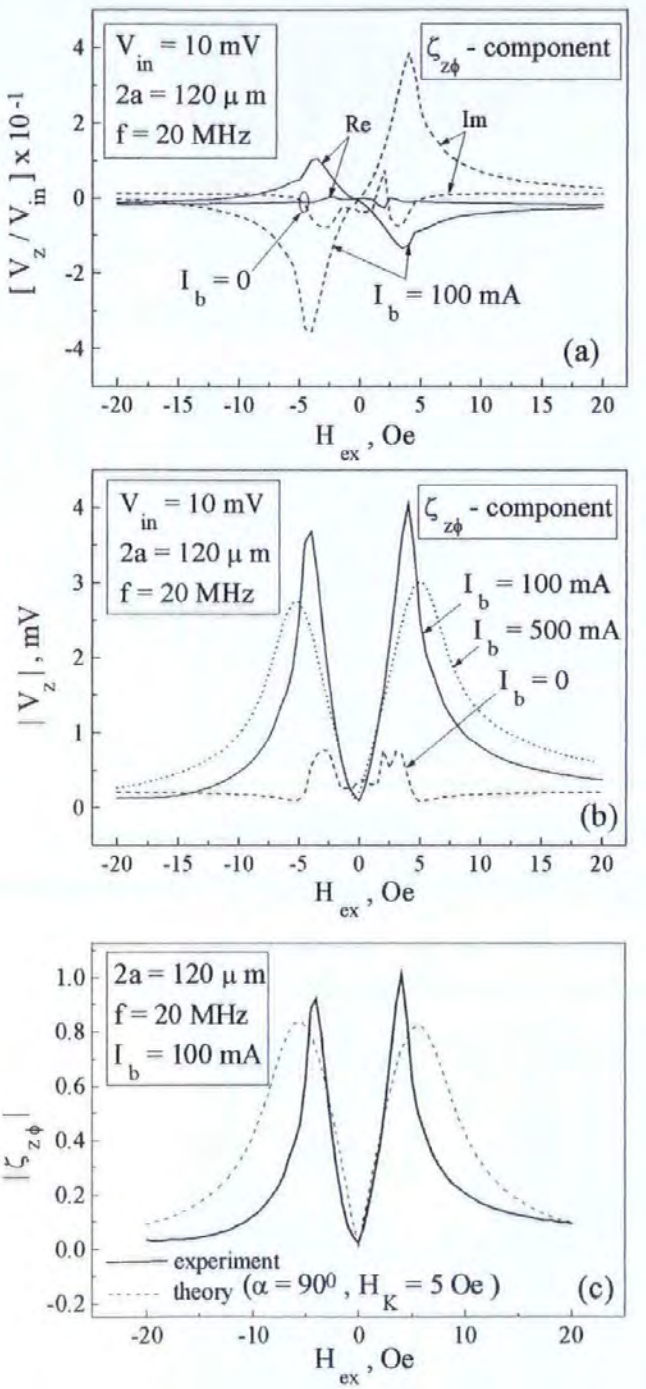

Fig. 2.20 *Experimental plots of the off-diagonal impedance $\varsigma_{z\varphi}(H_{ex})$ for different values of I_b. The result is presented in terms of the voltage ratio V_z / V_{in} (which is proportional to $\varsigma_{z\varphi}$): real and imaginary parts in (a), and the magnitude in (b). In (c), the impedance magnitude $|\varsigma_{z\varphi}|$ vs. H_{ex} (in values of $|V_z / V_{in}|$) is compared with the theoretical normalised plots for a frequency of 20 MHz and $I_b = 100$ mA.*

Figure 2.20(c) shows the comparison of the experimental dependence with the calculated one at $I_b = 100$ mA. The experimental plot exhibits considerably faster decrease which may be related to some structural changes at the surface due to demagnetising effects since this component is very sensitive to the domain formation.

Let us now suppose that a mixed excitation is used, when the wire is excited by both the ac current and the ac field h_{ex} (ac bias field) which is produced by the primary coil connected serially to the wire. The electrical scheme of the cell for the mixed excitation is shown in Fig. 2.21.

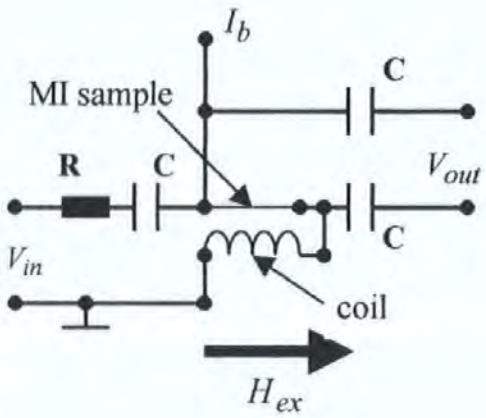

Fig. 2.21 *The electrical scheme of the cell for the mixed excitation.*

The voltage measured across the wire is determined by equation (8) with $h_{ex} = 4\pi nlj/c$. In this case, the voltage V_z involves both ς_{zz} and $\varsigma_{z\varphi}$ components of the impedance matrix, combining symmetric and antisymmetric terms with respect to H_{ex}. As a result, the voltage exhibits an asymmetric behaviour, even if the dc magnetic configuration does not have asymmetry, as shown in Fig. 2.22 The coil gives an additional source of e.m.f which may cause the amplitude of the ac current to change during the experiment as well.[33-35] In this case, the comparison with the theoretical result is more complicated (see Fig. 2.22). The mixed excitation will be concretised in Section 2.8.

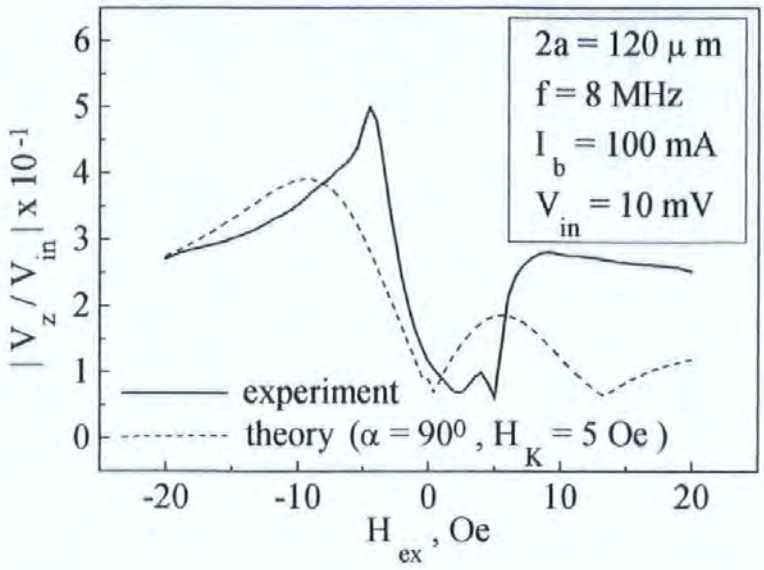

Fig. 2.22 *Asymmetrical voltage response in the presence of the ac bias field.* $I_b = 100$ *mA. Theoretical (normalised) and experimental curves are shown.*

2.7.3 Helical anisotropy

The case of helical anisotropy presents considerable interest since the effect of the dc current results in a completely different appearance of the field plots for the impedance. A tension-annealed 30 μm diameter CoSiB amorphous wire (magnetostriction $\lambda = -3 \cdot 10^{-6}$) has been studied. This wire has a spontaneous helical anisotropy due to a residual stress distribution, and relatively large anisotropy field of 8 Oe. As it has been reported in Refs. 31,32, it has a spontaneous helical anisotropy with the averaged angle of about 60°, which can be revealed by measuring the dc magnetisation loops in the presence of the dc current.[32] Figures 2.23 present the results for the longitudinal impedance ς_{zz}. In this case the impedance exhibits a hysteresis. In Ref. 36, where the impedance of a wire with a twist induced helical anisotropy has been investigated, the hysteretic behaviour was not seen. This is because, the impedance field behaviour is related to domain wall permeability averaged over the ac magnetisation cycle due to irreversible helical-wall movement. The indication of irreversible non-linear processes involved is the considerable deviation from a sine-wave form of the measured voltage. The amplitude of the ac current exciting the wire used in Ref. 36 is 15 mA, which is sufficient to induce irreversible displacements of domain walls. In our experiment, such processes are not possible since $|j|$ is just a few mA.

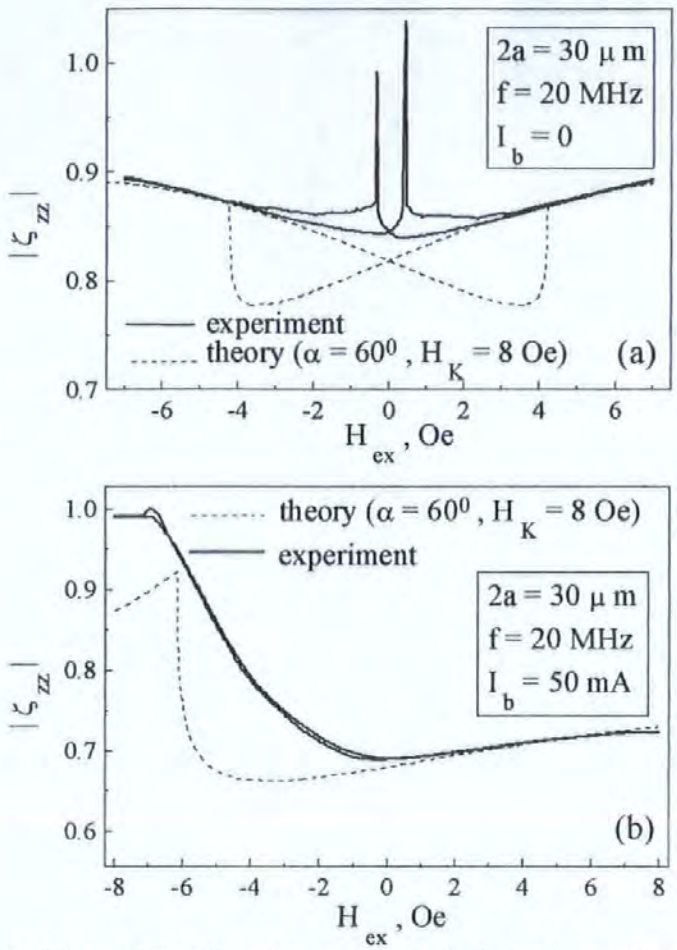

Fig. 2.23 *Theoretical (normalised) and experimental plots of* $|\varsigma_{zz}|$ *for a helical anisotropy vs.* H_{ex} *(in values of* $|V_z/V_{in}|$*) for a frequency of 20 MHz.*

$I_b = 0$ *in (a) and* $I_b = 50$ *mA in (b).*

For $I_b = 0$, the experimental plot shows two sharp peaks at very small field corresponding to the coercitivity field of the dc magnetisation process. The domain walls exist in this narrow field region and their linear dynamics gives a main contribution to the overall dynamic process. For fields larger than the coercivity, when the domain structure disappears, the impedance behaviour is determined by the ac magnetisation rotation. The theoretical jumps related to the irreversible rotational change in $\mathbf{M}_0$ are not seen in the experimental plot since the dc magnetisation reversal is due to the domain processes. For these higher fields, there is a reasonable agreement between the theory and the experiment. Thus, the effect of the dc current results in a gradual transition to non-hysteretic asymmetrical behaviour, as seen in Fig. 2.23(b). Certain discrepancy may be related to anisotropy dispersion, which is quite considerable in CoSiB amorphous wire.

Figures 2.24 and 2.25 present the field characteristics of $\varsigma_{\varphi\varphi}$ and $\varsigma_{z\varphi}$ components which change with the dc bias current in a characteristically similar manner. Note that $\varsigma_{z\varphi}$ versus H_{ex} plot is very sensitive to the anisotropy angle. The theoretical curves describe the rotational portion of the experimental probes very well for $\alpha = 60°$. This value of the anisotropy angle agrees with that found from the shift in the dc magnetisation loops.[32]

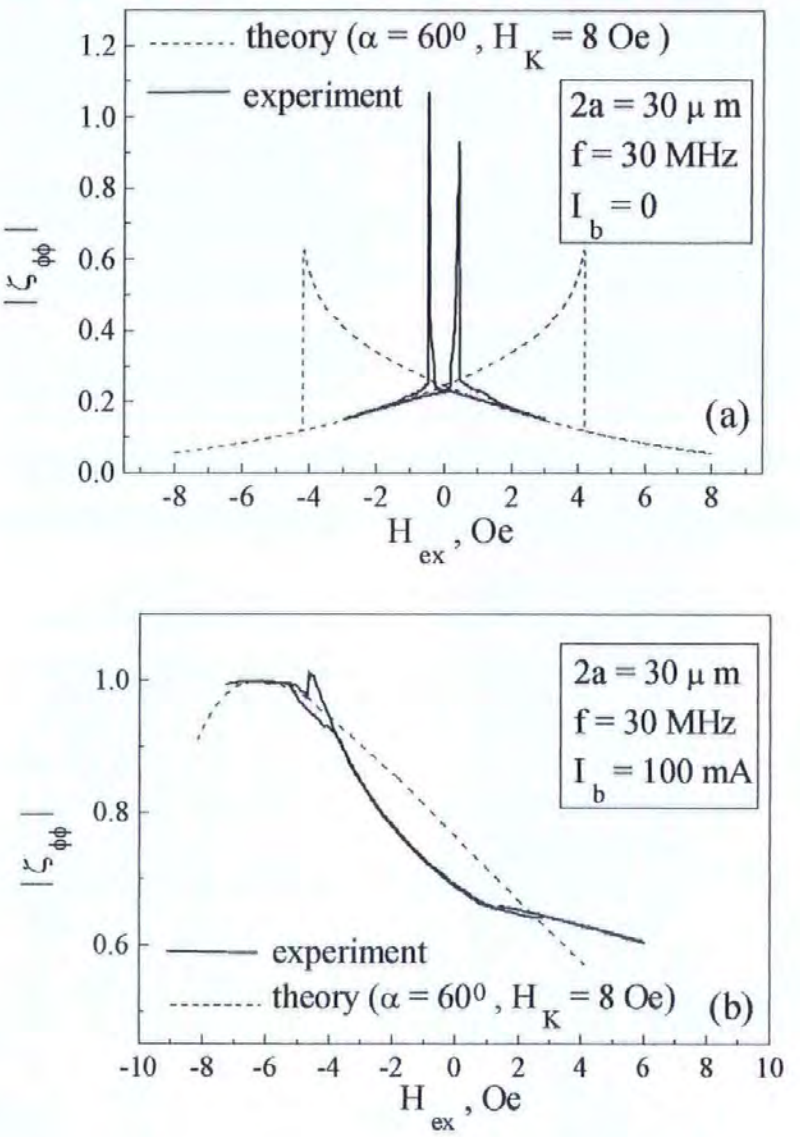

Fig. 2.24 *Theoretical (normalised) and experimental plots of* $|\varsigma_{\varphi\varphi}|$ *vs.* H_{ex} *(in values of* $|V_c / V_{in}|$*) for a helical anisotropy (*$\alpha = 60°$*) for a frequency of 30 MHz.* $I_b = 0$ *in (a) and* $I_b = 100$ *mA in (b).*

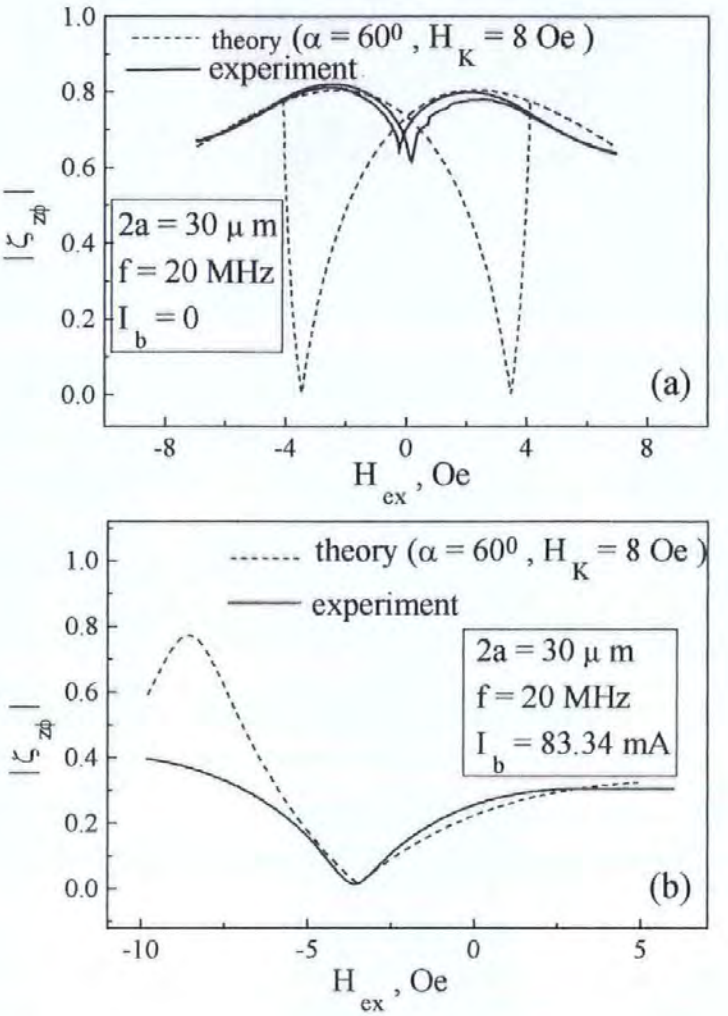

Fig. 2.25 *Theoretical (normalised) and experimental plots of* $|\varsigma_{z\varphi}|$ *vs.* H_{ex} *(in values of* $|V_z/V_{in}|$*) for a helical anisotropy* ($\alpha = 60°$) *for a frequency of 20 MHz.* $I_b = 0$ *in (a) and* $I_b = 83.34$ *mA in (b).*

In the above the wire with a spontaneous helical anisotropy has been considered. Also a helical anisotropy can be induced by annealing under a torsion stress.[37-40] In Ref. [40] the impedance matrix in a wire with an induced helical anisotropy was measured in a 120 μm-diameter $(Co_{0.95}Fe_{0.05})_{72.5}Si_{12.5}B_{15}$ amorphous wire with vanishing negative magnetostriction ($\lambda < 0$). Pre-annealing with 450 mA during 20 minutes was carried out without a torsion stress to relax internal stresses induced by the fabrication process. [37-39]. Thereupon the sample was annealed with the same conditions but under a torsion stress of $(\pi/4)\,\mathrm{rad/cm}$.

The magnetic structure in the wire is known to be dominated by the combined effect of the wire geometry and residual stress induced anisotropy. If no torsion stress is applied, there is a domain structure with an axially magnetised core and circularly magnetised sheath. A torsion stress modifies this by introducing a helically magnetised surface layer. The following annealing (under torsion stress) preserves this helical structure.

As it has been demonstrated theoretically in Section 2.6, the existence of the helical anisotropy can be reliably recognised by measurements of the axial or circumferential hysteresis loops in the presence of dc bias field. Figure 2.26 shows the axial ($B_z - H_{ex}$) hysteresis loops measured by a standard fluxmetric method with a dc bias current I_b as a parameter, which induces the circumferential bias field H_b.

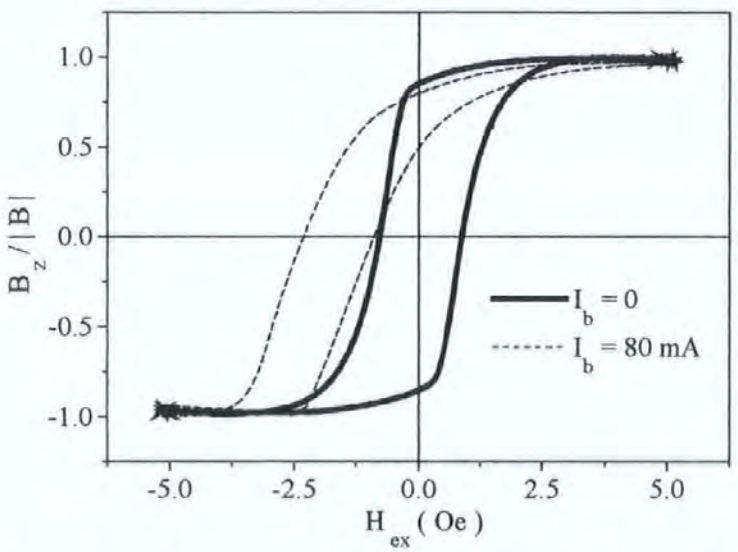

Fig. 2.26 *Longitudinal hysteresis loops ($B_z - H_{ex}$) for a helical anisotropy for different bias currents I_b.*

Without a bias current the hysteresis loop has a symmetrical and nearly rectangular shape. In the presence of $I_b \neq 0$ the rotational portions increase. Another manifestation of the bias effect is the decrease in the coercivity that is clearly observed in Fig. 2.26, where the hysteresis loop is narrower for $I_b = 80$ mA. The loop also shifts: combination of the induced helical anisotropy and the dc bias field results in asymmetry in the static magnetic configuration. As a result the magnetisation curves do not respond the same to the positive and negative directions of sweep field when the bias field is being applied.

The circumferential ($B_\varphi - H_\varphi$) loops were measured by the transverse magneto-optic Kerr effect.[41] The circular magnetic field H_φ (sweep field) has been induced by a low frequency current flowing through the wire. For Kerr effect the intensity of the reflected light is measured. A polarised light from a He-Ne laser is scattered from the wire and detected. For the transverse effect, the intensity is proportional to the magnetisation, which is perpendicular to the plane of the light. Figure 2.27 shows the ($B_\varphi - H_\varphi$) loops with a dc axial bias field H_{ex} as a parameter.

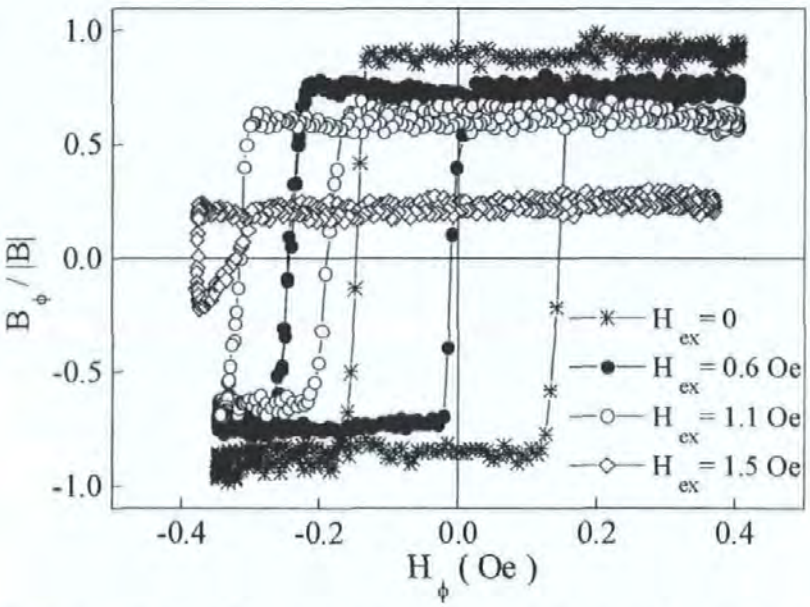

Fig. 2.27 *Circumferential hysteresis loops ($B_\varphi - H_\varphi$) for a helical anisotropy for different axial bias fields H_{ex}.*

The loops are modified by the bias field H_{ex} in a similar way to that for the longitudinal loops: (i) increase of rotational portion, (ii) the decrease in the coercivity, (iii) asymmetry with respect to the sweep field (with a shift).

The portions of the experimental hysteresis loop flattening out on the saturation correspond to the magnetisation rotational when the single domain state has reached. The domain processes define essentially the hysteresis behaviour when the driving field (sweep field) is smaller than coercivity H_c.[32] For the analysis of magnetisation loops, it is convenient to break down the total external field including the driving and bias fields can be resolved into two components, one parallel to and one perpendicular to, the anisotropy axis.

The perpendicular component is a hard-axis field for the domain wall and the longitudinal component is an easy-axis driving field. It is known [32] that the hard-axis field decreases the domain wall energy and thus the coercivity. The hard axis field also causes the suppression of the Barkhausen jumps, with the result that the parts of the hysteresis loop corresponding to the rotation processes increase.[42,32] In the case of the helical anisotropy, the easy-axis field results in the shifting of the hysteresis loop along the sweep field. The bias field gives the contribution to both the hard and easy axis fields. By this means, the combined effect results in the shifting and narrowness of the hysteresis loop along with the suppression of the Barkhausen jumps.

As it has been demonstrated in Section 2.6, the asymmetry in the static magnetic structure causes the asymmetrical field characteristics of the impedance matrix when high frequency current is combined with the dc bias current I_b. The modifications in the impedance plots due to I_b are of the same kind as those for the dc magnetisation loops. The wire sample has a length of 5 mm and a dc resistance of about 1 Ω. Coils have 25 turns and a length of 3 mm. The diameter of the larger (primary) coil was 1 mm. The wire is subjected to the axial dc magnetic field H_{ex} and the dc bias current I_b. The field dependences of normalised ς_{zz} component are shown in Fig. 2.28 for a frequency of 20 MHz. The following normalisation is used:

$$\frac{\Delta|V(H_{ex})|}{\Delta_0|V(H_{ex})|}=\frac{\left[|V(H_{ex})|-\min|V(H_{ex})|\right]_{I\neq 0}}{\left[\max|V(H_{ex})|-\min|V(H_{ex})|\right]_{I=0}}\equiv$$

$$\equiv\frac{\left[|\varsigma(H_{ex})|-\min|\varsigma(H_{ex})|\right]_{I\neq 0}}{\left[\max|\varsigma(H_{ex})|-\min|\varsigma(H_{ex})|\right]_{I=0}}=\frac{\Delta|\varsigma(H_{ex})|}{\Delta_0|\varsigma(H_{ex})|}. \qquad (53)$$

If no bias is applied, the impedance plot versus H_{ex} shows a symmetrical hysteresis (see Fig. 2.28(a)). Asymmetry in the field dependence appears in the presence of I_b (see Fig. 2.28(b)). For one field direction (negative in Fig. 2.28) the amplitude of the maximum and sensitivity increases, whereas for the opposite direction they both decrease. Moreover, a small shift of hysteresis accompanied by shrinkage of the hysteresis area is observed for this matrix component. Further increase in I_b causes a drop in sensitivity (see Fig. 2.28(c)) which is due to increasing the hardness in the hard-axis direction.

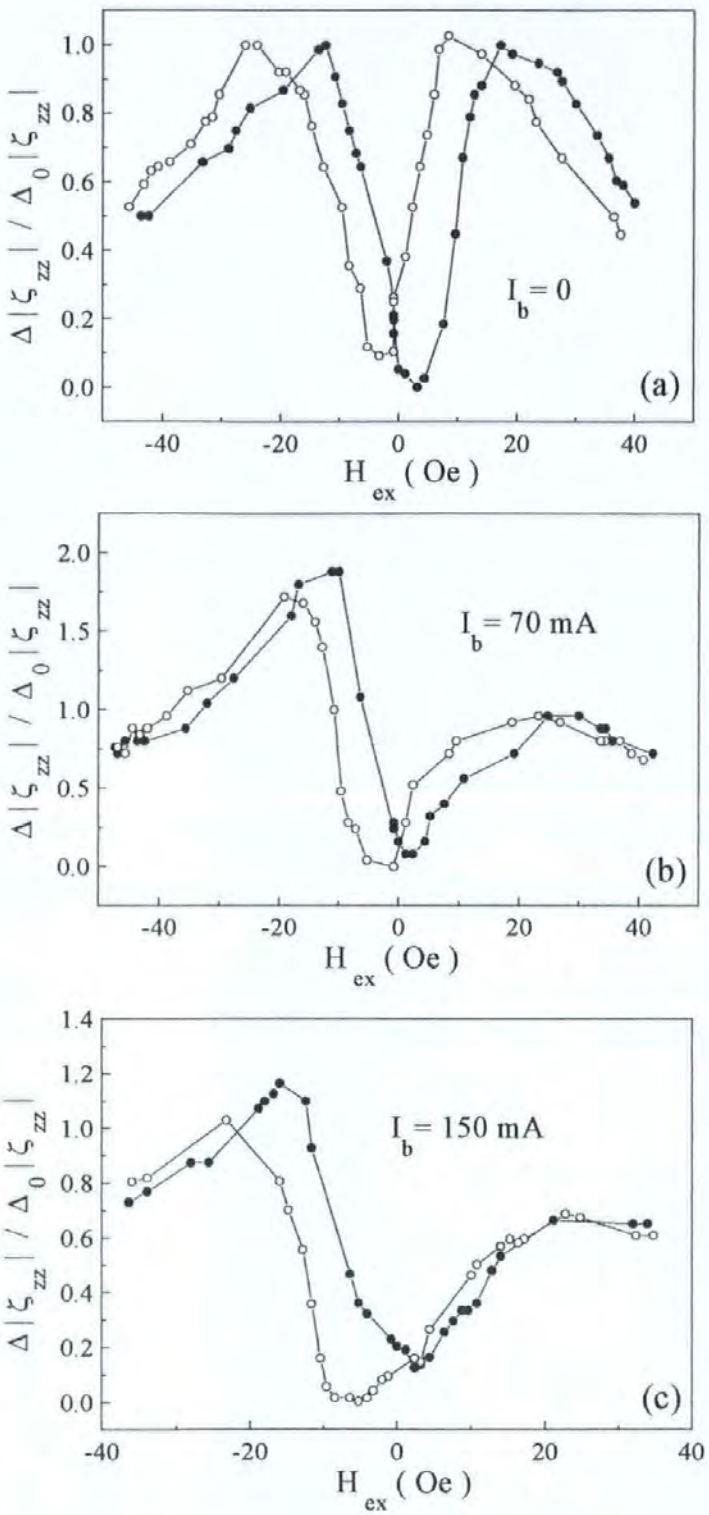

Fig. 2.28 *The hysteresis curves of the normalised field characteristics of* ς_{zz} *versus* H_{ex} *for different bias currents* I_b *at a frequency of 20 MHz.*

The other components of the impedance matrix show characteristically similar behaviour under the effect of bias current, as it is demonstrated in Figs. 2.29 and 2.30.

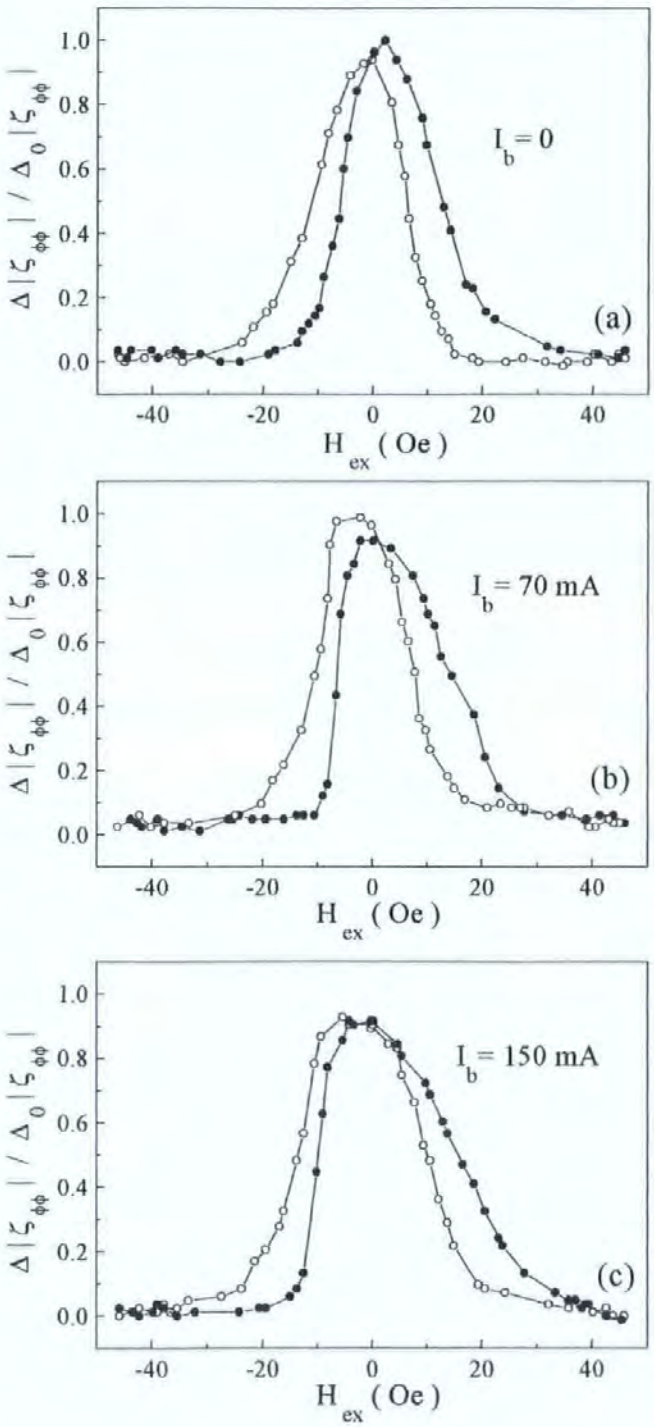

Fig. 2.29 *The hysteresis curves of the normalised field characteristics of* $\varsigma_{\varphi\varphi}$ *versus* H_{ex} *for different bias current* I_b *at a frequency of 20 MHz.*

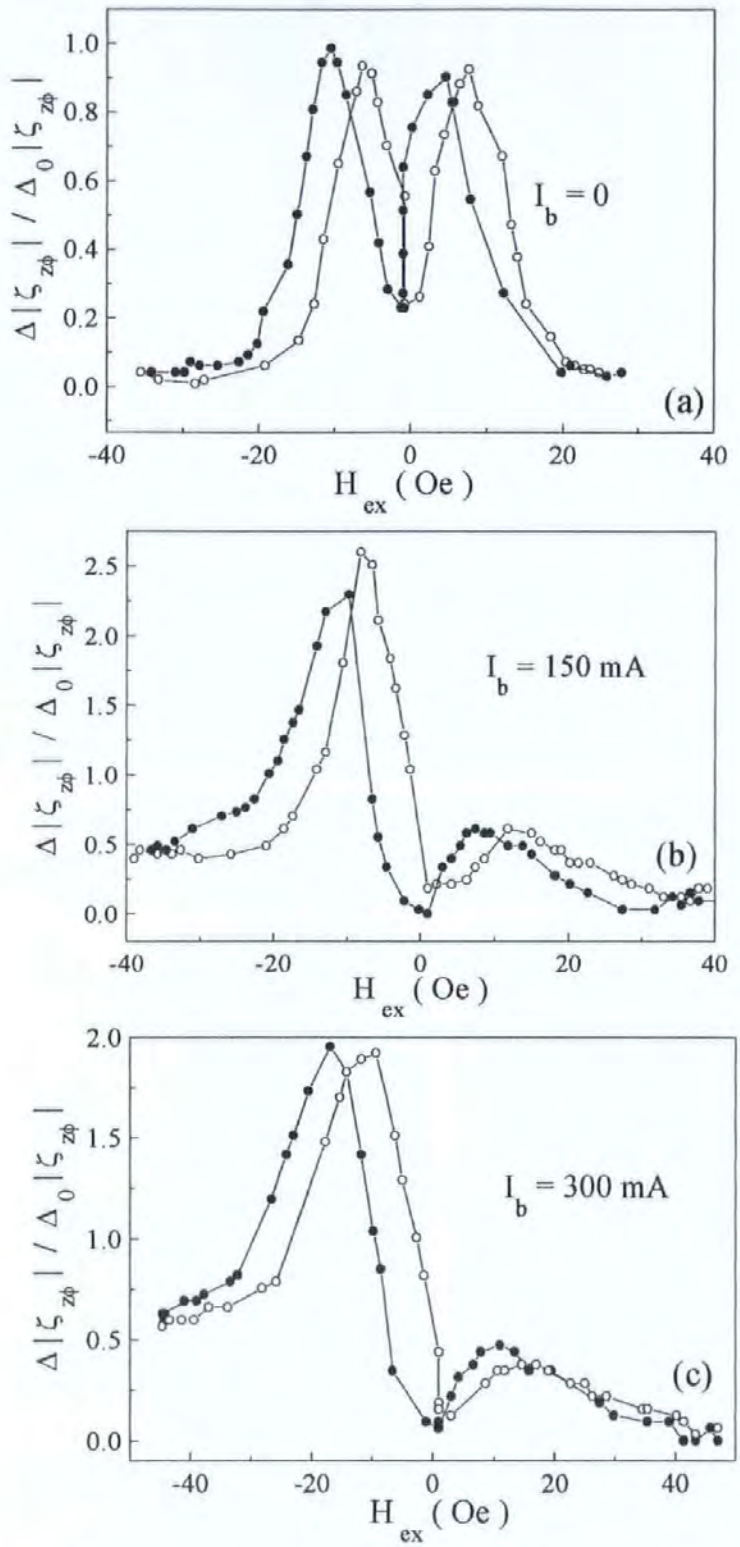

Fig. 2.30 *The hysteresis curves of the normalised field characteristics of* $\varsigma_{z\varphi}$ *versus* H_{ex} *for different bias currents* I_b *at a frequency of 20 MHz.*

In the case of $\varsigma_{\varphi\varphi}$, its maximum does not increase noticeably when I_b is applied (see Fig. 2.29(a)), whereas the sensitivity is improved significantly. For larger bias currents, $\varsigma_{\varphi\varphi}$- plots broaden with increasing I_b. As far as the off-diagonal component $\varsigma_{z\varphi}$ is concerned (see Fig. 2.30(b)), it appears to be most sensitive to current biasing: the field sensitivity increases more than twice at $I_b = 150$ mA.

We can conclude that the theoretical model based on the single-domain magnetic structure adequately describes the numerous experimental data for wires with different anisotropy types. It was shown that the ac rotational magnetisation processes are responsible in many respects for the impedance change. Comparing Figs. 2.12-2.14, Figs. 2.23-25 and Figs. 2.28-30, we have to conclude that the better qualitative agreement between experiment and theory is achieved for a wire with the helical anisotropy induced by annealing under torsion stress.

2.8 Asymmetrical giant magneto-impedance in wires with the circumferential anisotropy

This Section concerns the asymmetrical giant magneto-impedance (AGMI) in amorphous ferromagnetic wires with a circumferential anisotropy.[33-35] This case is different from that considered in Sections 2.6 and 2.7.3 since the dc magnetic structure does not have asymmetry. As it has been shown in Fig. 2.22 (Section 2.7.2), the voltage measured across the wire subjected to an ac current j and an ac axial bias field h_{ex} (see Fig. 2.21) exhibits a considerable asymmetry with respect to the axial dc magnetic field H_{ex}. The AGMI effect will be studied in terms of the surface impedance matrix, demonstrating that the extent of asymmetry is determined by the ratio of the diagonal ς_{zz} and off-diagonal $\varsigma_{z\varphi}$ components of this matrix. Strong effects on AGMI of the frequency of excitation and the dc bias current I_b applied to the wire are demonstrated. Both these factors effect on the linearity and sensitivity of the voltage output in a sensor circuit based on the AGMI elements.

AGMI characteristics are needed to realise linearisation. Generally, it can be done with the use of a dc bias field, applying a dc current to the external coil (circumferential anisotropy) or to the wire directly (helical anisotropy). In the case of magneto-impedance, the ac bias can be used for this purpose. This method has the following advantages: (i) the ac bias is generated by an ac bias current j_b in the external coil, requiring no additional power consumption, (ii) the helical anisotropy which can cause problems of stress stabilisation is not needed.

The effect of an ac bias field h_{ex} on the voltage characteristics is related to the ac cross-magnetisation process of inducing a circulatory magnetisation by h_{ex}. It is convenient to analyse this process in terms of the surface impedance matrix $\hat{\varsigma}$. The induced voltages are determined by Eqs. 8,9. The diagonal components ς_{zz}, $\varsigma_{\varphi\varphi}$ are even functions of the field (see Figs. 2.17-19) whereas the off-diagonal components $\varsigma_{z\varphi} = \varsigma_{\varphi z}$ are odd functions (see Figs. 2.20). Therefore, the way to produce an asymmetrical voltage response is to mix together the components of the impedance matrix, as shown in Fig. 2.21. The wire is subjected to an ac current $j = j_0 \exp(-i\omega t)$ and a variable axial magnetic bias field h_{ex} is induced by the same current: $h_{ex} = 4\pi n j / c$. In this case, the voltage measured across the wire is (see Eq. 8 with $j = j_b$):

$$V_z = \bar{e}_z(a)l = \frac{2l}{ca} j(\varsigma_{zz} \mp 2\pi n a \varsigma_{z\varphi}). \qquad (54)$$

Here signs "±" correspond to a "left" or "right" coil. The extent of asymmetry depends on the ratio $\varsigma_{z\varphi}/\varsigma_{zz}$. As it was shown in Section 2.7.2 for the circumferential anisotropy, the off-diagonal component is essential only for a single domain state, since the value of $\sin\theta\cos\theta$ averaged along domains with the opposite magnetisation is zero. The circular "bamboo" domain structure can be eliminated by the application of a dc circular field H_b produced by the dc current I_b in the MI element. The field H_b has to be larger than the coercivity, which is still a small field comparing to the anisotropy field – a characteristic field of a major MI change.

One more factor which strongly affects AGMI is the frequency of excitation since with increasing frequency to a MHz region (strong skin effect) $\varsigma_{z\varphi}$ becomes similar in magnitude to ς_{zz}. Unusual voltage behaviour can be observed in this case. Equation (54) for the voltage can be written in terms of the total impedance $Z = V_z / j$. For certain magnetic configurations (determined by H_{ex}) and frequencies the real part of Z decreases down to negative values (but the absolute value of Z never becomes zero), as if the system were active. However, in fact, the coil is an additional source of e.m.f. due to the mentioned cross-magnetisation, which has been discussed in Section 2.0 (inverse Wiedemann and Matteucci effects). The negative Z means that the two e.m.f.'s are opposing each other. Yet, there is no a mere signal summation, all is happening inside the wire and is related to the wire impedance properties.

AGMI is measured in amorphous $(Co_{0.94}Fe_{0.06})_{72.5}Si_{12.5}B_{15}$ wire with 120 μm diameter, having a circumferential anisotropy. The wire sample has a length of 5 mm. The coil has 30 turns, a length of 3 mm and a diameter of 1 mm. Figure 2.31 shows the components of the impedance matrix as functions of H_{ex}, for $I_b = 100$ mA and $f = 10$ MHz. For this current, the wire is in a single domain state.

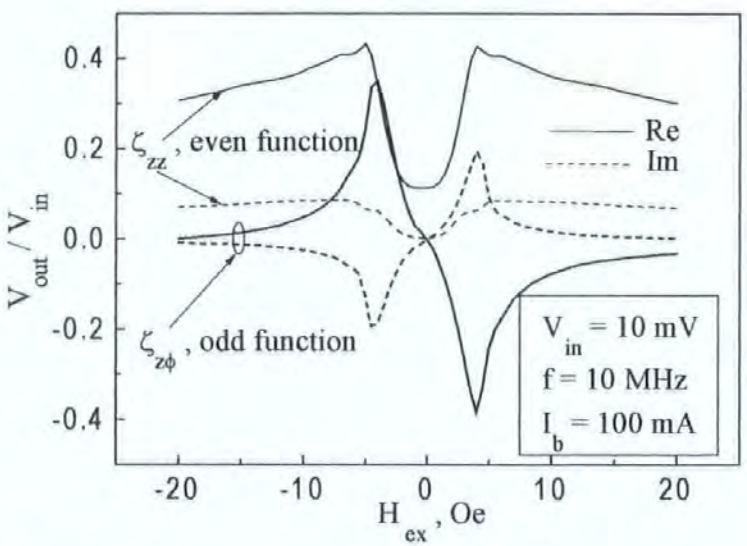

Fig. 2.31 *Field dependences of the diagonal ς_{zz} and off-diagonal $\varsigma_{z\varphi}$ components. The diagonal component is even function of the field whereas the off-diagonal component is odd function.*

The diagonal component ς_{zz} is an even function of H_{ex}. Its real part has two nearly symmetrical peaks at $H_{ex} = \pm H_K$ equal to the anisotropy field. On the contrary, $\varsigma_{z\varphi}$ is antisymmetric with respect to H_{ex}. The components of the impedance matrix are very sensitive to a frequency f and a dc current I_b as shown in Figs. 2.32(a),(b).

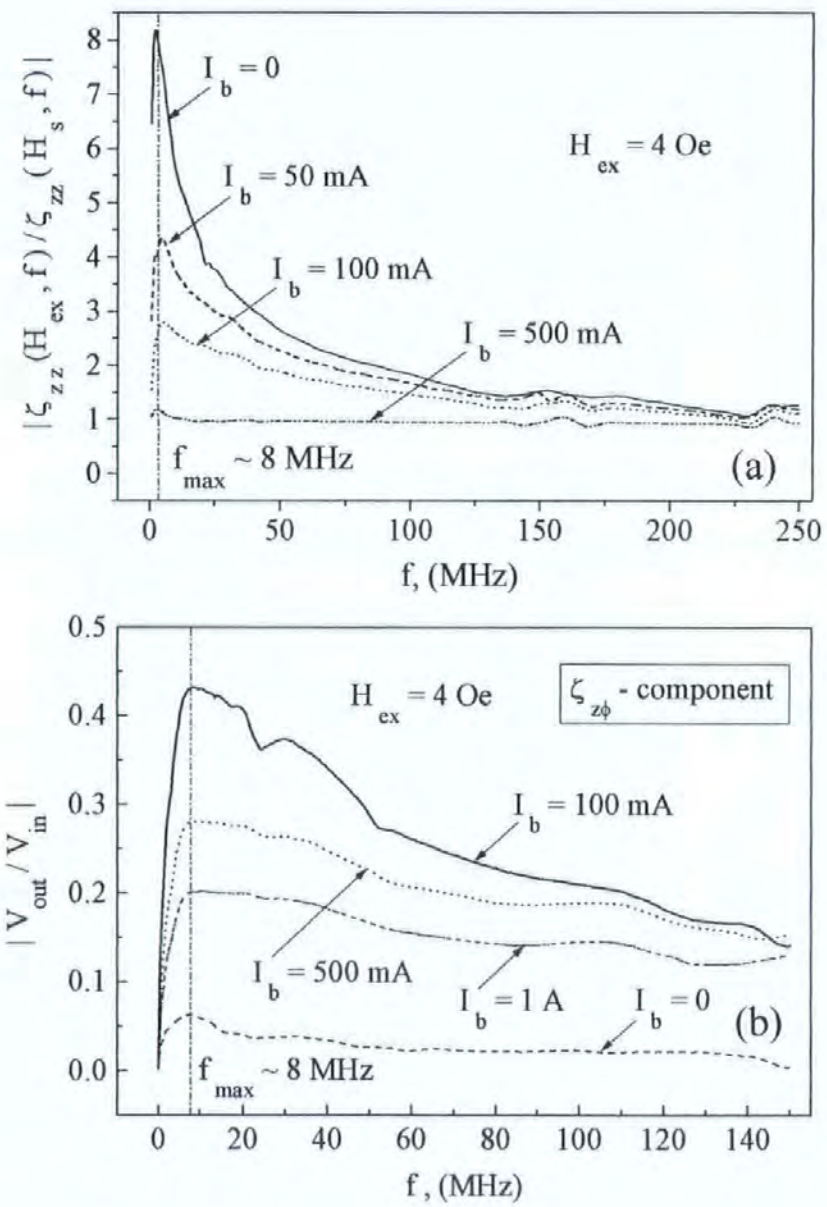

Fig. 2.32 *Frequency plots of the diagonal ς_{zz} and off-diagonal $\varsigma_{z\varphi}$ components measured for different bias currents I_b.*

As functions of a frequency, ς_{zz} and $\varsigma_{z\varphi}$ have a maximum at $f = 7-8$ MHz. The further decrease should be related to the frequency behaviour of the effective permeability $\tilde{\mu}$ (see Fig. 2.9). The application of a sufficient large I_b causes a transition to a single domain state, however, this also increases the magnetic hardness in the axial direction. In the case of ς_{zz} this results in a rapid drop in the nominal values at a given H_{ex}, as seen in Fig. 2.32(a), where H_s is the saturation field. Contrarily, $\varsigma_{z\varphi}$ would be zero for an ideal periodic circular domain structure ("bamboo"), therefore, it increases substantially when the current is enough to eliminate circular domains. Further increase in I_b results in a decrease in $\varsigma_{z\varphi}$ because of the same reasons as in the case of ς_{zz}.

The comparative analysis of the components ς_{zz} and $\varsigma_{z\varphi}$ as functions of H_{ex}, f, and I_b is useful to determine the best parameter range for the ac biased AGMI. Figure 2.33(a) shows the plots of the voltage magnitude $|V_z|$ versus H_{ex} for two frequencies and $I_b = 100$ mA. For a higher frequency of 10 MHz, the effect of h_{ex} results in a considerable asymmetry in $|V_z(H_{ex})|$, which can be compared with the same characteristic measured without the ac bias field h_{ex} (no coil, dashed line). As the frequency is increased, the real part R (is represented by the real part of V_z / V_{in}) of the total impedance Z becomes negative, as seen in Fig. 2.33(b). The "negative resistance" is a consequence of two opposing e.m.f., as discussed above. The voltage amplitude (or the absolute value of Z) never reaches zero, but in the region of negative R there is a characteristic "hill", as seen for the case of 10 MHz in Fig. 2.33(a).

AGMI characteristics can be used to obtain a near-linear voltage output in a differential scheme, which connects two wires oppositely biased by means of coils mounted in "left" and "right" sense. Figure 2.34 presents examples of a possible output in such a circuit. The best linearity is obtained for frequency of 8 MHz, for which the maximum of the off-diagonal component almost compares with that for ς_{zz}. The linear region is obtained in the field interval ±5 Oe, which is restricted by the value of the anisotropy field. On the other hand, the value of the ac bias can be made very small, it has to be of the order of the circular field at the wire surface, produced by the ac wire current. Application of AGMI for the magnetic sensors will be concretised in Chapter 4.

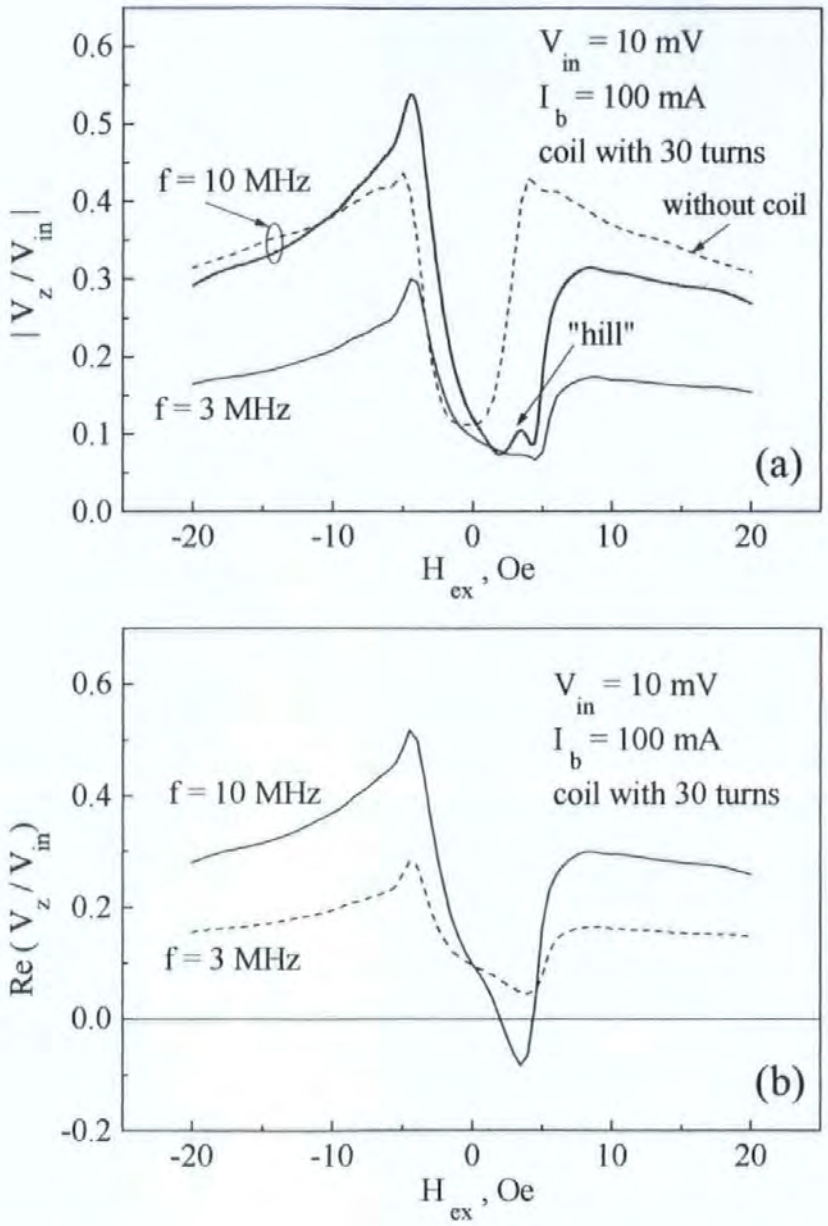

Fig. 2.33 *Asymmetrical voltage response versus* H_{ex}. *Amplitude of the wire voltage* $|V_z|$ *is given in (a). Here for comparison* $|V_z|$ *measured without the ac bias (no coil) is shown in dashed line. In (b), the real part of* V_z/V_{in} *(resistance R) versus* H_{ex} *is given.*

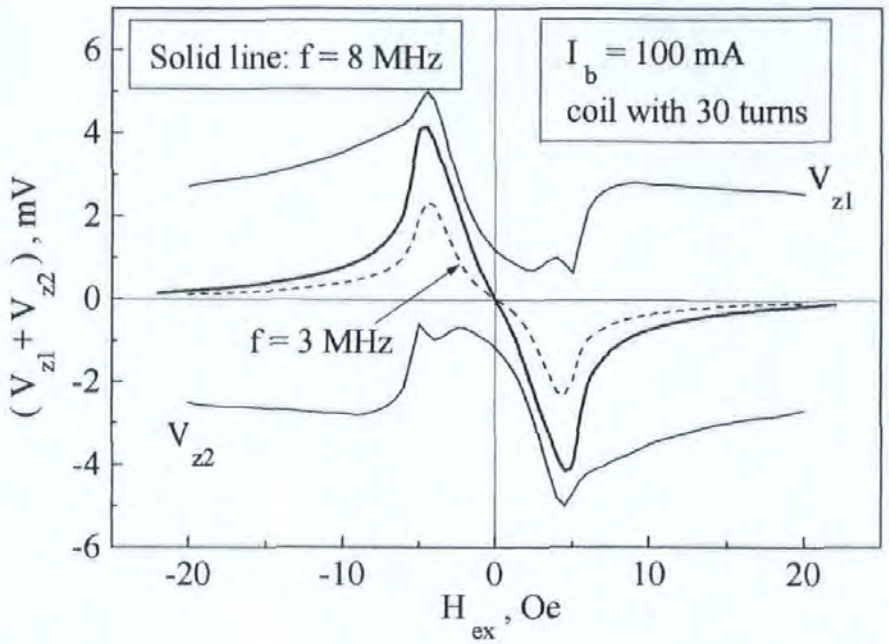

Fig. 2.34 *Principle of obtaining near-linear voltage output in the differential scheme.*

In summary, we would like to notice, that the method of obtaining AGMI with the use of the ac bias is not related with asymmetry in the dc magnetic configuration. This case seems to be especially important for developing auto-biased linear sensors since it does not require either introducing a special helical anisotropy or applying a large dc bias field.

2.9 Conclusion

The surface impedance matrix approach has been used to study various types of MI characteristics in amorphous wires with a helical (circumferential) anisotropy. Regarding conceptual aspects of the MI effect, it has been demonstrated that a high sensitivity to the external field is caused by the dependence of the current density distribution on the static magnetic structure. Therefore, the characteristic field of the major impedance change is the anisotropy field, and the MI spectra are very broad (from a few MHz to hundreds of MHz for 30 μm diameter Co-based amorphous wire). Modifying the static magnetic structure, various types of the MI characteristics can be obtained: symmetrical or asymmetrical with respect to H_{ex}, without a hysteresis or exhibiting a hysteresis including that of a bi-stable type. An interesting example is the change in MI characteristics in wires with a helical magnetic anisotropy under the effect of the dc current.

Considering a matrix nature of the impedance, the use of the off-diagonal components results in asymmetrical MI in the presence of the ac bias, which is especially important for linear magnetic sensing.

The theory is based on the asymptotic-series expansion of the Maxwell equations. The method has no restriction to a specific geometry. It can be expanded to consider practically important cases of 2-dimensional magnetic/metallic multilayers. The major limitation of the theory is considering a uniform magnetisation ignoring completely a radial distribution of permeability and the domain structure. Considering MI effects, the variation in permeability may not be important since the surface magnetisation gives predominant contribution. Regarding domain wall dynamics, it can be taken into account by modifying the permeability matrix on the basis of effective medium approximation for small field perturbations.[2,43] By this, the eddy currents due to the local wall displacements are averaged on the domain scale. Another restriction is the ignoring of the exchange effects. This is accurate if the exchange length is smaller than the skin-depth. The theoretical model has been tested comparing the results with the experimental data. For the sake of accurate comparison, a series of experiments was carried out. The theory agrees well with the numerical experimental data as far as the ac rotational magnetisation processes are responsible for the impedance change.

2.10 References

[1] D. P. Makhnovskiy, L. V. Panina, and D. J. Mapps, Phys. Rev. **B 63**, 144424 (2001).

[2] L. V. Panina and K. Mohri, Appl. Phys. Lett. **65**, 1189 (1994).

[3] L. V. Panina, K. Mohri, K. Bushida, and M. Noda, J. Appl. Phys. **76**, 6198 (1994).

[4] C. A. Grimes and J. V. Prodan, J. Appl. Phys. **73**, 6989, (1993).

[5] M. Vazquez and A. Hernando, J. Phys. D: Appl. Phys. **29**, 939, (1996).

[6] H. Chiriac and N. Lupu, Physica **B 299**, 293, (2001).

[7] M. Takajo, J. Yamasaki, and F. B. Humphrey, IEEE Trans. Magn. **29**, p. 3484 (1993).

[8] I. Ogasawara and S. Ueno, IEEE Trans. Magn. **31**, 1219 (1995).

[9] H. Chiriac and T. A. Ovari, Progress in Mater. Science **40**, p. 333 (1996).

[10] A. P. Zhukov, J. M. Blanco, J. Gonzalez, M. J. Garcia Prieto, E. Pina, and M. Vazquez, J. Appl. Phys. **87**, 1402 (2000).

[11] A. P. Zhukov, J. Gonzalez, J. M. Blanco, M. Vazquez, and V. S. Larin, J. Mat. Res. **15**, 2107 (2000).

[12] H. Chiriac, T. A. Ovari, and Gh. Pop, Phys. Rev. **B 52**, 10104 (1995).

[13] L. D. Landau and E. M. Lifshitz, *Electrodynamics of Continuous Media*, (Pergamon Press, 1975).

[14] A. N. Tihonov, Matematicheskiy Sbornik (in Russian) No. 3, 575 (1952).

[15] A. B. Vasilieva and V. T. Butuzov, *Singular perturbed differential equations of parabolic type. – Lecture notes in Mathematics 985, Asymptotic Analysis II.* (Springer – Verlag, 1983), p. 38.

[16] D. R. Smith, *Singular-Perturbation theory. An Introduction with Applications.* (Cambridge University Press, Cambridge, 1985).

[17] D. P. Makhnovskiy, A. S. Antonov, A. N. Lagarkov, and L. V. Panina, J. Appl. Phys **84**, 5698 (1998).

[18] V. Panina, D. P. Makhnovskiy, and K. Mohri, J. Appl. Phys. **85**, 5444 (1999).

[19] A. S. Antonov, I. T. Yakubov, and A.N. Lagarkov, J. Phys. D: Appl. Phys. **32**, 1204 (1999).

[20] A. S. Antonov, I. T. Yakubov, and A. N. Lagarkov, J. Magn. Magn. Mater. **187**, 252 (1998).

[21] S. Chikazumi, *Physics of Magnetism*, (John Wiley & Sons, Inc., New York – London – Sydney, 1964).

[22] D. Menard, M. Britel, P. Ciureanu, A. Yelon, V. P. Paramonov, A. S. Antonov, P. Rudkowski, and J. O. Strem-Olsen, J. Appl. Phys. **81**, 4032 (1997).

[23] M. R. Britel, D. Menard, L. G. Melo, P. Ciureanu, A. Yelon, R. W. Cochrane, M. Rouabhi, and B. Cornut, Appl. Phys. Lett. **77**, 2737 (2000).

[24] O. Acher, P.-M. Jacquart, and C. Boscher, IEEE Trans. Magn. **30**, 4542 (1994).

[25] W. P. Jayasekara, J. A. Bain, and M. H. Kryder, IEEE Trans. Magn. **34**, 1438 (1998).

[26] H. Garcia-Miquel and M. Vazquez, Physica **B 299**, 225 (2001).

[27] H. Garcia-Miquel, J. M. Garcia, J. M. Garcia-Beneytez, and M. Vazquez, J. Magn. Magn. Mater. **231**, 38 (2001).

[28] R. S. Beach and A. E. Berkowitz, J. Appl. Phys. **76**, 6209 (1994).

[29] J. Velazquez, M. Vazquez, D.-X. Chen, and A. Hernando, Phys. Rev. B **50**, 16737 (1994).

[30] P. Makhnovskiy, L. V. Panina, and D. J. Mapps, J. Appl. Phys. **87**, 4804 (2000).

[31] J. L. Costa, Y. Makino, and K. V. Rao, IEEE Trans. Magn. **26**, 1792 (1990).

[32] L. V. Panina, H. Katoh, and K. Mohri, IEEE Trans. Magn. **29**, 2524 (1993).

[33] T. Gunji, L. V. Panina, and K. Mohri, J. Mag. Soc. Japan **21**, 793 (1997).

[34] D. P. Makhnovskiy, L. V. Panina, and D. J. Mapps, Appl. Phys. Lett. **77**, 121 (2000).

[35] L. V. Panina, D. P. Makhnovskiy, D. J. Mapps, K. Mohri, and P. I. Nikitin, Materials Science Forum **373/376**, 741 (2001).

[36] T. Kitoh, K. Mohri, and T. Uchiyama, IEEE Trans. Magn. **31**, 3137 (1995).

[37] P. Aragoneses, J. M. Blanco, L. Dominguez, J. Gonzalez, and K. Kulakowski, J. Magn. Magn. Mater. **168**, 177 (1997).

[38] J. M. Blanco, A. Zhukov, and J. Gonzalez, J. Phys. D: Appl. Phys. **32**, 3140 (1999).

[39] J. M. Blanco, A. Zhukov, and J. Gonzalez, J. Magn. Magn. Mater. **196/197**, 377 (1999).

[40] V. A. Zhukova, A. B. Chizhik, J. Gonzalez, D. P. Makhnovskiy, L. V. Panina, D. J. Mapps, and A. P. Zhukov, J. Magn. Magn. Mater. **249**, 324 (2002).

[41] A. Chizhik, A. P. Zhukov, J. M. Blanco, and J. Gonzalez, Physica B **299**, 314 (2001).

[42] M. Wun-Fogle, J. B. Restorff, and A. E. Clark, J. Appl. Phys. **70**, 6519 (1991).

[43] P. J. Vulfovich and L. V. Panina, Sensor and Actuators **A 81**, 111 (2000).

Chapter 3 Magneto-impedance matrix in thin films

3.0 Magneto-impedance effect in thin films

Since the discovery of the MI effect in amorphous ferromagnetic wires [1-3] the variety of MI materials has increased significantly. These materials include glass-covered wires, ribbons and thin films made of amorphous or nanocrystalline ferromagnetic alloys. Although wires and ribbons provide very high MI field sensitivity (%/Oe), the need of miniaturisation of actual devices, compatibility with integrated circuit technology, and improvement of accuracy and reproducibility makes MI thin films attractive with their compromise on sensitivity and miniaturisation. Further to this, MI thin film devices can exhibit a much larger impedance change ratio and operate over a wider frequency range than wires.[4-8]

It is common knowledge that the inductance of a conductor increases when a high permeability material is placed nearby. Because of this, thin film structures containing magnetic layers have been used extensively as high inductance elements, which operate up to the GHz range.[9-11] Typically the inductor has two different types of structure: (i) planar solenoid with a magnetic core or (ii) thin multilayered film having a highly conductive lead sandwiched between two magnetic films. The latter structure is similar to the MI sandwich films [4-8, 12-15] considered in this Chapter. However, the anisotropy for the thin film inductors is typically chosen to be longitudinal.[11] Furthermore, the field dependence of the inductor parameters is not of interest. In the case of MI thin films, the transverse anisotropy [4-8] and crossed anisotropy [12-14, 16] are preferable since they provide higher sensitivity to H_{ex}: the state of high inductance is set by applying the longitudinal field.

The importance of the anisotropy to the MI effect has been understood from the onset of MI research.[1-3] By analogy with the wires, where the circumferential anisotropy is preferred, thin films with transverse anisotropy are typically chosen for MI applications as most sensitive. A detailed experimental investigation of the MI characteristics in multilayers with two types of anisotropy: transverse and longitudinal was reported in Ref. 17. For the case of the transverse anisotropy, $|Z(H_{ex})|$ has the expected behaviour with two maximums at $\pm H_K$, where H_K is the anisotropy field. In contrast, for longitudinal anisotropy, $|Z(H_{ex})|$ has a single maximum at zero field and then monotonically decreases until the saturation value. If the angle dispersion of the anisotropy is very small, the maximum becomes quite sharp. Therefore, anisotropy and its dispersion appear to be the important parameters when determining the MI characteristics.

The samples used in Ref. 17 were fabricated from ultrathin multilayers $[NiFe/Ag]_n$, where the number n of the NiFe/Ag bilayers could reach up to a hundred. Using such complicated structures, the authors were guided by the knowledge that in multilayers the NiFe layers have to be kept thin to preserve their soft magnetic properties. In this case no further thermal or field annealing processes would be required. However, the same results can be easily obtained for bilayer [8,16] or three layer [6] sandwich films made of a soft amorphous ferromagnetic alloy of composition CoSiB, FeCoSiB, CoFeB or CoNbZr. A nanometre laminated Cr or Nb layer between two magnetic layers has been successfully applied to form a perfect stripe domain structure with transverse anisotropy.[8] Nevertheless, an annealing and thermal treatments may play a significant role for improving the MI response in amorphous and nanocrystalline thin films as shown in this Chapter and other works.[18-20] For sputtered films it is widely known that annealing frequently helps to establish the required type of the anisotropy and domain structure,[20] as the internal stresses and other defects caused by the sputtering process may result in unexpected magnetic structures. In nanocrystalline materials annealing or thermal treatments increase the amorphous phase and therefore improve the MI response.[19]

The multilayer MI structure consisting of a conductive inner lead and two outer ferromagnetic layers has some advantages. Comparing to MI in a single layer film, this structure can exhibit a considerably larger change in impedance at lower frequencies of a passing current. It has been reported in Ref. 6 that the MI ratio in CoSiB/Cu/CoSiB multilayers of several micrometer thick reaches up to 300% for a frequency of 10 MHz and a magnetic field of about 10 Oe. On the other hand, for a single CoSiB magnetic layer of the same thickness the MI effect is very small (< 5%) at such conditions. For a sandwich film with a smaller total thickness of the order of 0.1 μm the MI effect decreases down to about 20%,[4] yet in the case of a similar single layer film the MI effect would not be noticeable. Usually the studies on MI in multilayers are restricted to the case of a transverse in-plain anisotropy induced in ferromagnetic layers. The analysis presented in this Chapter includes a special type of anisotropy, which is crossed in one film with respect to the other. By symmetry, this case is similar to a helical anisotropy in a wire and presents a considerable interest. Choosing proper angles, the crossed anisotropy can be reduced to the transverse or longitudinal ones. The NiFe/Au/NiFe sandwich thin films with different anisotropies (transverse, longitudinal and crossed) were fabricated to measure the field dependences of the longitudinal impedance.

Similar to the MI behaviour in wires with helical anisotropy, the MI field dependences in films with crossed anisotropy can be changed by the effect of a dc antisymmetric transverse magnetic field (or a dc current).[12-14, 16] With increasing the transverse field, the hysteresis portion of impedance plots shrinks and shifts and finally disappears, resulting in highly sensitive asymmetric MI characteristics, which are important to construct a linear auto-biased field sensor. General representations of the impedance matrix $\hat{\varsigma}$ for the bilayer (ferromagnetic/ferromagnetic) and three layer (ferromagnetic/conductor/ferromagnetic) films with various types of anisotropy have been given in Ref. 12 and Refs. 13,14, respectively. The experimental results on the asymmetrical MI in a bilayer CoFeB film with crossed anisotropy were reported in Ref. 16.

As it has been discussed in Chapter 2, if the equilibrium direction of the magnetisation is deflected by some angle away from the transverse, the ac current j induces both the longitudinal voltage V_z and the coil voltage V_c. Also, if the MI sample is placed in an ac longitudinal magnetic field h_{ex}, the longitudinal and circulatory ac magnetisations contribute to V_c and V_z respectively. Both cases can be described in terms of the surface impedance matrix $\hat{\varsigma}$ containing the off-diagonal components, so-called *off-diagonal impedances*. In this Chapter the off-diagonal response is studied theoretically and experimentally in the MI sandwich structures with the different anisotropies. A narrow NiFe/Au/NiFe sandwich thin film with an integrated planar helical microcoil was fabricated to measure the off-diagonal impedances in the high frequency range up to 100 MHz. For potential applications, the attractive feature of the off-diagonal impedance is that the field dependence of its real and imaginary parts are antisymmetrical with respect to the H_{ex} direction. However, we demonstrate that off-diagonal response in a film with a stripe domain structure is only possible in the presence of a dc longitudinal bias current I_b. It is shown that only a few milliamperes of bias current is required to cause the off-diagonal response where an optimum value was found within the range of a few tens of milliamperes. Without I_b the off-diagonal response is very poor and irregular. The features of the off-diagonal impedance mentioned above have been theoretically predicted in thin films [15] and wires [21], and experimentally demonstrated in a ferromagnetic wire [21,22], where similar effects take place for a circumferential anisotropy and "bamboo-like" domain structure.

As it has been noted above, in the multilayer MI structures a very large change in impedance can occur at much lower frequencies when the inductance caused by the outer magnetic layers becomes larger than the resistance determined mainly by the inner conductor. Then, the impedance varies linearly with the frequency and the permeability. Due to this advantage, MI in the sandwich films has a potential to be used in developing small sensitive magnetic heads for high density magnetic recording. Considering a real head, the effect of a sandwich width on MI has to be studied. In Section 3.8 the problem is approached by finding the ac field distributions over the film width under the condition of a weak skin effect.[23,24] If the edge effect is neglected (approximation of an infinite width), the magnetic flux generated by the current flowing along the inner lead is confined within the outer magnetic layers. In the sandwich of a finite width, the flux leaks across the inner conductor. This process eventually results in a considerable drop in the MI ratio if the film width is smaller than some critical value depending on the transverse permeability and the thickness of the magnetic and conductive layers. This result is similar to that known as an inductive head efficiency.[25,26]

3.1 Thin film fabrication

The radio frequency (rf) magnetron sputtering system used for depositing thin films was a Nordiko NM 2000. A schematic diagram of the system is shown in Fig. 3.1.[27] The chamber is firstly evacuated by the rotary pump. When an adequate base vacuum is achieved, the diffusion pump is used to evacuate the chamber to the high vacuum required prior to sputtering. The base pressure attained before sputtering was $2x10^{-7}$ bar, and the process gas pressure (Ar) during the sputtering process was kept at $4.5x10^{-3}$ mbar. RF sputtering is more widely used than dc sputtering, as it is more efficient and can be used to deposit insulators. If a low frequency alternating voltage was applied to the electrodes in a chamber the ions would be still mobile enough to complete the plasma discharge at each electrode on each half cycle, requiring a source of secondary electrons at both electrodes to be sustained. With applied voltages at frequencies above 50 KHz up to the MHz range the minimum pressure of the process gas (Ar) at which the glow discharge will be sustained is reduced. At these frequencies electrons oscillate in the glow space, acquiring enough energy from the rf field to generate ionising collisions. In this respect the rf glow discharge is very different to the dc glow discharge as the dependence on the secondary electrons is reduced and thus the breakdown voltage is lower.

Since rf can be coupled through non conductors, insulators can be sputtered. The sputtering yield is defined as the number of target atoms released for every bombarding ion for a particular target material. The sputtering rate is determined by the ion energy generated at the target surface. In the glow discharge only a small fraction of the ion energy is produced as kinetic energy at the target, with some 50% to 90% of the applied power being lost as heat. This means sputtering is a very inefficient process with most of the input power to the system ending up as target heating. Therefore, the target has to be cooled.

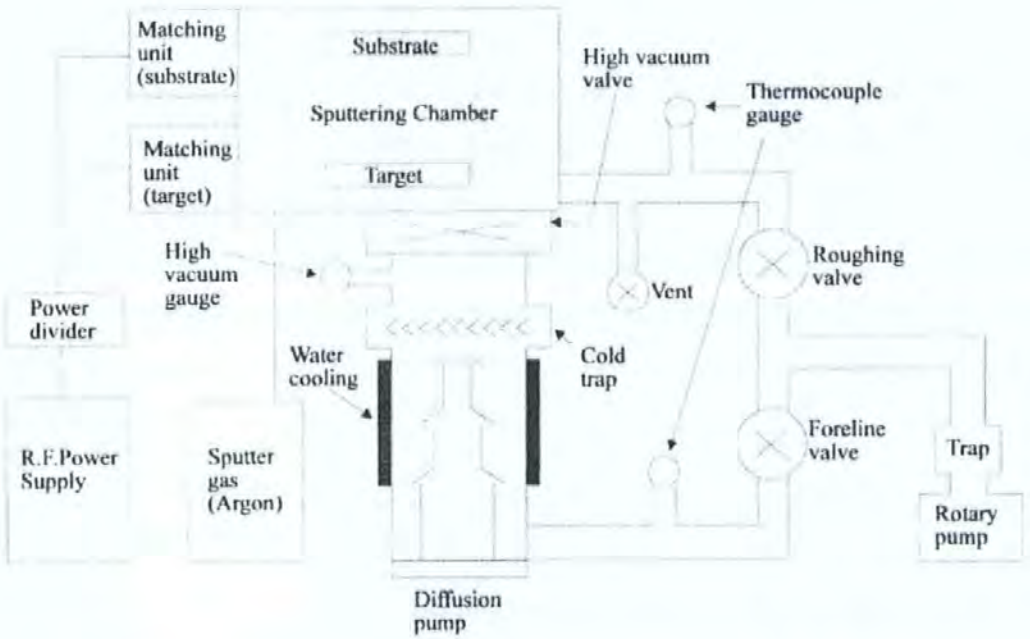

Fig. 3.1 *Schematic diagram of the rf sputtering system* (After N. Fry [27]).

In order for material to be sputtered from the target only, a high positive ion flux must be achieved at the target surface by giving it a high negative potential with respect to the plasma. This is achieved by placing a "blocking" capacitor in series with the target. Since electrons have much smaller mass than ions their velocities are much higher, and therefore the electron current is much greater than the ion current. With a rf voltage applied to the capacitor connected in series with the target a large electron current flows from the plasma to the target on the first half cycle. With the ion current from the plasma to the electrode on the second half cycle being smaller, a charge imbalance begins, eventually causing the target surface to build up a high negative charge at its surface over successive cycles.

Since there is no charge transferred through the capacitor (allowing only ac current to flow and blocking any dc one) the voltage on the electrode "self biased" negatively. Consequently, the target surface is subjected to high energy positive ion bombardment resulting in sputtering. At frequency above 1 MHz appreciable rates are achievable. Below this, a positive charge can be built at the target surface, thus reducing the ion bombardment energy. The upper frequency of operation is limited to about 20 MHz. At frequencies above this, inter-connection impedances cause problems. An L-C matching network is required in order to optimise the ac coupling between the power supply and the chamber.

Magnetron sputtering is used to enhance sputtering rates. The basic idea is to trap electrons near the target surface. The magnetic fields used in sputtering systems are typically of the order of 100 Gauss, which only affects the electrons, as the ions are too massive. The secondary electrons are constrained to follow a helical path due to the influence of the magnetic field. Since their trajectories are not in a straight line on leaving the target surface they travel further for a fixed mean free path, increasing the probability of ionising collisions before they reach the anode.

The target substrate can be biased by rf or dc voltage during the sputtering process.[27] This results in the preferential removal of film impurities in the growing film to improve the final film purity. The level of substrate bias has been found to be very important in determining how much of the process gas is incorporated into the growing film. There is normally an optimum bias to achieve minimum gas ion implantation. In many cases a negative bias is applied to the substrate to enhance ion bombardment of the growing film. A positive bias at the substrate however, would make the substrate becomes a virtual anode, so that a large electron current would flow to it, resulting in substrate heating and a non-uniform current distribution. Positive bias can also cause contamination by sputtering the anode. The most commonly used method of bias sputtering is to apply rf to both the target and the substrate. This is achieved with a single power splitter. A rf matching network is required for both the target and the substrate.

3.2 Magneto-impedance matrix in the sandwich film

In this section we consider MI in a multilayer film having an inner conductive lead of a thickness $2d_1$ and two identical magnetic layers of a thickness d_2, as shown in Fig. 3.2(a)). An ac current $j = j_0 \exp(-i\omega t)$ is flowing along the conductive lead in the length direction (z-axis). The anisotropy axes in the ferromagnetic layers are directed at an angle $\pm\alpha$ with respect to the current flow, respectively for the upper ($x > 0$) and lower ($x < 0$) layers. Such anisotropy can be induced by current annealing in the presence of a longitudinal field. The application of a dc longitudinal field H_{ex} and an antisymmetric transverse field $H_b(x > 0) = -H_b(x < 0)$ results in the antisymmetric arrangement of the dc magnetisation $\mathbf{M}_0$. The transverse bias field can be created by applying a dc current along the inner lead.

For such configuration, the ac current induces both the voltage (V_z) between the film ends and the coil voltage (V_c), as shown in Fig. 3.2(b), since the current flow gives rise to an antisymmetric transverse magnetisation (or circulatory magnetisation) and a non-zero total longitudinal magnetisation. If the film is placed in a variable longitudinal field h_{ex}, not only the longitudinal magnetisation, but also the circulatory magnetisation contributing to V_z is induced. The crossed magnetisation processes related to the voltages V_c and V_z (the inverse Wiedemann and Matteucci effects [28]) are similar to those having place in wires with the magnetisation deflected from the circular direction (see Chapter 2). For certain parameters, the voltages V_z and V_c are very sensitive to the longitudinal field H_{ex}. Applying the bias field H_b various kinds of sensitive MI behaviour can be obtained.

The induced voltages are described in terms of the surface impedance matrix $\hat{\varsigma}$ which relates the variable electric $\bar{\mathbf{e}}_t$ and magnetic $\bar{\mathbf{h}}_t$ fields taken on the external surfaces $x = \pm d$ ($d = d_1 + d_2$):

$$\bar{e}_{t\alpha} = \varsigma_{\alpha\beta}\left(\bar{\mathbf{h}}_t \times \mathbf{n}\right)_\beta, \quad \alpha,\beta = z,y, \tag{1}$$

where $\mathbf{n}$ is a unit vector directed inside the film, $\bar{\mathbf{e}}_t$ and $\bar{\mathbf{h}}_t$ lay along the surface. The voltage V_z is determined by the surface value of the longitudinal electric field $\bar{e}_z(d) = \bar{e}_z(-d)$ and is related to the current j and the variable field h_{ex} via the components ς_{zz} and ς_{zy}.

The contribution to V_z arising from the current flow only is expressed as $V_z = (2\pi l/cb)\varsigma_{zz} j$, where l is the film length and b is its width, and c is the velocity of light (Gauss system of units is used). The off-diagonal component ς_{yz} linking the circulatory electric field $\bar{e}_y(d) = -\bar{e}_y(-d)$ and the current is associated with the coil voltage V_c.

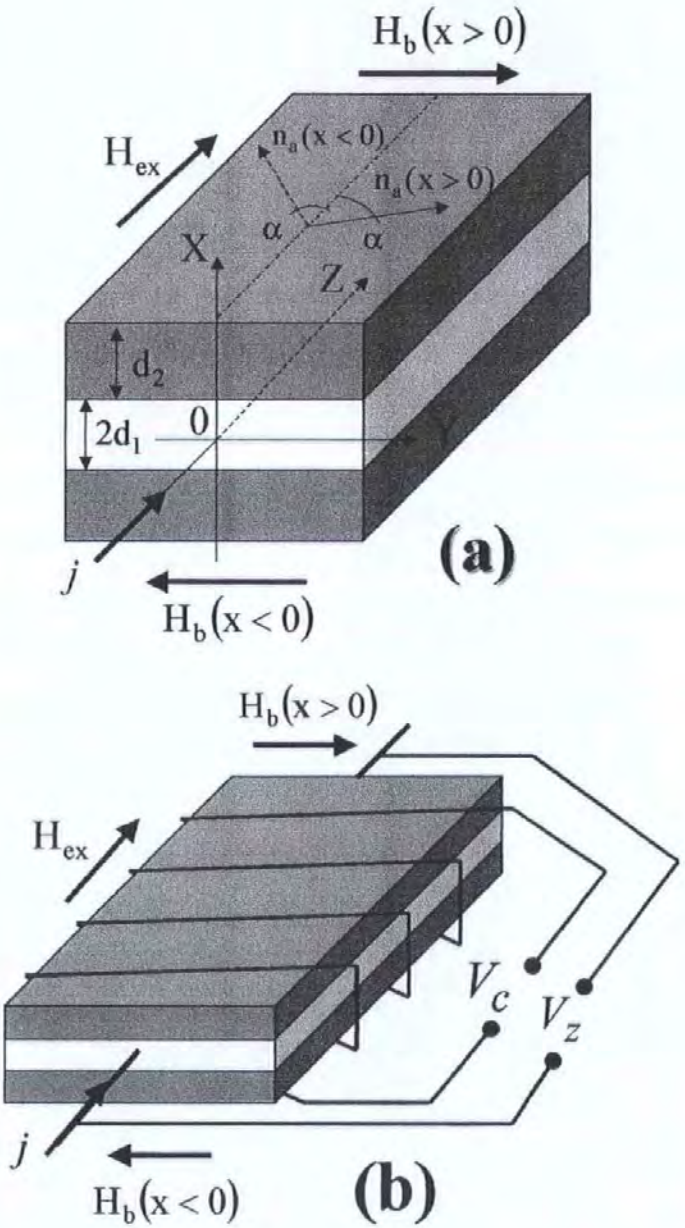

Fig. 3.2 *Schematic diagram of a multilayer MI showing principle directions and quantities used in (a) and induced voltages in (b).*

The calculation of $\hat{\varsigma}$ is based on the solution of the Maxwell's equations for the fields $\mathbf{e}$ and $\mathbf{h}$ together with the equation of motion for the magnetisation vector $\mathbf{M}$. In a linear approximation over the variable fields and magnetisation and assuming a local relationship between $\mathbf{m} = \mathbf{M} - \mathbf{M}_0$ and $\mathbf{h}$: $\mathbf{m} = \hat{\chi}\mathbf{h}$, the problem is reduced to finding the solutions of the Maxwell's equations with a given ac permeability matrix $\hat{\mu} = \hat{\mathbf{I}} + 4\pi\hat{\chi}$:

$$\mathrm{rot}\,\mathbf{e} = -\partial(\hat{\mu}\mathbf{h})/\partial t\,, \quad \mathrm{rot}\,\mathbf{h} = 4\pi\,\mathbf{j}/c\,, \qquad \mathbf{j} = \sigma\mathbf{e} \tag{2}$$

satisfying the boundary conditions on the external surface:

$$\bar{h}_y(\pm d) = \pm 2\pi\, j/cb\,, \quad \bar{h}_z(\pm d) = h_{ex}\,, \tag{3}$$

and the conditions of continuity across the boundaries and symmetry.

The permeability matrix $\hat{\mu}$ is related to certain magnetisation processes. At high frequencies the domain wall movement is strongly damped and contributes little to the ac magnetisation. Then, $\hat{\mu}$ can be determined by the magnetisation rotation only, depending on the direction of $\mathbf{M}_0$.

The dc magnetisation $\mathbf{M}_0$ in each layer is assumed to be independent of x, and directed at an angle $\pm\theta$ to the z-axis for $x > 0$ and $x < 0$, respectively. Neglecting the interaction between the layers, the stable direction of $\mathbf{M}_0$ is found by minimising the magnetostatic energy density U_0 of each layer: $\partial\left(-K\cos^2(\alpha-\theta) - M_0 H_{ex}\cos\theta - M_0 H_b \sin\theta\right)/\partial\theta = 0$ (see Sections 1.6 and 2.6). The domain processes may not be essential even for the reversal of $\mathbf{M}_0$. In films, the magnetisation vector during its rotation is held parallel to the surface, without going through high energy demagnetisation states. Besides, the critical field of the irreversible magnetisation flip quickly drops as the transverse bias is increased. This process has been demonstrated in Fig. 2.8(b) (see Section 2.6), where the magnetisation loops $M_{0z}(H_{ex})$ are shown for different values of dc bias H_b.

To solve Eqs. (2), we introduce two auxiliary co-ordinate systems $(\mathbf{x},\mathbf{y}',\mathbf{z}')$ and $(\mathbf{x},\mathbf{y}'',\mathbf{z}'')$ in the upper and lower magnetic layers respectively, where z'-axis and z''-axis are directed along the equilibrium position of the magnetisation $\mathbf{M}_0$ in each layer, as shown in Fig. 3.3.

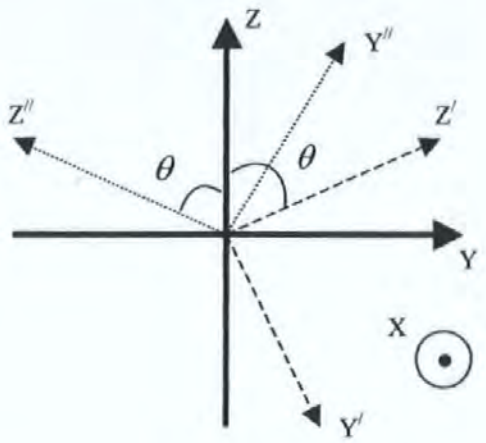

Fig. 3.3 *Auxiliary co-ordinate systems* **(x,y',z')** *and* **(x,y'',z'')** *in the upper and lower magnetic layers, respectively.*

The susceptibility matrix $\hat{\chi}$ found from the linearized Landau-Lifshitz equation has the simplest form in the co-ordinate systems **(x,y',z')** and **(x,y'',z'')**:

$$\hat{\chi} = \begin{pmatrix} \chi_1 & -i\chi_a & 0 \\ i\chi_a & \chi_2 & 0 \\ 0 & 0 & 0 \end{pmatrix}, \tag{4}$$

where the matrix components are defined as well as in Eq. (2.50) of Section 2.6. The permeability matrix is the same in both layers, as $\hat{\mu}(\alpha,\theta,H_b) = \hat{\mu}(-\alpha,-\theta,-H_b)$.

Equations (2) applied to the magnetic layers are easily solved in the co-ordinate systems, where the susceptibility matrix $\hat{\chi}$ is of quasi-diagonal form (4). Further, Eqs. (2) for the magnetic layers will be written only in **(x,y',z')**, since the equal form takes place in **(x,y'',z'')**. For the components of magnetic and electrical fields inside the magnetic layers ($d_1 < |x| < d$) we obtain the following system of equations:

$$\begin{cases} e_{x'} \equiv 0 \\ \dfrac{\partial^2 e_{y'}}{\partial x^2} + i\dfrac{4\pi\sigma_2\omega}{c^2} e_{y'} = 0 \\ \dfrac{\partial^2 e_{z'}}{\partial x^2} + i\dfrac{4\pi\sigma_2\omega}{c^2}\tilde{\mu} e_{z'} = 0 \end{cases}, \qquad \begin{cases} -(1+4\pi\chi_1) h_{x'} = 4\pi i \chi_a h_{y'} \\ \dfrac{\partial^2 h_{y'}}{\partial x^2} + i\dfrac{4\pi\sigma_2\omega}{c^2}\tilde{\mu} h_{y'} = 0 \\ \dfrac{\partial^2 h_{z'}}{\partial x^2} + i\dfrac{4\pi\sigma_2\omega}{c^2} h_{z'} = 0 \end{cases}, \tag{5}$$

where σ_2 is the conductivity of the magnetic layers, $\tilde{\mu} = 1 + 4\pi\left(\chi_2 - 4\pi\chi_a^2/(1+4\pi\chi_1)\right)$ is the effective permeability, which has been used in Chapter 2. The edge effect is neglected considering that in-plane film dimensions are sufficiently large. (The size effect in the narrow sandwich films will be studied later in Section 3.8) The solutions of Eqs. (5) are represented by two normal waves $\{e_{z'}, h_{y'}\}$, $\{e_{y'}, h_{z'}\}$ corresponding to a scalar permeability $\tilde{\mu}$ and a unit permeability, respectively. The solution of Eqs. (5) for the magnetic field is written in the form:

$$\begin{aligned} h_{y'}^{\pm} &= A_m^{\pm}\sinh(ik_m x) + B_m^{\pm}\cosh(ik_m x), \\ h_{z'}^{\pm} &= A_0^{\pm}\sinh(ik_0 x) + B_0^{\pm}\cosh(ik_0 x), \end{aligned} \tag{6}$$

where indices "$\pm$" are related to the upper and lower magnetic layers, respectively, and

$$\begin{aligned} &k_m = (1+i)/\delta_m, \quad k_0 = (1+i)/\delta_0, \quad \delta_0 = c/\sqrt{2\pi\sigma_2\omega}, \\ &\delta_m = \delta_0/\sqrt{\tilde{\mu}}, \quad \tilde{\mu} = 1 + 4\pi\left(\chi_2 - 4\pi\chi_a^2/(1+4\pi\chi_1)\right). \end{aligned}$$

Unknown constants $A_m^{\pm}, B_m^{\pm}, A_0^{\pm}, B_0^{\pm}$ are to be found from the boundary condition discussed below. Equations (6) can be re-written in the initial co-coordinate system $(\mathbf{x},\mathbf{y},\mathbf{z})$:

$$\begin{aligned} h_y^+ &= h_{y'}^+\cos\theta + h_{z'}^+\sin\theta, \\ h_y^- &= h_{y'}^-\cos\theta - h_{z'}^-\sin\theta, \\ h_z^+ &= h_{z'}^+\cos\theta - h_{y'}^+\sin\theta, \\ h_z^- &= h_{z'}^-\cos\theta + h_{y'}^-\sin\theta. \end{aligned} \tag{7}$$

The equations for the components of magnetic and electrical fields in the inner non-magnetic layer (lead) $|x| < d_1$ can be immediately written in the initial co-ordinate system $(\mathbf{x},\mathbf{y},\mathbf{z})$:

$$\begin{cases} \tilde{e}_x \equiv 0 \\ \dfrac{\partial^2\tilde{e}_y}{\partial x^2} + i\dfrac{4\pi\sigma_1\omega}{c^2}\tilde{e}_y = 0, \\ \dfrac{\partial^2\tilde{e}_z}{\partial x^2} + i\dfrac{4\pi\sigma_1\omega}{c^2}\tilde{e}_z = 0 \end{cases} \quad \begin{cases} \tilde{h}_x \equiv 0 \\ \dfrac{\partial^2\tilde{h}_y}{\partial x^2} + i\dfrac{4\pi\sigma_1\omega}{c^2}\tilde{h}_y = 0, \\ \dfrac{\partial^2\tilde{h}_z}{\partial x^2} + i\dfrac{4\pi\sigma_1\omega}{c^2}\tilde{h}_z = 0 \end{cases} \tag{8}$$

where the symbol "~" designates the inner non-magnetic layer and σ_1 is its conductivity. The solutions of Eqs. (8) for the magnetic field satisfying the symmetry conditions are of the form:

$$\tilde{h}_y = C_y \sinh\left(i\tilde{k}_0 x\right), \quad \tilde{h}_z = C_z \cosh\left(i\tilde{k}_0 x\right), \tag{9}$$

$$\tilde{k}_0 = (1+i)/\tilde{\delta}_0, \quad \tilde{\delta}_0 = c/\sqrt{2\pi\sigma_1\omega}.$$

The electric fields can be found from the first Maxwell equation (see Eqs. (2)). General solutions (6),(7) and (9) contain ten unknown constants, which can be determined from the symmetry conditions and matching the tangential field components across the boundaries $x = \pm d_1$:

$$\begin{aligned}
&h_y^+(|x|) = -h_y^-(-|x|), \quad |x| \in [d_1, d_1 + d_2], \\
&\tilde{h}_y(x) = -\tilde{h}_y(-x), \quad x \in [-d_1, d_1], \\
&\tilde{h}_z(x) = \tilde{h}_z(-x), \quad x \in [-d_1, d_1], \\
&h_y^{\pm}(\pm(d_1 + d_2)) = \pm 2\pi j/(cb) = \pm h_y, \\
&h_z^{\pm}(\pm(d_1 + d_2)) = h_{ex}, \\
&h_y^+(d_1) = \tilde{h}_y(d_1), \\
&h_z^+(d_1) = \tilde{h}_z(d_1), \\
&e_y^+(d_1) = \tilde{e}_y(d_1), \\
&e_z^+(d_1) = \tilde{e}_z(d_1).
\end{aligned} \tag{10}$$

Calculating the components of **e** and **h** on the external surface, the surface impedance matrix can be determined as:

$$\begin{aligned}
\varsigma_{zz} &= \frac{ik_0 c}{4\pi\sigma_2 D}\Big[\sqrt{\tilde{\mu}}\,Q_1 R_4 \cos^4\theta + Q_4 R_1 \sin^4\theta + \\
&\qquad + \left(2k_m\tilde{k}_0/(\sigma_1\sigma_2) + \sqrt{\tilde{\mu}}\,Q_3 R_2 + Q_2 R_3\right)\sin^2 2\theta/4\Big], \\
\varsigma_{zy} = \varsigma_{yz} &= \frac{ik_0 c}{8\pi\sigma_2 D}\sin 2\theta\Big[\left(\sqrt{\tilde{\mu}}\,Q_1 R_4 - Q_2 R_3\right)\cos^2\theta + \left(\sqrt{\tilde{\mu}}\,Q_3 R_2 - Q_4 R_1\right)\sin^2\theta - \\
&\qquad - \tilde{k}_0 k_m \cos 2\theta/(\sigma_1\sigma_2)\Big], \\
\varsigma_{yy} &= \frac{ik_0 c}{4\pi\sigma_2 D}\Big[Q_2 R_3 \cos^4\theta + \sqrt{\tilde{\mu}}\,Q_3 R_2 \sin^4\theta + \\
&\qquad + \left(\sqrt{\tilde{\mu}}\,Q_1 R_4 + Q_4 R_1 - 2\tilde{k}_0 k_m/(\sigma_1\sigma_2)\right)\sin^2 2\theta/4\Big],
\end{aligned} \tag{11}$$

where

$k_0 = (1+i)/\delta_0, \quad \delta_0 = c/\sqrt{2\pi\sigma_2\omega}$,

$D = Q_1Q_2\cos^2\theta + Q_3Q_4\sin^2\theta$,

$Q_1 = \tilde{k}_0 \sinh(i\tilde{k}_0 d_1)\sinh(ik_0 d_2)/\sigma_1 + k_0 \cosh(i\tilde{k}_0 d_1)\cosh(ik_0 d_2)/\sigma_2$,

$Q_2 = \tilde{k}_0 \cosh(i\tilde{k}_0 d_1)\sinh(ik_m d_2)/\sigma_1 + k_m \sinh(i\tilde{k}_0 d_1)\cosh(ik_m d_2)/\sigma_2$,

$Q_3 = \tilde{k}_0 \cosh(i\tilde{k}_0 d_1)\sinh(ik_0 d_2)/\sigma_1 + k_0 \sinh(i\tilde{k}_0 d_1)\cosh(ik_0 d_2)/\sigma_2$,

$Q_4 = \tilde{k}_0 \sinh(i\tilde{k}_0 d_1)\sinh(ik_m d_2)/\sigma_1 + k_m \cosh(i\tilde{k}_0 d_1)\cosh(ik_m d_2)/\sigma_2$,

$R_1 = \tilde{k}_0 \cosh(i\tilde{k}_0 d_1)\cosh(ik_0 d_2)/\sigma_1 + k_0 \sinh(i\tilde{k}_0 d_1)\sinh(ik_0 d_2)/\sigma_2$,

$R_2 = \tilde{k}_0 \sinh(i\tilde{k}_0 d_1)\cosh(ik_m d_2)/\sigma_1 + k_m \cosh(i\tilde{k}_0 d_1)\sinh(ik_m d_2)/\sigma_2$,

$R_3 = \tilde{k}_0 \sinh(i\tilde{k}_0 d_1)\cosh(ik_0 d_2)/\sigma_1 + k_0 \cosh(i\tilde{k}_0 d_1)\sinh(ik_0 d_2)/\sigma_2$,

$R_4 = \tilde{k}_0 \cosh(i\tilde{k}_0 d_1)\cosh(ik_m d_2)/\sigma_1 + k_m \sinh(i\tilde{k}_0 d_1)\sinh(ik_m d_2)/\sigma_2$.

If d_1 tends to be zero, Eqs. (11) reduce to that obtained in Ref. 12 for a bilayer magnetic film having a similar magnetic configuration.

For multilayers with a total thickness smaller than a few microns, the approximation of a weak skin effect is reasonable, up to the gigahertz range. In this case the following asymptotic formulas have been obtained in Refs. 13,14:

$$\varsigma_{zz} = \varsigma_0\left[1 - \frac{k_0^2 d_1 d_2(\sigma_1^2 d_1^2)}{3(\sigma_1 d_1+\sigma_2 d_2)\sigma_2 d_2} - \frac{k_0^2 d_2^2(\sin^2\theta + \tilde{\mu}\cos^2\theta)}{3} q_1\right],$$

$$\varsigma_{zy} = \varsigma_{yz} = -\varsigma_0 \frac{k_0^2 d_2^2(\tilde{\mu}-1)\sin\theta\cos\theta}{2} q_2, \tag{12}$$

$$\varsigma_{yy} = \varsigma_0[k_0^2 d_1 d_2 - k_0^2 d_2^2(\cos^2\theta + \tilde{\mu}\sin^2\theta)]q_3,$$

$$q_1 = \frac{3d_1^2\sigma_1^2 + 3d_1 d_2\sigma_1\sigma_2 + d_2^2\sigma_2^2}{(\sigma_1 d_1 + \sigma_2 d_2)\sigma_2 d_2}, \quad q_2 = \frac{2d_1\sigma_1 + d_2\sigma_2}{d_2\sigma_2}, \quad q_3 = \frac{d_1\sigma_1 + d_2\sigma_2}{d_2\sigma_2},$$

where $\varsigma_0 = c/4\pi(\sigma_1 d_1 + \sigma_2 d_2)$ is the dc longitudinal impedance of the layered film per unit length, $q_{1,2,3}$ are the normalisation constants. Equations (12) show that the surface impedance $\hat{\varsigma}$ in very thin films is a linear function of the permeability, thus, the dependence of impedance on the magnetic properties has an inductive origin.

The analytical representations (12) give the important conclusions concerning the role of the sandwich structure and certain features of the field dependence $\hat{\varsigma}(H_{ex})$. Firstly, it is important to note that for $d_1\sigma_1 > d_2\sigma_2$ the normalisation coefficients $q_{1,2,3} > 1$ amplify the field sensitivity of $\hat{\varsigma}(H_{ex})/\varsigma_0$ [13-15] in comparison with a bilayer structure,[12] where $d_1 \equiv 0$. Because of this, the inner lead should be chosen as a high-conductivity metal with $\sigma_1 >> \sigma_2$, for example, noble metals Cu, Ag or Au. Secondly, for the transverse anisotropy ($\alpha = 90^0$) the diagonal $\varsigma_{zz,yy}$ and off-diagonal $\varsigma_{zy,yz}$ components have a different symmetry with respect to H_{ex} direction.[12-15, 21,22]

3.3 Calculation of the field dependence of the impedance matrix

Here we are mostly interested in the field behaviour of ς_{zz} and ς_{yz} ($\equiv \varsigma_{zy}$) components. Since the field dependences of the impedance matrix for wires and films are similar in many respects, we will consider only the case of the crossed anisotropy, which recently has been realised in the MI film sample.[16] Asymmetrical field dependences predicted in the theoretical works [12-14] were verified for the first time in Ref. 16 by measurements of the longitudinal impedance $\varsigma_{zz}(H_{ex})$ in the bilayer film with easy axes crossed in the magnetic layers. Experimental results on $\varsigma_{zz}(H_{ex})$ in the NiFe/Au/NiFe sandwich films with the different types of anisotropy (transverse, longitudinal and crossed) will be presented in Section 3.5.

The calculations are made using exact formula (11), although for $d \leq 1\mu$m weak skin effect approximation (12) is applicable in a wide frequency range extending to the GHz range. The following parameters were chosen for calculations: $M_0 = 500$ G, $H_K = 6$ Oe, $\sigma_1 = 10^{18}$ s^{-1}, $\sigma_2 = 4.5 \cdot 10^{16}$ s^{-1}, $2(d_1 + d_2) = 1\,\mu m$, spin-relaxation parameter $\tau = 0.2$, and gyromagnetic constant $\gamma = 2.0 \cdot 10^7$ (rad/s)/Oe. For $2d = 1$ μm and $2d_1 = d_2$ a large impedance change occurs in a MHz frequency range. Figure 3.4 shows the plots of ς_{zz} (a) and ς_{yz} (b) versus H_{ex} with the bias field H_b as a parameter, for a frequency of 50 MHz.

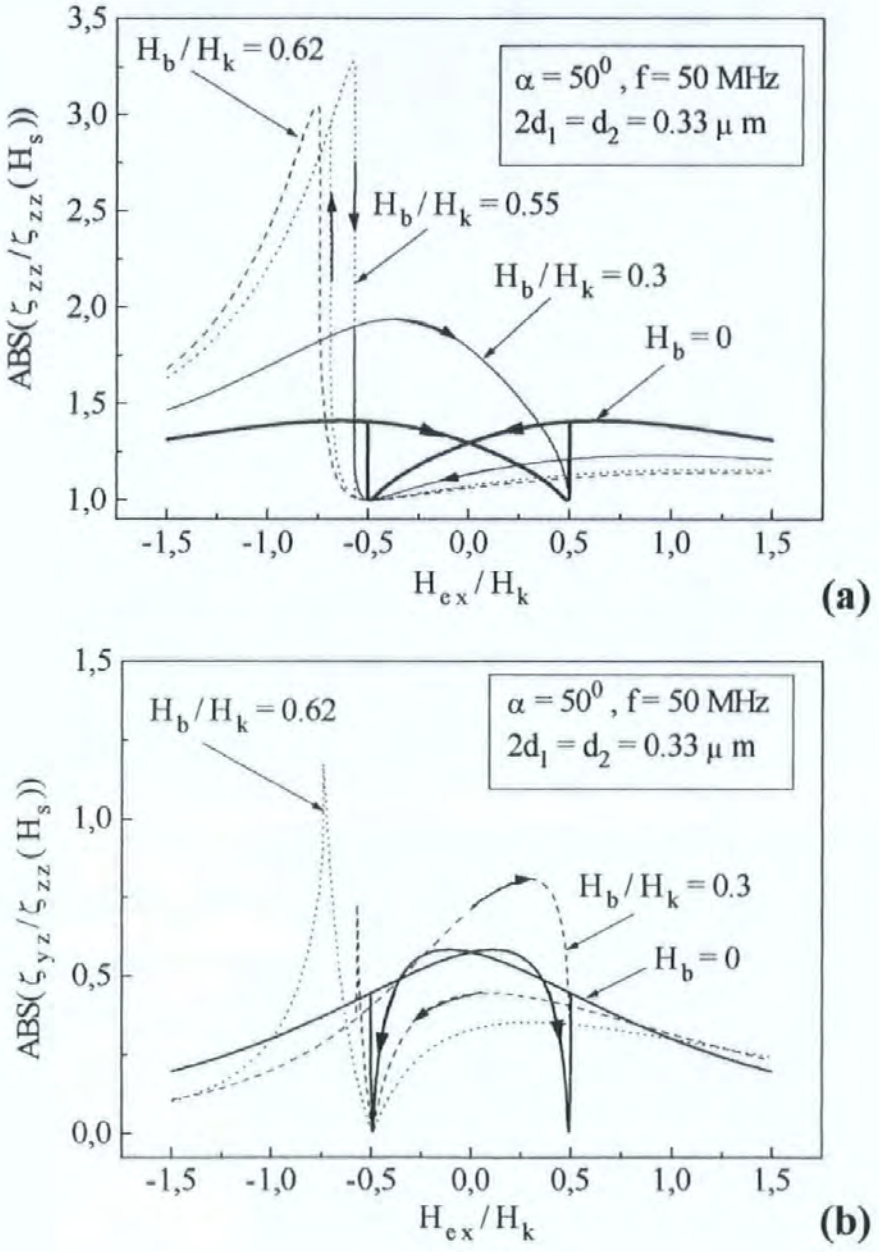

Fig. 3.4 *Diagonal component ς_{zz} in (a) and off-diagonal component ς_{yz} in (b) as a function of H_{ex} for different values of the dc bias H_b.*

The application of H_b results in asymmetry in the MI behaviour. When H_{ex} is decreased from the positive direction, ς_{zz} decreases slowly down to the value of ς_0 while at some negative field it jumps to a large value. The critical field of the impedance jump is associated with the irreversible jump of the dc magnetisation, as seen in Fig. 2.8(b) (see Section 2.6). Initially, the hysteresis area and the impedance jump slightly change with increasing H_b. However, further increase in H_b results in a sudden shift of the hysteresis to negative fields with the simultaneous shrinkage of the hysteresis area. For $H_b > H_K \cos\alpha$ the hysteresis disappears, resulting in asymmetrical highly sensitive MI characteristics. The highest field sensitivity is seen when H_b is only slightly larger than $H_K \cos\alpha$. The field behaviour of ς_{yz} is essentially similar, but can be even more sensitive since it drops down to zero for such H_{ex} that brings $\mathbf{M}_0$ in the $y-$ or $z-$ direction. Similar field behaviours have been obtained in Chapter 2 for a wire with the helical anisotropy.

Summarising, we conclude that the multilayer structures with crossed anisotropy allow various kinds of MI behaviour to be realized including the asymmetrical MI characteristics having a great importance for linear sensing.[3,29-33] The insertion of the inner conductive lead makes it possible to reduce considerably the MI element size without a loss in the field sensitivity.

3.4 Fabrication of the NiFe/Au/NiFe layered films with the different types of anisotropy

In this Section the fabrication technology developed in Ref. 34, 35 for the NiFe/Au/NiFe sandwich films with the different types of anisotropy is described. The substrates used for the magnetron rf deposition of the MI films were 50x50 mm^2 CM5 quality glass microscope slides having a thickness of 0.8 mm. These inexpensive slides are produced by a glass floating process. They have annealing and softening points of 535°C and 720°C respectively. The base pressure attained before sputtering was $2x10^{-7}$ bar, and the Ar gas pressure during the sputtering process was kept at $4.5x10^{-6}$ bar. Each of the NiFe/Au/NiFe sandwich layers were sputtered consecutively to a thickness of 0.5 microns during the same vacuum process, where the deposition rates for NiFe and Au were 2.35 Å/s and 5.75 Å/s respectively. The magnetic-alloy layers were sputtered from an 81wt%-19wt% NiFe target of 15 cm diameter and an rf bias of –80 Volts was applied to the substrate to improve film purity. The total sandwich thickness $h = 2d$ was 1.5 microns.

A substrate holder with an in-plane magnetic field of 60 Oe was used to induce an easy axis direction during film deposition. To induce the transverse anisotropy, the magnetic field was applied in the transverse direction with respect to the stripe length. In this case, all layers (NiFe and Au) can be sputtered at one sputtering cycle, because the field direction was not to be changed. To induce the crossed anisotropy, the magnetic field was applied at crossed directions: at $\pm 45^0$ with respect to the stripe length for the lower and upper magnetic layers, respectively. Therefore, the MI elements were removed from the vacuum chamber after deposition of the non-magnetic layer (Au) to change the field direction for the upper layer.

After deposition the layers were patterned by conventional photolithography methods using an in-contact mask aligner with an ultra-violet exposure source. The photo-masks shown in Figs. 3.5(a) and 3.5(b) gave MI elements with widths b of 200, 100, 50, 20 and 10 microns and lengths l of 5 mm and 2 mm. Each MI element had a 2 mm by 1.5 mm rectangular connection (bonding) pad at each end. Chemical etching was used for both the NiFe and Au layers in the fabrication of the MI structures. Au was used rather than Cu for the conduction layer in the MI structures because it was found to be more reliable and produce much better edge definition when chemically etched. It also provided the correct bonding surface to connect the MI element to its measuring cell using an Au ribbon bounder. The first photo-mask used (Fig. 3.5(a)) produced a positive photo-resist pattern of the complete MI structures with their connection pads on the surface of the sandwich layers. Both the upper NiFe and the Au layers were then chemically etched to this pattern (Fig. 3.6(a)). After etching the upper NiFe layer, the remaining NiFe pattern acted as a mask for etching the Au under-layer. For the final etching process a second photo-mask was required (Fig. 3.5(b)). This mask produced a positive photo-resist pattern that only covered the MI elements. During the final chemical etching process the lower NiFe layer was etched to this shape and the upper NiFe layer on top of the connection pads was removed (Fig. 3.6(b)).

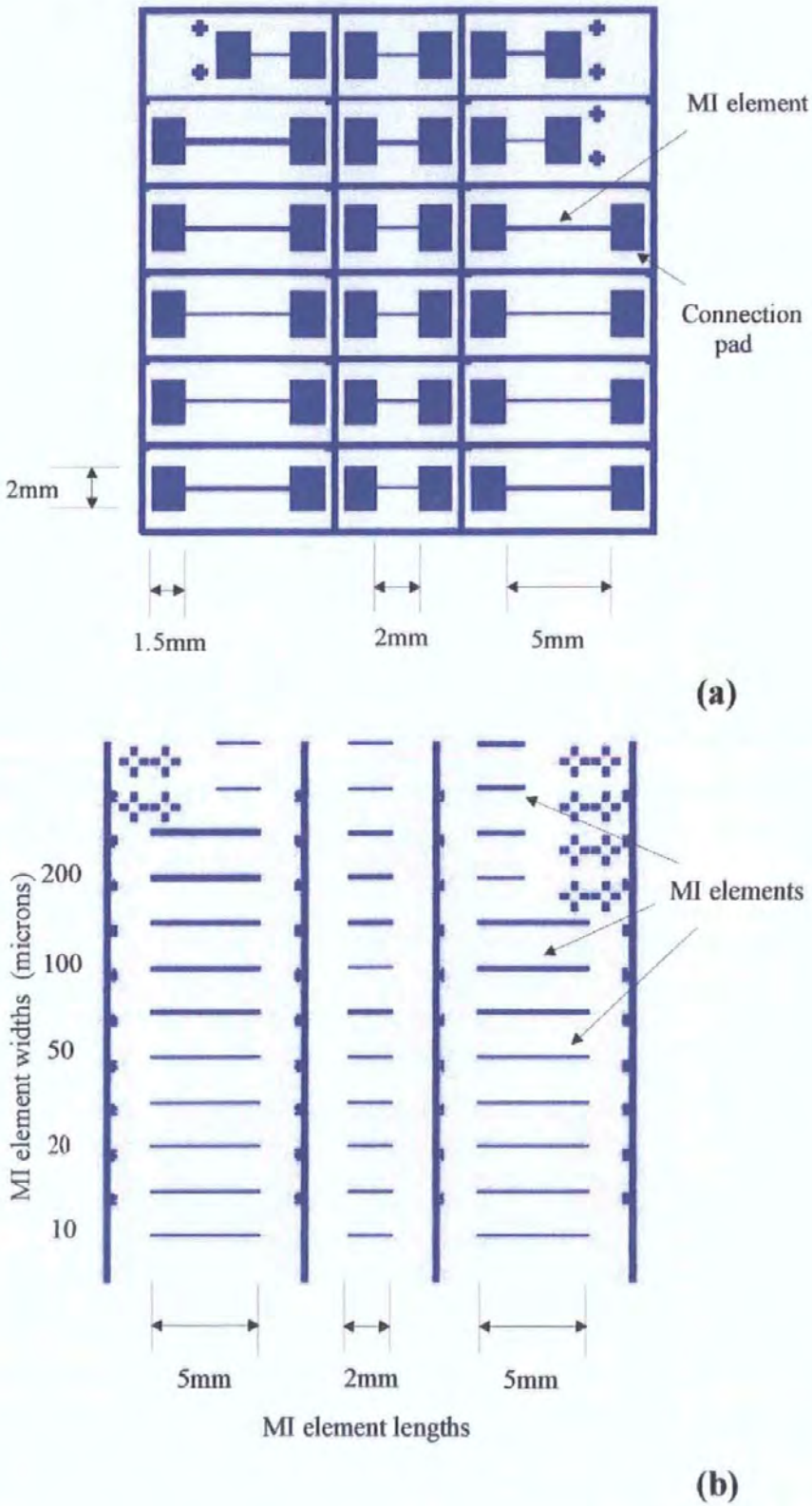

Fig. 3.5 *Photo-masks for the MI elements with different length and width.*

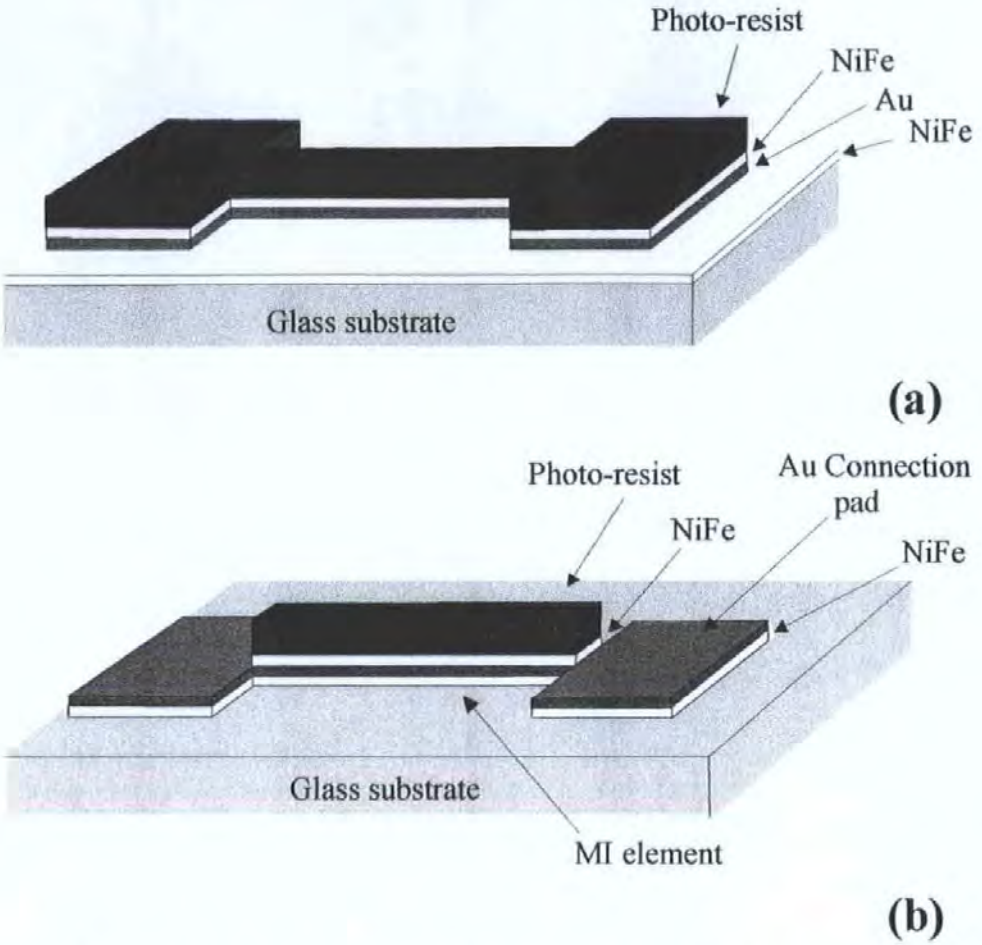

Fig. 3.6 *MI structure after the first etching process in (a) and after the final etching process in (b).*

As chemical etching is isotropic, a certain amount of undercutting (over-etching) and profile roughness was expected after each etching stage. Any undercutting that had occurred to the upper NiFe layer during the first etch process was masked against further undercutting during the second photo-lithographic process. Here, the second photo-resist layer covered the undercut edge of the upper layer. On completion of all etching processes of the sandwich structures the undercutting was found to be <2 microns and have an average profile roughness of <1 micron. Although not as accurate as the dry etching processes, chemical etching proved to be fast and generally reliable. With the comparatively large sizes of the MI structures used in this work (MI widths of 20 microns and above), the undercutting and profile roughness were considered to be acceptable.

For the sensor applications the transverse and crossed anisotropies are most preferred, since they demonstrate a largest field sensitivity.[3,21] In addition, the MI elements with the crossed anisotropy own the riches of field dependences modified by the dc bias field.[14,21] The type of anisotropy for the as-prepared sandwich films with 200 microns width was unambiguously defined by the field direction within which the sputtering was carried out: transverse, longitudinal or crossed. However, measurements of the longitudinal impedance of the as-prepared samples with the widths less than 200 microns (10-100) shown that the anisotropy is directed along its length in spite of the fact that sputtering was carried out in a strong transverse or crossed magnetic field (60 Oe). This effect is most probably associated with the resulting mutual stress between substrate and film layers during the sputtering process. After thermal treatment of the finished samples, the transverse or crossed anisotropies were established in the same directions as the strong magnetic field (60 Oe) within which the sputtering was carried out. For the re-stress of the final samples only thermal treatment was enough to get back the original anisotropy without any magnetic field during this process. Nevertheless, to decrease the dispersion of the transverse anisotropy direction the samples should be annealed in a strong transverse magnetic field (100 Oe). For obtaining a better result in the case of the crossed anisotropy the rotating magnetic field (100 Oe) can be applied to the MI samples during thermal treatment.

The annealing system has a small vacuum chamber within which the sample wafer or individual sample can be fixed securely. The chamber was evacuated down to a base pressure of 50 mTorr. The vacuum chamber is placed in an in-plane magnetic field (fixed or rotating) with a field strength of 100 Oe at its centre. The chamber would take approximately 2 hours to reach an annealing temperature of 450°C and a similar time to cool back down to room temperature. The annealing and softening points of the microscope slide glass substrates used, were 535°C and 720°C respectively. Once the heating was removed the vacuum was kept until the chamber had cooled down to room temperature. After annealing, the wafer was diced manually using a diamond scriber into individual samples. A sample was then glued in position onto a rf cell. Here, the connection pads of the sample were bounded to the cell using a gold ribbon bounder having ribbon dimensions of 200 microns by 25 microns.

3.5 Measurements of the field dependences of the longitudinal impedance

For measurement of the longitudinal impedance the single channel regime of the HP Vector Network Analyser can be used, as shown in Fig. 3.7.[35] For this regime the impedance of the sample (more generally, the rf cell including the sample) is calculated by means of the reflection coefficient S_{11} from the following equation:

$$Z = Z_0 \frac{1+S_{11}}{1-S_{11}}, \tag{13}$$

where $Z_0 = 50\Omega$ is the characteristic impedance.

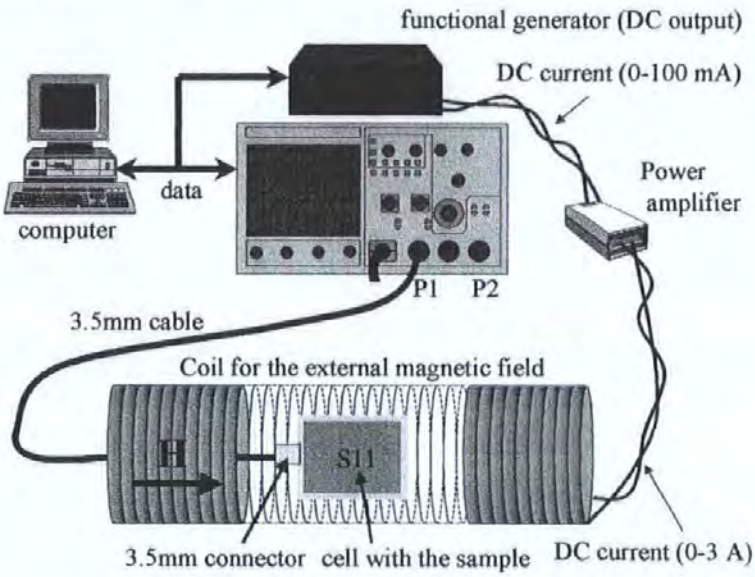

Fig. 3.7 *General view of the measuring system using the single channel regime.*

In comparison with the two channel regime (considered in Section 2.7.1), which is suitable for the measurement of all components of the impedance matrix, the single channel regime suits only for the longitudinal impedance. As a result, the electrical scheme of the rf cell can be simplified, as shown in Fig. 3.8. Blocking capacitor (C) prevents the dc bias current I_b from entering the Analyser. In the high frequency range a contribution to the total cell impedance from the capacitor is less than that from the MI impedance: $|1/\omega C| < |Z|$. Nevertheless, the field-independent addition from the capacitor may result in some decrease of the field sensitivity of the cell impedance and shifting its value. Furthermore, there are other uncontrollable field-independent contributions from the microwave tract and connections. To decrease these effects, all connections have to be shorter and rf matching would be useful as well.

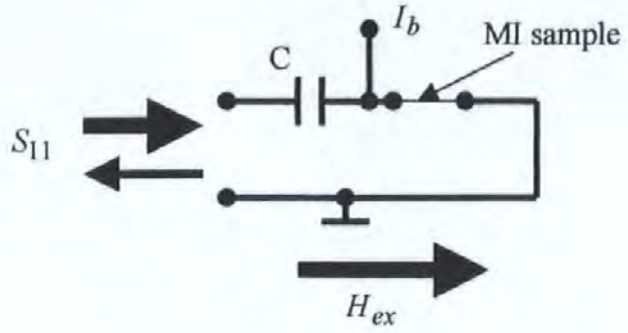

Fig. 3.8 *Electrical scheme of the rf cell for measurement of the longitudinal impedance in the single channel regime.*

Figures 3.9 and 3.10 show the field dependences of the longitudinal impedance ς_{zz} measured in the sandwich film before and after the thermal treatment respectively, when the films were sputtered in the presence of the transverse field (60 Oe).[34,35] The field curves shown in Fig. 3.9 correspond to the longitudinal anisotropy,[17,34,35] whereas a typical impedance field dependence for the transverse anisotropy [4-8, 17] is shown in Fig. 3.10.

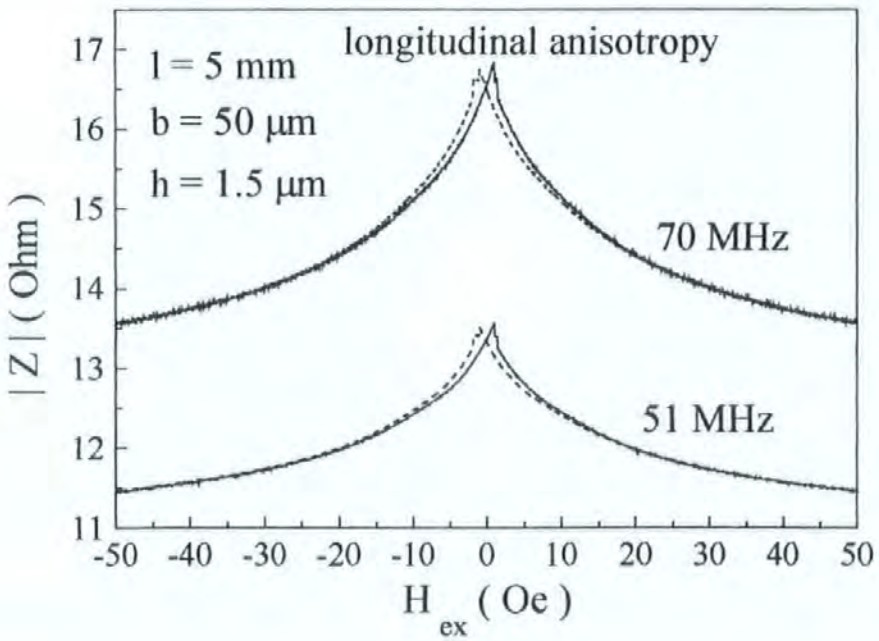

Fig. 3.9 *Field dependence of the longitudinal impedance measured in the sandwich film with the longitudinal anisotropy existing before thermal treatment. The film was sputtered in the presence of the transverse magnetic field. Dashed curves show the reversed field behaviour.*

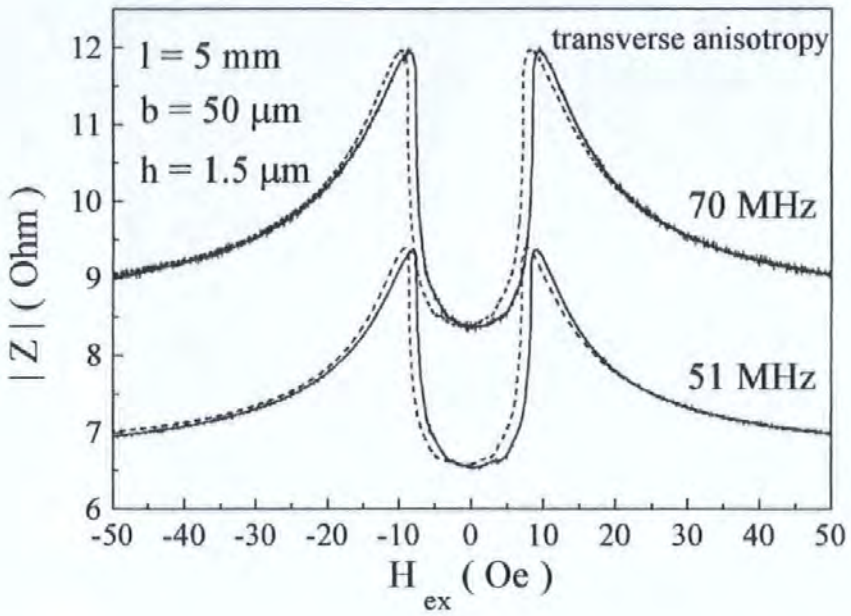

Fig. 3.10 *Field dependence of the longitudinal impedance measured in the sandwich film with the transverse anisotropy existing after thermal treatment. The film was sputtered in the presence of the transverse magnetic field. Dashed curves show the reversed field behaviour.*

The experimental curve in Fig. 3.10 can be reasonably well fitted by the theoretical one shown in Fig. 3.11. The field dependences of the impedance for the transverse (in film) and circumferential (in wire) anisotropies are usually very well described by a simple rotation model, which has been successfully used for wires in Chapter 2. Customary as a rule the effect of longitudinal anisotropy is fallen out of an attention because the overwhelming majority of the MI sensors are designed for the elements with the transverse (circumferential) anisotropy, which have more sensitive field dependences However, the longitudinal anisotropy could be useful for sensing larger fields. Below we will address this question.

As seen in Fig. 3.9, the maxima of the field dependences $Z(H_{ex})$ in the as-prepared films with longitudinal anisotropy have barely perceptible jumps in the vicinity of zero field ($\sim \pm 1$ Oe) and then the curves slowly fall down to the saturation values. Figure 3.12 shows the theoretical field dependence $Z(H_{ex})$ for the longitudinal anisotropy, where the angle α was chosen with a small dispersion about 1^0 around the longitudinal direction ($\alpha = 0$), and the anisotropy field $H_K = 1$ Oe. The theoretical curve qualitatively describes all mentioned features including small jumps and subsequent slow decay.

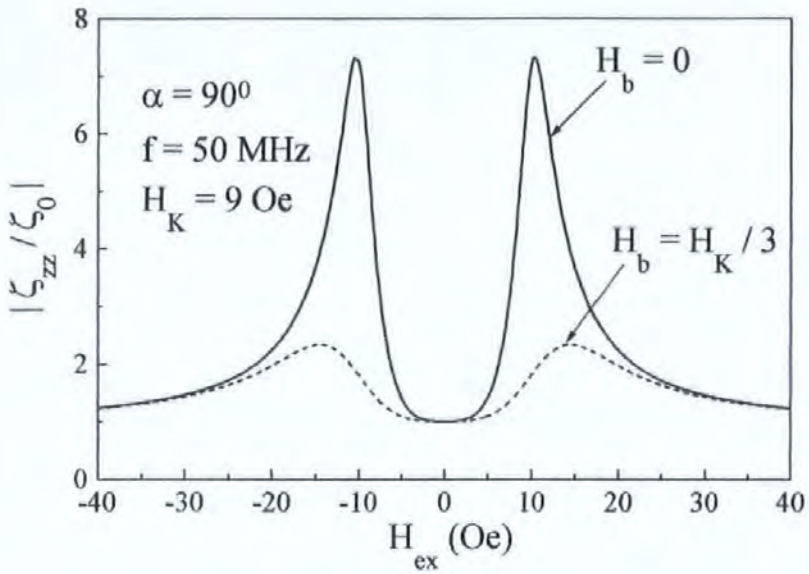

Fig. 3.11 *Typical field dependence of the longitudinal impedance calculated from Eqs. (11) in the sandwich film with the transverse anisotropy. The following parameters were used:* $M_0 = 500\ G$, $H_K = 9$ Oe, $\sigma_1 = 10^{18}\ s^{-1}$, $\sigma_2 = 4.5 \cdot 10^{16}\ s^{-1}$, $2(d_1 + d_2) = 1.5\,\mu m$, *spin-relaxation parameter* $\tau = 0.2$, *and gyromagnetic constant* $\gamma = 2.0 \cdot 10^7$ *(rad/s)/Oe.*

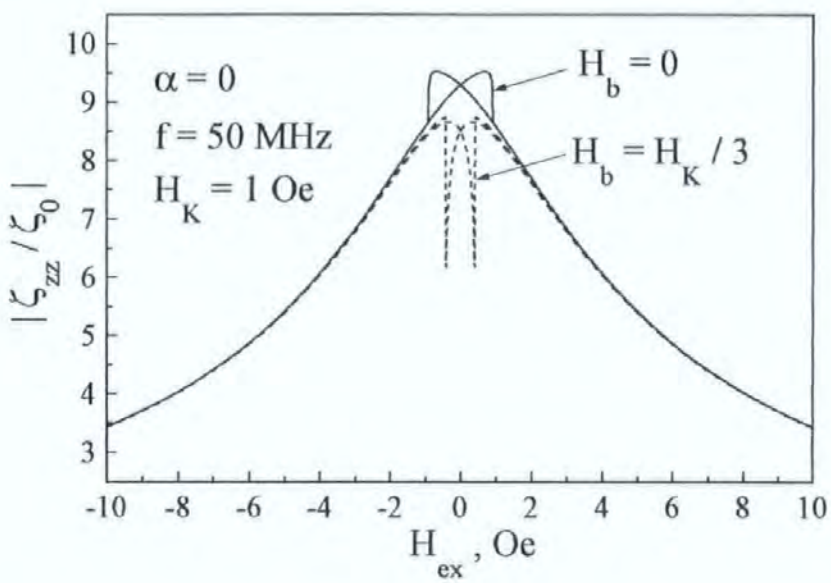

Fig. 3.12 *Typical field dependence of the longitudinal impedance calculated from Eqs. (11) in the sandwich film with the longitudinal anisotropy and small anisotropy field* H_K. *The material parameters were chosen as those in* ***Fig. 3.11.***

The magnetisation rotation in the sample plane does not result in large demagnetising fields. Thereby, the rotation is an energy-favourable process and hence it can be in charge of the small jumps seen in Fig. 3.9. On the contrary, the jumps in a wire with the longitudinal anisotropy should be attributed to the domain wall jumps because the magnetisation rotation is not energy-optimal due to the large demagnetising fields. To comply with the experimental field dependences in Fig. 3.9 the anisotropy field H_K in the calculated curves in Fig. 3.12 has to be chosen much smaller than that for the sample with a transverse anisotropy in Fig. 3.10. We used the experimental value of ~1 Oe, at which the jumps are observed. In this case, the rotation model describes well all features of the experimental curve in Fig. 3.10. Thus, we have to conclude that the thermal treatment produces a significant increase of the anisotropy field along with establishing a transverse anisotropy ($H_K \sim 9$ Oe) from a longitudinal one in as-cast state ($H_K \sim 1$ Oe).

Another interesting effect for the longitudinal anisotropy relates to the bias field H_b. In the presence of $H_b \neq 0$ the curve becomes similar to that for the crossed anisotropy with $H_b = 0$, as shown, for example, in Figs. 2.12 and 3.4. In other words, the bias field does not change the symmetry of hysteretic curve. The fact is that $\pm H_b$ (the sign differs for the lower and upper layers) deflects the equilibrium magnetisation $\mathbf{M}_0$ from the longitudinal direction, therefore the sample becomes effectively cross-magnetised – the artificial cross anisotropy. This effect is especially pronounced in samples with a small anisotropy field (see Fig. 3.12). On the contrary, for a higher H_K, the bias field H_b just constricts the hysteresis area, as shown in Fig. 3.13, where the large jumps take place. For any H_K the jumps occur at $\sim \pm H_K$ and their values strongly depend on H_K.

As it has been proven in Chapter 2, the following three main factors determine the field sensitivity of the MI effect: (i) value of the ac effective permeability $\tilde{\mu}$, (ii) skin-depth, and (iii) rf matching between the rf cell and microwave tract. As long as $\tilde{\mu}$ remains quite large and the field-independent additions in the total impedance from the rf circuit do not prevail over $Z(H_{ex})$, the field sensitivity of $Z(H_{ex})$ increases with the frequency due to stronger skin effect, as shown in Figs. 3.9 and 3.10.

A shifting in the impedance value for a higher frequency (70 MHz in Figs. 3.9 and 3.10) is related with the field-independent additions, which also increase with the frequency and, consequently, are of the inductive character. Therefore, at sufficiently large frequency the field sensitivity of the measured MI effect may reduce in spite of the fact that the MI field sensitivity of the "pure impedance" $Z(H_{ex})$ is still high. This process is clearly seen in Figs. 3.14 and 3.15 for the longitudinal and transverse anisotropies, respectively. Moreover, a widening of the field curves takes place in this frequency range. Thus, the rf matching will be strongly required for an actual device to avoid these effects.

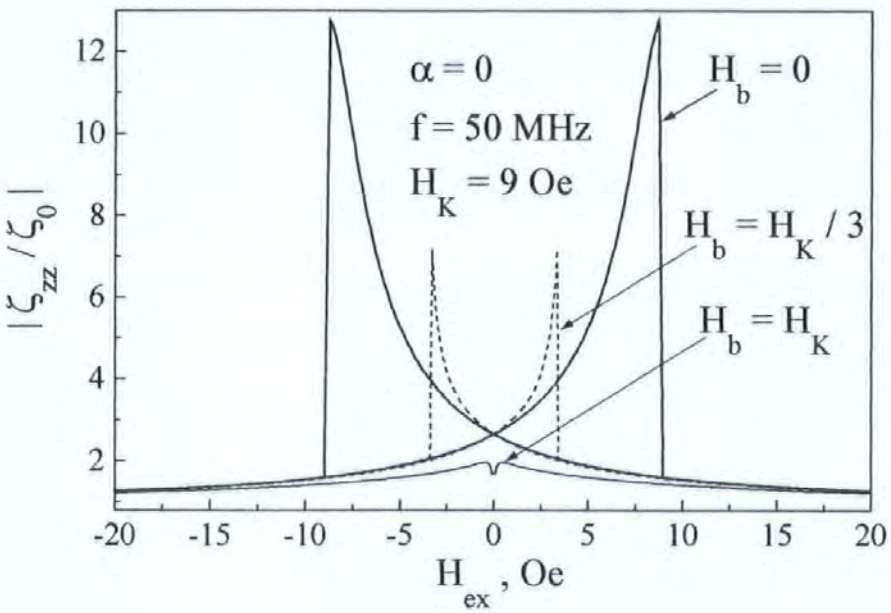

Fig. 3.13 *Typical field dependence of the longitudinal impedance calculated from Eqs. (11) in the sandwich film with the longitudinal anisotropy and large anisotropy field* H_K. *The material parameters were chosen as in* ***Fig. 3.11.***

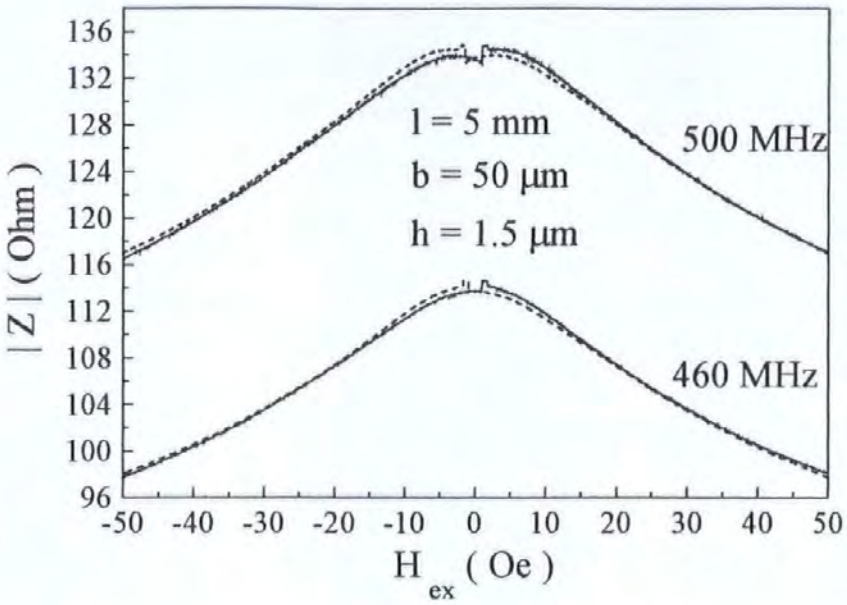

Fig. 3.14 *Field dependences of the longitudinal impedance measured in the high frequency range in the sandwich film with the longitudinal anisotropy (before thermal treatment). The film was sputtered in the presence of the transverse magnetic field.*

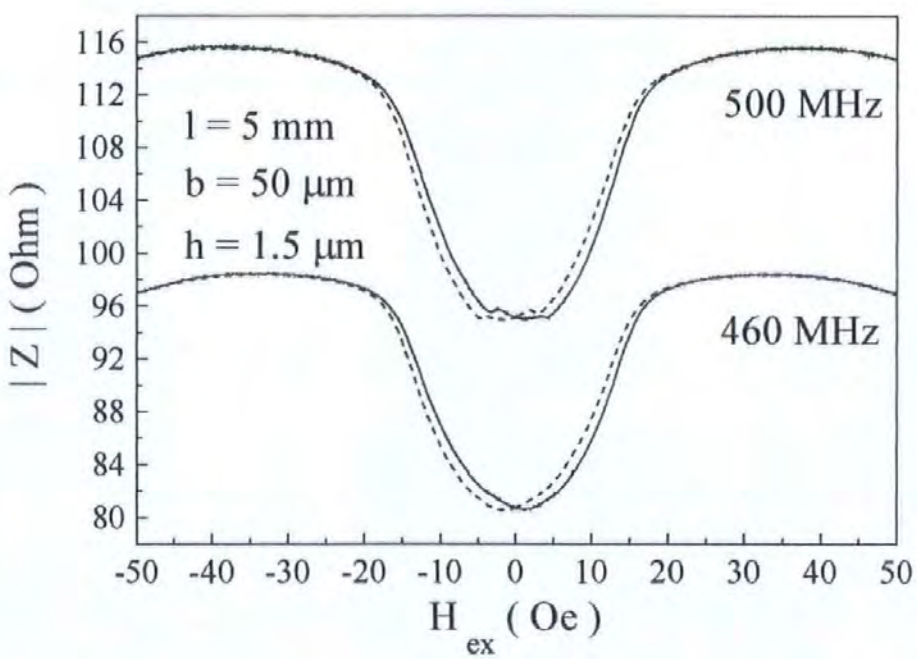

Fig. 3.15 *Field dependences of the longitudinal impedance measured at high frequency range in the sandwich film with the transverse anisotropy (after thermal treatment). The film was sputtered in the presence of the transverse magnetic field.*

Since the field-independent additions are mostly of imaginary character (inductive) and the effective permeability $\tilde{\mu}$ remains still large for frequencies up to several hundred megahertz, the real part of $Z(H_{ex})$ should demonstrate a larger field sensitivity than the imaginary one. The field dependences of the real and imaginary parts for two anisotropies are shown in Figs. 3.16 and 3.17. The "valve-like" behaviour of $|Z(H_{ex})|$ in Fig. 3.15, when it has two predetermined levels at $H_{ex}=0$ and $H_{ex}>H_K$, is caused by the mutually inverse field dependences of the real and imaginary parts, while $H_{ex}>H_K$: $\mathrm{Re}(Z(H_{ex}))$ decreases, whereas $\mathrm{Im}(Z(H_{ex}))$ increases. This effect has been observed in wires [36] and is typical for sufficiently high frequency range. In the GHz range we predict the constant dependences for both real and imaginary parts: $Z(H_{ex})\approx const$, while $H_{ex}>H_K$. As it has been explained in Section 2.6, such kind of behaviour is caused by that the effective permeability $\tilde{\mu}$ loses its field sensitivity, as shown in Fig. 2.9(c) (Section 2.6). In this case, the field dependence $Z(H_{ex})$ is entirely related with that for the static magnetisation orientation θ: $Z(H_{ex})\sim\cos^2\theta$ that results in the "valve-like" curve for the samples with the transverse or circumferential anisotropy, as it follows from Fig. 2.8(a). Figure 3.17 demonstrates just a beginning of this process because the frequency is not too high. Nevertheless, we can see a flattening of the field curve for $H_{ex}>H_K$, where a full saturation is not reached in comparison with the MHz range (see Figs. 3.10 and 3.11). In Chapter 5 the "valve-like" behaviour of $Z(H_{ex})$ in the GHz range will be used for the tuneable composites containing the short pieces of wires. Also this bistable field dependence can be used as a switch sensor.

The field sensitivity of $Z(H_{ex})$ for the samples with the longitudinal anisotropy usually is much lower than that for the transverse one (in the operating point). However, these samples may be of interest since in the vicinity of zero field they may have larger sensitivity than the samples with the transverse anisotropy. The latter ones often require an additional longitudinal bias field to shift the operating point to the most sensitive part of the field dependence, approximately in the middle point between zero field and H_K (see Figs. 3.10 and 3.11). Thus, if the larger sensitivity is not strongly required, the samples with the longitudinal anisotropy can be successfully used for the sensing without an additional bias field shifting.

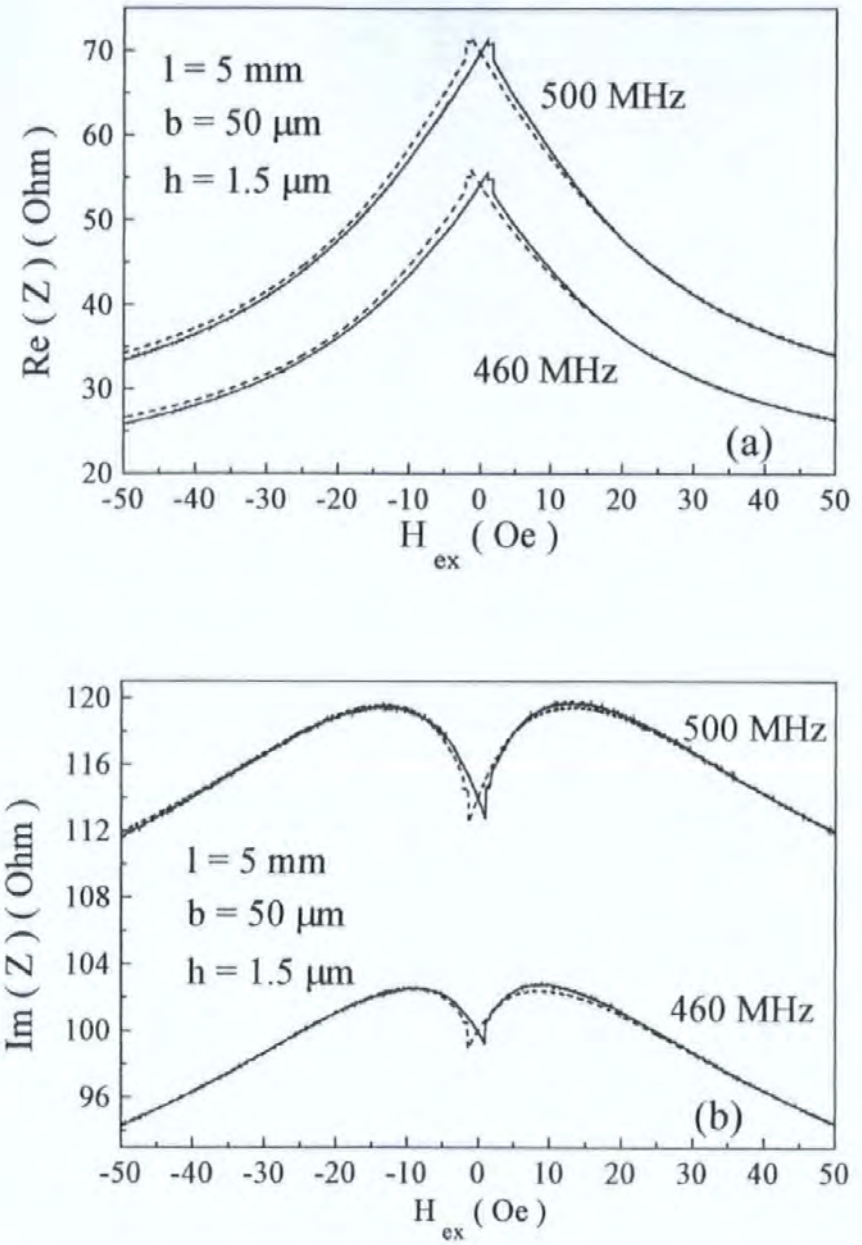

Fig. 3.16 *Field dependences of the real in (a) and imaginary in (b) parts of the longitudinal impedance measured in the high frequency range in the sandwich film with the longitudinal anisotropy (before thermal treatment). The film was sputtered in the presence of the transverse magnetic field.*

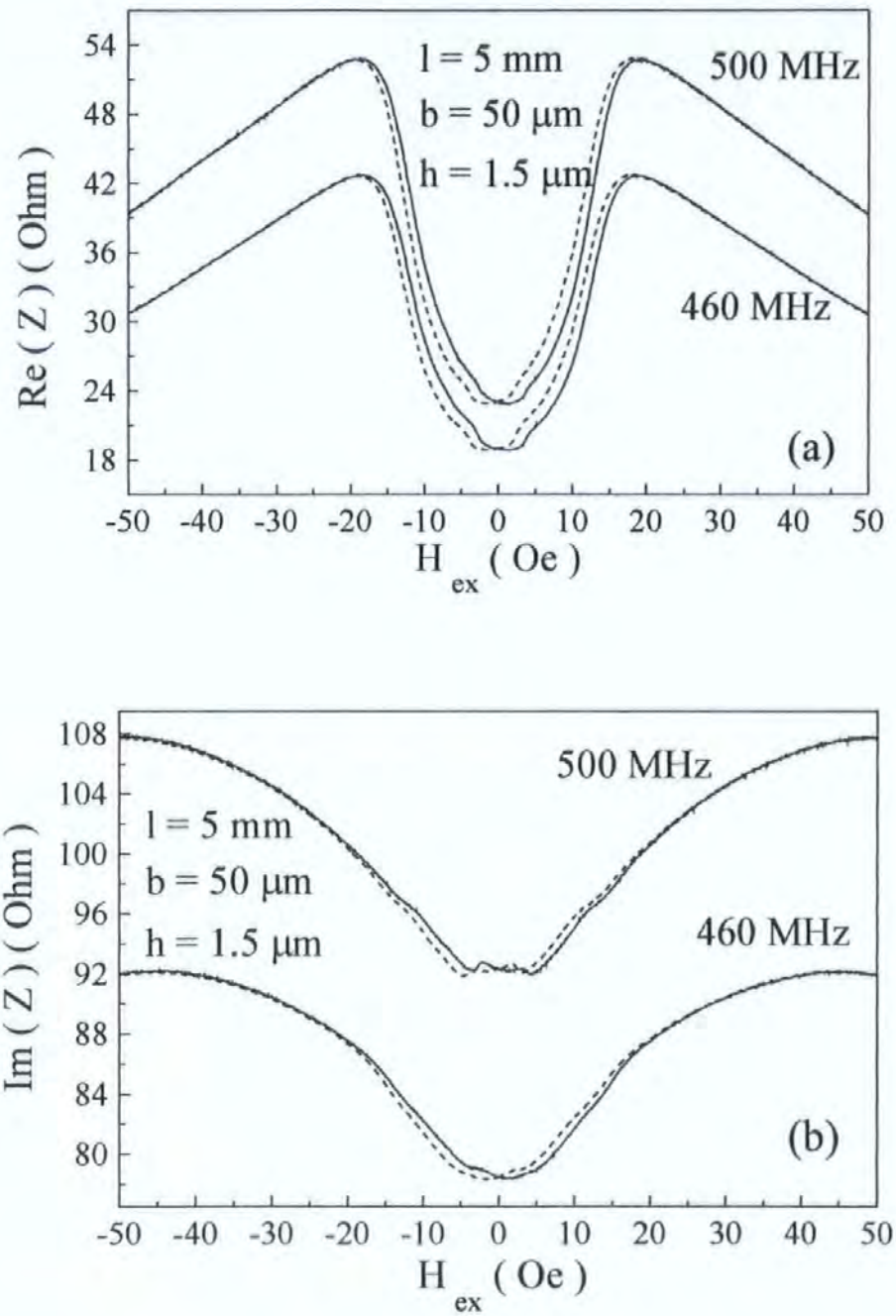

Fig. 3.17 *Field dependences of the real in (a) and imaginary in (b) parts of the longitudinal impedance measured in high frequency range in the sandwich film with the transverse anisotropy (after thermal treatment). The film was sputtered in the presence of the transverse magnetic field.*

Wide samples with 200 microns width do not need any additional thermal treatment to establish the required anisotropy, which coincides with the field direction applied during the sputtering. The field dependences of the impedance in wide samples with the transverse and longitudinal anisotropies are shown in Figs. 3.18 and 3.19. The samples with the transverse anisotropy demonstrate much higher field sensitivity than narrow ones because the anisotropy field is significantly reduced being about ~ 3 Oe. The field dependences for the longitudinal anisotropy do not show visible jumps in the vicinity of zero field that may be related with a larger dispersion of the anisotropy direction in wide samples. Also it is interesting to note that the theoretical curve in Fig. 3.11 better describes the narrow samples, where the field curve is smoother near zero field.

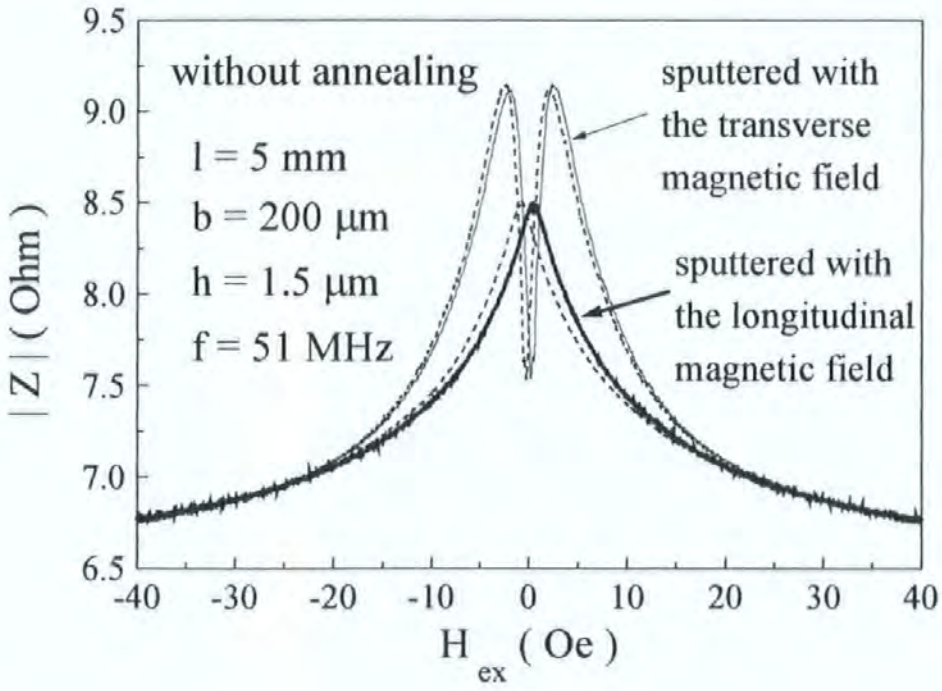

Fig. 3.18 *Field dependence of the longitudinal impedance in the wide sandwich film with the transverse or longitudinal anisotropy.*

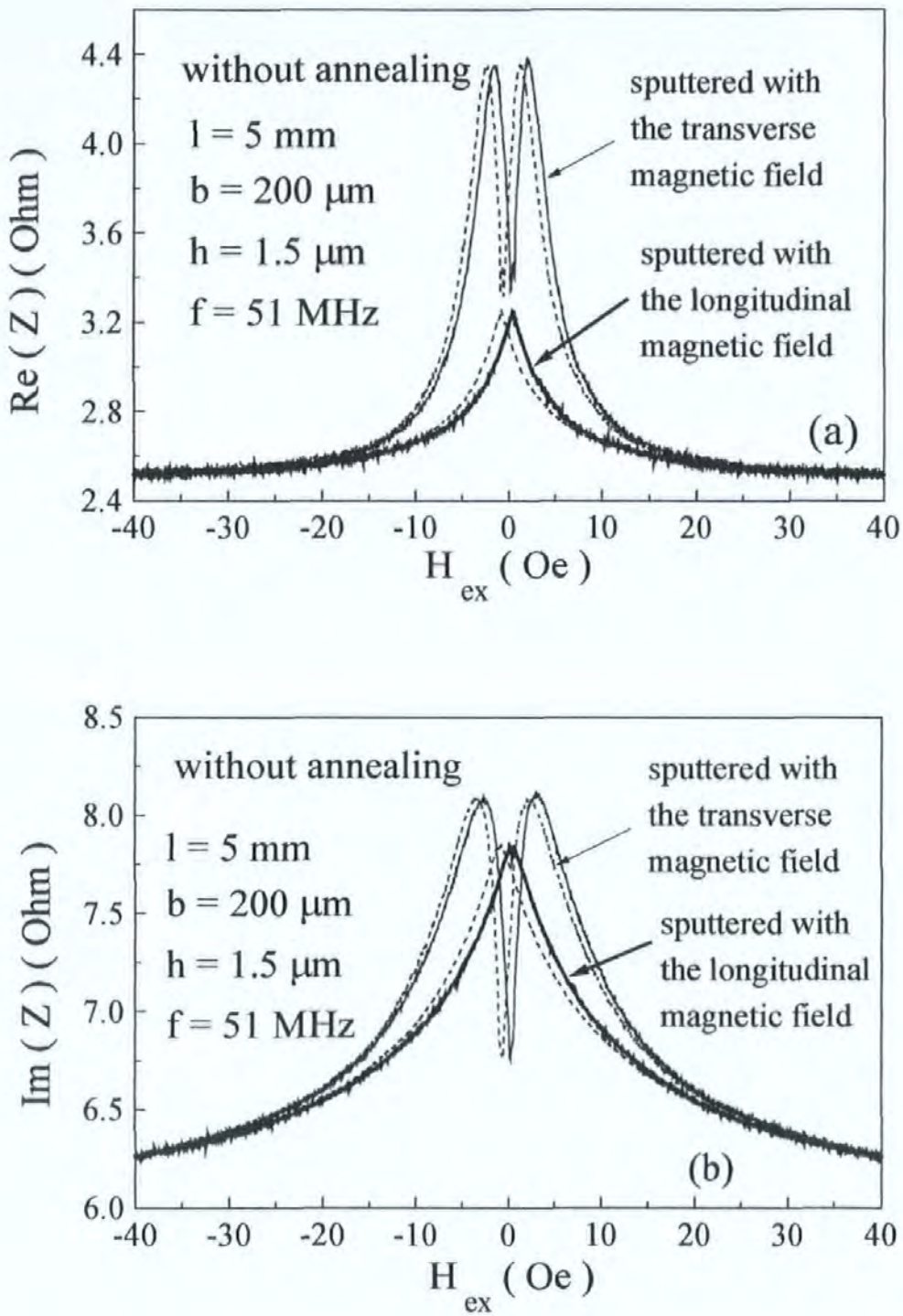

Fig. 3.19 *Field dependences of the real in (a) and imaginary in (b) parts of the longitudinal impedance measured in the wide sandwich film with transverse or longitudinal anisotropy.*

Figure 3.20 shows the asymmetrical impedance $Z(H_{ex})$ in the wide sample with the crossed anisotropy. The real part was chosen as it has a higher field sensitivity than imaginary one. The crossed anisotropy was induced during the sputtering process in the presence of the crossed magnetic field: at $\pm 45^0$ with respect to the stripe length for the lower and upper magnetic layers, respectively. The asymmetrical response obtained in the presence of the bias current I_b is very similar to the asymmetrical impedance which has been measured in the bilayer MI film with crossed anisotropy [16] and wire with the helical anisotropy induced by torsion stress [3] or annealing under torsion stress.[37] The latter has been considered in details in Section 2.7.3.

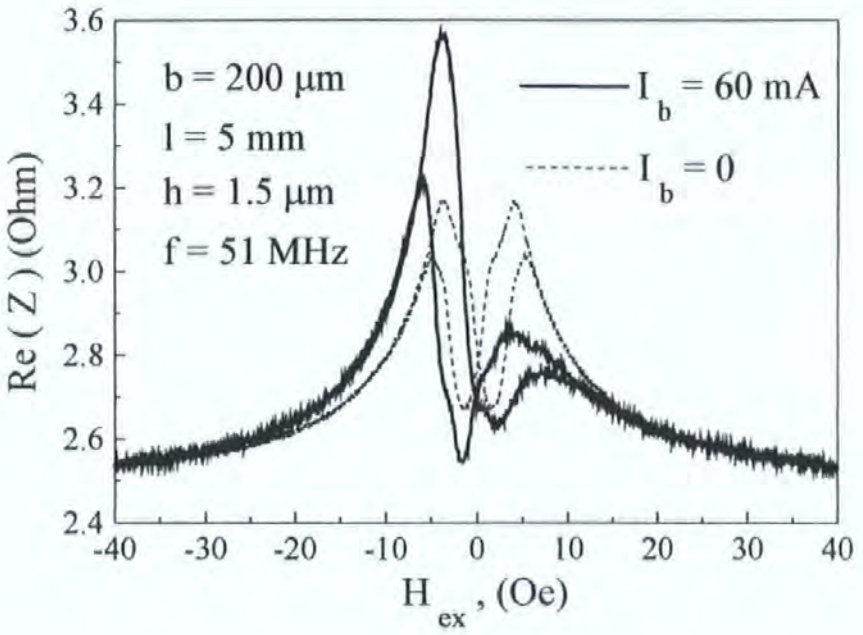

Fig. 3.20 *Asymmetrical longitudinal impedance in the wide sandwich film with the crossed anisotropy.*

All the results obtained above remain for the samples with 2 mm length. Therefore, the actual device dimension can be made quite small to include it into the integrated circuit. This is the main advantage of the thin film MI elements along with higher field sensitivity and simplicity of fabrication. Using dry etching it is possible to significantly decrease the sample width, avoiding the under-cutting problems related with the chemical etching. At the moment the technology developed by us guarantees quite good properties for the samples with a width higher than 20 microns.

Also, there is another effect, which causes the size restriction. The decrease of width up to a few microns may result to the so-called magnetic flux leakage through the inner lead, which eventually reduces the MI field sensitivity. This effect seriously cuts down the use of the MI effect in the devices with dimensions of the order of few microns.[23,24]

3.6 Fabrication of the NiFe/Au/NiFe layered film and helical microcoil

In this Section we describe the fabrication technology developed in Ref. 35 for a narrow NiFe/Au/NiFe sandwich thin film with an integrated planar helical microcoil. The sample was fabricated to measure the off-diagonal impedances in the high frequency range up to 100 MHz. The MI sandwich film has a transverse anisotropy with respect to the long z-axis. The sample can be excited by two different methods: ac longitudinal current j and ac longitudinal magnetic field h_{ex}, where the latter is induced in the planar helical microcoil. A plating-coil has been used before as a dc negative feed-back coil in a single layer NiFe MI sensor,[38] where the field dependence of the longitudinal impedance $Z(H_{ex})$ was measured. In our case the microcoil structure can be used for either ac excitation or ac measurement. For potential applications, the attractive feature of the off-diagonal impedance is that the field dependence of its real and imaginary parts are antisymmetrical with respect to the H_{ex} direction.

The sample was constructed from a NiFe/Au/NiFe layered film core, with a thin-film microcoil wound helically around it along its length. Both the core and coil layers were deposited by means of rf sputtering. All sputtering conditions were the same as for the sandwich films with the transverse anisotropy, where a strong transverse magnetic field (60 Oe) was applied during the sputtering process. The final sample was annealed in the presence of a strong transverse magnetic field (100 Oe) to establish a transverse anisotropy. Cured photo-resist was used to isolate the lower and upper coil structures from the core layers. The NiFe/Au/NiFe core layer was 2 or 5 mm long, 50 μm wide, and had a total thickness of 1.5 μm. The helical microcoil was constructed from two Au thin-film structures to give 10 or 23 turns (for 2 and 5 mm, respectively) with a 50 μm turn width. The film thicknesses of the lower and upper coil structures were 0.245 μm and 0.7 μm respectively.

Figures 3.21(a) to 3.21(f) show schematic cross-sections of the NiFe/Au/NiFe element and helical coil structures at key stages of fabrication (the layers are viewed along the length of the sample, through the centre of its width).

Standard 0.8 mm thick 50×50 mm^2 glass microscope slides were the preferred substrate. It was found that after the final annealing process, patterned NiFe/Au/NiFe layered films that were deposited directly onto microscope slide substrates, gave better results than those deposited on higher quality (corning 7059 borosilicate) glass substrates.

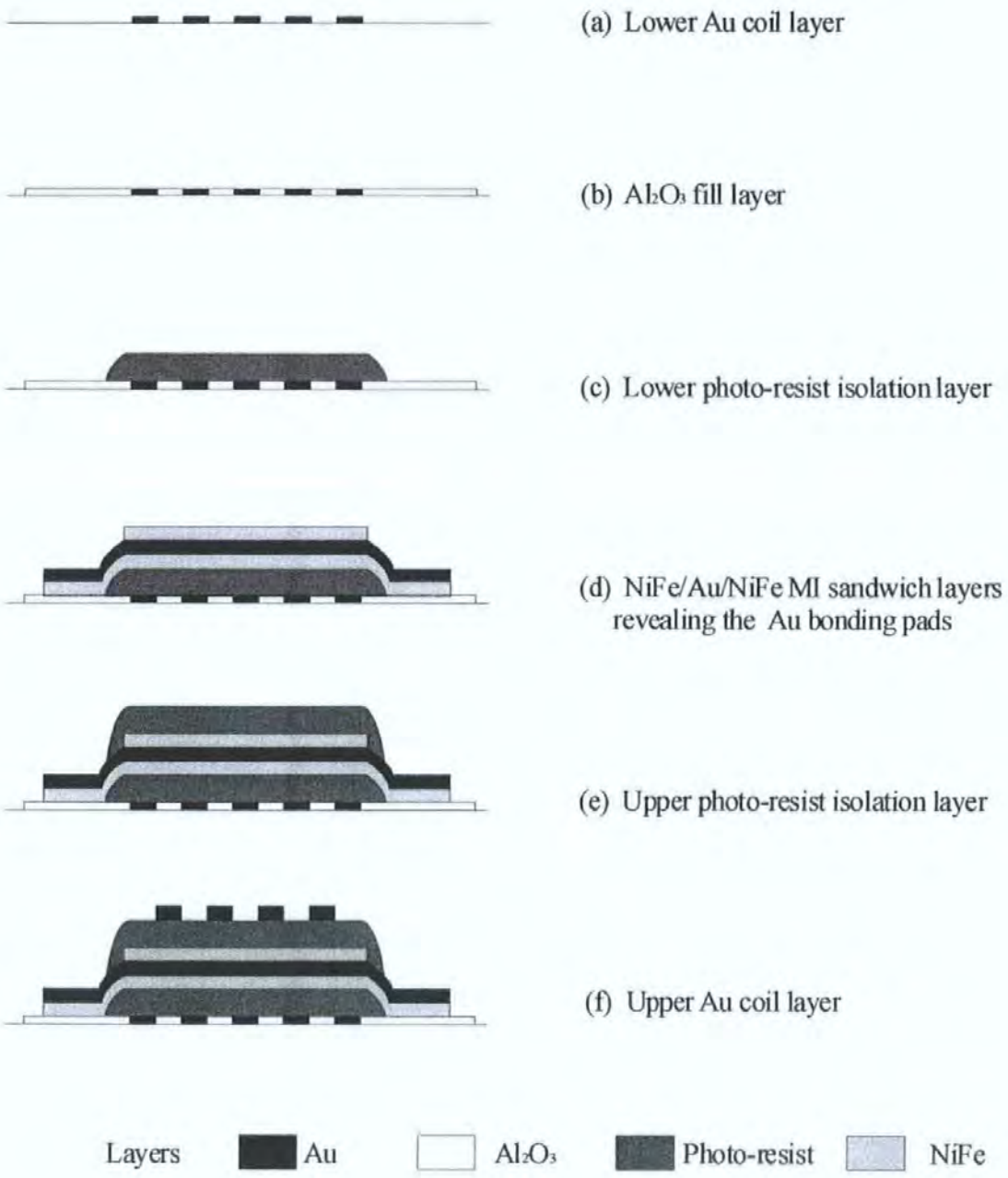

Fig. 3.21 *Schematic cross-sectional views of the NiFe/Au/NiFe element and helical coil structure at key stages of fabrication. The layers are viewed along the length of the sample, through the centre of its width.*

Positive photo-resist was used for every lithographic stage so the photo-mask design was replicated in the photo-resist once patterned. The sequence of photo-masks used for fabricating the layered film and helical microcoil is shown in Figs. 3.22(a) to 3.22(e). Chemical etching was used for fabricating all the metal layer structures of the sample. Au was the preferred conductor layer for the core element and main coil layers of the sample because it proved to be more reliable than Cu during the chemical etching processes, and produced better layer edge definition after etching. Au was also the correct bonding surface for connecting the finished device to the RF measuring cell using the Au ribbon bounder. Both the lower microcoil structure and the NiFe/Au/NiFe core layers produced by the photo-masks in Figs. 3.22(a) and 3.22(c) respectively, have rectangular Au bonding pads at each end.

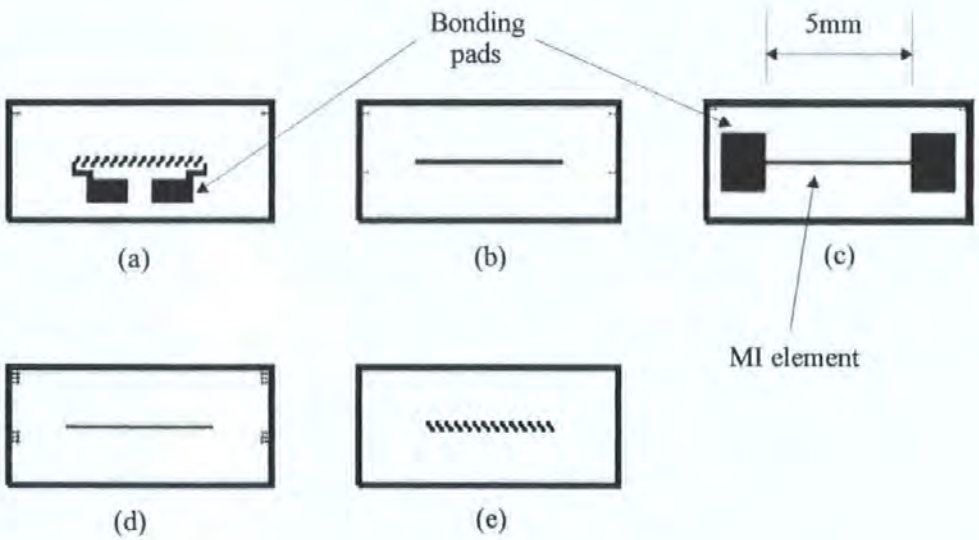

Fig. 3.22 *Sequence of photo-masks used for fabricating a typical 5 mm long MI element with helical microcoil.*

The first photo-mask used in the fabrication process, shown in Fig. 3.22(a) was used to produce the lower microcoil structure (see Fig. 3.21(a)). Here, a 240 nm thick layer of Au with a 5 nm Cr adhesion layer was deposited, patterned and chemically etched to the geometry shown. After etching the Au and Cr, the patterned substrate was placed back into the sputtering chamber where a further 245 nm of Al_2O_3 was deposited. The photo-resist was then removed revealing the lower microcoil pattern with the Al_2O_3 layer filling the gaps between each element of the lower microcoil structure as shown in Fig. 3.21(b).

This Al_2O_3 'lift-off' process helped provide a more planer surface for the first isolation layer. For the next layer, AZ 1813 photo-resist was spun and patterned on the substrate using photo-mask in Fig. 3.22(b). The photo-resist was then hard-baked to form the lower isolation layer. Once hard-baked the AZ 1813 photo-resist shrinks to an approximate thickness of 1 micron and provides a planerising isolation layer over the first microcoil structure (Fig. 3.21(c)). Gentle inclines are formed at the photo-resist edges that enable subsequent sputtered layers to traverse them more readily, maintaining good mechanical and electrical continuity. This was important for both the MI structure and the upper microcoil structure that were constructed above and over the isolation layers.

The NiFe/Au/NiFe sandwich layers were next to be deposited, patterned and etched to form the core. Using photo-mask in Fig. 3.22(c) a positive photo-resist pattern of the MI element (with its connection pads) was produced on the surface of the sandwich layers. Both the upper NiFe and the Au layers were then chemically etched to this pattern. The upper etched NiFe layer behaved as a mask for Au under-layer. To etch the lower NiFe layer of the sandwich film, a second photo-mask was required as shown in Fig. 3.22(d). This mask produced a positive photo-resist pattern that only covered the MI element. Whilst etching the lower NiFe layer to form the MI element core, the upper NiFe layer that had remained on top of the connection pads after the first etching process was removed, revealing the Au bonding pads. The resulting structure is shown in Fig. 3.21(d). As chemical etching is isotropic, a certain amount of undercutting (over-etching) and profile roughness was expected after each etching stage. Any undercutting that had occurred to the upper NiFe layer of the MI element during the first etching process was masked against further undercutting during the second photo-lithographic process. Here, the second patterned photo-resist layer covered the undercut edge of the upper NiFe layer. On completion of all the etching processes of the MI element the undercutting was found to be <2 microns and have an average profile roughness of <1 micron. Although not as accurate as the dry etching processes, chemical etching proved to be fast and generally reliable. With the comparatively large size of the MI element core used in this work the undercutting and profile roughness was considered to be acceptable.

Above the MI element a second isolation layer was required. Here, the photo-mask and processing used was the same as for the lower isolation layer. Other than its bonding pads, the MI element was then completely encapsulated between the upper and lower isolation layers as shown in Fig. 3.21(e). Finally, the upper microcoil layers of Au and Cr were deposited to a thickness of 500 nm and 200 nm respectively.

These layers were then patterned and etched to produce the upper microcoil structure using the photo-mask given in Fig. 3.22(e) to produce the cross-sectional pattern shown in Fig. 3.21(f). The end of each element of the upper microcoil structure connected to those of the lower microcoil structure to form a helical microcoil around the sandwich core. In the case of the lower microcoil layer, its thickness was kept small to maximise the effect of the subsequent isolation and planarising layers. Whereas, for the upper microcoil layer, its thickness was made large enough to ensure that good continuity was achieved at the edges over which each of its elements traversed. For the upper microcoil structure a thick Cr adhesion layer was used to cover and protect the exposed Au of the lower microcoil and MI structures chemically etching the upper microcoil Au layer. The photographs of the finished MI devices with 5 and 2 mm lengths are shown in Fig. 3.23(a) and 3.23(b), respectively. A close-up section of the helical microcoil can be seen in the photograph in Fig. 3.23(c).

3.7 Antisymmetrical field dependence of the off-diagonal impedance

The off-diagonal impedance ς_{zy} (or ς_{yz}) is measured by means of the Hewlett-Packard 8753E Vector Network Analyser configured in the two-ports measuring option for the S_{21}-parameter (forward transmission). The same configuration has been used to measure the off-diagonal impedance in wires (see Section 2.7.1). The electrical scheme of the cells for ς_{zy} and ς_{yz} are shown in Fig. 2.16(c) and Fig. 2.16(d), respectively (see Section 2.7.1).

The field dependences of the off-diagonal impedance have been measured up to frequencies of a 100 MHz, which is the preferred range for practical sensor circuit design. The sample investigated has the following parameters: 5 mm length, 50 μm width, and 1.5 μm total thickness. The helical microcoil has 23 turns with a 50 μm turn width. The sample photograph is shown in Fig. 3.23(a). Since the field behaviour of $\varsigma_{zy}(H_{ex})$ and $\varsigma_{yz}(H_{ex})$ are the same, either excitation scheme, shown in Figs. 2.16(c),(d), can be chosen. Figures 3.24(a),(b) and 3.25(a),(b) show the real and imaginary parts of the field dependences for two frequencies $f = 41$ MHz and $f = 100$ MHz, respectively. Without a bias current the off-diagonal response is very poor and irregular due to the averaging over the stripe domain structure. With $I_b = 30$ mA the off-diagonal response significantly increases showing antisymmetrical behaviour.[15]

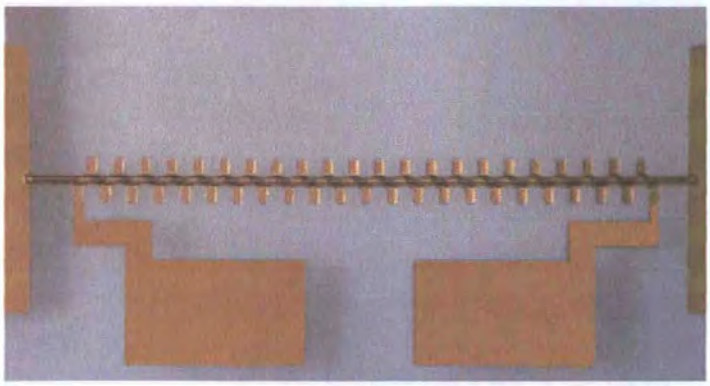

(a)

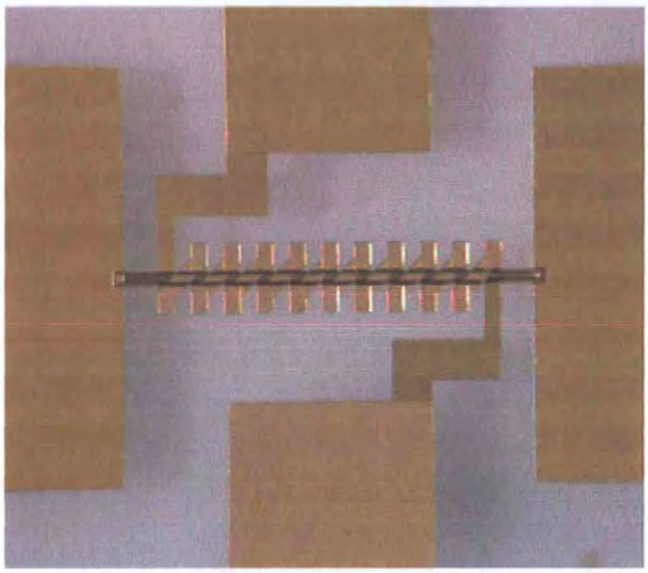

(b)

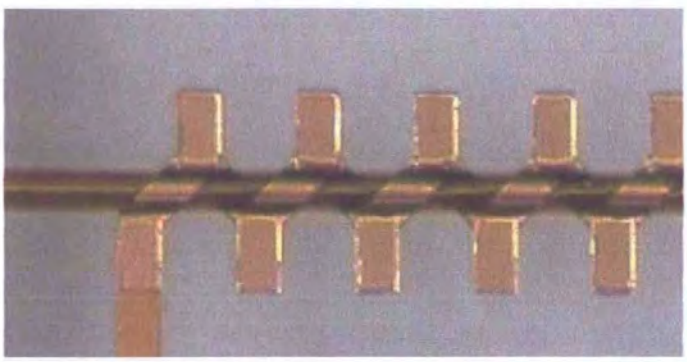

(c)

Fig. 3.23 *Photograph of the sample with the following parameters: 5 mm in (a) and 2 mm in (b) long, 50* μm *width, and 1.5* μm *total thickness. The helical microcoil has 23 turns in (a) and 10 turns in (b) with a 50* μm *turn width. A close-up view of the sample is shown in (c).*

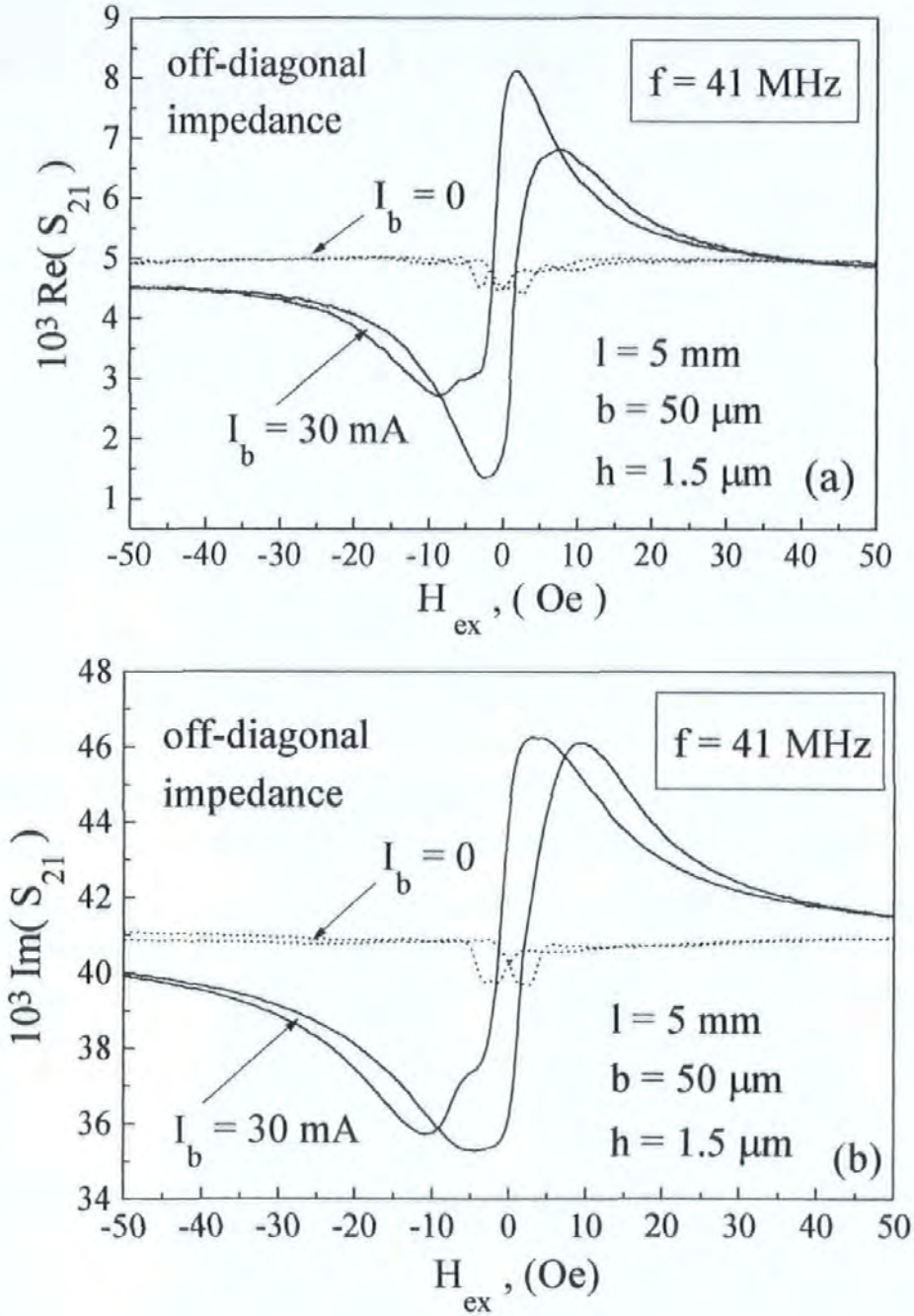

Fig. 3.24 *Real and imaginary parts (hysteresis curves) of the field dependence of the off-diagonal impedance for* $f = 41$ *MHz. Without a bias current* I_b *the off-diagonal response is very poor and irregular due to the averaging over the stripe domain structure. With* $I_b = 30$ *mA the off-diagonal response significantly increases showing antisymmetrical bihaviour, as predicted theoretically.*

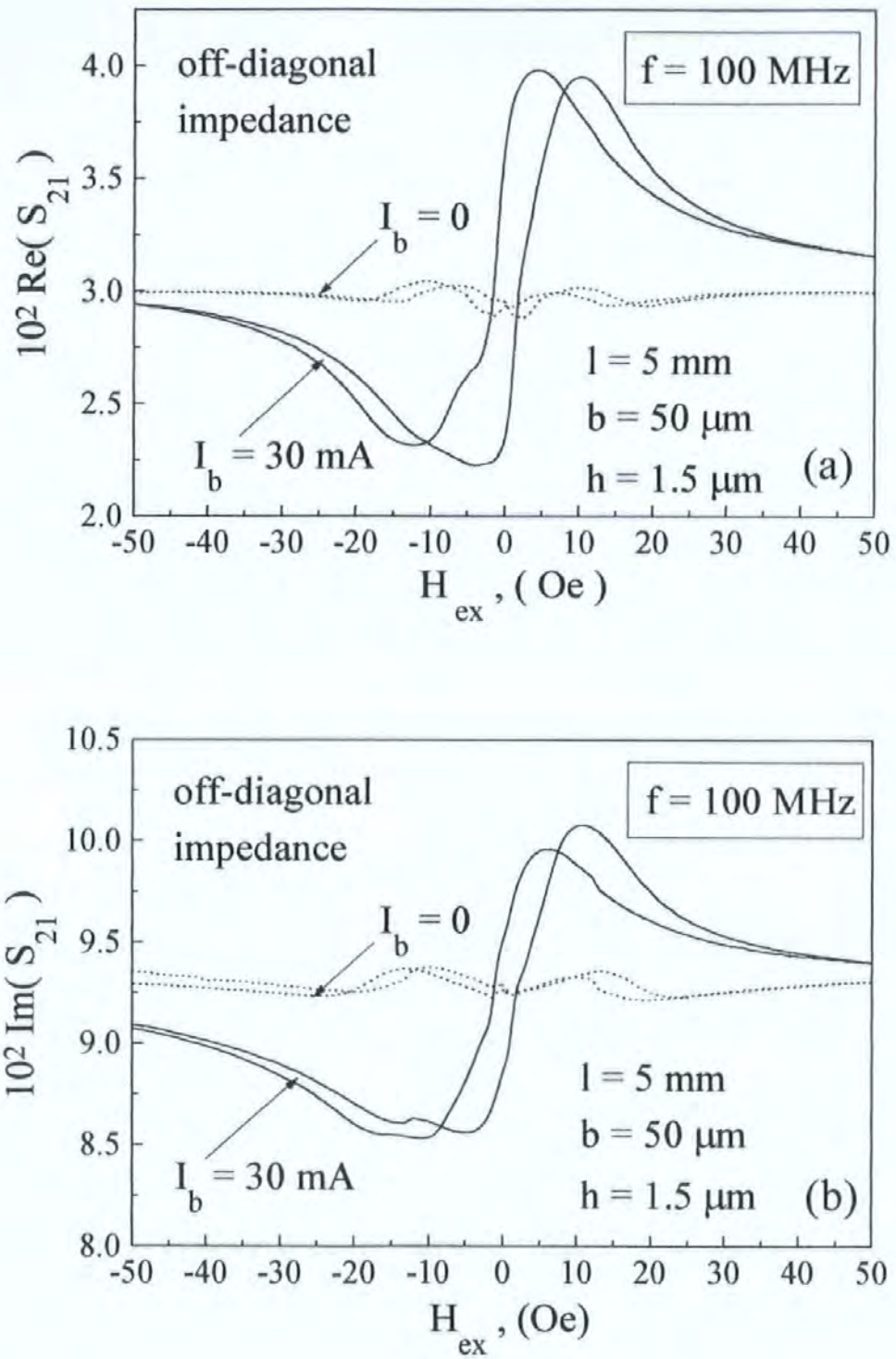

Fig. 3.25 *Real and imaginary parts (hysteresis curves) of the field dependence of the off-diagonal impedance for* $f = 100$ *MHz.*

A similar antisymmetrical response has been investigated experimentally and theoretically in Chapter 2 for a wire with the circumferential anisotropy, which is an analogue of the transverse anisotropy in thin film. Figure 3.26 shows a typical field dependence $\varsigma_{zy}(H_{ex})$ in the megahertz range with H_b as a parameter calculated for the following parameters: $\alpha = 90^0$, $M_0 = 500$ G, $H_K = 9$ Oe, $\sigma_1 = 10^{18}$ s^{-1}, $\sigma_2 = 4.5 \cdot 10^{16}$ s^{-1}, $2(d_1 + d_2) = 1.5\,\mu m$, $\tau = 0.2$, and $\gamma = 2.0 \cdot 10^7$ (rad/s)/Oe. As it follows from Eq. (12), the real and imaginary parts of the diagonal components $\varsigma_{zz} \sim \tilde{\mu}\cos^2\theta$ and $\varsigma_{yy} \sim \tilde{\mu}\sin^2\theta$ are symmetric when H_{ex} changes from negative to positive direction, whereas the off-diagonal components $\varsigma_{zy} \equiv \varsigma_{yz} \sim \tilde{\mu}\sin\theta\cos\theta$ are antisymmetrical (with respect to H_{ex}) following the equilibrium magnetisation $\cos\theta$. The dc bias field H_b does not change the type of impedance-field characteristics in a film with the transverse anisotropy, which is the consequence of equilibrium magnetisation behaviour (see Fig. 2.8(a)). However, in real samples having a domain structure, the off-diagonal impedances are made possible by H_b, which has been proven experimentally for a ferromagnetic wire with a circumferential anisotropy and "bamboo-like" domain structure.[21,22] In a film with the stripe domain structure, as shown in Fig. 3.27, the response from the whole sample is formed by the domain areas with opposite transverse magnetisation. Averaging over the domain structure nulls the off-diagonal impedances: $<\varsigma_{zy}>=<\varsigma_{yz}>=0$, since they are antisymmetric with respect to the equilibrium magnetisation. In reality, the system does not have a perfect stripe domain structure and therefore the averaging does not result to zero, but the off-diagonal response is significantly decreased. (*In contrast to this, the averaging in a sample with a crossed anisotropy (helical in the wire) does not eliminate the off-diagonal response even in the ideal stripe domain structure.*) The situation will change in the presence of a bias field. For $H_b \neq 0$, domains with the same direction of the magnetisation as H_b will grow, resulting in an uncompensated averaging: $<\varsigma_{zy}>=<\varsigma_{yz}>\neq 0$. In addition, at a sufficient value of H_b the sample will become a single domain state. As a result, the effect of H_b increases significantly the off-diagonal response. However, for larger values of H_b the field sensitivity decreases due to the magnetostatic hardness increase, determined by the magnetostatic energy $M_0 H_b \sin\theta$.

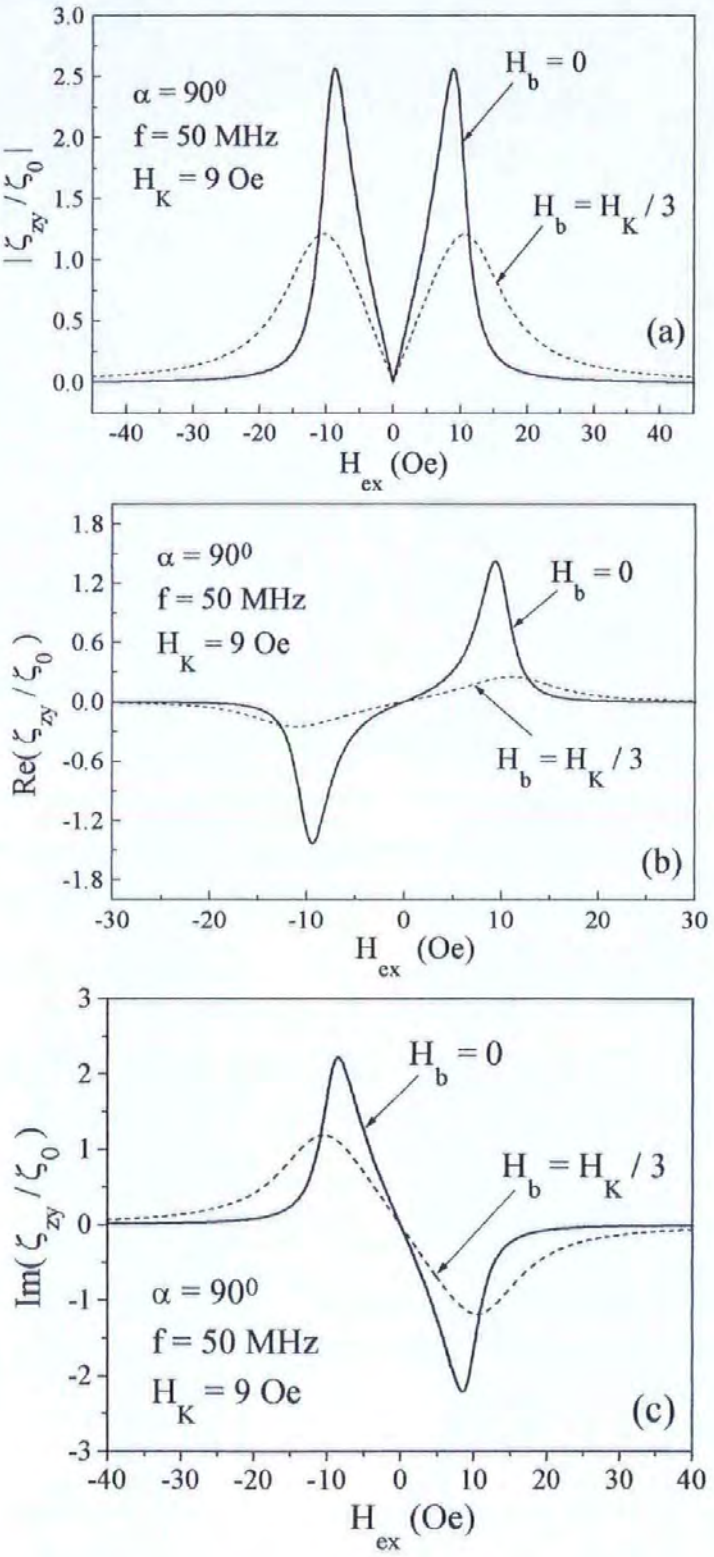

Fig. 3.26 *Typical field dependence of the normalised off-diagonal impedance* ς_{zy} $(\equiv \varsigma_{yz})$ *in the megahertz range for different values of the dc bias* H_b.

The real and imaginary parts of $\varsigma_{zy}(H_{ex})$ *are antisymmetrical with respect of* H_{ex}.

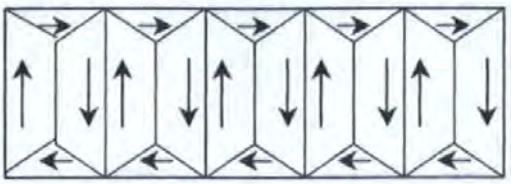

Fig. 3.27 *Stripe domain structure of a film with the transverse anisotropy.*

The measured MI characteristics are qualitatively similar to the theoretical ones, shown in Figs. 3.24 and 3.25, however, they exhibit a hysteresis and are shifted upward to positive values. The existence of hysteresis may be associated with the deviations of anisotropy from the precise transverse direction. The vertical shifting may be caused by additional impedance due to the measuring track and connections inside the cell via an ac interference. This is an unfavourable effect reducing the sensitivity. Changing the sample geometry and making the connections shorter can significantly reduce the shifting effect. For an actual device, this is achieved using an integrated circuit package where the sensor and drive electronics are placed compactly. Employing a differential scheme may also help considerably.

Summarising, we have shown that the real and imaginary parts of the off-diagonal impedances are antisymmetric within H_{ex} changes from negative to positive values. The significance of the dc bias current I_b through the film was also demonstrated. There are two competing processes related to the circulartory bias field H_b induced by the current I_b, which cause increasing or decreasing the field sensitivity of the off-diagonal impedances. Since the bias field H_b makes possible the existence of the off-diagonal response, even a small H_b (but larger than the coercivity) results in an effective increase. However, for larger values of H_b the field sensitivity decreases due to the magnetostatic hardness increase, determined by the magnetostatic energy. The antisymmetrical off-diagonal impedance can be utilised to develop a highly sensitive and linear MI sensors considered in Chapter 4.

3.8 Size effect on magneto impedance in sandwich films

The use of thin film technology is more preferable in a number of applications, because of compatibility with integrated circuit technology, avoiding wire soldering problems and allowing miniaturisation. However, in narrow films, which are important for miniaturisation, the impedance change ratio is considerably reduced. This Section concerns the effect of the in-plane film size (limited width b) on the magneto-impedance (MI) characteristics in magnetic/metallic multilayers.[23,24] The magnetic flux leakage through the conductive layer results in a considerable drop in MI ratio if the film width is less than a certain critical value depending on the transverse permeability and the layer thickness. This result is similar to that known as an inductive head efficiency.[25,26]

The problem is approached by a 2-D solution of the Maxwell equations in a symmetrical 3-layer film,[24] considering that the magnetic layers are characterised by a rotational permeability matrix, a specific form of which being defined by the transverse domain structure. The external problem of the field distribution outside the film is replaced by approximate boundary conditions at the film edges, which correspond to zero ac fringing flux. The magnetic layers are characterised by a permeability matrix defined by the stripe domain structure shown in Fig. 3.27. If the edge effect is neglected (approximation of an infinite width b), the ac magnetic flux generated by the current flowing along the film is confined within the outer magnetic layers. In the sandwich of a finite width b, the variable flux leaks across the inner conductor, as shown in Fig. 3.28.

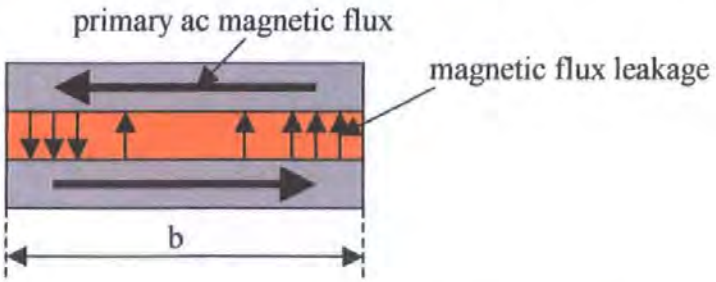

Fig. 3.28 *Cross section of a narrow sandwich film showing the flux leakage.*

This effect has been studied in planar inductors showing that it leads to a drop in efficiency.[25,26] In the case of MI multilayers, this process eventually results in a considerable decrease in the impedance change ratio if the film width is smaller than some critical value depending on the transverse permeability, layer thickness and frequency.

In the case of a weak skin effect, this result corresponds to that obtained in Ref. 23 for a static magnetic model.

The model under consideration is depicted in Fig. 3.2. The film length l is assumed to be large, so that the film can be treated as infinite in the z-direction (variable fields are functions of x and y only). It is assumed that the magnetic layers have a transverse anisotropy (y-axis is an easy direction) and a corresponding stripe domain structure, as shown in Fig. 3.27. The magnetisation forms nearly closed loops in the y-direction, causing no large magnetostatic energy even in the case of very narrow films. If the voltage V_z across the film ends is fixed, the impedance Z of the structure is defined as:

$$Z = V_z / j, \quad j = \int_{x=-d}^{x=d} \int_{y=-b/2}^{y=b/2} \rho(x,y)\,dx\,dy \tag{14}$$

where $\rho(x,y)$ is the current density distribution and $d = d_1 + d_2$. It is convenient to express the current density in terms of the vector potential $\mathbf{A}$ and the scalar potential φ from the Maxwell equations for the electric ($\mathbf{e}$) and magnetic ($\mathbf{h}$) fields:

$$\mathbf{j} = \sigma \mathbf{e}, \qquad \mathbf{e} = -\operatorname{grad}\varphi - \frac{1}{c}\frac{\partial \mathbf{A}}{\partial t}, \tag{15}$$

$$\hat{\mu}\,\mathbf{h} = \operatorname{rot}\mathbf{A}, \quad \operatorname{rot}\mathbf{h} = \frac{4\pi}{c}\mathbf{j}, \tag{16}$$

where $\hat{\mu}$ is the permeability matrix for the magnetic layers, and it is equal to the unit in the inner non-magnetic layer.

The variable magnetisation $\mathbf{m}$ is a linear function of the magnetic field $\mathbf{h}$ induced by the current j: $\mathbf{m} = \hat{\chi}\,\mathbf{h}$, where $\hat{\chi}$ is the susceptibility matrix. For sufficiently high frequencies, the main dynamic process is magnetisation rotation. In this case, the form of $\hat{\chi}$ is determined by the solution of the linearised Landau-Lifshitz equation. After averaging over all domains it becomes of a quasi-diagonal form. Then, the permeability matrix, $\hat{\mu} = \hat{\mathbf{I}} + 4\pi\hat{\chi}$, is written as:

$$\hat{\mu} = \begin{pmatrix} \mu_1 & -i\mu_a & 0 \\ i\mu_a & \mu_2 & 0 \\ 0 & 0 & \mu_3 \end{pmatrix}. \tag{17}$$

Considering, that current flows in z-direction, and the permeability matrix $\hat{\boldsymbol{\mu}}$ has quasi-diagonal form (17), the vector potential **A** and gradφ have only z-components. From Eqs. (15),(16) the following equation for $A_z = \tilde{A}$ is obtained in the inner non-magnetic layer:

$$\frac{\partial^2 \tilde{A}}{\partial x^2} + \frac{\partial^2 \tilde{A}}{\partial y^2} = -\tilde{k}_0^2 \tilde{A} - \frac{4\pi}{c}\tilde{J}, \tag{18}$$

$$\tilde{k}_0 = \frac{1+i}{\tilde{\delta}_0}, \quad \tilde{\delta}_0 = \frac{c}{\sqrt{2\pi\omega\sigma_1}}, \quad \tilde{J} = -\sigma_1 \frac{\partial \tilde{\varphi}}{\partial z} = \sigma_1 \frac{V_z}{l},$$

where the symbol "~" designates the inner non-magnetic layer, σ_1 is its conductivity, and $\tilde{J}$ is the initial current density in the inner core. The designations for $\tilde{k}_0$ and $\tilde{\delta}_0$ have been introduced in Eq. (9): wave number and skin-depth in the inner layer, respectively. In the case of the magnetic layers, $A_z = A$ is found from:

$$\eta_2 \frac{\partial^2 A}{\partial x^2} + \eta_1 \frac{\partial^2 A}{\partial y^2} = -k_0^2 A - \frac{4\pi}{c} J, \tag{19}$$

$$k_0 = \frac{1+i}{\delta_0}, \qquad \delta_0 = \frac{c}{\sqrt{2\pi\omega\sigma_2}}, \qquad J = -\sigma_2 \frac{\partial \varphi}{\partial z} = \sigma_2 \frac{V_z}{l},$$

where σ_2 is the conductivity of magnetic layers, and J is the initial current density in the magnetic layers. The designations for k_0 and δ_0 have been introduced in Eq. (6): non-magnetic wave number and skin-depth in the magnetic layers, respectively. The parameters η_1 and η_2 are the corresponding components of the inverse permeability matrix $\hat{\boldsymbol{\eta}} = \hat{\boldsymbol{\mu}}^{-1}$:

$$\hat{\boldsymbol{\eta}} = \begin{pmatrix} \mu_2/\mu_0^2 & i\mu_a/\mu_0^2 & 0 \\ -i\mu_a/\mu_0^2 & \mu_1/\mu_0^2 & 0 \\ 0 & 0 & 1/\mu_3 \end{pmatrix} = \begin{pmatrix} \eta_1 & \eta_a & 0 \\ -\eta_a & \eta_2 & 0 \\ 0 & 0 & \eta_3 \end{pmatrix}, \tag{20}$$

where $\mu_0^2 = \mu_1\mu_2 - \mu_a^2$.

The solutions of the inhomogeneous Helmholtz equations (18),(19) will be found as a sum of the general solution of the corresponding homogeneous equation and the particular solution of inhomogeneous equation. The homogeneous equations can be solved by the separation of variables, $A(x,y) = \Phi(x)\Psi(y)$ and $\tilde{A}(x,y) = \tilde{\Phi}(x)\tilde{\Psi}(y)$, which yields:

$$\begin{cases} \dfrac{\partial^2\tilde{\Phi}}{\partial x^2}+\tilde{\lambda}^2\tilde{\Phi}=0 \\ \dfrac{\partial^2\tilde{\Psi}}{\partial y^2}-\tilde{\beta}^2\tilde{\Psi}=0, \\ -\tilde{\beta}^2+\tilde{\lambda}^2=\tilde{k}_0^2 \end{cases} \quad \begin{cases} \eta_2\dfrac{\partial^2\Phi}{\partial x^2}+\lambda^2\Phi=0 \\ \eta_1\dfrac{\partial^2\Psi}{\partial y^2}-\beta^2\Psi=0 \\ -\eta_1\beta^2+\eta_2\lambda^2=k_0^2 \end{cases} . \tag{21}$$

The constants λ^2, $\tilde{\lambda}^2$ and $\beta^2, \tilde{\beta}^2$ were chosen with different signs reasoning from the physical meaning that the solution is to be oscillating by x, whereas the width effect has to decrease exponentially with $b \to \infty$. The assumption concerning the width effect has been proven in Chapter 2, when the boundary and shape effects were taken into account by the singular perturbation series. In this series all terms decrease exponentially with a distance from the boundary. Moreover, the conclusion on the exponential character of boundary effects is a general result for any system, as it is shown in the theory of singular perturbations.[40,41]

The general solutions of Eq. (21) can be constructed from the following linear combinations:

$$C_1\cos\tilde{\lambda}x\cdot\cosh\tilde{\beta}y+C_2\sin\tilde{\lambda}x\cdot\sinh\tilde{\beta}y+C_3\cos\tilde{\lambda}x\cdot\sinh\tilde{\beta}y+C_4\sin\tilde{\lambda}x\cdot\cosh\tilde{\beta}y, \tag{22}$$

$$D_1\cos\lambda x\cdot\cosh\beta y+D_2\sin\lambda x\cdot\sinh\beta y+D_3\cos\lambda x\cdot\sinh\beta y+D_4\sin\lambda x\cdot\cosh\beta y.$$

In general, the spectrum λ^2, $\tilde{\lambda}^2$ and $\beta^2, \tilde{\beta}^2$ can be discrete, continues or mixed, thus the solution is presented as a sum or integral of the linear combinations over all spectrum values.

Since the width effect can be completely attributed to Eqs. (22), the particular solutions of Eqs. (18),(19) can be constructed in the form independent on y:

$$C_5\cosh i\tilde{k}_0x+C_6\sinh i\tilde{k}_0x-\frac{4\pi}{c\tilde{k}_0^2}\tilde{J}, \tag{23}$$

$$D_5\cosh i\bar{k}_0x+D_6\sinh i\bar{k}_0x-\frac{4\pi}{ck_0^2}J,$$

where $\bar{k}_0=k_0/\sqrt{\eta_2}$.

By virtue of the system geometry, the longitudinal electrical field e_z must be symmetrical with respect to the transformation $(x)\to(-x)$: $e(x,y)\equiv e(-x,y)$ for any y. On the contrary, the transverse magnetic induction (y-component) must be antisymmetrical with respect to the transformation $(x,y)\to(-x,-y):(\hat{\boldsymbol{\mu}}\mathbf{h})_y\big|_{x,y}=(\hat{\boldsymbol{\mu}}\mathbf{h})_y\big|_{-x,-y}$. Physically this condition mirrors the circulatory character of the ac induced magnetic field inside the film. For the film with infinite width this condition has to be replaced by $(x)\to(-x)$. The symmetry and antisymmetry conditions together with Eq. (15),(16) yield the following requirements for A_z:

$$e_z-symmetry:\ A_z(x,y)=A_z(-x,y), \tag{24}$$

$$(\hat{\boldsymbol{\mu}}\mathbf{h})_y-antisymmetry:\ \frac{\partial A_z(x,y)}{\partial x}=-\frac{\partial A_z(-x,-y)}{\partial x}.$$

The conditions of continuity for the tangential components e_z, h_y and the normal magnetic induction $(\hat{\boldsymbol{\mu}}\mathbf{h})_x=\partial A_z/\partial y$ (x-component) imposed at the metallic/magnetic interface ($x=\pm d_1$) yield:

$$h_y-continuity:\ \frac{\partial\widetilde{A}}{\partial x}(\pm d_1,y)=\eta_a\frac{\partial A}{\partial y}(\pm d_1,y)+\eta_2\frac{\partial A}{\partial x}(\pm d_1,y) \tag{25}$$

$$e_z-continuity:\ \widetilde{A}(\pm d_1,y)=A(\pm d_1,y) \tag{26}$$

$$(\hat{\boldsymbol{\mu}}\mathbf{h})_x-continuity:\ \frac{\partial\widetilde{A}}{\partial y}(\pm d_1,y)=\frac{\partial A}{\partial y}(\pm d_1,y) \tag{27}$$

The boundary conditions at the external surfaces $x=\pm d$ and $y=\pm b/2$ require certain approximations. In the analysis of the magnetic/metallic multilayers used for planar inductors it is proven that the fringing ac magnetic flux at the edges is small and can be neglected.[26] This implies that the y-component of the variable magnetic induction, $b_y=(\hat{\boldsymbol{\mu}}\mathbf{h})_y=\partial A_z/\partial x$, averaged over the half thickness turns to zero at $y=\pm b/2$, viz.:

$$\int_{-d}^{0}b_y(x,\pm b/2)\,dx=\int_{0}^{d}b_y(x,\pm b/2)\,dx. \tag{28}$$

Boundary condition (28) does not contradict the existence of dc fringing flux due to transverse stripe domain structure, since in a linear approximation the total magnetisation partitions into static and variable parts as mentioned above and the static structure is not altered by the ac field.

In terms of the vector potential and taking account of symmetry, Eq. (28) becomes:

$$A(d,\pm b/2)=\tilde{A}(0,\pm b/2) \tag{29}$$

The normal magnetic flux through the external surfaces $x=\pm d$ is also considered to be negligibly small, which is reasonable for $d<<b$. This means that the x-component of the magnetic induction is zero at $x=\pm d$, or $A(\pm d,y)=\text{const}$. This constant can be found considering the relationship between the voltage V_z and the surface value of the electric field:[39]

$$e_z(\pm d,y)=\frac{V_z}{l}+\frac{i\omega}{c^2}\cdot\frac{L_e j}{l} \tag{30}$$

where L_e is the external inductance depending only on the geometry of the film. Comparing Eqs. (30) and (15) the last boundary condition is obtained:

$$A(\pm d,y)=\frac{L_e}{lc}j. \tag{31}$$

Now we are in position to make the main assumption concerning the wave processes in the layered thin film considered here, namely, that the wave processes in the sandwich film involve the single modes in each layer.[24] These modes can be considered as surface ones. The dispersion equation, wrote for each layer, defines the spectrum of "long-living" propagating modes inside the layer. The number of modes is always limited and depends on the layer thickness, its material parameters and environment.[42] (This paper is enclosed in Appendix C of Chapter 5) With the infinite increase of the layer thickness this discrete spectrum becomes everywhere dense in a certain interval. On the contrary, with the decrease of the thickness the spectrum degenerates in a single mode. If the transverse boundary conditions (in the y-direction) have a dumping character and hence do not give rise to the wave re-scattering, they will not increase the number of modes existing in the bounded layer. Therefore, the assumption about the single mode regime is quite reasonable for a thin film structure. Also it is supported by the averaged boundary conditions (28),(29) at the film ends in the y-direction.

For the single mode approximation the general solutions of Eq. (18) accounting for Eq. (24) can be written as:

$$\tilde{A}=C_1\cos\tilde{\lambda}x\cdot\cosh\tilde{\beta}y+C_2\sin\tilde{\lambda}x\cdot\sinh\tilde{\beta}y+C_5\cosh i\tilde{k}_0x-\frac{4\pi}{c\tilde{k}_0^2}\tilde{J}. \tag{32}$$

General solutions of Eq. (19) in the single mode state accounting for the independence of y at $x=\pm d$ can be wrote separately for $x>0$ and for $x<0$ without the accounting Eq. (24). For $x>0$ it obeys:

$$A=\sin\lambda(d-x)\cdot(D_2\sinh\beta y+D_4\cosh\beta y)+ \\ +D_5\cosh i\bar{k}_0 x+D_6\sinh i\bar{k}_0 x-\frac{4\pi}{ck_0^2}J, \tag{33}$$

The dependence on y of the vector potential $\tilde{A}$ implies the existence of normal magnetic flux in the inner layer: the ac flux associated with the magnetic layers leaks across the inner spacer, shown in Fig. 3.28.)

On account of the symmetry all equations can be considered only for $x>0$ .To comply with the boundary conditions (25)-(27) for any y, the wave numbers $\tilde{\beta}$ and β in Eqs. (32),(33) are to be equal: $\tilde{\beta}\equiv\beta$. In other words, a strong coupling between the single modes in the layers takes place. This strong correlation results in the common wave number for all wave processes in the y-direction. The wave numbers $\tilde{\lambda}$, λ, corresponding to the x-direction, are found from the coupling dispersion equation:

$$2\eta_2\tilde{\lambda}\lambda\tan\lambda d_2+\left(\eta_2^2\lambda^2-\left(\eta_a^2(\tilde{\lambda}^2-\tilde{k}_0^2)+\tilde{\lambda}^2\right)\tan^2\lambda d_2\right)\tan 2\tilde{\lambda}d_1=0 \tag{34}$$

$$\lambda^2\eta_2=k_0^2+\left(\tilde{\lambda}^2-\tilde{k}_0^2\right)\eta_1$$

Calculating the current distribution in the film, the impedance Z can be found from equation (1). Neglecting the part associated with the external inductance, Z is written in the form

$$Z=R_{dc}\frac{f_1(x_1,x_2)(\nu x_1+x_2)}{x_2\left(f_1(x_1,x_2)-1\right)g(b)+f_2(x_1,x_2)}, \tag{35}$$

where $R_{dc}=l/2b(\sigma_1 d_1+\sigma_1 d_1)$ is the dc resistance,

$$f_1(x_1,x_2)=\cosh x_1\cosh x_2+\nu\sinh x_1\sinh x_2, \tag{36}$$

$$f_2(x_1,x_2)=\cosh x_1\sinh x_2+\nu\sinh x_1\cosh x_2, \tag{37}$$

$$g(b)=\frac{2\tan(\beta b/2)}{\beta b}\left(\frac{\sigma_1 d_1}{\sigma_2 d_2}\cdot\frac{\sin\tilde{\lambda}d_1}{\tilde{\lambda}d_1}+\frac{\tan(\lambda d_2/2)}{\lambda d_2}\cdot\cos\tilde{\lambda}d_1\right), \tag{38}$$

$$\beta^2=\tilde{\lambda}^2-\tilde{k}_0^2, \qquad x_1=i\tilde{k}_0 d_1, \qquad x_2=i\bar{k}_0 d_2, \qquad \nu=\frac{\tilde{k}_0}{\bar{k}_0\eta_2}=\sqrt{\frac{\sigma_1}{\sigma_2\eta_2}}.$$

Equation (34) is solved numerically by a standard iteration procedure. Analysing equations (35)-(38), it is seen that the effect of the film width is described by the function $g(b)$. For $\beta b/2 >> 1$, it tends to be zero and Eq. (35) reduces to that known for an infinite in the y-direction film.[4] It means that the parameter $b^* = 2/\beta$ plays the role of a critical width: for $b < b^*$ all the film dimensions b, d_1, d_2 influence the value of the impedance. Figure 3.29 shows the parameter b^*/d as a function of frequency for $d = 0.5$ μm and $d = 0.1$ μm ($d_1 = d_2$). With increasing frequency, b^* decreases stronger for a thicker film. In the low frequency limit ($x_1, x_2 << 1$), $b^* = \sqrt{d_1 d_2 / \eta_2}$. This result can be obtained by linearising Eq. (34) with the additional condition that the transverse permeability is sufficiently large ($\eta_1, \eta_2, \eta_a << 1$), which corresponds to the results of Ref. 23 obtained in a similar approximation.

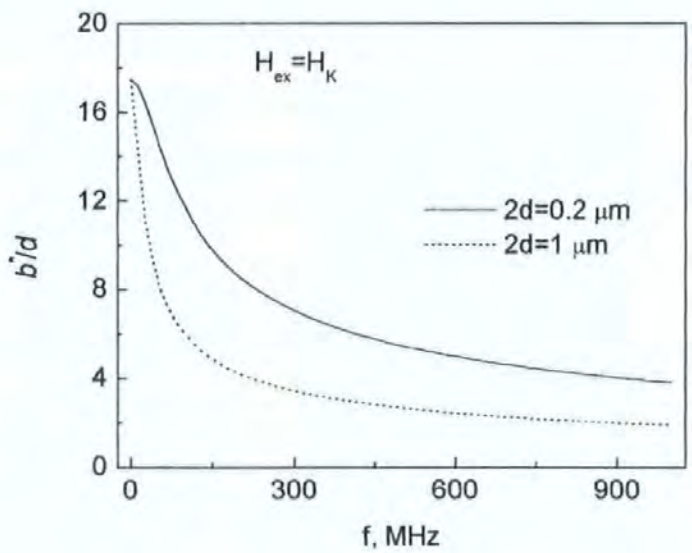

Fig. 3.29 *Critical parameter b^*/d as a function of frequency. The calculation uses the following parameters: $4\pi M_0 = 6000\,\mathrm{G}$, $H_K = 9\,\mathrm{Oe}$, $\gamma = 2.0 \cdot 10^7$ (rad/s)/Oe, $\tau = 0.2$. To avoid the divergence of $\hat{\eta}$ at $H_{ex} = H_K$, $\omega = 0$ a small anisotropy deviation of 5^0 from the y-axis is introduced, $\sigma_1 = 10^{18}\,\mathrm{s}^{-1}$, $\sigma_2 = 4.5 \cdot 10^{16}\,\mathrm{s}^{-1}$.*

Typical parameters for structures of interest are $d_1 \approx d_2 \approx 0.1-0.5$ μm, $b = 10-50$ μm, $1/\eta_2 \approx 10^3$, for which $b^* \approx 3-15$ μm and is comparable to the half-width, which means that the size effects can not be neglected.

Figure 3.30 shows the plots of $\Delta Z/Z$ versus frequency with the film width b as a parameter for $d = 0.5$ μm and $d = 0.1$ μm ($d_1 = d_2$). The impedance change ratio is defined as $\Delta Z/Z = |Z(H_K) - Z(0)|/|Z(0)| \cdot 100\%$.

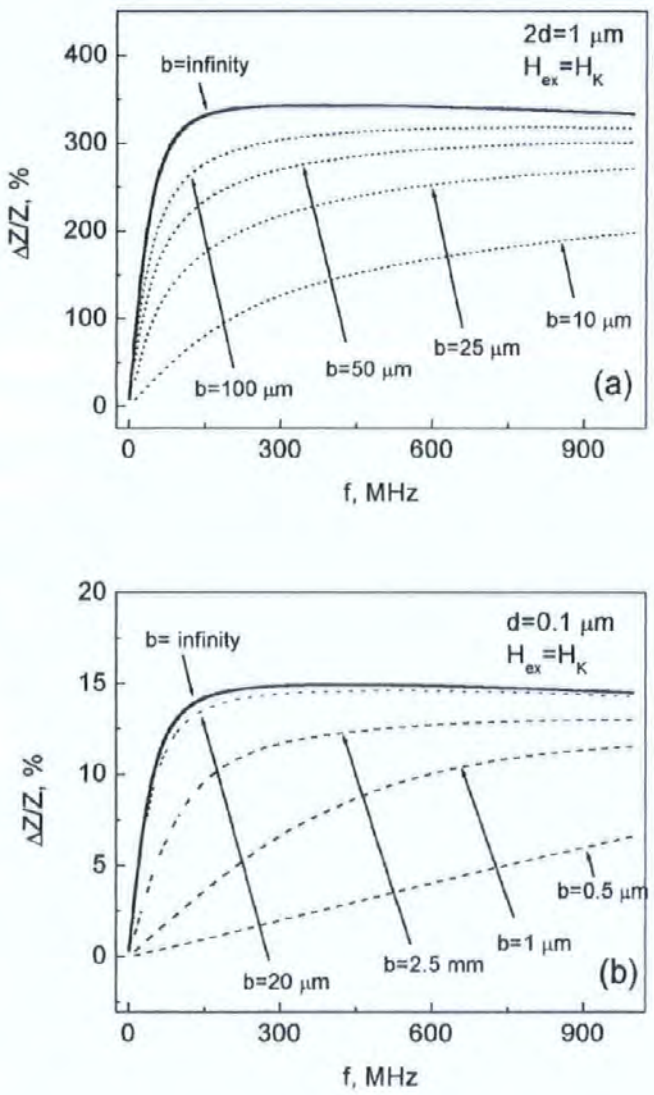

Fig. 3.30 *Plots of the MI ratio vs. frequency with the film width as a parameter for different film thicknesses. The parameters are the same as those used in* ***Fig. 3.29****.*

The function $|Z(H_{ex})|$ has a maximum at $H_{ex} \approx H_K$, associated with that for the parameter $1/\eta_2$. Therefore, the MI ratio introduced gives the maximum impedance change. For a wide film ($b > 100$ μm for $d = 0.5$ μm and $b > 10$ μm for $d = 0.1$ μm) the results are very close to those obtained for an infinite in-plane film. With decreasing b, the MI ratio decreases substantially: for example, at 150 MHz for 100 μm-wide films $\Delta Z / Z$ reaches more than 300% at a frequency of, whereas its value is only about 70% for $b = 10$ μm at this frequency. The decrease in MI is stronger at lower frequencies where the critical width b^* is larger. In the example above, $\Delta Z / Z$ recovers up to 200% at a frequency of 900 MHz. As a result, the impedance plots do not show flat regions for small values of b.

Summarising, we can conclude that the 2-D analysis of MI in magnetic/metallic multilayers becomes important when the film width b is smaller than a certain critical value depending on the permeability, layer thickness and frequency. Physically, the effect of the in-plane dimensions corresponds to the variable flux leakage across the inner conductor, resulting in a decrease in the transverse flux in the magnetic layers, and eventually, a decrease in the MI ratio.

3.9 References:

[1] L. V. Panina and K. Mohri, Appl. Phys. Lett. **65**, 1189 (1994).

[2] L. V. Panina, K. Mohri, K. Bushida, and M. Noda, J. Appl. Phys. **76**, 6198 (1994).

[3] L. V. Panina, K. Mohri, T. Uchiyama, K. Bushida, and M. Noda, IEEE Trans. Magn. **31**, 1249 (1995).

[4] K. Hika, L. V. Panina, and K. Mohri, IEEE Trans. Magn. **32**, 4594 (1996).

[5] L. V. Panina and K. Mohri, Sensors and Actuators **A81**, 71 (2000).

[6] T. Morikawa, Y. Nishibe, H. Yamadera, Y. Nonomura, M. Takeuchi, and Y. Taga, IEEE Trans. Magn. **33**, 4367 (1997).

[7] N. Jiang, K. Yamakawa, N. Honda, and K. Ouchi, IEEE Trans. Magn. **34**, 1339 (1998).

[8] M. Takezawa, H. Kikuchi, M. Yamaguchi, and K. I. Arai, IEEE Trans. Magn. **36**, 3664 (2000).

[9] V. Korenivski and R. B. van Dover, J. Appl. Phys. **82**, 5247 (1997).

[10] V. Korenivski, J. Magn. Magn. Mater. **215/216**, 800 (2000).

[11] A. Sukstanskii, V. Korenivski, and A. Gromov, J. Appl. Phys. **89**, 775 (2001).

[12] D. P. Makhnovskiy, A. S. Antonov, A. N. Lagarkov, and L. V. Panina, J. Appl. Phys. **84**, 5698 (1998).

[13] L. V. Panina, D. P. Makhnovskiy, and K. Mohri, J. Magn. Soc. Japan **23**, 925 (1999).

[14] D. P. Makhnovskiy, A. N. Lagarkov, L. V. Panina, and K. Mohri, Sensor and Actuators **A81**, 106 (2000).

[15] D. P. Makhnovskiy, L. V. Panina, and D. J. Mapps, J. Magn. Magn. Mater. **215/216**, 629 (2000).

[16] K. Ueno, H. Hiramoto, K. Mohri, T. Uchiyama, and L. V. Panina, IEEE Trans. Magn. **36**, 3448 (2000).

[17] R. L. Sommer, A. Gundel, and C. L. Chien, J. Appl. Phys. **86**, 1057 (1999).

[18] D. Garcia, J. L. Munoz, G. Kurlyandskaya, M. Vazquez, M. Ali, and M. R. J. Gibbs, IEEE Trans. Magn. **34**, 1153 (1998).

[19] Shu-Qin Xiao, Yi-Hua Liu, Lin Zhang, Chen Chen, Jian-Xin Lou, Shao-Xiong Zhou, and Guo-Dong Liu, J. Phys.: Condens. Matter **10**, 3651 (1998).

[20] You-Yong Dai, Yi-Hua Liu, Shu-Qin Xiao, Lin Zhang, Long-Qiang Yue, Hou-Zheng Wu, and Yan-Zhong Zhang, Phys. Stat. Sol. **181**, 413 (2000).

[21] D. P. Makhnovskiy, L. V. Panina, and D. J. Mapps, Phys. Rev. B **63**, 144424 (2001).

[22] D. P. Makhnovskiy, L. V. Panina, and D. J. Mapps, J. Appl. Phys. **87**, 4804 (2000).

[23] D. P. Makhnovskiy and L. V. Panina, Sensor and Actuators **A81**, 91 (2000).

[24] L. V. Panina, D. P. Makhnovskiy, D. J. Mapps, and D. S. Zarechnyuk, J. Appl. Phys. **89**, 7221 (2001).

[25] A. Paton, J. Appl. Phys. **42**, 5868 (1971).

[26] G. F. Hughes, J. Appl. Phys. **54**, 4168 (1983).

[27] N. Fry, MPh Thesis, (Centre for Research in Information Storage Technology (CRIST), University of Plymouth, Plymouth, United Kingdom, 1996).

[28] M. Vazquez and A. Hernando, J. Phys. D: Appl. Phys. **29**, 939 (1996).

[29] N. Kawajiri, M. Nakabayashi, C. M. Cai, K. Mohri, and T. Uchiyama, IEEE Trans. Magn. **35**, 3667 (1999).

[30] K. Mohri, T. Uchiyama, L. P. Shen, C. M. Cai, and L. V. Panina, Sensors and Actuators **A91**, 85 (2001).

[31] K. Mohri, T. Uchiyama, L. P. Shen, C. M. Cai, L. V. Panina, and Y. Honkura, IEEE Trans. Magn. **38**, 3063 (2002).

[32] D. P. Makhnovskiy, L. V. Panina, and D. J. Mapps, Appl. Phys. Letters **77**, 121 (2000).

[33] L. V. Panina, D. P. Makhnovskiy, D. J. Mapps, K. Mohri, and P. I. Nikitin, Materials Science Forum **373/376**, 741 (2001).

[34] L. V. Panina and D. P. Makhnovskiy, *Key lecture: "Giant magneto-impedance in structured materials"*, The International Symposium on Optical Science and Technology, Complex Mediums III: Beyond Linear Isotropic Dielectrics; Seattle, July 2002. Published in The Proceedings SPIE International Society for Optical Engineering, vol. 4806, pp. 18-31, 2002.

[35] N. Fry, D. P. Makhnovskiy, L. V. Panina, S. I. Sandacci, M. Akhter, and D. J. Mapps, submitted to IEEE Trans. Magn. (November 2002).

[36] A. S. Antonov, A. Granovsky, A. Lagarkov, N. Perov, N. Usov, and T. Furmanova, Physica **A 241**, 420 (1997).

[37] V. A. Zhukova, A. B. Chizhik, J. Gonzalez, D. P. Makhnovskiy, L. V. Panina, D. J. Mapps, and A. P. Zhukov, J. Magn. Magn. Mater. **249**, 324 (2002).

[38] A. Takayama, T. Umehara, A. Yuguchi, H. Kato, K. Mohri, and T. Uchiyama, IEEE Trans. Magn. **35**, 1339 (1998).

[39] L. D. Landau and E. M. Lifshitz, *Electrodynamics of Continuous Media.* (Pergamon Press, Oxford, 1975).

[40] J. Kevorkian and J. D. Cole, *Multiple Scale and Singular Perturbation Methods.* (Springer, 1996).

[41] D. R. Smith, *Singular-Perturbation theory. An Introduction with Applications.* (Cambridge University Press, Cambridge, 1985).

[42] D. P. Makhnovskiy, L. V. Panina, D. J. Mapps, and A. K. Sarychev, Phys. Rev. **B 64**, 134205 (2001).

Chapter 4 Magneto-impedance sensors

4.0 General requirements for magnetic sensors

Recent developments in the fields of computer peripherals, information apparatus, mechatronics such as: automobiles and industrial robots, power electronics, medical electronics, and industrial measurements require new high performance micro magnetic sensors to detect localised weak magnetic flux. General requisite conditions for the commercial sensors are as follows:[1]

1) Miniature size of less than 1 mm is needed to detect localized weak magnetic flux such as the surface flux of magnetic recorded media and rotary encoder ring magnets.
2) Sensitivity or resolution of flux detection should be $10^{-7} - 10^{-10}$ T to allow precise non-contact sensing.
3) A quick response with signal frequencies from zero to 10 MHz is needed to detect surface flux change of a high density hard disk memory.
4) High temperature stability and maximum operating temperature in the range from –50 to +180 ^{0}C are needed for use in the commercial devices.
5) Small power consumption of less than 10 mW, which makes it possible to produce portable microsensors working with a self-contained power supply.

In this Section we shall consider several types of the MI sensors, which based on different principles. A great many of the physical effects display dependence on the external factors, such, for example, as electromagnetic fields. Thus, a special type of a sensor can be considered as a certain projection using one or several physical principles. Conventional sensors such as: search-coil magnetometer (inductive coil), Hall's sensor, magneto-resistive (MR) and giant magneto-resistive (GMR) sensors, spin-tunnelling sensor, and flux-gate sensor can not satisfy at once all conditions 1)–5) cited above. Therefore, the choice of a physical principle is determined by a specific target. We would like to discuss the main factors, which allow the classification of the sensors of the various types. Such an inputted "coordinate system" shall clarify many aspects of MI sensors and their position in respect to the other sensors. We shall demonstrate that the MI sensor presents a complicated variety of these factors, combining attributes of other sensors. This complicated behaviour gives an extremely rich palette of the effects, making it attractive and versatile for sensor applications.

The field sensitivity (%/Oe) has to be calculated as the averaged field sensitivity at the operation point of the sensor, where it has the maximum sensitivity with a linear output. As has been shown in Chapters 2 and 3, in the MI sensors the operation point is located between zero and anisotropy fields.

4.1 SDUID and maximal field resolution

The detectable field is one of the main sensor parameters. The superconducting quantum interference device (SQUID) occupies the leading position with the field resolution of about $10^{-15}-10^{-14}$ T.[2] The great sensitivity of the SQUID devices is associated with measuring changes in magnetic field associated with one flux quantum, as shown in Fig. 4.1. If a constant biasing current is maintained in the SQUID device, the measured voltage oscillates with the changes in phase at the two junctions, which depends upon the change in the magnetic flux. Counting the oscillations allows you to evaluate the flux change which has occurred.

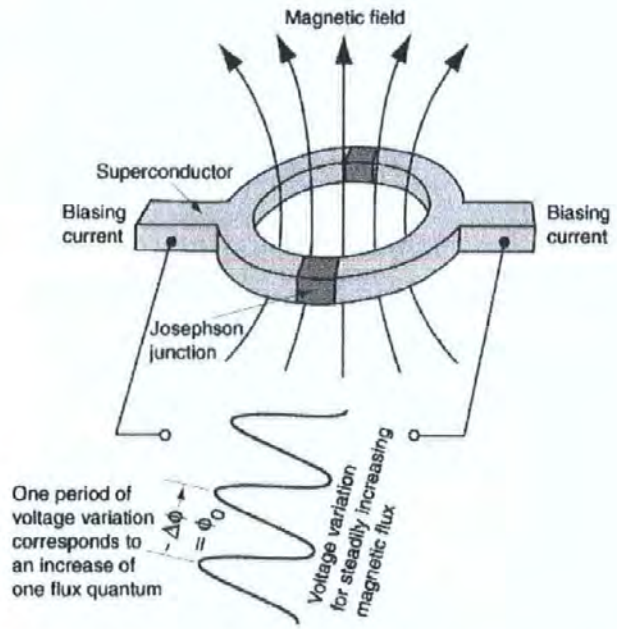

Fig. 4.1 SDUID sensing element with two Josephson functions (after J. Clarke [2]).

The device may be configured as a magnetometer to detect incredibly small magnetic field — small enough to measure the magnetic fields in living organisms. For example, the heart and brain magnetic fields are of about 10^{-10} T and 10^{-13} T, respectively. SQUID's have been used to measure the magnetic fields in mouse brains to test whether there might be enough magnetism to attribute their navigational ability to an internal compass. However, SQUID needs a very low operating temperature that makes it difficult to use for a wide range of commercial applications.

Some exotic sensors, for example, the optically pumped or nuclear precession magnetometers are quite complicated in realisation and can be used only for specific targets. So, we shall concentrate on the main row of the sensors most frequently discussed in the literature. In spite of accessibility, these sensors may demonstrate excellent qualities at low cost such as: a wide range of the detectable fields, high stability in a large temperature range, rather small dimensions and low power consumption. Sensitivity most often conflicts with other parameters. Then, the achievement of consensus between all the requirements becomes the main problem of the overall sensor design.

4.2 Inductive coil sensor

One of the simplest magnetic sensors is a search-coil magnetometer (inductive coil sensor), shown in Fig. 4.2.

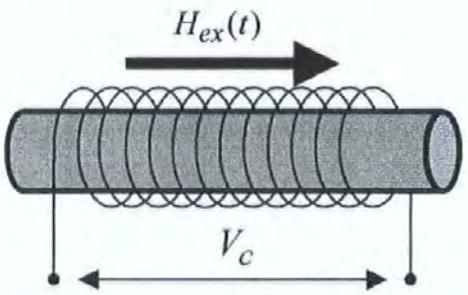

Fig. 4.2 *Search-coil magnetometer based on Faraday's law of induction.*

The space inside the coil is occupied by a material with a high permeability to concentrate the surrounding magnetic field and increase the flux density, and hence, to improve the overall sensitivity. The voltage V_c measured in the coil is defined by Faraday's law of induction (in the CGS system of units):

$$V_c = -\mu\left(\frac{NS}{c}\right)\frac{\partial H_{ex}}{\partial t}, \qquad (1)$$

where μ is the relative permeability of core, N is the number of turns, S is the core cross-section, H_{ex} is the sensed magnetic field, and c is the velocity of light.

As it immediately follows from Eq. (1), the method allows the detection of only an ac external magnetic field $H_{ex}(t)$. The voltage response V_c is directly proportional to the frequency of H_{ex} and the number of the coil turns. This principle strictly limits the response speed and possibility to miniaturise. Nevertheless, the sensor can be made very sensitive, and hence, successfully used if the size and response speed are not critical parameters. For example, a sensor made of a multiple-turn coil on a ferromagnetic ring has been employed by **PBT LTD** (Power Break Technology LTD, UK) for a remote control of a current leakage in the household electrical devices, where it detects the current deference (caused by a leakage) of the order of a few mA. Some commercial search-coil magnetometers provide the field resolution of about 10^{-9} T.

4.3 Hall's sensors

The Hall sensor ("Hall's cross") is shown in Fig. 4.3. When a magnetic field H_{ex} is applied to a conducting material carrying an electrical current, there is a transverse force (known as the Lorentz force) on the charge carrier.[3] The Lorentz force, which is perpendicular to both the electric current direction and the direction of the applied magnetic field, deflects the path of the electric current passing through a sample of the material. This perpendicular motion of the current carriers results in the cross voltage V_{Hall}.

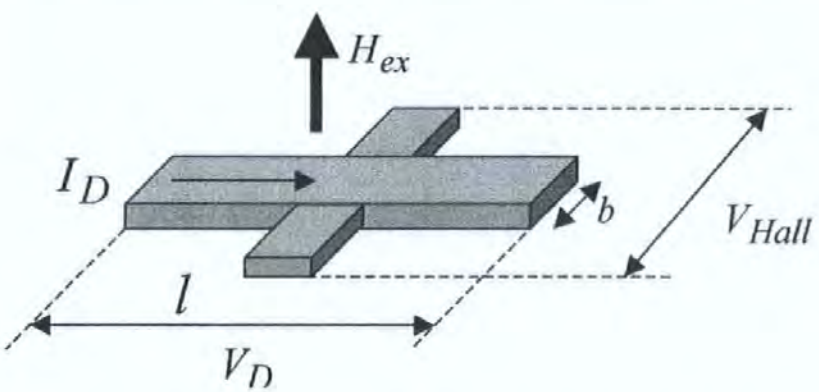

Fig. 4.3 *Hall's sensor. The Hall voltage V_{Hall} as a function of the applied magnetic field H_{ex} is measured for current ($I_D(H_{ex}) = const$) or voltage ($V_D(H_{ex}) = const$) drive.*

The relationship between the Hall effect (the potential difference V_{Hall}) and the passing distance b of charge carrier is to be given by (in the CGS system of units):

$$V_{Hall} = \Re \frac{I_D H_{ex}}{b}, \tag{2}$$

where I_D is the dc current passing along the sheet, $\Re = A/cn_s q$ is the Hall constant, q is the charge (electron or hole), n_s is the concentration of current carrier, A is a dimensionless factor of the order of unity depending on the statistic character of the velocity distribution of the current carriers, and c is the velocity of light. The sign of $\Re$ coincides with that for the current carriers. If the two types of the current carriers are observed in a semiconductor (electrons and holes) then the total type of conductivity can be determined from the sign of $\Re$.

The Hall effect is very small in metallic conductors, but some semiconductors give a much larger effect.[4-6] Then, in work [6] a low-noise scanning Hall probe microscope having unprecedented magnetic field has been developed for studying flux profiles at surfaces. A submicron Hall probe manufactured in a GaAs/AlGaAs two-dimensional electron gas is scanned over the sample to measure the surface magnetic fields using conventional scanning tunneling microscopy positioning techniques. The magnetic field resolution of the Hall probe was 3.8×10^{-6} T/$\sqrt{Hz}$ at 300 K and 2.9×10^{-8} T/$\sqrt{Hz}$ at 77 K (including the amplifier noise).

Another class of magnetic sensor based on an integrated combination of Hall element and ferro-magnetic structure has been proposed to increase the field resolution.[7,8] The idea of combining a sensor with ferromagnetic structures came to many researchers in the past.[9] In order to amplify the magnetic field "seen" by a sensor element, it is placed in the air gap between two long ferromagnetic specimens. In this way they considerably increased the effective sensitivity and the resolution of the sensor element. The operation of this device is based on the following well-known effect: if a ferromagnetic rod is placed in a magnetic field parallel with the long axes of the rod, the rod tends to collect the magnetic field lines in itself: it operates as a magnetic flux concentrator. The hybrid Hall sensor with the magnetic flux concentrator can measure quasistatic magnetic fields down to milli-gauss range (10^{-7} T) at room temperature. *The idea of the hybrid sensor is still waiting its application in GMI sensors.*

4.4 MR and GMR sensors

The magneto-resistive effect (MR) was actually discovered way back in 1857 by British scientist Lord Kelvin. MR material is typically a nickel-iron alloy that shows higher electrical resistance when the current flow is parallel to the magnetic orientation. The resistance drops back to the initial value when the magnetic field is removed. Typical MR sensor element is shown in Fig. 4.4.

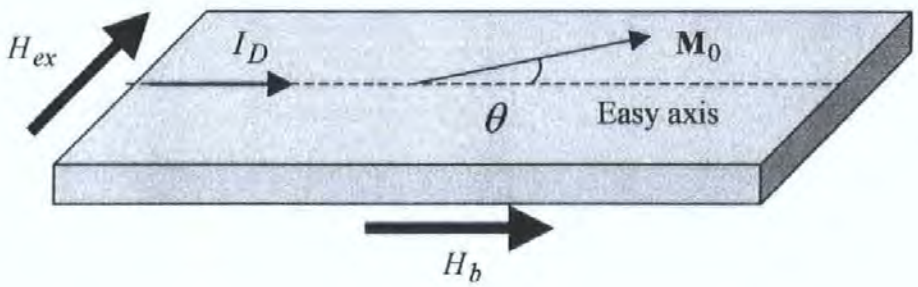

Fig. 4.4 *Schematic diagram of a thin-film magneto-resistor showing the principle directions. I_D is the dc current drive and H_b is the dc bias field.*

In the general case, the easy axis can be deflected from the longitudinal direction (current flow) on some angle α as it occurs in a ferromagnetic wire with a helical anisotropy considered in Chapter 2. The equilibrium angle θ of the magnetisation $\mathbf{M}_0$ is found from energy minimisation (see Eq. (2.47)). The relationship between the resistance change and the external magnetic field can be given by:

$$R = R_0 + \Delta R \cos^2(\theta). \tag{3}$$

The MR sensors have the usual advantages of a thin film sensor: miniature size, small power consumption, and metal-film technology. The resistance change can measure up 2%. However, to initiate this change a quite strong field is required (tens Oersted), and so the field sensitivity "%/Oe" remains small to detect very weak field.

The giant magneto-resistive effect (GMR), discovered in 1988,[10,11] is not just a scaled version of MR. GMR is actually a quantum effect. The simplest GMR structure is shown in Fig. 4.5. The free ferromagnetic layer forms the sensing element and usually consists of NiFe or NiFe/CoFe or NiFe/Co bilayer.

The pinned ferromagnetic layer is coupled by exchange to an antiferromagnetic layer (FeMn, NiO, MnIr, MnNi, MnPt, MnRh, TbCo) or an antiferromagnetically coupled multilayer. Free and pinned layer easy axes can be either parallel or orthogonal (in Fig. 4.5 they are parallel). The GMR element is extremely thin, and the dimensions will become even smaller in the future.

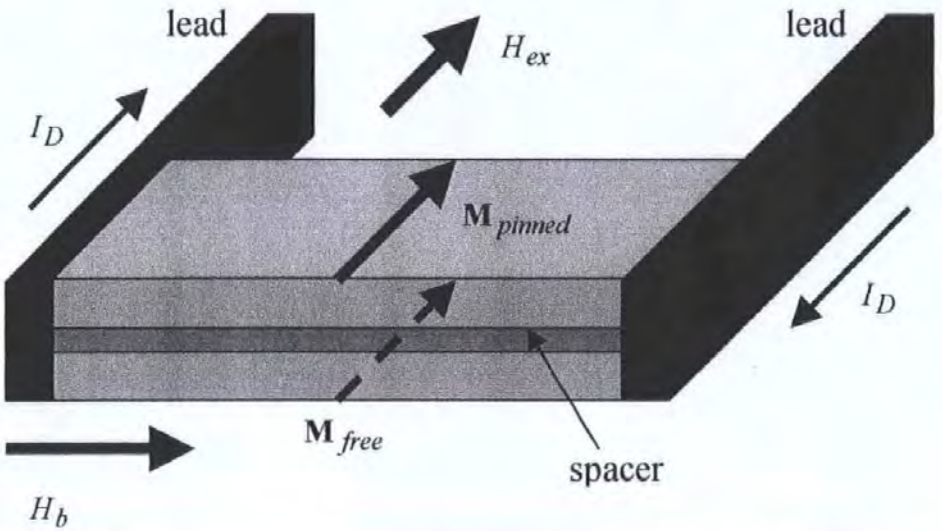

Fig. 4.5 *Schematic drawing of GMR sensor element ("spin-valve").* $\mathbf{M}_{free}$ *is the free ferromagnetic layer with the longitudinal anisotropy, and* $\mathbf{M}_{pinned}$ *is the pinned ferromagnetic layer with the transverse anisotropy.* I_D *is the dc current drive. Free and pinned layer easy axes are parallel.*

The GMR sensors utilise the quantum nature of electrons that have two spin states, up and down. The so-called "spin valve" head structure incorporates a design where one magnetic film is pinned (magnetic orientation is fixed) and the second sensor film has a variable (free) orientation. These films are placed close together so that electrons of either spin direction can move back and forth. Changes in the external magnetic field orientation cause magnetic rotation of the sensor film's orientation. This changing magnetic orientation alters the electrical resistance of the sensor array. Low resistance occurs when the sensor and pinned films are magnetically orientated in the same direction because electrons with parallel spin direction move freely in both films. Higher resistance occurs when magnetic orientations of the pinned and sensor films are opposite because the electron movement of either spin direction is hampered by one or the other films. This mechanism is demonstrated in Figs 4.6(a,b).

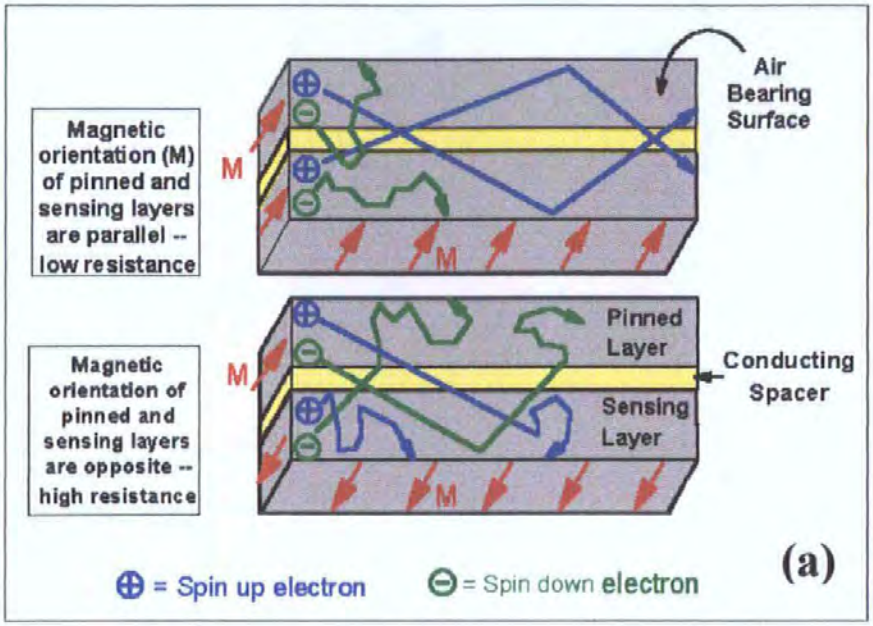

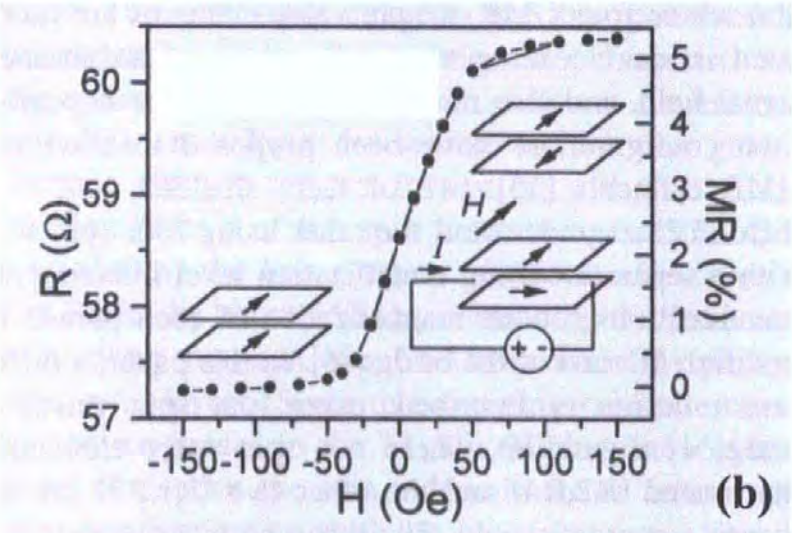

Fig. 4.6 *GMR basics in (a) and spin-valve resistance vs. external magnetic field in (b). The field sensitivity in (b) does not exceed 0.05%/Oe.*

The resistance of the sensing layer is also changed by the MR effect, however the GMR effect is dominant. The field dependence of the spin-valve resistance is given by the following equation:

$$R = R_0 + \Delta R(1 - \cos(\theta_f - \theta_p)), \tag{4}$$

where θ_f and θ_p are the angles of the magnetisation of the free and pinned layers with respect to the current flow.

While older MR heads typically exhibit a resistance change when passing from one magnetic polarity to another of about 2%, for GMR heads this is anywhere from 5% to 8%.

4.5 Magneto-resistive spin tunnelling sensors

The magneto-resistive spin-tunnelling (MRST) effect occurs in sandwiched thin film FM/D/FM structures, where FM being ferromagnetic films (Fe, Co, Ni and their alloy) and D being dielectric layer (Al_2O_3 or SiO_2).[12,13] As well as for a spin-valve structure, one of the ferromagnetic layers is the free layer, and the other is the pinned layer. The main difference between the spin valve and spin tunnelling lies in the dc current drive: in the spin tunneling it is applied perpendicularly to the layers. This current transport depends on the spin polarization at the Fermi level, thus the mutual magnetisation directions of the two ferromagnetic layers.

The MRST structures have many advantages over the spin valve MR structures, namely: the enhanced sensitivity, thicker magnetic nanolayers that simplifies growth of films with different magnetic properties, the perpendicular current flow that provides high resistivity, low magnitudes of operating current and power consumption. The extreme sensitivity of this polarized tunnel current to the FM/D interface allows one to study the magnetism at the monolayer level. In particular, FM/D/FM tunnelling has shown a large MRST effect at room temperature reaching 15-20% in a field less than 20 mT.[12] This combined with the non-volatile memory effect seen in such a threelayer system is ideally suited as a magnetic random access memory (MRAM) element, and as read head sensors capable of achieving magnetic storage densities greater than 100 Gb/in^2. Magnetic tunnel junctions, down to fractions of a square micron in area, with good characteristics at ambient conditions have been successfully fabricated, showing their potential for nanotechnological storage applications. From the physics point of view, there are some unique properties for these junctions. For example, despite the density of states dependence of the tunnel current, intrinsically there is significant dependence of MRST on dc bias. The bias dependence has only been partially understood, and has been attributed to magnetic excitations as seen in inelastic tunnelling measurements.

Spin transport through a metal or semiconductor is another hotly investigated topic.[15] For example, the spin tunnelling studies through an interfacial normal metal layer adjacent to the barrier has shown rapid decay as well as features attributable to quantum well states. The promising half-metal ferromagnetic materials, with their possible 100% spin polarized conduction electrons, are ideal candidates to achieve even bigger effects.

4.6 Fluxgate sensors

In this Section we would like to consider in more detail the different types of fluxgate sensors [16-19] since their geometries coincide in many respects with the different measurement schemes of the impedance components described in Section 2.7.1. Nevertheless, the physical principles account for MI and fluxgate sensors are completely different.

The fluxgate principle is based on the detection of the higher harmonics from the non-linear response in ferromagnetic materials with the non-linear B-H curve. The amplitude of the higher harmonics turns out to be proportional to the external magnetic field H_{ex}. There are two types of the fluxgate sensors: parallel-gated and orthogonal-gated, as shown in Fig. 4.7 and Fig. 4.8, respectively.[16] In the parallel fluxgate a ferromagnetic core (or cores) with the axial magnetisation is driven periodically into saturation by the low frequency longitudinal magnetic field H_{excit} induced by the excitation coil. The pickup coil located on the same core measures the changes of the magnetic flux within the core. The sensor signal shows higher harmonics of the excitation frequency due to the non-linear behaviour of the ferromagnetic material. The even harmonics (2f, 4f ...) especially depend on the magnetic field parallel to the axis of the core. When the parallel fluxgate contains two opposite magnetized cores (see Fig. 4.7(b)), the output signal exists only in the presence of H_{ex}. Such a balanced sensor is mostly used in practice including modern planar fluxgates.[17-19]

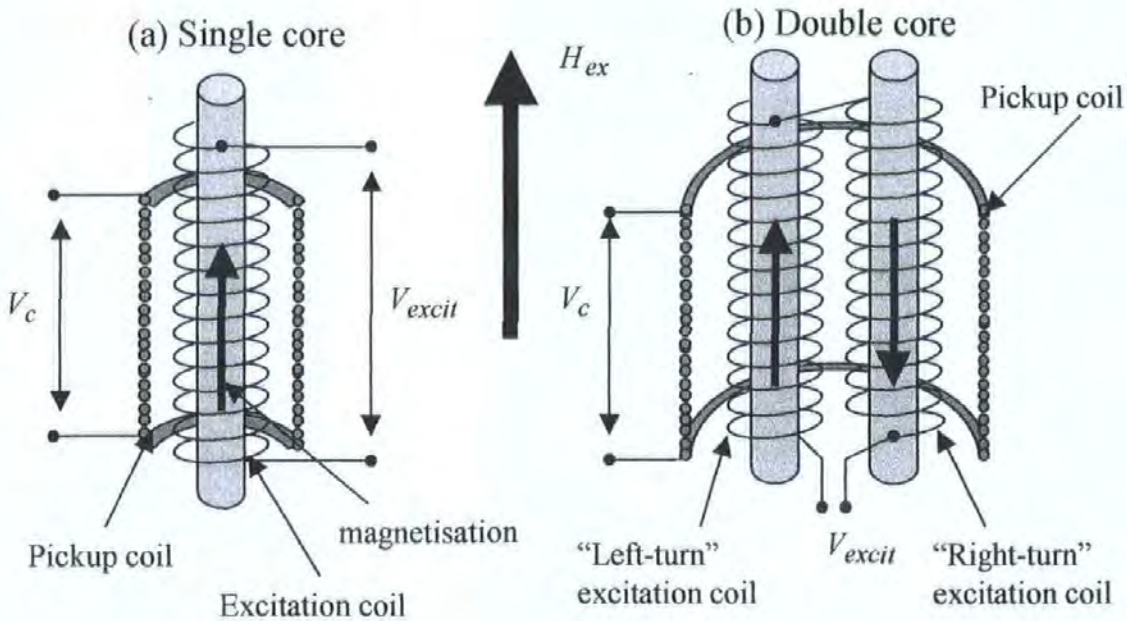

Fig. 4.7 *Parallel-gated fluxgates with single core in (a) and double core in (b).*

In the orthogonal fluxgate a ferromagnetic core with the circumferential magnetisation is driven periodically into saturation by the low frequency excitation current J, which induces circular magnetic field. The signal is registered in the pickup coil located on the same core.

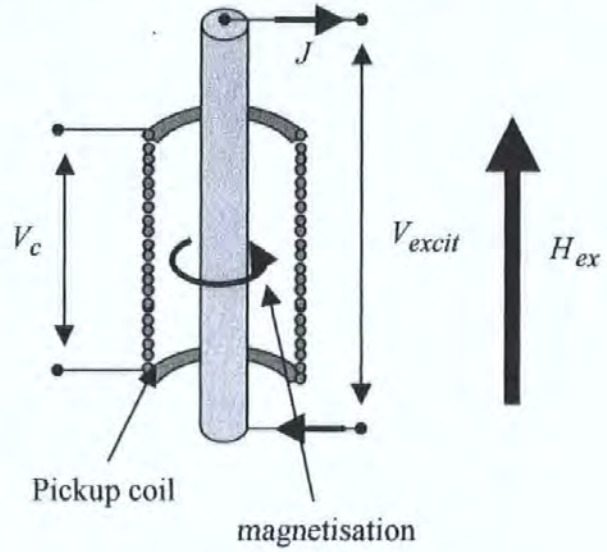

Fig. 4.8 *Orthogonal-gated fluxgate.*

Here we shall consider only the parallel fluxgate with two cores, because it is most widely used in practice.[17-19] The two cores $Cor1$ and $Cor2$ are exposed to the excitation longitudinal field $H_{excit}(t)$ and to the external field H_{ex}. For $H_{ex}=0$ a common operating point $P=H_{excit}(t)$ describes the magnetic state of both cores, the induction in each of them being B and the net induction through a common pickup coil being zero, as B is opposed in the two cores. A small external longitudinal field H_{ex} splits the operating point P into two points $P1=(H_{excit}-H_{ex})$ and $P2=(H_{excit}+H_{ex})$ representing cores $Cor1$ and $Cor2$ respectively. For a small H_{ex} the resulting inductive field through the pickup coil can be given by the following equation:

$$\Delta B = B(P1) - B(P2) \cong 2H_{ex}\frac{dB}{dH} \tag{5}$$

The output signal in the pickup coil is defined by Faraday's law, just as it has been done in Eq. (1) for the inductive coil sensor:

$$V_c = -\left(\frac{NS}{c}\right)\frac{d(\Delta B)}{dt} = \\ = -2H_{ex}\left(\frac{NS}{c}\right)\frac{d}{dt}\left(\frac{dB}{dH}\right)\Bigg|_{H=H_{excit}} = -2H_{ex}\left(\frac{NS}{c}\right)\frac{\partial H_{excit}}{\partial t}\left(\frac{d^2B}{d^2H}\right)\Bigg|_{H=H_{excit}}, \quad (6)$$

where N is the number of turns in the pickup coil, S is the total cross-section area of both cores, $H_{excit} = H_0 \sin(\omega t)$ is the periodical excitation magnetic field, and c is the velocity of light. In the absence of a hysteresis the non-linear function $B(H)$ can be decomposed in the following power series:

$$B(H) = a_0 + a_1 H + a_2 H^2 + a_3 H^3 + \ldots \quad (7)$$

Substituting Eq. (7) into Eq. (6) and replacing H by $H_{excit} = H_0 \sin(\omega t)$ we obtain the following representation for the second harmonic $(V_c)_2$:[16]

$$(V_c)_2 = NS\omega H_{ex}\left[3a_3 H_0^2 + 5a_5 H_0^4 + \ldots + \frac{n}{2^{(n-3)}}\begin{bmatrix} n-1 \\ (n-3)/2 \end{bmatrix} a_n H_0^{n-1}\right]\sin(2\omega t). \quad (8)$$

The Eq. (8) is valid for pure sinusoidal excitation, perfect balance between the two cores and no hysteresis. By using a similar technique all these factors can be taken into account.

The fluxgate sensors are most sensitive in the family of commercial sensors with the field resolution of about 10^{-12} T. This provides for their wide use in the sensing of very weak magnetic field. The modern PCB-like and thin film technologies allow the sensor with rather small dimension.[20,21] However, the miniature dimensions and high speed response for fluxgate sensors lead to a substantial decrease in sensitivity. In addition, they require a quite large power consumption due to the magnetisation reversal.

4.7 Position of MI sensor in the family of magnetic sensors

Consideration of sensors of different types allowed us to bring to light the main physical principles used there. The quantities, which are exposed to the external magnetic field, are the drive magnetic field or flux, and current. By these features the sensors can be divided into two main groups: "inductive" and "resistive". In turn, the drive field and current can be alternating or constant. Along with this, the anisotropic properties of the magnetic medium and multilayer structures are widely used in magnetic sensors. The search-coil sensor is an ac inductive sensor, where the magnetic core may be isotropic or anisotropic.

The Hall sensor also should be attributed to a dc inductive isotropic sensor, since the Hall voltage is induced by the dc external magnetic field. The MR, GMR and MRST sensors are dc anisotropic resistive sensors.

The MI effect combines a number of features used in other sensors. The different components of the field dependent impedance matrix $\hat{\varsigma}$ exhibit the resistive or inductive effects. The longitudinal diagonal component ς_{zz} defines the complex resistance of the ferromagnetic sample, when it is excited by a high frequency current. Therefore ς_{zz} exhibits a purely resistive effect. The circular diagonal component $\varsigma_{\varphi\varphi}$ (the transverse diagonal component ς_{yy} in the case of MI film) can also be considered as the complex resistance but for the circular eddy currents induced in an MI sample by the ac longitudinal magnetic field. On the other hand, it is also an inductive coefficient, which relates the voltage induced in the secondary coil to the ac magnetic flux from the primary coil. Thus, it has a double nature. The diagonal components of the impedance matrix are present in magnetic and non-magnetic conductors. The off-diagonal components exhibit the inductive effect, when a certain polarisation of the excitation field is transformed into another one. These effects are absent in a non-magnetic sample but they can be present both in conducting and non-conducting magnetic samples. In our approach all resistive and inductive effects are unified in the total impedance matrix $\hat{\varsigma}$, which expresses the generalised Ohm's law, as has been explained in Chapters 2 and 3. The anisotropy plays a key role in forming the MI field dependences and their modifications by a dc bias field. A combination of anisotropy, bias field, different ac excitation and measuring methods results in various MI field dependences. Such vast options make the MI effect very attractive for multifunctional applications.

An MI thin film can have a multilayer structure, which looks like GMR or MRST structures. They coincide in the case of the magnetic anisotropy in the free layer (in MI multilayer structures all magnetic layers are "free"). However, the physical meaning and function of multilayer structures in MI and GMR/MRST are absolutely different. In the case of MI, the non-magnetic high conducting spacer is used to reduce the dc resistance of the multilayer structure and thereby to increase the normalised MI effect with respect to the dc level (zero frequency). Whereas in the case of GMR/MRST, the conducting spacer defines the quantum-tunnelling properties of the polarised electrons, and hence can be chosen extremely thin.

Now we would like to discuss the fundamental difference between MI and fluxgate sensors. In spite of the fact that the measurement schemes for parallel and orthogonal fluxgates are similar to those for measurements of $\varsigma_{\varphi\varphi}$ and $\varsigma_{\varphi z}$ respectively (see Fig. 2.16(b,d)), the physical mechanisms involved are completely different. In the case of the MI effect, a linear response is measured in an anisotropic magnetic system. A small ac excitation induces the magnetisation precession and domain wall displacements near the equilibrium state established by the magnetic anisotropy, dc external magnetic field H_{ex} and dc bias field H_b applied in the orthogonal way. The relationship between the induced ac magnetisation and the ac magnetic field can be expressed by a permeability matrix, which depends on the equilibrium state and determines the field dependence of the surface impedance matrix.

Contrariwise, in the case of the fluxgate mechanism a quite large ac excitation (current or field) realises the magnetisation reversal process in a ferromagnetic material with the non-linear B-H curve. The non-linear response is measured in the pickup coil, the amplitude of the higher harmonics turns out to be proportional to the external magnetic field H_{ex}. The magnetisation reversal is due mainly to domain wall irreversible processes and requires relatively low frequencies (less then 10 KHz). As a result, the sensitivity of fluxgate sensors rapidly degrades with increasing frequency.

Primary investigations of some MI sensors have been carried out by Professor Mohri's research group in the University of Nagoya, Japan.[1,22-25] For practical use, an MI element is incorporated into self oscillation circuits. Typical examples are: Colpitts oscillator or C-MOS IC multivibrator. The best performances of sensitive MI sensors show a field resolution of about 10^{-6} Oe (10^{-10} T) for the full scale of ± 1.5–2 Oe even with a sensor head length of about 1 mm. The cut-off frequency of the detected field is about 1/10 of the circuit oscillation frequency f_0 (100 kHz – 1 MHz for f_0 of 1-10 MHz, respectively). In the next Sections we will consider practical schemes of the MI sensors. Recently, **Aichi Steel LTD** (Japan) has started mass-production of portable earth's-field sensors based on the MI effect for cellar communication.

4.8 MI sensor with a Colpitts oscillator

Figure 4.9 shows a typical MI sensor design, in which an MI element (wire or thin film) is connected to a Colpitts oscillator – high frequency self-oscillation circuit. The MI element and two capacitors $C_{1,2}$ constitute a resonant circuit whose oscillation is maintained by the transistor. The oscillation frequency f_{res} depends on the dc external magnetic field H_{ex} and is of the form:

$$f_{res} = \frac{1}{2\pi\sqrt{LC_1C_2/(C_1+C_2)}}, \tag{9}$$

where $L(H_{ex})$ is the inductance of the MI element ($Z(H_{ex}) = R(H_{ex}) + i\omega L(H_{ex})$). Thus, the amplitude of ac current flowing through the MI element will strongly depend on H_{ex} because the oscillations occur near the resonance. The amplitude-modulated voltage due to H_{ex} is detected through a diode D and low frequency filter (R2-C3). Such a circuit can give a several times more sensitive output, than can the classical characteristics obtained at the condition of a constant current amplitude. However, the circuit does not have a high stability due to the resonance regime.

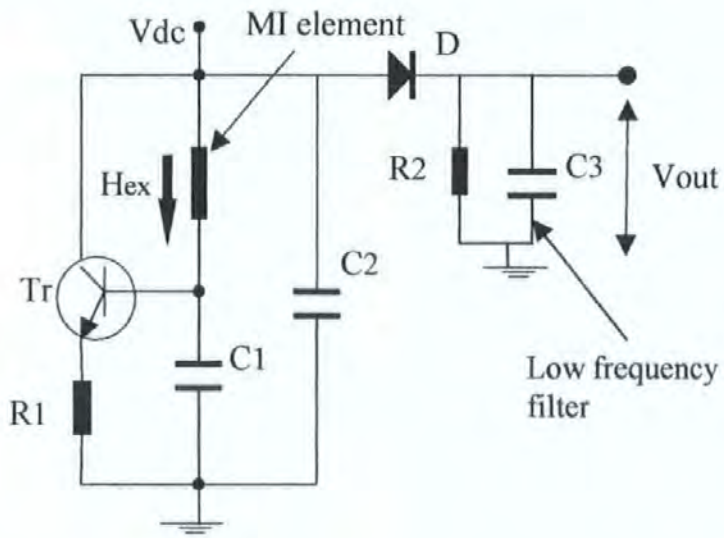

Fig. 4.9 *Principle MI sensor design with a Colpitts oscillator.*

On the other hand, the stability can be improved with other circuits, namely, C-MOS transistor multivibrator producing sharp voltage pulses at the MI element. Such a sensor scheme is considered in the next Section.

4.9 MI sensor with a C-MOS IC multivibrator

The circuit with a C-MOS IC multivibrator produces a sharp-pulsed current of duration 10–50 ns. Pulse excitation is preferred over sinusoidal excitation for several reasons, which include: simplicity of electronic design, low cost components, and high stability since the C-MOS multivibrator oscillation frequency almost does not depend on the impedance characteristics of the MI elements. Power consumption of this circuit is also small (10mW). In addition, such pulsed current involves both high frequency (20–100 MHz) and low (quasi-dc) harmonics. Therefore, it can be ideally used for the asymmetrical MI requiring dc or ac bias.

A circuit design shown in Fig. 4.10 was developed in the Centre for Research in Information Storage Technology (CRIST, University of Plymouth). The 74AC04 is a C-MOS TTL device used for its high-speed switching and low current capability. U1:A and U1:B are configured as a multivibrator with capacitor C1 and resistor R2 forming the timing network to give an approximate 250 KHz square wave pulse generator. The output of the multivibrator is fed to a differentiator circuit comprising R1 and C2 that causes the leading edge of the square wave to become a positive going 50 ns pulse. This pulse is applied to U1:C to improve its shape and applied directly to the MI element. The power consumption of the above circuit is minimal due to the drive for the MI element being a pulse of 50 ns at a pulse repetition rate of 8.5 ns achieving a 1/165 of the maximum reduction in power. The impedance of the MI element (wire or thin film) is connected between points "1" and "3" of the J2 connector, and its impedance is changed by an external magnetic field H_{ex} causing a change in the amplitude of the positive going pulse. The resistance R12 is chosen much bigger then the absolute value of MI impedance (at any H_{ex}) to keep excitation pulse-current constant. A Schottky high-speed detector D1 removes the negative half cycle caused by ringing of the MI and charges up C3 via R3 (100 Hz low pass filter) to give a DC voltage proportional to the applied magnetic field. Amplification of the DC is achieved by U3 (AD524) with a zero offset RV1, stabilised by D2, current set by R11 and decoupled by C6 to set the DC level to zero. U3 (AD524) is used to prove the system and would not be used in a working concern. The final DC output signal is taken from the J3 connector. It is envisaged that the basic components of the system would be a pulse generator, rectifier, and filter.

Often the MI field dependence has low sensitivity in the vicinity of zero field. Then, to achieve a maximum field sensitivity the operating point should be shifted from zero value by an additional dc bias field along the sample. In this case the electronic scheme will include an additional bias coil.

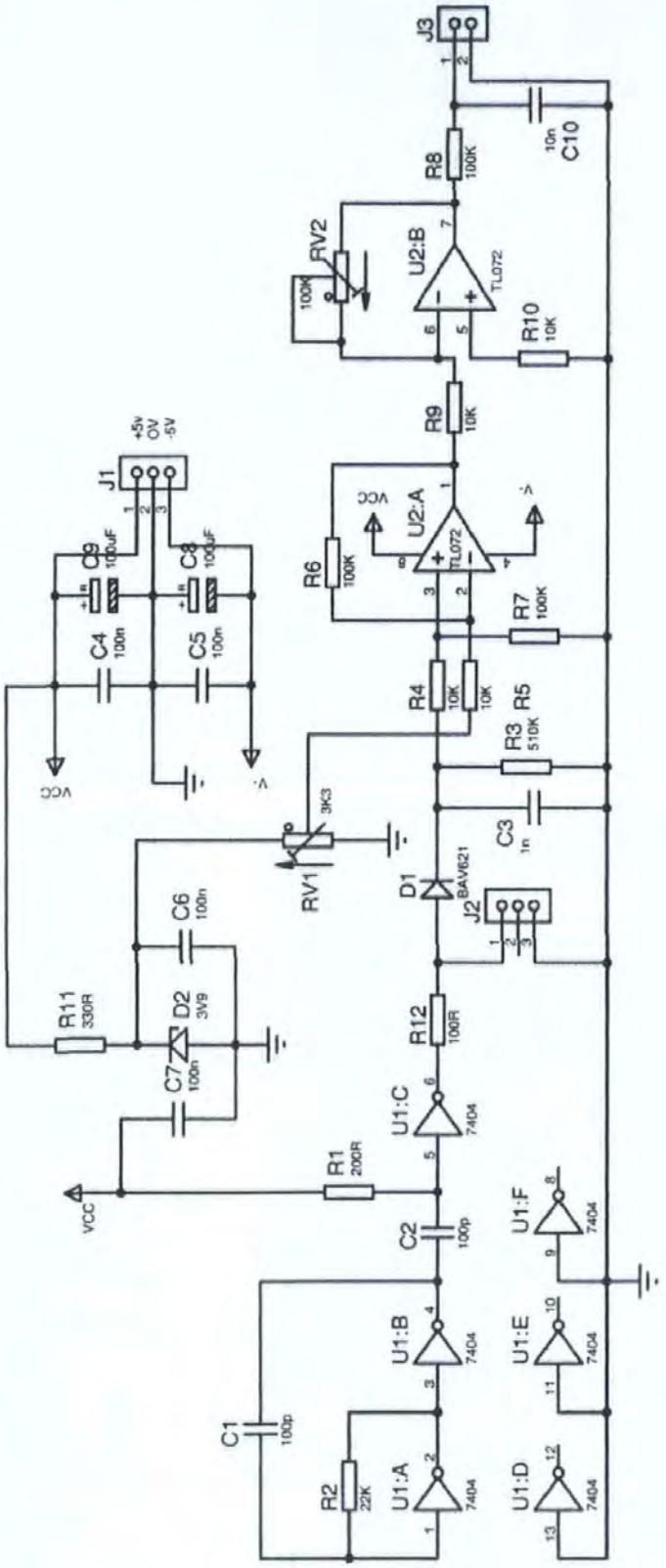

Fig. 4.10 *Principle MI sensor electronics design with a C-MOS IC multivibrator. MI element is connected between the points "1" and "2" of the J2 connector.*

4.10 Sensors using the antisymmetrical and asymmetrical MI effects

Typical MI sensors considered in Sections 4.8 and 4.9 are based on diagonal impedance (ς_{zz}) characteristics. In this case, a biasing technique is needed to set properly the operational region and realise linear sensing. In a number of recent works,[24,25] an output voltage is taken as a coil voltage, therefore, the off-diagonal impedance characteristics are used. In this case, the circuit design can be simplified and sensor parameters such as linearity and temperature stability are improved.

The antisymmetrical off-diagonal impedance studied in Chapters 2 and 3 (for more details see Sections 2.7.2, 2.8 and 3.7) can be successfully employed for the creation of a sensitive linear magnetic sensor. Several electronic schemes using a MI sensor with off-diagonal impedance in a wire have been proposed.[24] Here, we consider a circuit where the off-diagonal response ($\varsigma_{\varphi z}$ or ς_{yz}) is taken from the pick-up coil (V_c) and a single MI element (wire or thin film) is used. The principle electronic circuit is shown in Fig. 4.11, and includes: C-MOS IC multivibrator with invertors (Q), differential circuit (C1-R1), analogous synchronised switch, rectifier (R2-C2), differential amplifier, and negative feed-back. The C-MOS IC multivibrator (with invertors Q) produces smoothed rectangular pulses at a frequency of a few hundred kilohertz. After the differential circuit (C1-R1), the pulse is sharpened and so high frequency harmonics exist in its spectrum.

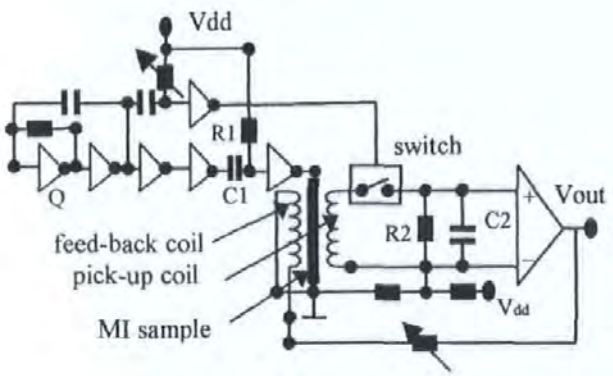

Fig. 4.11 *Principle electronic scheme using the off-diagonal impedance for a linear sensor.*

Pulse excitation is preferred over sinusoidal excitation for several reasons, these include: simplicity of electronic design, low cost components and high stability. In addition, the pulse spectrum contains a dc offset (zero harmonic) that provides a dc bias required for the existence of the off-diagonal response, as it has been discussed in Sections 2.72 and 3.7. Thus, the pulse circuit produces both the high-frequency excitation and dc bias. The ac off-diagonal pulsed response V_c is taken from the pick-up coil using the analogous synchronised switch and converted by the rectifier (R2-C2). The synchronous rectification suppresses noise that appears during the rectification time and produces a quasi-dc voltage of value, which is proportional to the original pulse amplitude. After this, the rectified voltage is amplified. This amplified signal is characterised by the amplitude and sign, both of which are sensitive to the dc external magnetic field H_{ex} since the off-diagonal response is used. Thus, a near-linear output voltage signal can be obtained without use of negative feed-back, which, however, can be added to further improve the linearity (feed-back coil is shown in Fig. 4.11). The circuit proposed in work [24] uses two MI elements and two analogous switches to create a balanced circuit with very high temperature stability.

Another method for obtaining a linear response is provided by so-called mixed excitation, the principle of which was considered in Sections 2.7.2 and 2.8 (see Fig. 2.21) for a wire with the circumferential anisotropy excited by both the ac longitudinal current j and the ac longitudinal magnetic field h_{ex}.[26,27] The same result is obtained for the film with transverse anisotropy and the coil round it (for example, planar microcoil described in Section 3.6). The excitation can be pulsed or sinusoidal. For the sinusoidal excitation an additional dc bias current is required to make off-diagonal response possible. The field h_{ex} can be induced by a coil mounted around the sample and connected in series. The output signal V_z is measured across the MI sample (see Fig. 2.21). The ac response is formed by the sum of the diagonal $\varsigma_{zz}(H_{ex})$ and off-diagonal $\varsigma_{zy}(H_{ex})$ (or $\varsigma_{z\varphi}(H_{ex})$) impedances with corresponding coefficients. Since $\varsigma_{zz}(H_{ex})$ and $\varsigma_{zy}(H_{ex})$ (or $\varsigma_{z\varphi}(H_{ex})$) are symmetrical and antisymmetrical, respectively, the field dependence of the output voltage module $|V_z(H_{ex})|$ is asymmetrical. The principle scheme of a linear sensor is shown in Fig. 4.12.

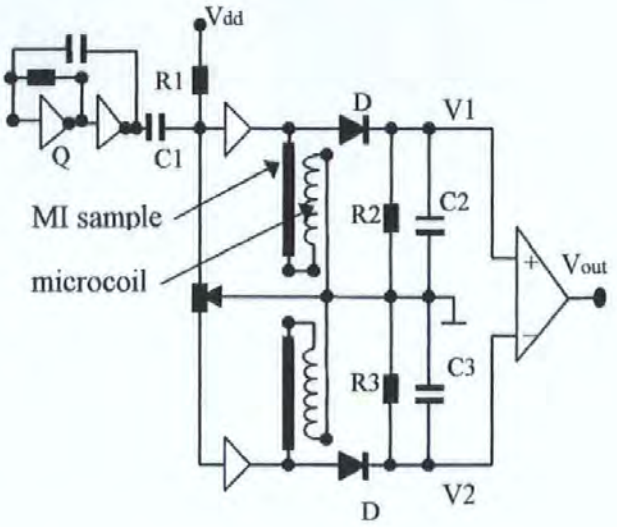

Fig. 4.12 *Electronic scheme using the mixed excitation for a linear sensor.*

The signals $V1(H_{ex})$ and $V2(H_{ex})$, taken from the two MI sensors with reverse asymmetries, are detected in a differential sense to produce the total linear field response $V_{dif}(H_{ex})$, as shown in Fig. 4.13.[27] Therefore, no additional bias field to produce a linear output response is required in this case as well. Theoretical investigation of the mixed excitation in a sandwich film has been carried in work [28].

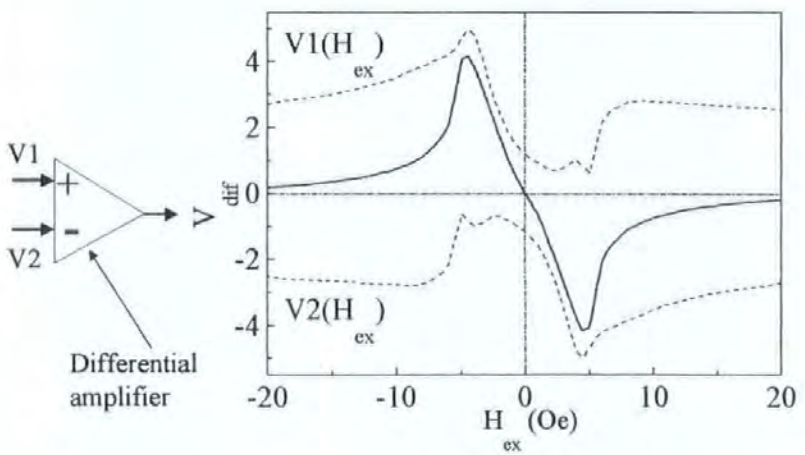

Fig. 4.13 *Principle of obtaining near-linear field dependence in the differential scheme. The signals* $V1(H_{ex})$ *and* $V2(H_{ex})$, *taken from the two MI sensors with reverse asymmetries, are detected in a differential amplifier to produce a final linear field response* $V_{dif}(H_{ex})$.

Also, the asymmetrical signals V1(H_{ex}) and V2(H_{ex}) can be obtained from the longitudinal impedance in wires with helical anisotropy (see Sections 2.6 and 2.7.3) or sandwich films with crossed anisotropy (see Section 3.5). For such sensors no additional coil (ac bias) is needed, but a dc bias current must be applied to produce asymmetry in the field dependence of an individual element.

4.11 References

[1] K. Mohri, L. V. Panina, T. Uchiyama, K. Bushida, and M. Noda, IEEE Trans. Magn. **31**, 1266 (1995).

[2] J. Clarke, "SQUIDs", Scientific American **271**, #2, 46 (1994).

[3] S. R. de Groot and L. G. Suttorp, *"Foundations of Electrodynamics"*, (North-Holland Publishing Company, Amsterdam 1972).

[4] J.-S. Lee, K.-H. Ahn, Y. H. Joeng, and D. M. Kim, Sensors and Actuators **A 57**, 183 (1996).

[5] M. Behet, J. Bekaert, J. De Boeck, and G. Borghs, Sensors and Actuators **A 81**, 13 (2000).

[6] A. Oral, S. J. Bending, M. Henini, Appl. Phys. Lett. **69**, 1324 (1996).

[7] G. A. Prinz, Science **250**, 1092 (1990).

[8] R. S. Popovic et al., Sensors and Actuators **A 91**, 46 (2001).

[9] L. M. Ross et al., J. Electronics **2**, 223 (1955)

[10] M. N. Baibich, M. Broto, A. Fert, F. Nguyen Van Dau, F. Petroff, P. Etienne, G. Creuzei, A. Frederic, and J. Chazelas, Phys. Rev. Lett. **61**, 2472 (1988).

[11] P. Grunberg, "Magnetic Field Sensor With Ferromagnetic Thin Layers Having Magnetically Antiparallel Polarized Components", U.S. Patent 4,949,039.

[12] J. S. Moodera, L. R. Kinder, T. M. Wong, and R. Meservey, Phys. Rev. Lett. **74**, 3273 (1995).

[13] E. Y. Tsymbal, O. N. Mryasov, and P. R. LeClair, J. Phys.: Condens. Matter **15**, 109 (2003).

[14] S. S. P. Parkin, K. P. Roche, M. G. Samant, P. M. Rice, R. B. Beyers, R. E. Scheuerlein, E. J. O'Sullivan, S. L. Brown, J. Bucchigano, D. W. Abraham, Yu Lu, M. Rooks, P. L. Trouilloud, R. A. Wanner, and W. J. Gallagher, J. Appl. Phys. **85**, 5828 (1999)

[15] Y. Ohno, D. K. Young, et. al, Nature **402**, 790 (1999).

[16] F. Primdahl, IEEE Trans. Magn. **MAG-6**, 376 (1970).

[17] P. Ripka, Sensors and Actuators **A 33**, 129 (1992).

[18] P. Ripka, J. Magn. Magn. Mater. **215/216**, 735 (2000).

[19] O. Dezuari, E. Belloy, S. E. Gilbert, and M. A. M. Gijs, Sensors and Actuators **A 81**, 200 (2000).

[20] S. Choi, S. Kawahito, K. Tahashi, Y. Matsumoto, M. Ishida, and Y. Tadokoro, Sensors and Materials **9**, 241 (1997).

[21] P. Kejik, L. Chiesi, B. Janossy, and R. S. Popovic, Sensors and Actuators **A 81**, 180 (2000).

[22] K. Mohri, T. Uchiyama, and L. V. Panina, Sensors and Actuators **A 59**, 1 (1997).

[23] K. Mohri, T. Uchiyama, L. P. Shen, C. M. Cai, and L. V. Panina, Sensors and Actuators **A 91**, 85 (2001).

[24] N. Kawajiri, M. Nakabayashi, C. M. Cai, K. Mohri, and T. Uchiyama, IEEE Trans. Magn. **35**, 3667 (1999).

[25] Y. Honkura, M. Yamamoto, Y. Kohtani, and K. Mohri, **Digest CD 10**, The Intermag Conference 2002, Amsterdam, The Netherlands.

[26] D. P. Makhnovskiy, L. V. Panina, and D. J. Mapps, Appl. Phys. Letters **77**, 121 (2000).

[27] L. V. Panina, D. P. Makhnovskiy, D. J. Mapps, K. Mohri, and P. I. Nikitin, Materials Science Forum **373/376**, 741 (2001).

[28] D. P. Makhnovskiy, L. V. Panina, and D. J. Mapps, J. Magn. Magn. Mater. **215/216**, 629 (2000).

Chapter 5 Tuneable composites

5.0 Field-dependent permittivity of composite containing the MI wire inclusions

Up to the present, the GMI effect has been investigated for the use in highly sensitive magnetic sensors, however, the applications of this effect can be much wider.[1] Typically, MI sensors are designed for MHz frequencies,[2] which is dictated by the related electronics. On the other hand, the field sensitivity of the surface impedance in wires with a circumferential anisotropy remains very high even at the GHz range. *In this Chapter, a new type of the composite material is advanced, the effective microwave permittivity of which can be controlled by the static magnetic field* H_{ex}.[1] Short pieces of ferromagnetic microwires [3-5] are proposed as filling inclusions. They interact with the electromagnetic radiation similar to microantennas. Then, the wire length l and dielectric matrix permittivity ε define the operating frequency range with the characteristic frequency related to the antenna resonance. In the vicinity of the antenna resonance, even small variations in the surface impedance result in a considerable change in the current density distribution at the wire and, consequently, in the induced dipole moment of the elementary wire-scatterer. Thus, the MI effect can be useful to design microwave composites with tuneable properties and tuneable band-gap structures.[6]

Metal-dielectric composite materials have received much attention because of their importance in modern technology.[see, for example, [7] and references therein] Metallic inclusions, in particular metallic wires, can reinforce the dielectric and magnetic properties of ceramics and plastic materials. [7-14] Electromagnetic properties of the composite materials are analysed customarily in terms of the effective macroscopic parameters: dielectric permittivity ε_{eff} and magnetic permeability μ_{eff}, which are calculated by averaging the responses from material constituents.[1] Composite materials containing elongated conducting inclusions – finite length wires [8-10] or arrays of infinitely long wires [11-14] – present a considerable interest since their dielectric response can exhibit various dispersive behaviours. The composite can be prepared as a thin sheet or bulk sample. The microstructures of the thin composite samples are indicated in Figs. 5.1(a),(b) for "short" and "long" wires embedded into a thin dielectric sheet (matrix). The typical length of the short wire inclusions is less than 1 cm. The sheet thickness h is made much less than the wire length l, and hence usually it is about a few millimetres or less.

The short wire inclusions have random orientations in the plane of the sample, whereas the long wires usually are oriented in a certain direction. The dc magnetic field H_{ex} is applied along the plane of the sample.

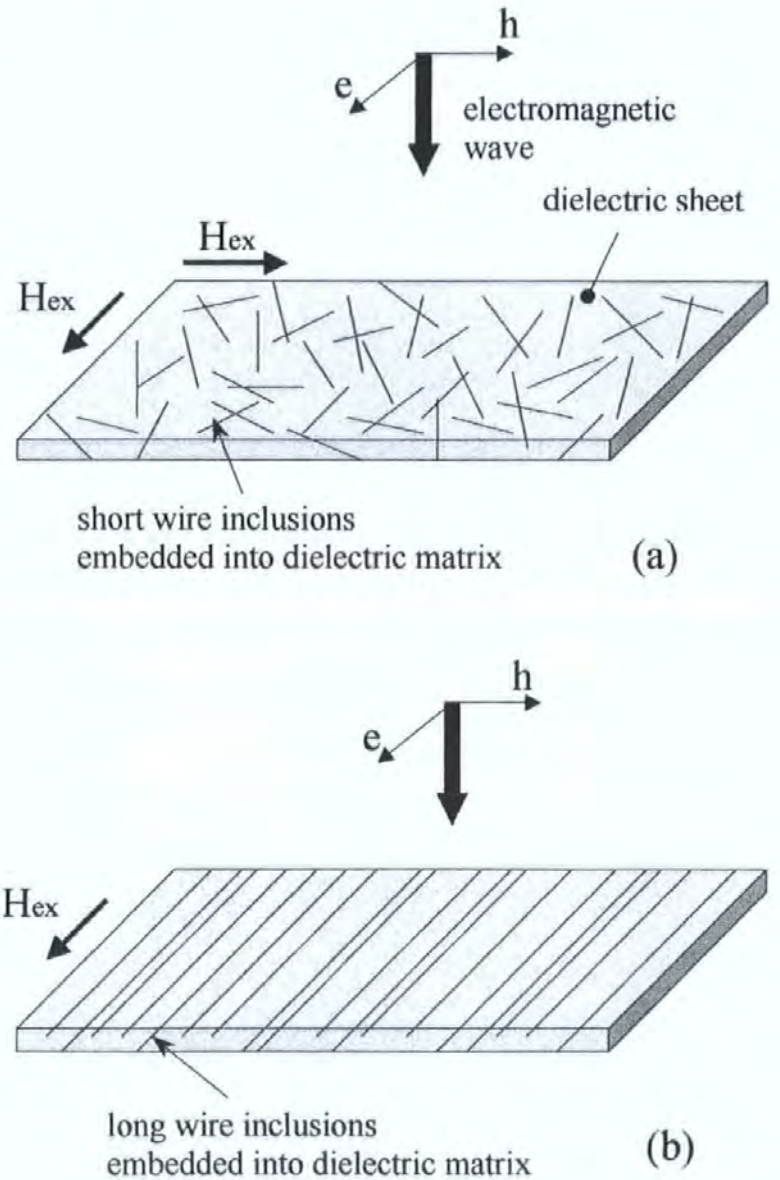

Fig. 5.1 *The microstructures of the thin composite samples for "short" in (a) and "long" in (b) wires embedded into a thin dielectric sheet (matrix). The sheet thickness h is much less than the wire length l. The short wire inclusions have random orientations in the plane of the sample, whereas the long wires usually are oriented in a certain direction.*

The bulk sample with long wires can be formed as a 3D "wire crystal", where a periodic structure is composed of wires arranged in a lattice. Figure 5.2 demonstrates a simple cubic cell of the wire crystal.[13]

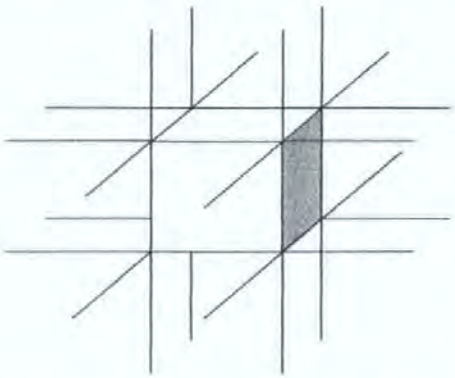

Fig. 5.2 *A periodic structure is composed of wires arranged in a simple cubic lattice, which is a cell of the wire crystal.*

Finite-wire inclusions behave as electric dipole scatterers. In this case, the dispersion of the effective permittivity can range from a relaxation type to a resonance one, depending on the inclusion conductivity and dimension.[8-10] The resonant spectrum of ε_{eff} occurs near the antenna resonance for an individual wire-inclusion. The real part of ε_{eff} can take negative values past the resonance, which is very important for a recent trend to create materials with a negative refraction index.[15,11-14] This characteristic behaviour of the effective permittivity was experimentally confirmed for diluted composites with carbon wires having a low conductivity (relaxation spectrum) and highly conductive aluminium–coated wires (resonant spectrum).[9] In such composites, the concentration of the percolation threshold is proportional to the aspect ratio $p_c \propto 2a/l$,[10] where a is the wire radius and l is the wire length. In the limit $2a/l << 1$, p_c is very small, however, the inclusion contribution to the effective dielectric constant becomes large already for very small concentrations $p << p_c$. *In this Chapter we demonstrate that the physical quantity controlling the dispersion characteristics of* ε_{eff} *in diluted wire-composites is the surface impedance, which involves both the conductivity and permeability of inclusions.* Therefore, in the case of ferromagnetic wires the effective permittivity may depend on a static magnetic field via the corresponding dependence of the ac permeability matrix.

The theory developed is based on solving the scattering problem for a wire with the impedance boundary conditions. A new integro-differential equation for the current density distribution in a wire is obtained, which is valid for the surface impedance matrix of a general form. The electric polarisability of an inclusion is represented by the integral over the longitudinal current density and is proven to be very sensitive to the impedance changes near the antenna resonance. In Ref. 10, the current distribution at a conducting stick was determined from an approximate differential equation of a transmission line type. Our approach has a number of advantages. It gives a rigorous mathematical algorithm as an expansion in serious of $1/2\ln(l/a)$ valid for any frequency and the surface impedance of a general matrix form. There is no need to introduce the effective distributed parameters such as a specific capacitance and an inductance which have to be determined separately. The most important is that the method accounts correctly for the radiation effects and can be generalised to the case of interacting inclusions or inclusions interacting with boundaries and interfaces. Then, it can be useful to calculate the effective permittivity of composites containing periodically spaced wires, without invoking the effective medium theory. For thin composite sheets, the effective permittivity depends on the thickness due to the depolarisation effect from the boundaries.[16,17] As a result, the dispersion region of ε_{eff} is shifted to higher frequencies.

The composite material made of an array of infinitely long conductive wires [13,14] has characteristic features of a metallic response to radiation, but in the GHz range. Contrary to the composite with short inclusions, the electromagnetic field is applied locally to a certain portion of the material excluding the ends of wires. In this case the current distribution in the wire can be neglected. The most interesting results are obtained for the wave polarisation where the electric field is along the wires. Such wire-mesh systems model the response of a diluted plasma,[7,13] giving a negative permittivity $\varepsilon_{eff}(\omega)$ below the normalised plasma frequency $\tilde{\omega}_p = \omega_p / \sqrt{\varepsilon}$ somewhere in the gigahertz range: $\varepsilon_{eff}(\omega) = \varepsilon - \omega_p^2 / \omega^2$, where ε is the matrix permittivity and ω_p is the "plasma frequency". In a general case, when the skin effect is not very strong, the plasma frequency depends on the wire impedance.[7] Therefore, the effective permittivity of wire-mesh materials can be also controlled by a magnetic field, as will be considered elsewhere.

5.1 General approach to the effective permittivity of wire-composites

In this Section we consider general properties of the effective permittivity of composites with finite-wire inclusions. From the above discussion it follows that the dispersion of ε_{eff} has different origins for "short" and "long" inclusions. In the first case, the composites demonstrate the Lorentz dipole dispersion,[18] whereas the second type of material is characterised by the Drude dispersion typical of free-electron gas.[7,13,14]

The Lorentz model of dispersion is applicable to insulator materials. The composite with short inclusions is similar in many respects to an isolator since the wire-inclusions play a role of "atoms" (elementary dipole scatterers), which are polarised with an ac electric field. The local electrical field $e_{loc}\exp(-i\omega t)$ induces the current with a linear density $j(z)\exp(-i\omega t)$ distributed along the inclusion length (z is the coordinate along the conductor). The electric dipole moment D and the dielectric polarisability $\wp$ of the inclusion are calculated using the continuity equation $\partial j(z)/\partial z = i\omega\rho(z)$ and integrating by parts with boundary conditions $j(\pm l/2)\equiv 0$ (ρ is the charge density per unit length):

$$D = \frac{i}{\omega}\int_{-l/2}^{l/2} j(z)dz\,, \qquad \wp = D/(V\,e_{loc})\,, \tag{1}$$

where V is the inclusion volume. As it will be shown later, the density $j(z)$ of a linear current can be approximated by a linear differential equation of the second order with the boundary conditions $j(\pm l/2)\equiv 0$ and involving a certain damping caused by radiation and internal resistive and magnetic losses. Thus, as in the case of a Lorentz oscillator the polarisability $\wp$ has the following form:[18]

$$\wp = \sum_n \frac{A_n}{(\omega_{res,n}^2 - \omega^2) - i\Gamma_n\omega}, \tag{2}$$

where the summation is carried out over all antenna resonance frequencies $\omega_{res,n} = 2\pi c/\lambda_{res,n}$ in increasing order, $\lambda_{res,n} = 2l\sqrt{\varepsilon}/(2n-1)$ [19] are the resonance wavelengths, ε is the matrix permittivity, A_n are the amplitude constants, Γ_n are the dumping parameters. The first resonance $n=1$ with the lowest frequency has a maximum amplitude A_1 and gives the main contribution to the polarisability.

Each Γ_n can be decomposed into two parts Γ_n^{rad} and $\Gamma_n^{mr}(H_{ex})$ related to the radiation and internal (magnetic and resistive) losses, respectively. The damping parameter Γ_n^{mr} involving magnetic losses may depend on an external magnetic field H_{ex}. Thus, in the vicinity of the antenna resonance the polarisability ϑ will depend on H_{ex} if the condition $|\Gamma_n^{mr}| \geq |\Gamma_n^{rad}|$ is held.

The bulk polarisation $\mathbf{P}$ of the composite is of the form: $\mathbf{P} = < e_{loc} > p\wp = \mathbf{e}_0 \vartheta_{eff}$, where $< e_{loc} >$ is the averaged local field, p is the volume concentration of the inclusions, $\mathbf{e}_0$ is the external electrical field, and ϑ_{eff} is the effective bulk susceptibility. Although the wire length is comparable with the wavelength, it is still possible to introduce the susceptibility ϑ_{eff} since the scattered electromagnetic field has a dipole character at large distances from the composite. To relate the polarisability $\wp$ to the effective bulk susceptibility ϑ_{eff}, it is necessary to know the relation between the local field e_{loc} and the external field e_0. For very low inclusion concentrations $p << p_c$, where p_c is the percolation threshold, it is possible to assume that $< e_{loc} > \approx e_0$, which leads to the simplest equation for the effective permittivity:

$$\varepsilon_{eff} \approx \varepsilon + 4\pi p < \wp >, \qquad (3)$$

where $< \wp >$ is the polarisability averaged over the inclusion orientations. In the limit of a small concentration, the difference between the local and mean fields can be taken into account using the Lorentz approach [18] and its generalisations.[20] A consistent effective medium theory for the considered composites valid for any concentration employs the concept of the scale-dependent local-field permittivity.[10,9,17] This approach gives the percolation threshold p_c that is linearly proportional to the aspect ratio of the conducting inclusions ($p_c \propto 2a/l$) in accordance with the experimental data. In this Chapter we restrict ourselves to the case of non-interacting inclusions since this model provides all the essential features to describe the dispersion and field-dependent properties of ε_{eff} in diluted composite materials ($p << p_c$).

5.2 Antenna approximation and impedance boundary conditions

Within the framework of a single particle approximation the scattering problem for a thin conductor has to be solved. Considering the electromagnetic response from a thin conductor, the induced current in it can be replaced with the effective linear current flowing along the axis and having only the axial distribution. This approach is known as the antenna approximation.[21] It is important to re-examine the conditions when the antenna approximation is valid.

Let us consider a thin conductor irradiated by an electromagnetic field. The wavelength λ and the conductor length l are assumed to be much larger than the conductor cross size $2a$: $2a << \lambda$ and $2a << l$. The incident electromagnetic wave is supposed to be of a plane type. In this case, the external electric field does not induce a circular current, and the external magnetic field does not give a contribution to a circular magnetic field on the conductor surface. First we consider that the incident wave has a longitudinal electric field $\bar{e}_{z0}$ at the surface of a nonmagnetic conductor. In this case, the induced current is longitudinal, which determines the scattered electromagnetic field having longitudinal electric $\bar{e}_z$ and circular magnetic $\bar{h}_\varphi$ components on the conductor surface (cylindrical conductor is considered, φ is the azimuthal coordinate). The same polarisation $(\bar{e}_z, \bar{h}_\varphi)$ can be induced by a linear current with the volume density $j(z)\delta_S$ flowing along the axis, where z is a point on the axis and δ_S is a two dimensional Dirac function. Further the function $j(z)$ will be referred to as "linear density" or "density". Thus, the linear longitudinal current plays a role of an effective current producing the surface field of the required polarisation $(\bar{e}_z, \bar{h}_\varphi)$ and intensity. If the incident electromagnetic field contains a longitudinal magnetic component $\bar{h}_{z0}$, a circular electric field $\bar{e}_\varphi$ will be induced in the conductor. In this case, a longitudinal linear current does not provide the total polarisation of the scattered field. In a general case of a magnetic conductor the field $\bar{h}_{z0}$ will induce $\bar{e}_z$ and the field $\bar{e}_{z0}$ will induce $\bar{h}_\varphi$. However, the total scattered field can be decomposed into two basic waves with polarisations: $(\bar{e}_z, \bar{h}_\varphi)$ and $(\bar{e}_\varphi, \bar{h}_z)$, where $(\bar{e}_z, \bar{h}_\varphi)$ is determined by the linear current. The other polarisation $(\bar{e}_\varphi, \bar{h}_z)$ can be calculated directly from the impedance boundary condition, which represents a linear relationship between $\bar{e}$ and $\bar{h}$ (see below).

The polarisation effects arising due to the radial electric and magnetic fields can be neglected in this case. Thus, the concept of the linear effective current describes correctly the scattered field at any polarisation of the incident wave.

In the antenna approximation, the external scattering problem with the boundary conditions at the conductor surface completely determines the response from a thin inclusion irradiated by an external electromagnetic field. The most general form of such linear boundary relationship can be written with the use of the surface impedance matrix $\hat{\varsigma}$:[22]

$$\bar{\mathbf{E}}_t = \hat{\varsigma}(\bar{\mathbf{H}}_t \times \mathbf{n}), \tag{4}$$

where $\mathbf{n}$ is the unit normal vector directed inside the conductor, $\bar{\mathbf{E}}_t$ and $\bar{\mathbf{H}}_t$ are the tangential vectors of the total electric and magnetic fields at the conductor surface, which include both the scattered and external electromagnetic fields, $\hat{\varsigma}$ is the second order matrix. In the case of an ideal conductor (conductivity $\sigma = \infty$) boundary condition (4) reduces to a simple generally used form: $\bar{\mathbf{E}}_t \equiv 0$. Boundary condition (4) is convenient to express in the local cylindrical coordinate system (z, φ, r) related to the conductor:

$$\begin{aligned} \bar{E}_z &= \varsigma_{zz}\bar{H}_\varphi - \varsigma_{z\varphi}\bar{H}_z \\ \bar{E}_\varphi &= \varsigma_{\varphi z}\bar{H}_\varphi - \varsigma_{\varphi\varphi}\bar{H}_z \end{aligned}. \tag{5}$$

The matrix $\hat{\varsigma}$ has been found in Sections 2.4 and 2.5 for a ferromagnetic wire with an arbitrary type of the magnetic anisotropy for the strong and weak skin-effect, respectively. In a nonmagnetic conductor this parameter has a diagonal form where $\varsigma_{z\varphi} = \varsigma_{\varphi z} \equiv 0$.

As it follows from the antenna approximation conditions, the field $\bar{H}_\varphi(z)$ contains only the circular field $\bar{h}_\varphi(z)$ induced by a current with the linear density $j(z)$. On the contrary, the longitudinal field $\bar{H}_z$ is entirely defined by the excitation field. The scattered field $\bar{h}_\varphi(z)$ will be found together with the antenna equation in the next Section. Note that in a cylindrical conductor the impedance boundary condition (5) is valid for any frequency including a weak skin effect.

5.3 Antenna equation with the impedance boundary condition

Now we are in a position to obtain the basic integro-differential equation for the current density $j(z)$ using impedance boundary condition (5). The time dependence is taken as $\exp(-i\omega t)$, where $\omega = 2\pi f$ and f is the frequency of the electromagnetic field. Gaussian units are used throughout the Chapter. Let us introduce the vector $\mathbf{A}$ and scalar φ potentials:

$$\mathbf{h} = \frac{4\pi}{c}\operatorname{rot}\mathbf{A}, \qquad \mathbf{e} = -\operatorname{grad}\varphi - \frac{4\pi\mu}{c^2}\frac{\partial \mathbf{A}}{\partial t}, \tag{6}$$

where c is the velocity of light, ε and μ are the scalar dielectric and magnetic constants outside the conductor (complex in general). In Section 3.8, where the magnetic permeability was a matrix, we used another representation for the potentials (see Eqs. 3.15 and 3.16). The Lorentz gauge is accepted for the potentials: $\varepsilon\partial\varphi/\partial t + 4\pi\operatorname{div}\mathbf{A} = 0$. The electrical field $\mathbf{e}$ can be expressed through the vector potential in a frequency representation:

$$\mathbf{e} = \frac{4\pi i\omega\mu}{c^2}\mathbf{A} - \frac{4\pi}{i\omega\varepsilon}\operatorname{grad}\operatorname{div}\mathbf{A}. \tag{7}$$

For $\mathbf{A}$ we obtain the Helmholtz equation:

$$\Delta\mathbf{A} + k^2\mathbf{A} = \mathbf{j}, \tag{8}$$

where $k = (\omega/c)\sqrt{\varepsilon\mu}$ is the wave number, $\mathbf{j}$ is the vector of the current density $j(z)$.

The solution of Eq. (8) can be written in the form of the convolution of $\mathbf{j}(\mathbf{z})$ with the Green function $G(r)$ of the Helmholtz operator:

$$\mathbf{A}(\mathbf{r}_0) = (G * \mathbf{j}) = \int_V \mathbf{j}(\mathbf{z})G(r)dV_{\mathbf{z}}, \qquad G(r) = \frac{\exp(ikr)}{4\pi r}, \tag{9}$$

where the integration is carried out over the total volume V containing $\mathbf{j}$. In Eq. (9) $\mathbf{r}_0$ is the coordinate of the point where $\mathbf{A}$ is calculated (observation point), $\mathbf{z}$ is the vector directed to the coordinate of the integration point, and $r = |\mathbf{r}_0 - \mathbf{z}|$ is the distance between the observation and integration points.

From Eqs. (6) and (9) we obtain the representation for the magnetic field induced by a linear current (operator "rot" in (6) is taken at $\mathbf{r}_0$):

$$\mathbf{h}(\mathbf{r}_0)=\frac{1}{c}\int_V \frac{(1-ikr)\exp(ikr)}{r^3}(\mathbf{j}(\mathbf{z})\times\mathbf{r})dV_{\mathbf{z}}, \tag{10}$$

where $\mathbf{r}=\mathbf{r}_0-\mathbf{z}$ is the vector directed to the observation point from the integration one. In the case of a linear current, when $\mathbf{j}$ is taken at the contour L, the field projection on the unit vector υ reduces to a kind of a contour integral:

$$h(\mathbf{r}_0)=\frac{1}{c}\int_L \frac{(1-ikr)\exp(ikr)}{r^3} j(s)\xi(s,\mathbf{r})ds, \tag{11}$$

where $\mathbf{j}=j(s)\boldsymbol{\tau}_s$, $\boldsymbol{\tau}_s$ is the tangential vector along L taken at the integration point s, $\xi(s,\mathbf{r})=((\boldsymbol{\tau}_s\times\mathbf{r})\cdot\upsilon)$ is the scalar multiplication designating the projection of $(\boldsymbol{\tau}_s\times\mathbf{r})$ on the unit vector υ. Considering a cylindrical symmetry, a circular magnetic field is equal to a projection of $\bar{\mathbf{h}}(\mathbf{r}_0)$ on the direction $(\boldsymbol{\tau}_s\times\mathbf{r})$:

$$\bar{h}_\varphi(z,a)=\frac{a}{c}\int_{-l/2}^{l/2} \frac{(1-ikr)\exp(ikr)}{r^3} j(s)ds, \tag{12}$$

where $r=\sqrt{(z-s)^2+a^2}$. In (12) the equality $|(\boldsymbol{\tau}_s\times\mathbf{r})|=a$ was used. Contrary to the static case ($\omega=0$) where $\bar{h}_\varphi=2I/ac$ and I is the total current, Eq. (12) takes into account the retarding effects. Note that integral (12) has extremely fast convergence, therefore, the field $\bar{h}_\varphi$ appears to be almost local even for very high frequencies.

The component A_z of the vector potential $\mathbf{A}$ describes the scattered field from a straight piece of a thin conductor. Using Eqs. (7) and (9), the longitudinal scattered field $e_z(x,y,z)$ can be expressed in terms of an integro-differential operator, where the convolution is carried out along the longitudinal coordinate z:

$$e_z(x,y,z)=-\frac{4\pi}{i\omega\varepsilon}\left[\frac{\partial^2}{\partial z^2}(G*j)+k^2(G*j)\right]. \tag{13}$$

Here $(G*j)=\int_{-l/2}^{l/2} j(s)G(r)ds$ and $r=\sqrt{(z-s)^2+y^2+x^2}$. On the conductor surface, it is necessary to put $r=\sqrt{(z-s)^2+a^2}$. Using the impedance boundary condition (5) and Eq. (13) we obtain the integro-differential equation for the current density $j(z)$:

$$\bar{E}_z \equiv -\frac{4\pi}{i\omega\varepsilon}\left[\frac{\partial^2}{\partial z^2}(G*j)+k^2(G*j)\right]+\bar{e}_{0z}(z)=\varsigma_{zz}\bar{h}_\varphi(z)-\varsigma_{z\varphi}\bar{h}_{0z}(z), \tag{14}$$

where $\bar{E}_z \equiv \bar{e}_z+\bar{e}_{0z}$ is the total longitudinal electric field on the conductor surface, $\bar{e}_z$ is the scattered electrical field on the conductor surface, $\bar{e}_{0z}$ and $\bar{h}_{0z}$ are the external electrical and magnetic fields on the conductor surface. The components ς_{zz} and $\varsigma_{z\varphi}$ can also be functions of the variable z, but this case is not considered here.

The surface field $\bar{h}_\varphi$ is useful to be written in terms of convolution with $j(z)$:

$$\bar{h}_\varphi(z,a)=\frac{2}{ac}(G_\varphi * j)=\frac{2}{ac}\int_{-l/2}^{l/2} j(s)G_\varphi(r)ds, \tag{15}$$

where $G_\varphi(r)=\dfrac{a^2(1-ikr)\exp(ikr)}{2r^3}$.

Finely, we obtain the basic integro-differential equation for $j(z)$:

$$\frac{\partial^2}{\partial z^2}(G*j)+k^2(G*j)=\frac{i\omega\varepsilon}{4\pi}\bar{e}_{0z}(z)-\frac{i\omega\varepsilon\varsigma_{zz}}{2\pi ac}(G_\varphi * j)+\frac{i\omega\varepsilon\varsigma_{z\varphi}}{4\pi}\bar{h}_{0z}(z). \tag{16}$$

Equation (16) has to be completed imposing the boundary conditions at the ends of the conductor:

$$j(-l/2)=j(l/2)\equiv 0. \tag{17}$$

Equation (16) takes into account both the radiation losses and losses consumed inside the conductor (resistive and magnetic). The convolution $(G_\varphi * j)$ and ς_{zz} determine the internal losses, which are absent in usual antenna equations where the condition of the ideal conductivity ($\sigma=\infty$) is assumed. The imaginary part of $(G*j)$ determines the radiation losses.

Along with this, there is an additional term in the right part of Eq. (16), related with the off-diagonal component $\varsigma_{z\varphi}$. Thus, the ferromagnetic conductor can be excited not only by a longitudinal electric field, but also by a longitudinal magnetic field.[23]

As it follows from Eqs. (13) and (15), the real functions Re(G) and Re(G_φ), considered at the conductor surface, have a sharp peak at $r = a$. Thus, Re(G) and Re(G_φ) give the main contribution to Eq. (16): $|(\mathrm{Im}(G) * j)| << |(\mathrm{Re}(G) * j)|$ and $|(\mathrm{Im}(G_\varphi) * j)| << |(\mathrm{Re}(G_\varphi) * j)|$. However, the convolutions with the imaginary parts are important in the vicinity of the resonance and can be taken into account by an iteration procedure, which is described in Appendix A. For the calculation of convolutions with functions Re(G) and Re(G_φ) it is possible to use an approximate method:[24,16,17]

$$(\mathrm{Re}(G) * j) \approx j(z) \int_{-l/2}^{l/2} \mathrm{Re}(G(r))ds = j(z)Q,$$

$$Q = \int_{-l/2}^{l/2} \mathrm{Re}(G(r))ds \propto \frac{1}{4\pi} \int_{-l/2}^{l/2} \frac{ds}{\sqrt{s^2 + a^2}} \sim \frac{\ln(l/a)}{2\pi}, \tag{18}$$

$$(\mathrm{Re}(G_\varphi) * j) \approx j(z) \int_{-l/2}^{l/2} \mathrm{Re}(G_\varphi(r))ds = j(z)Q_\varphi,$$

$$Q_\varphi = \int_{-l/2}^{l/2} \mathrm{Re}(G_\varphi(r))ds \propto \frac{a^2}{2} \int_{-l/2}^{l/2} \frac{ds}{(s^2 + a^2)^{3/2}} + \frac{a^2k^2}{2} \int_{-l/2}^{l/2} \frac{ds}{\sqrt{s^2 + a^2}} \propto (1 + a^2k^2 \ln(l/a)) \sim 1,$$

where $r = \sqrt{(z-s)^2 + a^2}$, Q and Q_φ are the positive form-factors. For the estimation of Q_φ it was taken into account that $ak << 1$ in the antenna approximation.

From Eq. (16) and inequalities $|(\mathrm{Im}(G) * j)| << |(\mathrm{Re}(G) * j)|$ and $|(\mathrm{Im}(G_\varphi) * j)| << |(\mathrm{Re}(G_\varphi) * j)|$ we obtain differential equation for the zero approximation $j_0(z)$ where the radiation losses are neglected:

$$\frac{\partial^2}{\partial z^2} j_0(z) + \left(\frac{\omega}{c}\right)^2 \varepsilon\mu \left(1 + \frac{ic\,\varsigma_{zz}}{2\pi a \omega \mu} \frac{Q_\varphi}{Q}\right) j_0(z) \approx \frac{i\omega\varepsilon}{4\pi Q} \left[\bar{e}_{0z}(z) + \varsigma_{z\varphi} \bar{h}_{0z}(z)\right]. \tag{19}$$

As it follows from Eq. (19), the implementation of the impedance boundary condition leads to the renormalisation of the wave number which becomes:

$$\tilde{k} = \frac{\omega}{c}\sqrt{\varepsilon\mu}\left(1+\frac{ic\varsigma_{zz}}{2\pi a\omega\mu}\frac{Q_\varphi}{Q}\right)^{1/2} \propto \frac{\omega}{c}\sqrt{\varepsilon\mu}\left(1+\frac{ic\varsigma_{zz}}{a\omega\mu\ln(l/a)}\right)^{1/2}. \qquad (20)$$

The effective wave number $\tilde{k}$ defines the normalised resonance wavelength ($k_{res}l = \pi(2n-1)$):[19]

$$\lambda_{res,n} = \frac{2l}{2n-1}\sqrt{\varepsilon\mu}\,\mathrm{Re}\left(1+\frac{ic\varsigma_{zz}}{2\pi a\omega\mu}\frac{Q_\varphi}{Q}\right)^{1/2} \propto \frac{2l}{2n-1}\sqrt{\varepsilon\mu}\,\mathrm{Re}\left(1+\frac{ic\varsigma_{zz}}{a\omega\mu\ln(l/a)}\right)^{1/2}. \qquad (21)$$

$n = 1,\ 2,\ 3\ \ldots$

Further we will consider only the first resonant frequency $f_{res} = c/\lambda_{res,1}$ at which the composite produces a maximal response. It is useful to investigate the forms of the current density distribution along the wire for different frequencies, as shown in Figs. 5.3 and 5.4.

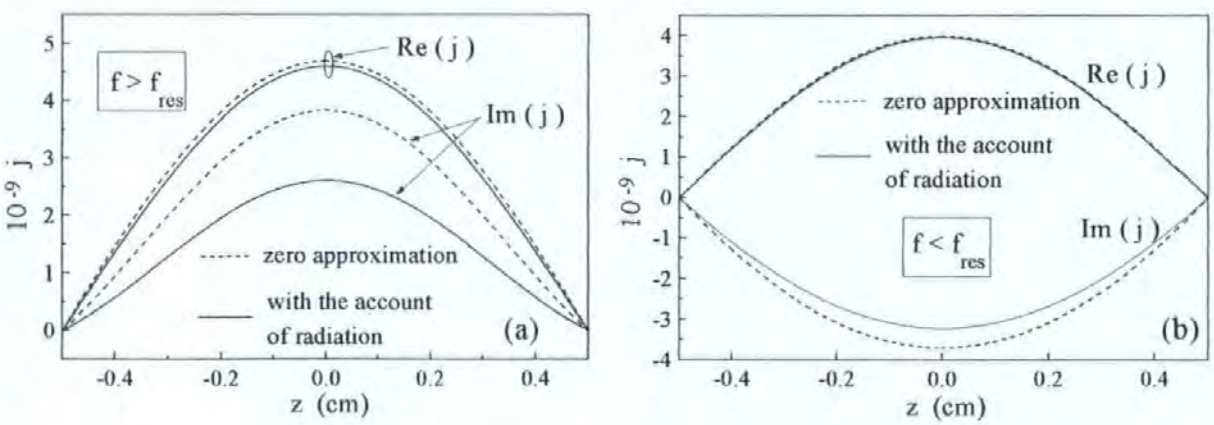

Fig. 5.3 *Typical current density distribution along a wire inclusion above ($f > f_{res}$ in (a)) and below ($f < f_{res}$ in (b)) the antenna resonance. The dashed and solid curves correspond to the zero (Eq. (19)) and first (Eq. (A9)) approximations, respectively.*

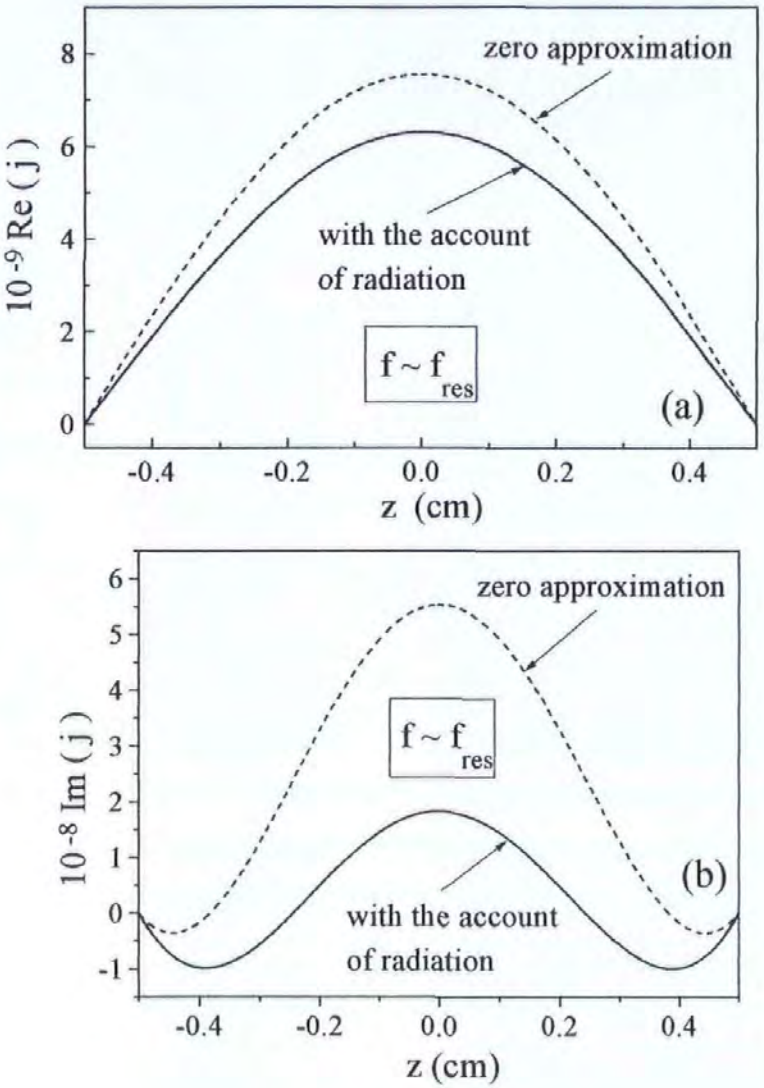

Fig. 5.4 *Current density distribution along a wire in the vicinity of the antenna resonance. The dashed and solid curves correspond to the zero (Eq. (19)) and first (Eq. (A9)) approximations, respectively.*

The current density distribution is calculated using formulae (19) and (A9) obtained in the zero approximation and using the first iteration, respectively. At $f > f_{res}$ and $f < f_{res}$ the distribution of the current density has a "bell-shape" both for the real and imaginary parts. As it follows from Eq. (1), the real part of the wire dipole moment is proportional to the integral from the imaginary part of the current density.

Therefore, passing f_{res} the distribution of the imaginary part has to change sign (say, from negative to positive towards high frequencies), as it is seen in Fig. 5.3. The real part of $j(z)$ is always positive since it corresponds to the positive imaginary part of the dipole moment. It is seen in Fig. 5.4, that the imaginary part of $j(z)$ is most sensitive to the radiation losses. Closer to the resonance, it undergoes rapid transformations and any small factors such as radiation may introduce essential changes. Outside the resonance, the zero and first approximations almost coincide and the radiation effects can be neglected.

5.4 Field dependent impedance matrix

The field dependence of the effective permittivity ε_{eff} of the composite is caused by the field dependence of the surface impedance matrix $\hat{\varsigma}(H_{ex})$, which determines the losses inside the inclusions. These internal losses characterise the quality factor of the entire composite system and the type of dispersion of ε_{eff}.

The impedance matrix $\hat{\varsigma}$ has been found in Chapter 2.0. We use simple model of a ferromagnetic wire where only the rotation of magnetisation is taken into account. This model gives all the important features of the field dependence of $\hat{\varsigma}$. In general, the anisotropy axis $\mathbf{n}_K$ has an angle α with the wire axis (z-axis), as shown in Fig. 2.7. The wire is assumed to be in a single domain state with the static magnetisation $\mathbf{M_0}$ directed in a helical way having an angle θ with the z-axis. The stable direction of $\mathbf{M_0}$ is found by minimising the magnetostatic energy density U_0 without bias field H_b (compare with Eq. (2.47), where $H_b \neq 0$):

$$\begin{aligned} &\partial U_0 / \partial \theta = 0, \\ &U_0 = -K\cos^2(\alpha-\theta) - M_0 H_{ex}\cos\theta. \end{aligned} \qquad (22)$$

Equation (22) describes the rotational magnetisation process demonstrated in Fig. 5.5, where the magnetisation plots are given for three types of anisotropy: longitudinal ($\alpha = 0$), circumferential ($\alpha = 90°$) and helical ($\alpha = 60°$). The domain processes may not be essential for the reversal of $\mathbf{M_0}$, since the magnetisation vector during its rotation is held parallel to the surface, without going through high-energy demagnetisation states.

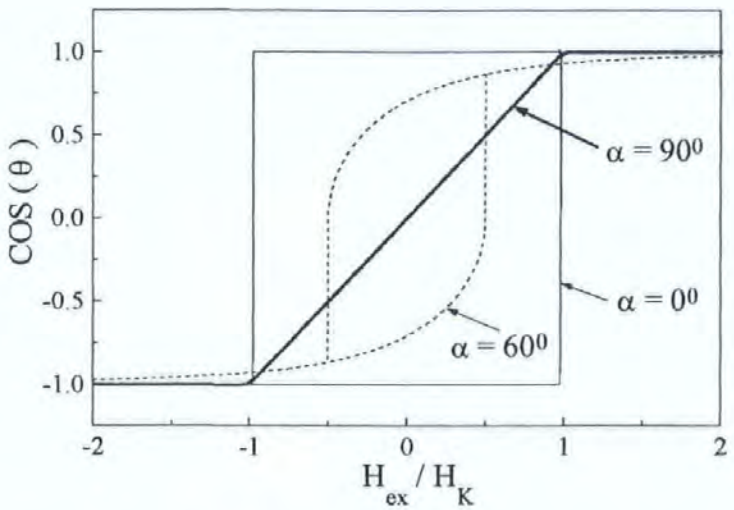

Fig. 5.5 *Typical rotational hysteresis curves $M_{0z}(H_{ex})$ for the different types of anisotropy: longitudinal ($\alpha = 0$), circumferential ($\alpha = 90^0$), and helical ($\alpha = 60^0$).*

The impedance matrix $\hat{\varsigma}$ has been calculated in Chapter 2 in the following limits: ($\delta_m / a << 1$) and ($a/\delta << 1$, $a/\delta_m \sim 1$, $\delta = c/\sqrt{2\pi\sigma\omega}$) with the general susceptibility matrix. The intermediate case is obtained by the extrapolation. The details can be found in Chapter 2 (Eqs. (31) and (44)-(46)), and here only the final results are listed:

a) strong magnetic skin-effect ($\delta_m / a << 1$)

$$\hat{\varsigma} = \begin{pmatrix} \varsigma_{zz} & \varsigma_{z\varphi} \\ \varsigma_{\varphi z} & \varsigma_{\varphi\varphi} \end{pmatrix} = \frac{c(1-i)}{4\pi\sigma\delta} \begin{pmatrix} \sqrt{\tilde{\mu}}\cos^2(\theta) + \sin^2(\theta) & \left(\sqrt{\tilde{\mu}} - 1\right)\sin(\theta)\cos(\theta) \\ \left(\sqrt{\tilde{\mu}} - 1\right)\sin(\theta)\cos(\theta) & \cos^2(\theta) + \sqrt{\tilde{\mu}}\sin^2(\theta) \end{pmatrix}, \tag{23}$$

where $\tilde{\mu} = 1 + 4\pi\tilde{\chi}$ and $\tilde{\chi} = \chi_2 - 4\pi\chi_a^2/(1 + 4\pi\chi_1)$ are the effective permeability and susceptibility respectively.

b) weak nonmagnetic skin-effect ($a/\delta << 1$ or $a/\delta \sim 1$, $a/\delta_m \sim 1$)

$$\varsigma_{zz} = \frac{k_1 c}{4\pi\sigma} \frac{J_0(k_1 a)}{J_1(k_1 a)} + \frac{1}{54}\left(\frac{a}{\delta}\right)^4 \frac{c\mu_3^2}{\pi\sigma a},$$

$$\varsigma_{\varphi\varphi} = -\frac{k_2 c}{4\pi\sigma}\frac{J_1(k_2 a)}{J_0(k_2 a)} + \frac{1}{36}\left(\frac{a}{\delta}\right)^4 \frac{c\mu_3^2}{\pi\sigma a}, \tag{24}$$

$$\varsigma_{\varphi z} = \varsigma_{z\varphi} = i\frac{a\omega}{3c}\mu_3 - \left(\frac{a}{\delta}\right)^4\left[\frac{\mu_1\mu_3}{60} + \frac{\mu_2\mu_3}{30}\right]\frac{c}{\pi\sigma a},$$

where $J_{0,1}$ are the Bessel functions, $\mu_1 = 1+4\pi\cos^2(\theta)\tilde{\chi}$, $\mu_2 = 1+4\pi\sin^2(\theta)\tilde{\chi}$, $\mu_3 = -4\pi\sin(\theta)\cos(\theta)\tilde{\chi}$, $k_{1,2}^2 = \mu_{1,2}\left(4\pi i\omega\sigma/c^2\right)$,

$\chi_1 = \omega_M(\omega_1 - i\tau\omega)/\Delta,$
$\chi_2 = \omega_M(\omega_2 - i\tau\omega)/\Delta,$
$\chi_a = \omega\omega_M/\Delta,$
$\Delta = (\omega_2 - i\tau\omega)(\omega_1 - i\tau\omega) - \omega^2,$
$\omega_1 = \gamma[H_{ex}\cos(\theta) + H_K\cos 2(\alpha-\theta)],$
$H_K = 2K/M_0$
$\omega_2 = \gamma[H_{ex}\cos(\theta) + H_K\cos^2(\alpha-\theta)],$
$\omega_M = \gamma M_0.$

Equations (23),(24) demonstrate that the surface impedance matrix depends on both the ac susceptibility parameter $\tilde{\chi} = (\tilde{\mu}-1)/4\pi$ and the static magnetisation orientation angle θ. At high frequencies the latter will give the main contribution to the field dependence of the impedance since $\tilde{\chi}$ looses its the field sensitivity, as it has been discussed in Section 2.6. The components of $\hat{\varsigma}$ were obtained in the assumption of a uniform magnetisation. For the multidomain structure, the components of $\hat{\chi}$ should be understood as averaged over domains. The contribution to $\hat{\chi}$ due to domain wall displacements can be neglected at high frequencies due to a considerable damping effect.

Usually ferromagnetic microwires have a circular ($\alpha = 90^0$) or longitudinal ($\alpha = 0$) magnetisation in the outer shell. The central part of the wire always consists of a longitudinally magnetised inner core. A helical magnetisation ($0 < \alpha < 90^0$) can be obtained as a result of a special treatment of a wire sample with a circular anisotropy, for example, by means of twisting or annealing under a torsion stress (see Section 2.7.3 and Ref. 2, 25-27) Wires with a circular anisotropy exhibit the most sensitive MI effect.

Here, we use the parameters of Co-rich glass-coated wires with a negative magnetostriction and low coercitivity.[5,27] A circular "bamboo-like" domain structure with opposite magnetisations in the adjacent domains [28] exists almost in the entire wire which exhibits nearly a non-hysteretic B-H curve, as it is shown in Fig. 5.5 for $\alpha = 90^0$. Due to such domain structure, the averaged off-diagonal components $\varsigma_{z\varphi}$ and $\varsigma_{\varphi z}$ are zero, as was proved theoretically [23] and experimentally [29] (see Chapter 2). Thus, the effects related to the off-diagonal components (see Eq. (16)) are possible only in a wire with a helical magnetisation where such averaging does not occur.

Figures 5.6 and 5.7 demonstrate the field dependence of $\varsigma_{zz}(H_{ex})$ for various frequencies. The wire has 10 μm diameter, conductivity $\sigma = 7.6\times10^{15}$ s^{-1}, anisotropy field $H_K = 2$ Oe, saturation magnetisation $M_0 = 500$ G, and gyromagnetic constant $\gamma = 2\times10^7$ (rad/s)/Oe.

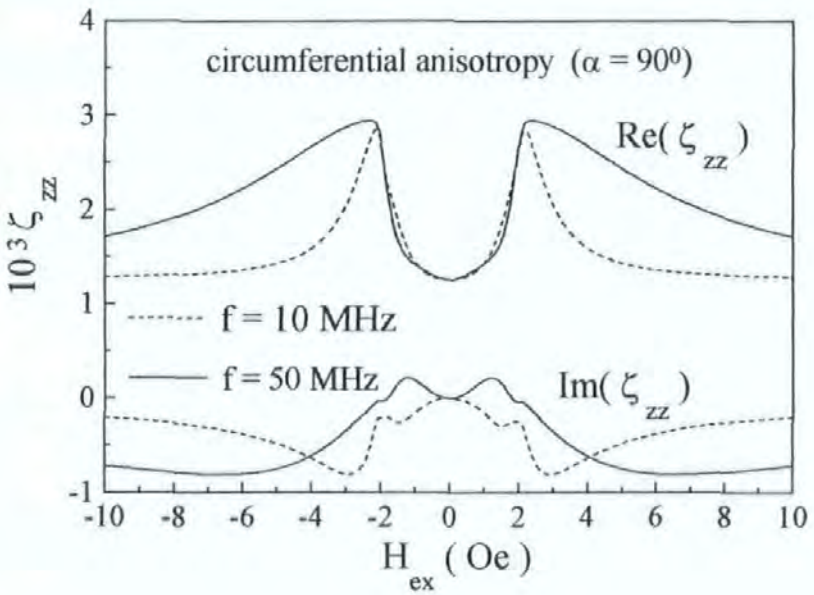

Fig. 5.6 *Typical field dependence of the longitudinal impedance in Co-based wire with a circumferential anisotropy in the megahertz range.*

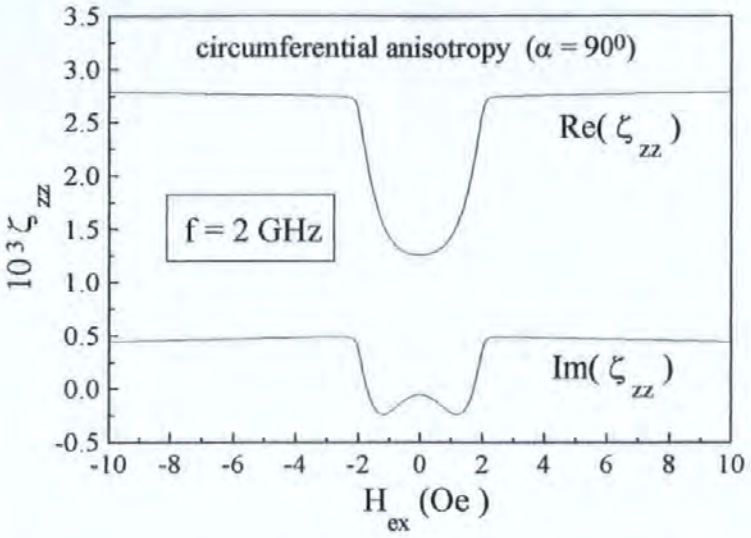

Fig. 5.7 *Typical "valve-like" field dependence of the longitudinal impedance in the gigahertz range, where* $\varsigma_{zz}(H_{ex})$ *has approximately a constant value for* $H_{ex} \geq H_K$ *reflecting the field dependence of* $\cos^2(\theta)$, *since* $\tilde{\mu}$ *loses its field sensitivity.*

The calculations have been carried out in a low frequency limit (24) since the magnetic skin-depth δ_m is of the order of the wire radius. As it will be shown below, not very strong skin effect is the basic requirement for obtaining the field-dependent effective permittivity. For this reason the wire diameter is chosen to be sufficiently small. At the megahertz range the real part (see Fig. 5.6) and module of $\varsigma_{zz}(H_{ex})$ have two well-defined peaks at $H_{ex} \approx \pm H_K$. With $H_{ex} > H_K$ the impedance decreases slowly reaching the level of $\varsigma_{zz}(0)$. With increasing a frequency the curve of $\varsigma_{zz}(H_{ex})$ flattens at $H_{ex} > H_K$ and even for large values of $H_{ex} >> H_K$ does not reach the saturation. In the gigahertz range $\varsigma_{zz}(H_{ex})$ has approximately a constant value for $H_{ex} \geq H_K$, as it is shown in Fig. 5.7, reflecting the field dependence of $\cos^2(\theta)$ (see Eq. (24) and Fig. 5.5) since the permeability parameter $\tilde{\mu}$ looses its field sensitivity, as it has been discussed in Section 2.6, Fig. (2.9). Such kind of the transformation of $\varsigma_{zz}(H_{ex})$ is supported by a number of experiments where the magneto-impedance spectra were measured in ferromagnetic wires in a wide frequency range from 1 kHz up to 1.2 GHz.[30,31]

The field dependence $\varsigma_{zz}(H_{ex})$ at very high frequencies may be of a considerable interest since it has two predetermined levels at $H_{ex}=0$ and $H_{ex}>H_K$, between which a smooth transition can be achieved by applying H_{ex}. Thus, at very high frequencies the impedance $\varsigma_{zz}(H_{ex})\sim\cos^2(\theta)$ exhibits a "valve-like" behaviour, switching from one stable level to the other, following the dc magnetisation.

5.5 Field dependent resonance effective permittivity

It is quite natural to expect that the field dependence $\varepsilon_{eff}(H_{ex})$ becomes most sensitive in the vicinity of the antenna resonance where any small variations in the inclusion parameters cause a strong change of the current distribution and the inclusion dipole moment. This results in a remarkable transformation of the dispersion curve $\varepsilon_{eff}(\omega)$ under the external magnetic field. The resonance frequency range is determined by the wire length l and the matrix permittivity ε. Practically, it is not desirable to construct composite materials with inclusions having a length larger than 1 cm. In this case, the first resonance frequency in air $f_{res}=c/2l$ would be in the range of tens gigahertz. However, for such high frequencies the magnetic properties of ferromagnetic wires under consideration tail off completely and $\tilde{\mu}$ tends to be unity. Without increasing the wire length, the operating frequencies can be lowered (in $\sqrt{\varepsilon}$ times) by using a dielectric matrix with higher permittivity $\varepsilon>>1$. Some polymer or commercial epoxy (shipley photoepoxy with $\varepsilon=3$) can be used as a dielectric matrix. A fine-dispersion filler (powder) containing particles with a large polarisability can be used for further increasing ε, for example, the powder of $BaTiO_3$ ceramic microparticles with $\varepsilon=17.8$.[32,33] The average radius of ceramic particles usually is smaller than 1 micron that is much smaller than the wire diameter. Another method of increasing ε uses finely dispersed metal powder.[9,16] Both methods allow the matrix permittivity ε to be made very large but having a small loss tangent. In our calculations we use $\varepsilon=16$ and $\varepsilon=64$. This results in lowering the antenna resonance frequency down to ~3.75 GHz and ~1.9 GHz, respectively, for the wire length of 1 cm. These characteristic frequencies are much greater than the frequency of the ferromagnetic resonance in wires, where the impedance behaviour is of a "valve-like" type shown in Fig. 5.7.

The condition of a moderate skin-effect ($a/\delta_m \sim 1$) is proving to be important to realise a high sensitivity of $\varepsilon_{eff}(H_{ex})$. If the magnetic skin-depth is much smaller than the wire radius ($\delta_m / a << 1$), the normalised wave number $\tilde{k}$ differs little from the wave number k of the free space. Substituting the high frequency impedance (23) into (20) gives:

$$\tilde{k} \sim \frac{\omega}{c}\sqrt{\varepsilon\mu}\left(1 + \frac{(1-i)}{2\mu \ln(l/a)}\frac{\delta}{a}\sqrt{\tilde{\mu}}\cos^2(\theta)\right)^{1/2} \tag{25}$$

From Eq. (25) it immediately follows that if $\delta/a << 1$ the wave number becomes $\tilde{k} \approx \omega\sqrt{\varepsilon\mu}/c$, whence it follows that an essential field dependence $\varepsilon_{eff}(H_{ex})$ can be reached in the case when the nonmagnetic skin depth is of the order of wire radius.

At a very low inclusion concentration $p << p_c \propto 2a/l$ the effective permittivity $\varepsilon_{eff}(\omega)$ can be represented by Eq. (3) as the dipole sum with the polarisability $<\wp>$ averaged on the inclusion orientations. The polarisability $\wp$ has to be calculated from Eq. (1) using the first $j_1(x)$ approximation for the current density distribution, which takes into account all losses in the system (see Eq. (A9) in Appendix A). In the case of a planar composite (see Fig. 5.1), the averaging gives a coefficient 1/2 ($<\wp>=\wp/2$), and $<\wp>$ determines the effective permittivity in the plane of the sample. The total permittivity matrix of a planar composite is of the form:

$$\hat{\varepsilon}(H_{ex}) = \begin{pmatrix} \varepsilon_{eff}(H_{ex}) & 0 & 0 \\ 0 & \varepsilon_{eff}(H_{ex}) & 0 \\ 0 & 0 & \varepsilon \end{pmatrix} \tag{26}$$

Figures 5.8 and 5.9 demonstrate the dispersion of the polarisability $\wp(\omega) = \wp'(\omega) + i\wp''(\omega)$ in the gigahertz range as a function of H_{ex} for two values of the matrix permittivity: $\varepsilon = 16$ and $\varepsilon = 64$. The dashed curves correspond to zero approximation (19) neglecting the radiation losses. When the dispersion region falls into lower frequencies due to larger matrix permittivity ($\varepsilon = 64$), the internal losses (both magnetic and resistive) become much greater than the radiation ones and the latter can be ignored, as it is seen in Fig. 5.9. In general, when the skin effect becomes essential the radiation losses are dominant and determine the resonance peak value. As a result, the system becomes insensitive to the internal parameters.

The field-dependent effect shows up in changing the character of the dispersion curves. In the absence of H_{ex} the dispersion curves are of a resonance type: at $f = f_{res}$ the imaginary part reaches a maximum and the real part equals zero. Applying a magnetic field $H_{ex} > H_K$, the impedance $\varsigma_{zz}(H_{ex})$ is increased and, as a consequence, the internal losses in the inclusion, which results in the dispersion of a relaxation type. In the presence of H_{ex} the resonance frequency also slightly shifts towards higher frequencies.

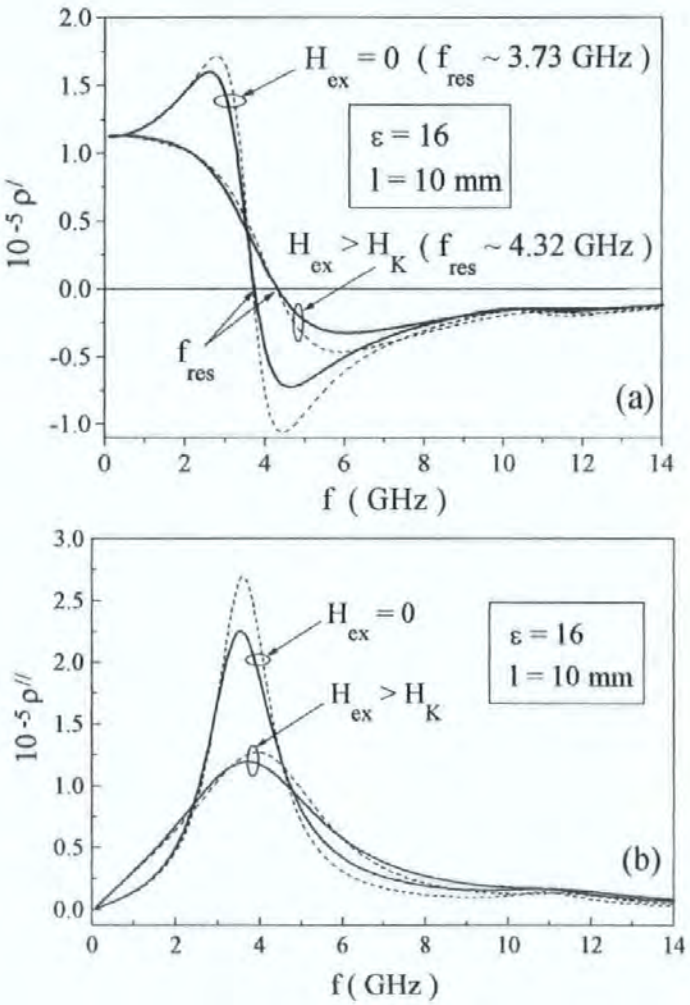

Fig. 5.8 *Transformation of the polarisability dispersion from a resonance type to a relaxation one due to H_{ex} in the vicinity of the antenna resonance. The matrix permittivity is $\varepsilon = 16$. The dashed and solid curves correspond to the zero (Eq. (19)) and first (Eq. (A9)) approximations, respectively.*

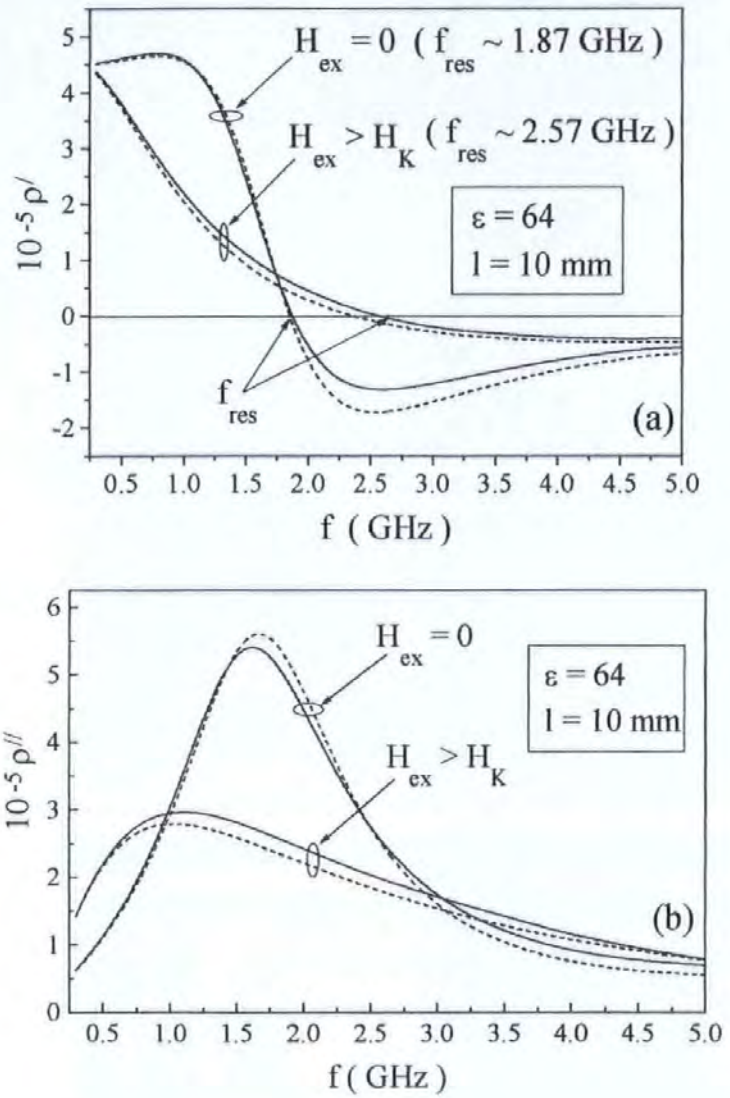

Fig. 5.9 *Transformation of the polarisability dispersion from a resonance type to a relaxation one due to* H_{ex} *in the vicinity of the antenna resonance. The matrix permittivity is* $\varepsilon = 64$. *The dashed and solid curves correspond to the zero (Eq. (19)) and first (Eq. (A9)) approximations, respectively.*

Figures 5.10 and 5.11 demonstrate the dispersion curves of the effective permittivity $\varepsilon_{eff}(\omega)$ at the gigahertz range as a function of the external magnetic field H_{ex} for $\varepsilon = 16$ and two volume concentrations $p = 0.001\%$ or $p = 0.01\%$. Both concentrations are considerably smaller than the percolation threshold $p_c \propto (2a/l)\times 100\% \sim 0.1\%$ ($2a = 10\,\mu m$ and $l = 1\,cm$).

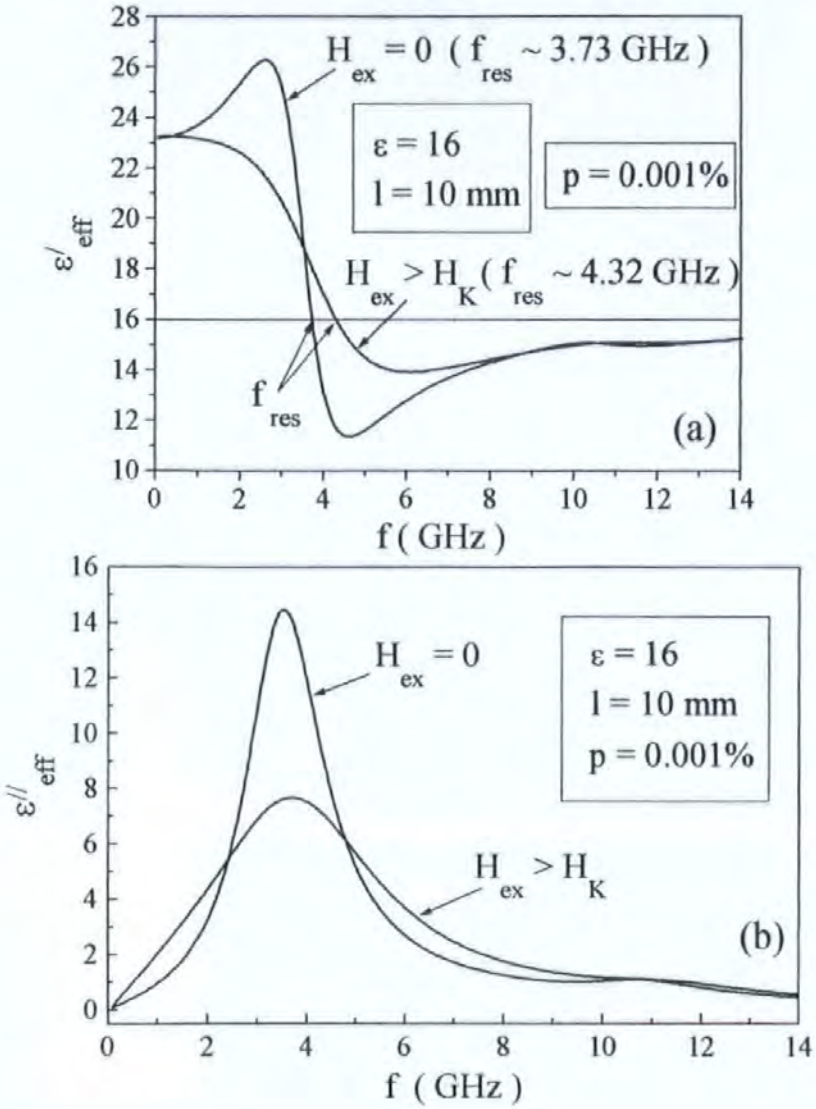

Fig. 5.10 *Transformation of the dispersion of the effective permittivity from a resonance type to a relaxation one due to* H_{ex} *in the vicinity of the antenna resonance.*

The inclusion concentration is $p = 0.001\%$ *and matrix permittivity is* $\varepsilon = 16$.

The dispersion of $\varepsilon_{eff}(\omega)$ has completely the same features as those for the polarisability $\wp(\omega)$. In Ref. 10 the transformation of the dispersion $\varepsilon_{eff}(\omega)$ from a resonant type to relaxation one was associated with a different wire conductivity σ, which defines the resistive loss. In our case it is provided through the field dependent impedance $\varsigma_{zz}(H_{ex})$ instead of conductivity.

At a larger wire concentration (for example, $p = 0.01\%$) the real part of $\varepsilon_{eff}(\omega)$ becomes negative in the vicinity of the resonance. Applying H_{ex}, it is possible to change gradually $\mathrm{Re}(\varepsilon_{eff}(\omega))$ from negative to positive values.

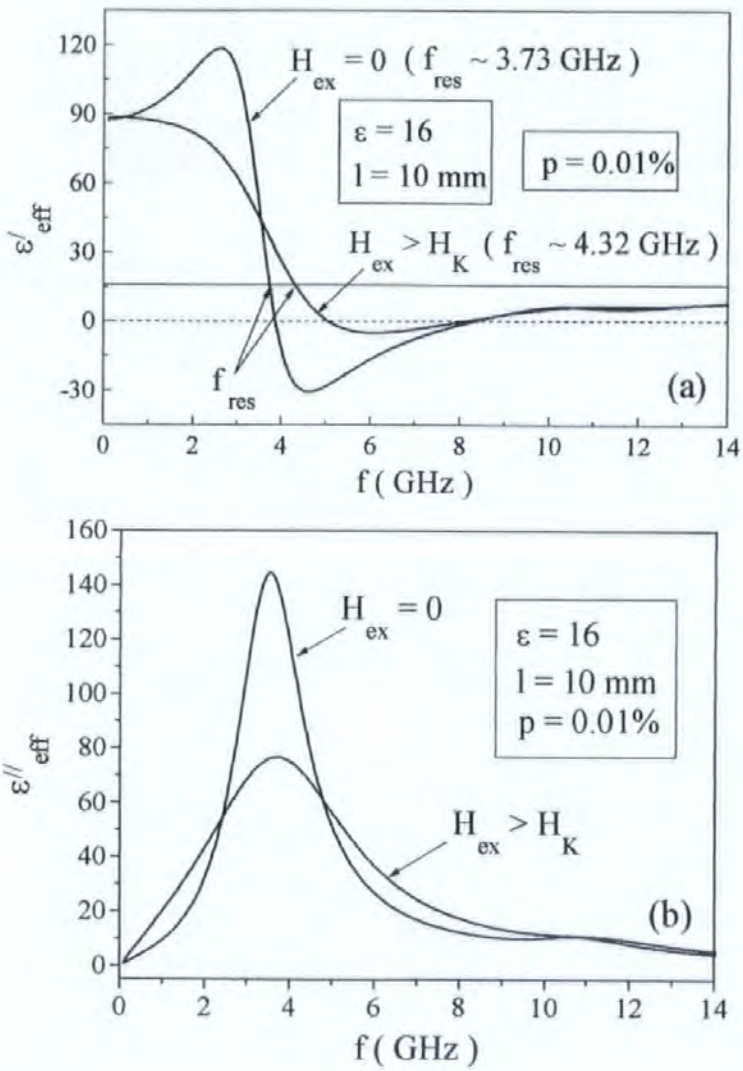

Fig. 5.11 *Transformation of the dispersion of the effective permittivity from a resonance type to a relaxation one due to H_{ex} in the vicinity of the antenna resonance. The inclusion concentration is $p = 0.01\%$ and matrix permittivity is $\varepsilon = 16$. Applying H_{ex}, the negative peak of $\mathrm{Re}(\varepsilon_{eff})$ continuously decreases as the dispersion tends to become of a relaxation type with $\mathrm{Re}(\varepsilon_{eff}) > 0$.*

The field-dependent permittivity matrix $\hat{\varepsilon}(H_{ex})$ can be used in tuneable microwave covers. Figure 5.12 shows the dispersion curves of the reflection $\mathbf{R}(\omega)$ and transmission $\mathbf{T}(\omega)$ coefficients for a thin wire-composite slab in the case of normal incidence of the electromagnetic wave for two values of H_{ex}. The energy absorption $\mathbf{A} = (1 - \mathbf{R} - \mathbf{T})$ in such kind of a composite is rather strong, therefore it has to be sufficiently thin to be used as a wave passage.

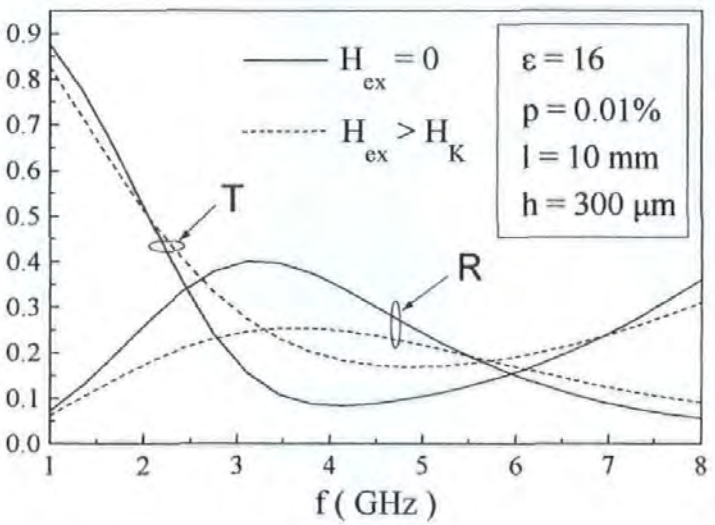

Fig. 5.12 *Dispersion curves of the reflection* $\mathbf{R}(\omega)$ *and transmission* $\mathbf{T}(\omega)$ *coefficients for a thin wire-composite slab in the case of normal incidence of the electromagnetic wave as a function of* H_{ex}. *The sample thickness is* $h = 300\,\mu m$.

Another promising application is suggested to employ these composites as an internal cover in the partially filled waveguides or layered waveguides with a "dielectric/composite" structure. The waveguide with an internal composite cover is proving to operate similar to the waveguide containing absorption ferromagnetic layers,[34] for example, a thin-film "dielectric/Fe" structure considered in Ref. 35,36. The schematic representation of such a waveguide structure is given in Fig. 5.13. In both systems there is an anisotropic field-dependent layer with resonance properties and large energy losses, but in our case the field-dependent layer is made of a composite material with $\hat{\varepsilon}(H_{ex})$.

The operating frequency range is determined by the antenna resonance. Such a waveguide system, by analogy to that already designed for the waveguides with ferromagnets, can be used for tuneable filters and phase shifters operating up to tens gigahertz.

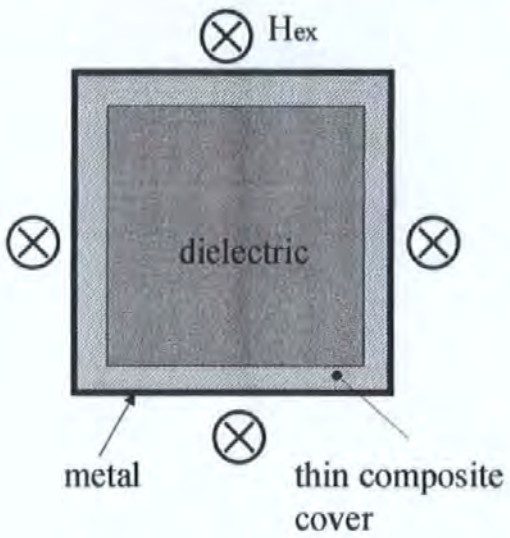

Fig. 5.13 *Schematic representation (cross section) of a tuneable waveguide with the internal composite cover.*

5.6 Nanocomposites in the optical range

In the last years, interest is being intensively focused on wires with more reduced dimensions, i.e. nanowires. There are two main techniques to prepare these nanowires, namely by lithography and electroplating. Interest of such novel materials lies in their technological connections to magnetic recording media, but also in studying fundamental aspects as magnetic interactions in arrays of magnetic nanowires and magnetic switching. However, nonmagnetic nanowires (for example, made of Ag or Au) also are of great interest for the creation of novel types of composite media having unusual properties in the optical range. In Ref. 37 a new type of metal-dielectric composite has been proposed that is characterised by a resonance-like behaviour of the effective permeability μ_{eff} in the infrared and visible spectral ranges. This material can be referred to as optomagnetic medium. Here we would like to present the review of the basic results obtained in Ref. 37 (this paper is enclosed in Appendix B after Section 5.9).

The composite consists of conducting nonmagnetic inclusions in the shape of non-closed contours or pairs of parallel sticks with length of 50-100 nm embedded in dielectric matrix. The composite structures based on ring-shaped inclusions (with a split large enough to neglect the edge capacitance) and pairs of parallel conducting sticks (connected via displacement currents) are shown in Fig. 5.14(a) and Fig. 5.14(b), respectively.

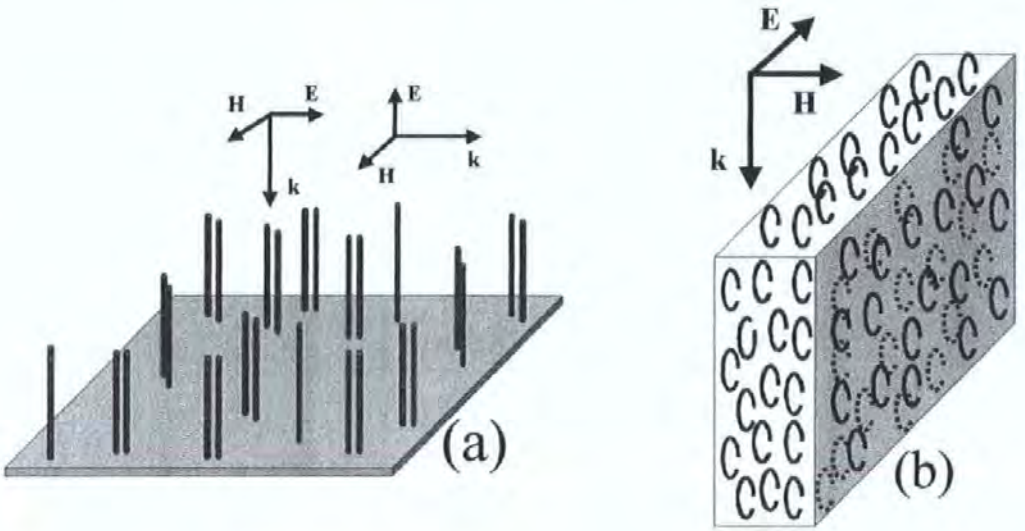

Fig. 5.14 *Composite medium with effective permeability at optical frequencies. A possible polarisation of the electromagnetic wave associated with induced magnetic properties is indicated. In (a), a system of nanowires grown on a substrate is shown, in which two parallel wires form a constituent element. The spacing in the pair of wires is much smaller than the distance between the pairs. In (b), a nanoring-composite is shown.*

The analytical formalism used in Ref. 37 is similar in many respects to what has been developed in this Chapter: the scattering problem is considered with an impedance boundary condition, which yields the current and charge distributions within the inclusions. It is known that the macroscopic magnetic properties originated by localised electrons in atoms have no physical meaning from optical frequencies onward.[22] In contrast, the effective permeability of the proposed composite is proven to be consistent with the macroscopic Maxwell equations even at optical frequencies, having values that can differ substantially from unity within a dispersion band.

The magnetic properties originated by induced currents are enhanced by localised plasmon modes, which make an inclusion resonate at a much lower frequency than that of the half-wavelength requirement at microwaves. It implies that microstructure can be made on a scale much less than the wavelength and the effective permeability is a valid concept. Figure 5.15 demonstrates an effective permeability μ_{eff} and permittivity ε_{eff} of composite containing wire pairs versus frequency for the volume concentration of 3%.[37] In Figure 5.15 the following designations are used: l is the nanowire length, a is the nanowire radius, d is the distance between axes of two nanowires in a pair.

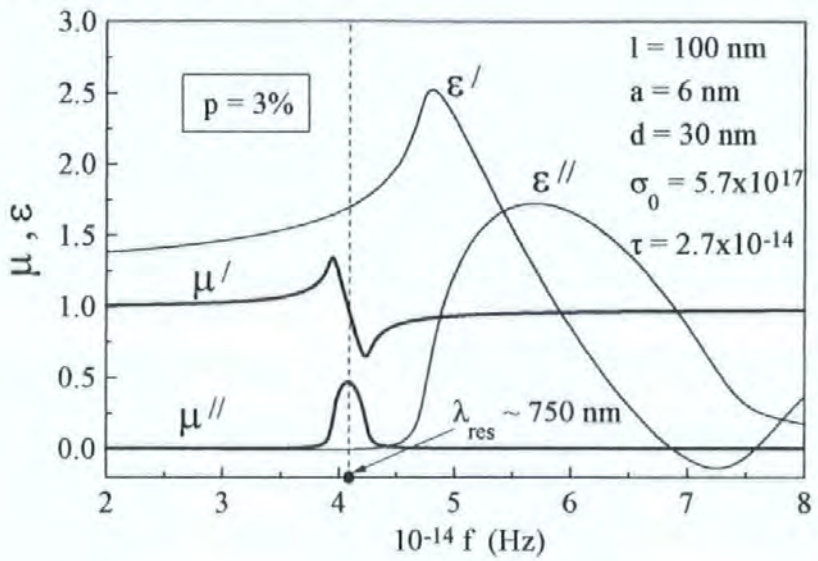

Fig. 5.15 *Effective permeability* $\mu_{eff} = \mu' + i\mu''$ *and permittivity* $\varepsilon_{eff} = \varepsilon' + i\varepsilon''$ *of composite containing wire pairs vs. frequency for the volume concentration of 3%.*

In optical and infrared spectral ranges, metal conductivity σ can be approximated by Drude formula:

$$\sigma(\omega) = \frac{\sigma_0}{1 - i\omega t}, \tag{27}$$

where $\sigma_0 = \omega_p^2 t / 4\pi$, ω_p is the plasma frequency, t is the relaxation time (for silver, $\sigma_0 = 5.7 \times 10^{17}$ s^{-1} and $t = 2.7 \times 10^{-14}$ s). In the high frequency range considered here ($\omega \sim 10^{15}\, s^{-1}$) losses in metal grains are relatively small, $\omega t >> 1$.

Therefore, the metal conductivity is characterised by the dominant imaginary part. This is very important for our analysis since the current can have a resonance for a considerably larger wavelength $\lambda >> 2l$. Physically, this is associated with the resonance of localised plasmon modes.

The resonance region for ε_{eff} is shifted towards higher frequencies. In the area of magnetic resonance, $\mu_{eff} \sim \varepsilon_{eff}$ with very small losses: $\varepsilon'' << 1$, $\mu'' << 1$. The presence of the effective magnetic permeability and its resonant properties lead to novel optical effects and open new possible applications. In particular, the condition for Brewster's angle becomes different resulting in reflectionless normal incidence from air (vacuum) if the effective permeability and permittivity are the same ($\mu_{eff} \sim \varepsilon_{eff}$). The resonant behaviour of the effective permeability of the proposed optomagnetic medium could be used for creation of optical polarizes, filters, phase shifters and selective lenses.

5.7 Conclusion

A comprehensive analysis of a magnetic-field dependent dielectric response in diluted metal-dielectric composite materials containing ferromagnetic microwires is presented. We have developed a rigorous mathematical method of calculating the electric current density distribution at the wire-inclusion irradiated by an electromagnetic field, which determines the electric polarisability contributing to the effective permittivity. The wire polarisability is proven to be very sensitive to the surface impedance changes near the antenna resonance. Therefore, in the composites with ferromagnetic wires as filling inclusions the effective permittivity may depend on a static magnetic field via the corresponding dependence of the impedance.

The field dependence of the impedance remains very sensitive even for gigahertz frequencies much higher than the characteristic frequency of the ferromagnetic resonance. In this case, the impedance reflects the field behaviour of the static magnetisation orientation showing a characteristic "valve-type" behaviour versus magnetic field. In the case of a Co-based microwires, a moderate magnetic field of a few Oe changes the static magnetisation from the circular direction to the axial one. During this process, the dispersion characteristics of permittivity can be changed considerably, say, from a resonance to a relaxation type.

A number of applications of this effect are proposed including microwave materials with the field-dependent reflection/transmission coefficients and tuneable waveguides where the composite material is used as an additional field-dependent cover.

The theory can be generalised to the case of interacting wires and applied for the exact calculation of the effective response from composites containing periodically spaced wires (wire crystals). This presents a considerable interest for studying field-tuneable band-gap [6] and negative index materials,[11-15] and is intended to be published elsewhere.

The analytical formalism developed can be successfully used for the analysis of nanocomposites with the nanoinclusions of different shapes.[37]

5.8 Appendix A

The iteration procedure proposed here allows the analytical expression for the current density $j(z)$ with the account of all the losses in the system to be obtained. Let us write once again the basic integro-differential equation (16):

$$\frac{\partial^2}{\partial z^2}(G*j)+\left(\frac{\omega}{c}\right)^2 \varepsilon\mu\left[(G*j)+\frac{ic\varsigma_{zz}}{2\pi a\omega\mu}(G_\varphi * j)\right]=\frac{i\omega\varepsilon}{4\pi}\left[\bar{e}_{0z}(z)+\varsigma_{z\varphi}\bar{h}_{0z}(z)\right]. \quad \text{(A1)}$$

The general solution of Eq. (A1) for the zero approximation (19) has the following form:

$$j_0(z)=A\sin(\tilde{k}z)+B\cos(\tilde{k}z)+\frac{i\omega\varepsilon}{4\pi Q\tilde{k}}\int_{-l/2}^{z}\sin(\tilde{k}(z-s))(\bar{e}_{0z}(s)+\varsigma_{z\varphi}\bar{h}_{0z}(s))ds\,. \quad \text{(A2)}$$

For the zero approximation with $\bar{e}_{0z}=\bar{e}_0=const$ and $\bar{h}_{0z}=\bar{h}_0=const$ we obtain:

$$j_0(z)=A\sin(\tilde{k}z)+B\cos(\tilde{k}z)+\frac{i\omega\varepsilon(\bar{e}_0+\varsigma_{z\varphi}\bar{h}_0)}{4\pi Q\tilde{k}^2}. \quad \text{(A3)}$$

Zero approximation (A3), satisfying the boundary conditions $j_0(-l/2)=j_0(l/2)\equiv 0$, is of the form:

$$j_0(z)=\frac{i\omega\varepsilon(\bar{e}_0+\varsigma_{z\varphi}\bar{h}_0)}{4\pi Q\tilde{k}^2}\frac{(\cos(\tilde{k}l/2)-\cos(\tilde{k}z))}{\cos(\tilde{k}l/2)}. \quad \text{(A4)}$$

For the ideal conductor ($\sigma=\infty$) and $\mathrm{Im}(\varepsilon)=\mathrm{Im}(\mu)\equiv 0$ solution (A4) has singularities at the resonance wavelengths λ_{res} defined by Eq. (21). The account of a limited conductivity and radiation losses eliminates the singularities.

The iteration procedure determines the next approximations. Let us extract the real and imaginary parts of the convolutions in Eq. (A1). To calculate the convolutions with real parts the proposed method given by (18). As a result we obtain the following integro-differential equation:

$$\frac{\partial^2}{\partial z^2}\left[j(z)+\frac{i}{Q}(\mathrm{Im}(G)*j)\right]+\tilde{k}^2\left[j(z)+\frac{i}{Q}(\mathrm{Im}(G)*j)\right]= \\ =\frac{i\omega\varepsilon}{4\pi Q}\left[\bar{e}_{0z}(z)+\varsigma_{z\varphi}\bar{h}_{0z}(z)\right]+\frac{i(\tilde{k}^2-k^2)}{Q}(\mathrm{Im}(G)*j)+\frac{\omega\varepsilon\varsigma_{zz}}{2\pi acQ}(\mathrm{Im}(G_\varphi)*j) \quad (A5)$$

Equation (A5) can be considered as a non-uniform differential equation with respect to the operator $\partial^2/\partial z^2+\tilde{k}^2$. Finding the inverse operator, we obtain the integral equation:

$$j(z)=A\sin(\tilde{k}z)+B\cos(\tilde{k}z)+\frac{i\omega\varepsilon}{4\pi Q\tilde{k}}\int_{-l/2}^{z}\sin(\tilde{k}(z-s))(\bar{e}_{0z}(s)+\varsigma_{z\varphi}\bar{h}_{0z}(s))ds+ \\ +\frac{i(\tilde{k}^2-k^2)}{Q\tilde{k}}\int_{-l/2}^{z}\sin(\tilde{k}(z-s))(\mathrm{Im}(G)*j))ds+ \\ +\frac{\omega\varepsilon\varsigma_{zz}}{2\pi acQ\tilde{k}}\int_{-l/2}^{z}\sin(\tilde{k}(z-s))(\mathrm{Im}(G_\varphi)*j)ds-\frac{i}{Q}(\mathrm{Im}(G)*j) \quad (A6)$$

where the constants A and B should be chosen to satisfy the boundary conditions $j(-l/2)=j(l/2)\equiv 0$. Equation (A6) is the Fredholm integral equation of the second kind, therefore it is well adapted to an iterative method. For the n-th estimation the following iteration procedure is used:

$$j_n(z)=j_0(z)+\frac{i(\tilde{k}^2-k^2)}{Q\tilde{k}}\int_{-l/2}^{z}\sin(\tilde{k}(z-s))(\mathrm{Im}(G)*j_{n-1}))ds+ \\ +\frac{\omega\varepsilon\varsigma_{zz}}{2\pi acQ\tilde{k}}\int_{-l/2}^{z}\sin(\tilde{k}(z-s))(\mathrm{Im}(G_\varphi)*j_{n-1})ds-\frac{i}{Q}(\mathrm{Im}(G)*j_{n-1}) \quad (A7)$$

Constants A and B are calculated at the final step of the iteration procedure $n=N>1$ so that to satisfy the boundary conditions $j_N(-l/2)=j_N(l/2)\equiv 0$.

Let us rewrite iteration representation (A7) in the following compact form:

$$j_n(z) = j_0(z) + \int_{-l/2}^{l/2} S(z,q) j_{n-1}(q) dq, \qquad \text{(A8)}$$

where

$$S(z,q) = S_1(z,q) + S_2(z,q) + S_3(z,q),$$

$$S_1(z,q) = -\frac{i}{Q}\mathrm{Im}(G(r)), \quad r = \sqrt{(z-q)^2 + a^2},$$

$$S_2(z,q) = \frac{i(\tilde{k}^2 - k^2)}{Q\tilde{k}} \int_{-l/2}^{z} \sin(\tilde{k}(z-s))\,\mathrm{Im}(G(r))ds, \; r = \sqrt{(s-q)^2 + a^2},$$

$$S_3(z,q) = \frac{\omega\varepsilon\varsigma_{zz}}{2\pi a c Q\tilde{k}} \int_{-l/2}^{z} \sin(\tilde{k}(z-s))\,\mathrm{Im}(G_\varphi(r))ds, \; r = \sqrt{(s-q)^2 + a^2}.$$

As it follows from Eq. (A8), the radiation losses consist of three parts. The first one, related to the local kernel S_1, is responsible for a "pure radiation" in the free space as though the conductor had the ideal conductivity $\sigma = \infty$. This part of the radiation is independent of conductor internal properties, therefore the kernel S_1 is defined by the wave number k of the free space and is local. Second part, related to the non-local kernel S_2, is responsible for the radiation in the free space, which partly penetrates inside the conductor. Non-locality, defined by the convolution with $\sin(\tilde{k}(z-s))$, is caused by the presence of an electric connection between spatial points through the conductor. The third part, related to the non-local kernel S_3, is caused by the infringement of the quasistatic approximation when calculating $\bar{h}_\varphi(z,a)$ at the conductor surface. All the three parts contain a small parameter $1/4\pi Q \sim 1/2\ln(l/a)$, which leads to a fast convergence of the iteration procedure.

Let us calculate the first iteration substituting (A3) as the zero approximation:

$$j_1(z) = A\left(\sin(\tilde{k}z) + \int_{-l/2}^{l/2} S(z,q)\sin(\tilde{k}q)dq\right) + B\left(\cos(\tilde{k}z) + \int_{-l/2}^{l/2} S(z,q)\cos(\tilde{k}q)dq\right) + \frac{i\omega\varepsilon(\bar{e}_0 + \varsigma_{z\varphi}\bar{h}_0)}{4\pi Q\tilde{k}^2}\left(1 + \int_{-l/2}^{l/2} S(z,q)dq\right) \qquad \text{(A9)}$$

For the unknown constants A and B we obtain the following system of linear equations:

$$\begin{pmatrix} \sin(\tilde{k}l/2)+a_{11} & \cos(\tilde{k}l/2)+a_{12} \\ -\sin(\tilde{k}l/2)+a_{21} & \cos(\tilde{k}l/2)+a_{22} \end{pmatrix} \otimes \begin{pmatrix} A \\ B \end{pmatrix} = \begin{pmatrix} C \\ D \end{pmatrix}, \tag{A10}$$

where

$$\begin{pmatrix} a_{11} & a_{12} \\ a_{21} & a_{22} \end{pmatrix} = \begin{pmatrix} \int_{-l/2}^{l/2} S(l/2,q)\sin(\tilde{k}q)dq & \int_{-l/2}^{l/2} S(l/2,q)\cos(\tilde{k}q)dq \\ \int_{-l/2}^{l/2} S(-l/2,q)\sin(\tilde{k}q)dq & \int_{-l/2}^{l/2} S(-l/2,q)\cos(\tilde{k}q)dq \end{pmatrix}, \tag{A11}$$

$$\begin{pmatrix} C \\ D \end{pmatrix} = -\frac{i\omega\varepsilon(\bar{e}_0+\varsigma_{z\varphi}\bar{h}_0)}{4\pi Q\tilde{k}^2} \begin{pmatrix} 1+\int_{-l/2}^{l/2} S(l/2,q)dq \\ 1+\int_{-l/2}^{l/2} S(-l/2,q)dq \end{pmatrix}.$$

From (A10) we obtain the final expressions for A and B:

$$A = \frac{(C-D)+B(a_{22}-a_{12})}{2\sin(\tilde{k}l/2)+a_{11}-a_{21}} \tag{A12}$$

$$B = \left(\frac{C+D}{2}+\frac{(D-C)(a_{11}+a_{21})}{4\sin(\tilde{k}l/2)+2(a_{11}-a_{21})}\right) \Bigg/ \left(\cos(\tilde{k}l/2)+\frac{(a_{22}-a_{12})(a_{11}+a_{21})}{4\sin(\tilde{k}l/2)+2(a_{11}-a_{21})}+\frac{a_{12}+a_{22}}{2}\right)$$

The denominator of the parameter B determines the resonant frequencies and magnitude of the resonant peaks. We shall extract real and imaginary parts of the denominator of B:

$$\mathrm{Re} = \cos(\mathrm{Re}(\tilde{k})l/2)\,\mathrm{ch}(\mathrm{Im}(\tilde{k})l/2)+\mathrm{Re}\left(\frac{(a_{22}-a_{12})(a_{11}+a_{21})}{4\sin(\tilde{k}l/2)+2(a_{11}-a_{21})}+\frac{a_{12}+a_{22}}{2}\right), \tag{A13}$$

$$\mathrm{Im} = -\sin(\mathrm{Re}(\tilde{k})l/2)\,\mathrm{sh}(\mathrm{Im}(\tilde{k})l/2)+\mathrm{Im}\left(\frac{(a_{22}-a_{12})(a_{11}+a_{21})}{4\sin(\tilde{k}l/2)+2(a_{11}-a_{21})}+\frac{a_{12}+a_{22}}{2}\right). \tag{A14}$$

The resonance frequencies are found out from the dispersion equation $\mathrm{Re} = 0$:

$$\cos(\mathrm{Re}(\tilde{k})l/2)\,\mathrm{ch}(\mathrm{Im}(\tilde{k})l/2)+\mathrm{Re}\left(\frac{(a_{22}-a_{12})(a_{11}+a_{21})}{4\sin(\tilde{k}l/2)+2(a_{11}-a_{21})}+\frac{a_{12}+a_{22}}{2}\right)=0. \tag{A15}$$

Since the radiation losses are smaller than the internal ones, Eq. (21) can be used as a dispersion equation for the resonance frequency.

5.9 References

[1] D. P. Makhnovskiy and L. V. Panina, J. Appl. Phys. **93**, 4120 (2003).

[2] K. Mohri, L. V. Panina, T. Uchiyama, K. Bushida, and M. Noda, IEEE Trans. Magn. **31**, 1266 (1995).

[3] I. Ogasawara and S. Ueno, IEEE Trans. Magn. **31**, 1219 (1995).

[4] H. Chiriac and A. T. Ovari, Progress in Mater. Science **40**, 333 (1996).

[5] A. P. Zhukov, J. Gonzalez, J. M. Blanco, M. Vazquez, and V. S. Larin, J. Mat. Res. **15**, 2107 (2000).

[6] A. Figotin, Y. A. Godin, and I. Vitebsky, Phys. Rev. B **57**, 2841 (1998).

[7] A. K. Sarychev and V. M. Shalaev, Physics Reports **335**, 275-371 (2000).

[8] N. Kolesnikov, A. N. Lagarkov, L. N. Novogrudskiy, S. M. Matytsin, K. N. Rozanov, and A. K. Sarychev, in *Optical and Electrical Properties of Polymers*, edited by J. A. Emerson and J. M. Torkelson (Material Research Society, Pittsburgh, 1991), **No 214**, p. 119.

[9] A. N. Lagarkov, S. M. Matytsin, K. N. Rozanov, and A. K. Sarychev, J. Appl. Phys. **84**, 3806 (1998).

[10] A. N. Lagarkov and A. K. Sarychev, Phys. Rev. **B 53**, 6318 (1996).

[11] J. B. Pendry, Phys. Rev. Lett. **85**, 3966 (2000).

[12] R. A. Shelby, D. R. Smith, and S. Schultz, Science **292**, 77 (2001).

[13] J. B. Pendry, A. J. Holden, D. J. Robbins, and W. J. Stewart, J. Phys. Condens. Matter. **10**, 4785 (1998).

[14] J. B. Pendry, A. J. Holden, D. J. Robbins, and W. J. Stewart, IEEE Trans. Microwave Theory Tech. **47**, 2075 (1999).

[15] V. G. Veselago, Sov. Phys. Usp. **10**, 509 (1968).

[16] A. P. Vinogradov, D. P. Makhnovskiy, and K. N. Rozanov, J. Commun. Tech. and Electronics **44**, 317 (1999).

[17] D. P. Makhnovskiy, L. V. Panina, D. J. Mapps, and A. K. Sarychev, Phys. Rev. **B 64**, 134205 (2001).

[18] M. Born and E. Wolf, *Principles of Optics*, (Fourth edition, Pergamon Press, 1968).

[19] E. Hallen, *Electromagnetic theory*, (Chapman and Hall, London, 1962).

[20] B. Cichocki and B. U. Felderhof, Physica **A 241**, 6 (1997).

[21] R. King and G. Smith, *Antennas in Matter. Fundamentals, Theory and Applications*, (The MIT Press, Cambridge, Massachusetts, and London, England, 1981).

[22] L. D. Landau and E. M. Lifshitz, *Electrodynamics of Continuous Media*, (Pergamon Press, 1975).

[23] D. P. Makhnovskiy, L. V. Panina, and D. J. Mapps, Phys. Rev. **B 63**, 144424 (2001).

[24] L. Hermander, *The analysis of Linear Partial Differential Operators* **I**, *Distribution Theory and Fourier Analysis*, (Springer-Verlag, Berlin Heidelberg, New York, Tokyo, 1983).

[25] L. V. Panina, T. Kitoh, M. Noda, and K. Mohri, J. Mag. Soc. Japan **20**, 625 (1996).

[26] J. M. Blanco, A. P. Zhukov, and J. Gonzalez, J. Phys. D: Appl. Phys. **32**, 3140 (1999).

[27] A. P. Zhukov, J. M. Blanco, J. Gonzalez, M. J. Garcia Prieto, E. Pina, and M. Vazquez, J. Appl. Phys. **87**, 1402 (2000).

[28] M. Takajo, J. Yamasaki, and F. B. Humphrey, IEEE Trans. Magn. **29**, p. 3484 (1993).

[29] D. P. Makhnovskiy, L. V. Panina, and D. J. Mapps, J. Appl. Phys. **87**, p. 4804 (2000).

[30] D. Menard, M. Britel, P. Ciureanu, A. Yelon, V. P. Paramonov, A. S. Antonov, P. Rudkowski, and J. O. Strem-Olsen, J. Appl. Phys. **81**, 4032 (1997).

[31] A. S. Antonov, A. Granovsky, A. Lagarkov, N. Perov, N. Usov, and T. Furmanova, Physica **A 241**, 420 (1997).

[32] D. K. Dasgupta and K. Doughty, Thin Solid Films **158**, 93 (1988).

[33] Y. Rao, J. Qu, C. P. Wong, and T. Marinis, IMAPS/IEEE Proceeding of 5rd Int. Symposium on Advanced Packaging Materials, 2000.

[34] A. G. Gurevich, *Ferrites at Microwave Frequencies*, (New York: Consultants Bureau, 1963).

[35] E. Schloemann, R. Tutison, J. Weissman, H. J. Van Hook, and T. Vatimos, J. Appl. Phys. **63**, 3140 (1988).

[36] R. J. Astalos and R. E. Camley, J. Appl. Phys. **83**, 3744 (1998).

[37] L. V. Panina, A. N. Grigorenko, and D. P. Makhnovskiy, Phys. Rev. **B 66**, 155411 (2002).

Chapter 6 Future work

Future applications of the MI effect cement the different subjects expounded in this work making the interdisciplinary dialog a powerful tool for the synthesis of new ideas. The impedance matrix approach forms the universal conceptual language that provides these interdisciplinary penetrations.

By now, the basic physical principles of the MI effect have been well understood. This is because the main work will spread in the applications of MI for developing high sensitive magnetic sensors and, as ascertained in this work, for tuneable composite materials. Up to the present, MI magnetic sensors utilised the field dependence of the longitudinal (diagonal) impedance in accordance with its introduction in the first works.[1-3] Further analysis has revealed the different field behaviours of the longitudinal impedance in MI samples with different types of magnetic anisotropy: circumferential and helical in wires,[4-6] and transverse, longitudinal and crossed in films.[4, 7-12] Recently, the off-diagonal components of the impedance matrix [6,8,9,11] have founded their applications as the field sensitive characteristics with the antisymmetrical field behaviour.[13] The diagonal circumferential $\varsigma_{\varphi\varphi}$ and diagonal transverse ς_{yy} impedances (for wire and films, respectively) are still waiting for their applications as the field dependent characteristics. *In general, each component of the impedance matrix has a unique field behaviour, which differs from those of the other components (at the same magnetic structure). Therefore, it becomes possible to obtain a wide set of the magnetic sensors by varying a magnetic structure in combination with different methods of excitation and detection. Another perspective research concerns the miniaturisation of the MI sensors and creation of integrated circuit designs. Thin film MI elements will play here the key role.* In work [14], the MI sandwich film with a planar microcoil has been prepared to allow the off-diagonal impedance to be measured. We believe that all the components of the impedance matrix will be used in future miniature MI sensors. Of course, the usual problems of magnetic sensors related with the signal/to/noise ratio remain actual for the MI sensors. The research in this direction only has just started and will increase. *Also, new opportunities for the MI sensor will appear with a widening of the frequency operating range.* At the moment, the MHz range is widely used what is dictated by the electronic circuit components. However, the GHz range brings very unusual properties of MI. *For the time being, only one high frequency property, the so-called MI-valve, has been used in tuneable composites.[15] Nevertheless, the MI element operating in the GHz range may be used as a reading head.[16]*

A remarkable application of the MI effect is tuneable composite materials. This direction of investigation was opened by two recent publications [15] and [17]. In Ref.17, long wires build the composite structure. Contrary to the composite with short inclusions, the electromagnetic field is applied locally to a certain portion of the material excluding the ends of wires. In this case the current distribution in the wire can be neglected. Such system has the response of a diluted plasma and it is characterised by the Drude dispersion typical of free-electron gas. In a general case, when the skin effect is not very strong, the plasma frequency depends on the wire impedance.[17-19] The composite with long wire inclusions is similar in many respects to usual thin metal ferromagnetic film, and so it does not demonstrate any new properties. *On the contrary, the composite with short wire inclusions [15] exhibits the Lorentz model of dispersion since the wire-inclusions play a role of "atoms" (elementary dipole scatterers), which are polarised with an ac electric field. As compared with usual dielectrics we can drive the "atom polarisation" by the external magnetic field.* In this work, only a simple case of normal incidence and random orientations of wires in the composite slab has been considered. For these conditions, the effective permittivity may demonstrate the resonance and tuneable properties in the vicinity of the antenna resonance. In general case of $\varsigma_{z\varphi} \neq 0$ (which takes place in wires with a helical anisotropy), any wire inclusion can be excited not only by the ac longitudinal electrical field $\bar{e}_{0z}$ but also by the longitudinal magnetic field $\bar{h}_{0z}$, as it follows from the basic integro-differential equation (see Eq. 16 in Chapter 5):

$$\frac{\partial^2}{\partial z^2}(G * j) + k^2(G * j) = \frac{i\omega\varepsilon}{4\pi}\bar{e}_{0z}(z) - \frac{i\omega\varepsilon\varsigma_{zz}}{2\pi a c}(G_{\varphi} * j) + \frac{i\omega\varepsilon\varsigma_{z\varphi}}{4\pi}\bar{h}_{0z}(z). \qquad (1)$$

Here the impedance component $\varsigma_{z\varphi}$ transfers the magnetic field $\bar{h}_{0z}$ into the effective electromotive force (e.m.f.), which induces the current and dipole moment in the wire. The material relations in such kind of systems have very unusual form. *The bulk electrical polarisation* $\mathbf{P}$ *of the planar composite becomes proportional to both the electrical* $\mathbf{e}_0$ *and magnetic* $\mathbf{h}_0$ *excitation fields (this is the so-called* ***"chiral medium"****)*:

$$\mathbf{P} = (\vartheta\mathbf{e}_0 + \vartheta_{eff}\mathbf{e}_{0\|}) + \beta_{eff}\mathbf{h}_{0\|}, \qquad (2)$$

where ϑ is the electrical susceptibility of the dielectric matrix, ϑ_{eff} and β_{eff} are the effective bulk susceptibility due to the wire polarisation for the field projections $\mathbf{e}_{0\|}$ and $\mathbf{h}_{0\|}$ in the plane of the composite slab.

For the electric intensity vector $\mathbf{d}$ inside the planar composite we obtain the following representation:

$$\mathbf{d} = \mathbf{e}_0 + 4\pi\mathbf{P} = (1+4\pi\vartheta)\mathbf{e}_0 + 4\pi\vartheta_{eff}\mathbf{e}_{0||} + 4\pi\beta_{eff}\mathbf{h}_{0||} \quad (3)$$

or

$$\mathbf{d} = \varepsilon\mathbf{e}_0 + 4\pi\vartheta_{eff}\mathbf{e}_{0||} + 4\pi\beta_{eff}\mathbf{h}_{0||},$$

where $\varepsilon = 1+4\pi\vartheta$ is the matrix permittivity. If $\mathbf{e}_0$ and $\mathbf{h}_0$ are polarised in the plane of the composite slab ($\mathbf{e}_0=\mathbf{e}_{0||}$ and $\mathbf{h}_0 = \mathbf{h}_{0||}$) we can write:

$$\mathbf{d}_{||} = \varepsilon_{eff}\mathbf{e}_0 + 4\pi\beta_{eff}\mathbf{h}_0, \quad (4)$$

where $\varepsilon_{eff} = \varepsilon + 4\pi\vartheta_{eff}$ is the effective permittivity of composite.

However, since $\varsigma_{z\varphi} << 1$ (and hence $\beta_{eff} << 1$), the electrical excitation will prevail over the magnetic one in the geometry and polarisation considered in Chapter 5. In this case, we can neglect β_{eff} in Eq. (4) with the result that $\mathbf{d}_{||} \approx \varepsilon_{eff}\mathbf{e}_0$, as it was excepted in Chapter 5. Nevertheless, there are some polarisations of the electromagnetic wave and corresponding composite microstructures when the magnetic excitation becomes important. For example, the electrical excitation is absent at all for the electromagnetic wave propagating along the composite surface, while the electrical field is perpendicular to it, as shown in Fig. 6.1.

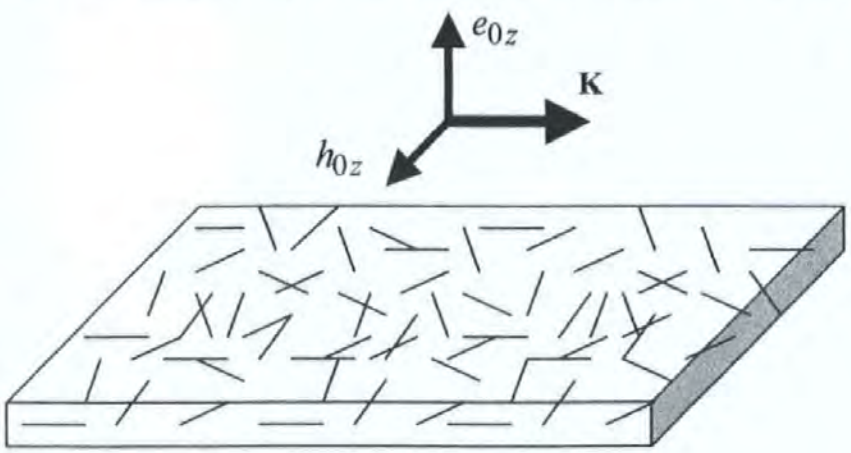

Fig. 6.1 *Polarisation of the electromagnetic wave providing the magnetic excitation in the composite slab with the random orientations of the wire inclusions.*

In this case, Eq. (1) gets the following form:

$$\frac{\partial^2}{\partial z^2}(G*j) + k^2(G*j) = -\frac{i\omega\varepsilon\varsigma_{zz}}{2\pi ac}(G_\varphi * j) + \frac{i\omega\varepsilon\varsigma_{z\varphi}}{4\pi}\bar{h}_{0z}(z). \quad (5)$$

The same magnetic excitation can be provided even for the normal incidence of the electromagnetic wave, when the wire inclusions are ordered in one direction and the electrical field is directed perpendicular to them, as shown in Fig. 6.2.

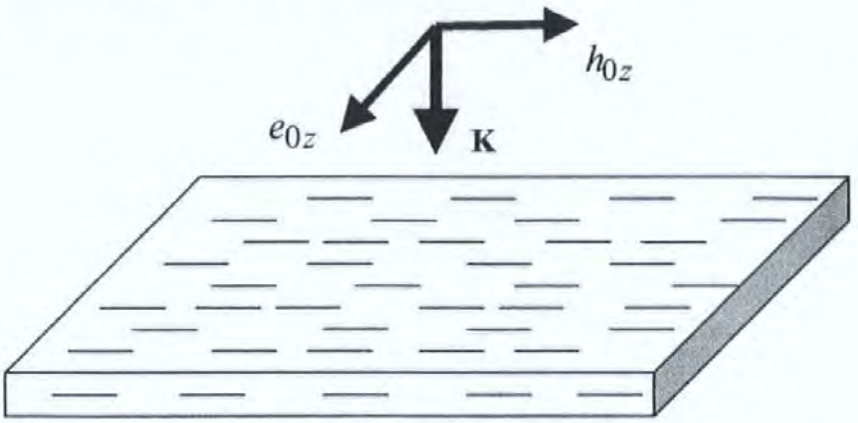

Fig. 6.2 *Polarisation of the electromagnetic wave providing the magnetic excitation in the composite slab with the ordered wire inclusions.*

Since $\varsigma_{z\varphi} << 1$, in both cases shown in Figs. 6.1 and 6.2 the inclusion concentration has to be chosen quite large to observe a sufficient field effect on the effective response. In this case, the strong interaction between wires will take place, which may result in a shifting of the resonance frequency. To the contrary, for the composite structure and wave polarisation considered in Chapter 5 the inclusions concentration was very small because the electrical dipole polarisation is very large. The interaction can be most easily accounted for in a periodical lattice of unidirectional wires, where the current distribution in each wire is the same due to symmetry and geometry. In this case, the Green function G in Eq. (1) must be replaced with the so-called structural Green function $\hat{G}$ (in other words, "Greenian"),[20] which is the sum of the Green functions over the lattice:

$$\frac{\partial^2}{\partial z^2}(\hat{G} * j) + k^2(\hat{G} * j) = \frac{i\omega\varepsilon}{4\pi}\bar{e}_{0z}(z) - \frac{i\omega\varepsilon\varsigma_{zz}}{2\pi a c}(G_{\varphi} * j) + \frac{i\omega\varepsilon\varsigma_{z\varphi}}{4\pi}\bar{h}_{0z}(z), \tag{6}$$

$$\hat{G}(z-s,y,x) = \sum_{q,l,m}\frac{\exp(ik r_{q,l,m})}{4\pi r_{q,l,m}}. \tag{7}$$

In Eq. (7) $r_{q,l,m} = \sqrt{(z - s - z_q)^2 + (y - y_l)^2 + (x - x_m)^2}$, the point (z, y, x) lies onto the wire surface, (q, l, m) is the 3D integer index of a wire in the wire array, when the summation is carried over the lattice of unidirectional wires. The vector (z_q, y_l, x_m) is directed to the wire centre. With $q, l, m \equiv 0$, $r_0 = \sqrt{(z - s)^2 + a^2}$, where a is the wire radius (see Chapter 5). With $l \neq 0$ and $m \neq 0$, $r_{q,l,m} \approx \sqrt{(z - s - z_q)^2 + (y_l)^2 + (x_m)^2}$ since a is assumed to be much smaller, than the lattice constants. *This "wire crystal" [19] is of its own interest because it can exhibit band-gap properties, which in our case will be field dependent. Such system has not been analysed yet in terms of the rigorous periodical solution.*

Another perspective research is related with the nanocomposite consisting of the nanowires and nanorings and considered in the optical range.[21] The succession of the analytical methods allows us to perfect the ideas, which have been developed in the microwave range. In particular, the effective tuneable properties may be realised in the nanocomposites since the conductivity of the nanoinclusions (or structured nanoinclusions) also may depend on the external fields.[21] Further more, such composites along with the effective permittivity can have the effective magnetic permeability for the non-magnetic inclusions. This artificial magnetism opens up extraordinary possibilities for the creation of new mediums with unusual optical properties. Recently, the idea of electromagnetic complex materials with both negative real permittivity and permeability has attracted a great deal of attention. *This idea dates back to 1960's when Russian physicist Veselago [22] postulated theoretically the monochromatic electromagnetic plane wave propagation in a lossless medium with simultaneously negative real permittivity and permeability at a given frequency, and he theoretically showed that in such media the direction of Poynting vector is antiparallel to the direction of phase velocity for a uniform monochromatic plane wave.* Such kind of a material was named as the "left-handed materials" or "metamaterials". The recent resurgence of interest in this medium began when Smith, Schultz and Shelby in their research group at University of California (San Diego),[23-26] after the work of Pendry of Imperial College (London),[27,28,19] constructed such a composite medium for the microwave regime. This composite medium is organised as the periodical system of the coupled rings and wires. Many researchers from all over the world have now been exploring various aspects of this class of complex media, and several potential future applications of these media have been speculated.[29-32]

In principle, the tuneable composites proposed in works [15] and [17] may be used for the creation of the field-controlled left-handed materials and band-gap structures.[33]

References:

[1] L. V. Panina and K. Mohri, Appl. Phys. Lett. **65**, 1189 (1994).

[2] L. V. Panina, K. Mohri, K. Bushida, and M. Noda, J. Appl. Phys. **76**, 6198 (1994).

[3] R. S. Beach and A. E. Berkowitz, J. Appl. Phys. **76**, 6209 (1994).

[4] L. V. Panina and D. P. Makhnovskiy, *"Magneto-impedance in Multilayered Films for Miniature Magnetic Sensors"*, **Book chapter** in *"Introduction to Complex Mediums for Optics and Electromagnetics"*, Editors: W. S. Weiglhofer and A. Lakhtakia, SPIE Optical Engineering Press, 2003.

[5] L. V. Panina, K. Mohri, T. Uchiyama, K. Bushida, and M. Noda, IEEE Trans. Magn. **31**, 1249 (1995).

[6] D. P. Makhnovskiy, L. V. Panina, and D. J. Mapps, Phys. Rev. **B 63**, 144424 (2001).

[7] K. Hika, L. V. Panina, and K. Mohri, IEEE Trans. Magn. **32**, 4594 (1996).

[8] D. P. Makhnovskiy, A. S. Antonov, A. N. Lagarkov, and L. V. Panina, J. Appl. Phys. **84**, 5698 (1998).

[9] L. V. Panina, D. P. Makhnovskiy, and K. Mohri, J. Magn. Soc. Japan **23**, 925 (1999).

[10] R. L. Sommer, A. Gundel, and C. L. Chien, J. Appl. Phys. **86**, 1057 (1999).

[11] D. P. Makhnovskiy, A. N. Lagarkov, L. V. Panina, and K. Mohri, Sensor and Actuators **A81**, 106 (2000).

[12] L. V. Panina and K. Mohri, Sensors and Actuators **A81**, 71 (2000).

[13] N. Kawajiri, M. Nakabayashi, C. M. Cai, K. Mohri, and T. Uchiyama, IEEE Trans. Magn. **35**, 3667 (1999).

[14] N. Fry, D. P. Makhnovskiy, L. V. Panina, S. I. Sandacci, M. Akhter, and D. J. Mapps, submitted to IEEE Trans. Magn. (**November 2002**).

[15] D. P. Makhnovskiy and L. V. Panina, J. Appl. Phys. **93**, 4120 (2003).

[16] P. Delooze, L. V. Panina, D. J. Mapps, K. Ueno, and H. Sano, accepted to J. Magn. Magn. Mater. (2003).

[17] O. Reynet, A.-L. Adenot, S. Deprot, O. Acher and M. Latrach, Phys. Rev. **B 66**, 094412 (2002).

[18] A. K. Sarychev and V. M. Shalaev, Physics Reports **335**, 275-371 (2000).

[19] J. B. Pendry, A. J. Holden, D. J. Robbins, and W. J. Stewart, J. Phys. Condens. Matter. **10**, 4785 (1998).

[20] J. M. Ziman, *"Principles of the theory of solids"*, 2d edition, Cambridge at the University Press, 1972.

[21] L. V. Panina, A. N. Grigorenko, and D. P. Makhnovskiy, Phys. Rev. **B 66**, 155411 (2002).

Left-handed materials:

[22] V. G. Veselago, "The electrodynamics of substances with simultaneously negative values of epsilon and mu", Sov. Phys. USPEKHI, vol. 10, no. 4, pp. 509-514, January-February 1968.

[23] D. R. Smith, W. J. Padilla, D. C. Vier, S. C. Nemat-Nasser and S. Schultz, "Composite medium with simultaneously negative permittivity and permeability", Phys. Rev. Lett. **84**, 4184 (2000).

[24] D. R. Smith, D. C. Vier, N. Kroll and S. Schultz, "Direct calculation of permeability and permittivity for a left-handed metamaterial" Appl. Phys. Lett. **77**, 2246 (2000).

[25] D. R. Smith and N. Kroll, "Negative refractive index in left-handed materials" Phys. Rev. Lett. **85**, 2933 (2000).

[26] R. Shelby, D. R. Smith and S. Schultz, "Experimental verification of a negative index of refraction", Science **292**, no. 77 (2001).

[27] J. B. Pendry, A. J. Holden, W. J. Stewart, and I. Youngs, Phys. Rev. Lett. **76**, 4773 (1996).

[28] J. B. Pendry, A. J. Holden and W. J. Stewart, "Magnetism from conductors and enhanced nonlinear phenomena", IEEE Trans. Microwave Theory Tech. **47**, 2075 (1999).

[29] R. W. Ziolkowski, "Wave propagation in media having negative permittivity and permeability", Phys. Rev. **E 64**, 1 (2001).

[30] C. Caloz, C.-C. Chang and T. Itoh, "Full-wave verification of the fundamental properties of left-handed materials in waveguide configurations", J. Appl. Phys. **90**, 5483 (2001).

[31] T. Weiland, R. Schuhmann, R. Greegor, C. Parazzoli, A. Vetter, D. R. Smith, D. C. Vier and S. Schultz, "Calculation of S-parameters for a left-handed metamaterial and comparison with experimental data", J. Appl. Phys. **90**, 5419 (2001).

[32] S. T. Chui and L. Liangbin, "Theoretical investigation on the possibility of preparing left-handed materials in metallic magnetic granular composites", Phys. Rev. **B 65**, 1 (2002).

[33] A. Figotin, Y. A. Godin, and I. Vitebsky, Phys. Rev. **B 57**, 2841 (1998).

Appendix B:

Nanocomposite materials at the optical range

Optomagnetic composite medium with conducting nanoelements

L. V. Panina, A. N. Grigorenko, and D. P. Makhnovskiy
Department of Communication, Electronic and Electrical Engineering, University of Plymouth, Drake Circus, Plymouth, Devon PL4 8AA, United Kingdom
(Received 24 April 2002; published 8 October 2002)

A type of metal-dielectric composites has been proposed that is characterized by a resonancelike behavior of the effective permeability μ_{eff} in the infrared and visible spectral ranges. This material can be referred to as an optomagnetic medium. It consists of conducting inclusions in the shape of nonclosed contours or pairs of parallel sticks with length of 50–100 nm embedded in a dielectric matrix. The analytical formalism developed is based on solving the scattering problem for considered inclusions with impedance boundary condition, which yields the current and charge distributions within the inclusions. The magnetic properties originated by induced currents are enhanced by localized plasmon modes, which make an inclusion resonate at a much lower frequency than that of the half-wavelength requirement at microwaves. It implies that microstructure can be made on a scale much less than the wavelength and the effective permeability is a valid concept. The presence of the effective magnetic permeability and its resonant properties lead to unusual optical effects and open interesting applications. In particular, the condition for Brewster's angle becomes different resulting in reflectionless normal incidence from air (vacuum) if the effective permeability and permittivity are the same. The resonant behavior of the effective permeability of the proposed optomagnetic medium could be used for creation of optical polarizes, filters, phase shifters, and selective lenses.

DOI: 10.1103/PhysRevB.66.155411 PACS number(s): 78.67.−n, 75.75.+a, 41.20.−q, 42.70.−a

I. INTRODUCTION

Metal-dielectric composites, in which small metal particles are embedded into dielectric host, present an exciting area of study. The overall electric, magnetic, and optical properties are not governed by the behavior of the raw materials. A vast amount of literature exists on this topic. In the limit of high metal concentration, the percolation across the connected clusters results in critical dielectric[1] and magnetic[2] responses, strong local field fluctuation,[3] and enhancement of transport[4,5] and optical[6,7] nonlinearities. In the limit of diluted composites, individual metal inclusions contribute to the effective electromagnetic properties; however, small metallic scatters may show completely different behavior as compared with bulk metals. In both cases, the effective permittivity ε_{eff} and permeability μ_{eff} can be tuned to values not easily possible in natural materials.

Recent advances in microfabrications make possible creation of composite materials with constituents of different forms and sizes down to nanoscales.[8,9] This offers a way to engineer various dielectric and magnetic metamaterials, since the effective parameters ε_{eff} and μ_{eff} are determined by microstructure. Composites containing rings, helix on Ω particles exhibit resonancelike behavior of both the permittivity and permeability in overlapping frequency bands,[10,11] which is quite unusual in nature. In a medium of three-dimensional array of intersecting wires the propagation modes have a dispersion characteristic similar to that in a neutral plasma with negative ε_{eff} below the plasma resonance somewhere in the gigahertz range.[12,13] It was further shown that the composites built of two-dimensional arrays of split copper rings[14] and wires have a range of frequencies over which both the permittivity and permeability are negative in microwaves.[15]

These materials have generated a considerable interest as they offer a possibility to realize a negative index of refraction n. Many surprising effects are possible in these so-called left handed materials theoretically predicted by Veselago,[16] which would be of great importance for communications and electronics. These include reversed Doppler and Cherenkov effects and a reversed Snell's angle, which could result in lenses without limitations on the resolution by wavelength.[17] So far, the concept of negative refraction has been predicted and proven at microwave frequencies. In the experiment on deflection of a beam of microwave radiation by a prism made of wire-and-ring material negative refraction angles were found,[18] which correspond to the negative index n appropriate to Snell's law. The transmission spectra measured in these materials also confirm the concept of negative n.[15]

An immediate question is whether left-handed materials can be realized at optical frequencies. (We exclude from consideration photonic crystals where it is difficult to assign an effective equivalent n and where the phenomenon of negative refraction has been recently predicted near negative group velocity bands.[19]) On one hand, negative dielectric constant is natural for metals below the plasma resonance that falls above visible frequencies. For example, silver would be a good choice for negative permittivity at optical frequencies since the resistive part is very small. On the other hand, quite rigid limitations exist with respect to the permeability at high frequencies. There is a widespread believe that the concept of permeability has no physical meaning at optical frequencies and onward, as was proven for atomic magnetism (see, for example, Ref. 20). *The aim of this paper is to elucidate the implications related to high-frequency magnetic properties and to demonstrate that metal-dielectric composites with nanoinclusions can have a considerable magnetic activity at optical frequencies.*

We consider two types of metal-dielectric composites with inclusions forming different current contours: two-wire contour and a single ring with a gap (see Fig. 1). The math-

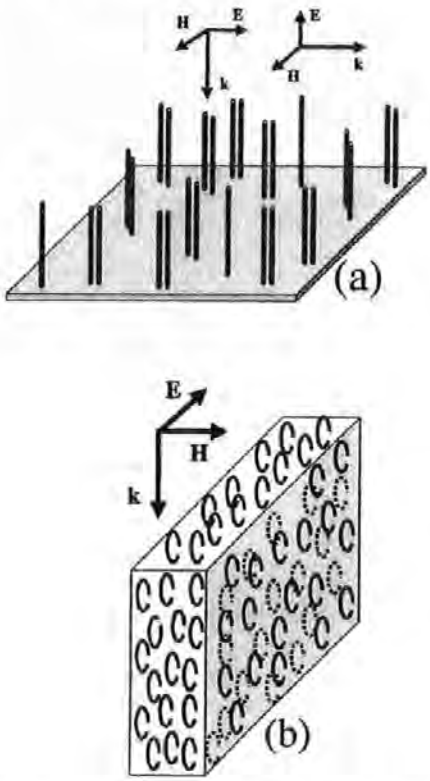

FIG. 1. Composite medium with effective permeability at optical frequencies. A possible polarization of the electromagnetic wave associated with induced magnetic properties is indicated. In (a), a system of nanowires grown on a substrate is shown, in which two parallel wires form a constituent element. The spacing in the pair of wires is much smaller than the distance between the pairs. In (b), a nanoring composite is shown.

ematical formalism developed is based on a modified antenna theory, which provides a bridge between the microwave methods using distributed parameters and the optical description based on plane waves and surface plasmons. We show that the magnetic properties at optical frequencies can be generated by localized plasmon modes. The theory predicts resonancelike behavior of the effective permeability over certain frequency range in the infrared and visible parts of spectrum in such composites. The negative values of μ_{eff} are possible past the resonance; however, high volume fractions are needed to realize $\mu_{\text{eff}}<0$ since the magnetic dipole interaction strongly reduces the resonance peaks. Nevertheless, other unusual optical effects can be realized in the presence of some μ_{eff} noticeably different from unity (which do not require negative μ_{eff}). In particularly, the condition under which there is no reflected waves (Brewster's angle) changes. In the case $\mu_{\text{eff}}=\varepsilon_{\text{eff}}$ a normal incidence from air (vacuum) gives no reflection. This effect known at microwaves could be useful for optical filters and isolators.

The phenomenon of nontrivial permeability at optical frequencies can be named optomagnetism (and the area of study is then referred to as optomagnetics) in order to distinguish it from the magnetic field influence on light propagation known as magnetooptics. The proposed optomagnetic medium is foreseen to find a variety of applications in optics and optoelectronics. The resonance properties of the effective permeability at optical frequencies can be exploited for the production of tuneable narrow bandwidth optical filters (either on reflection or on absorption). The presence of permeability may be used in optoelectronic interferometers to measure phase shifts induced by magnetic fields and is likely to result in a new generation of all optical sensors. The dependence of permeability dispersion upon carrier concentration inside the inclusion and external parameters could be used for creation of tuneable optical elements.

Natural ferromagnetic behavior tails off completely at gigaherz frequencies. In the case of ferrite materials with few magnetic sublattices, there exists so-called exchange modes of magnetic excitations with eigenfrequencies in the infrared, but their intensity is very small. Then, only the electron movement under the Lorentz force would contribute to μ_{eff} at optical frequencies. In this case, there appears a problem of using a concept of permeability in the averaged macroscopic Maxwell equations. The situation is different for composite materials containing nanosized metal inclusions. The effective permeability is obtained by averaging the magnetic moments of closed currents in metal inclusions and can have quite high values as a result of the resonance interaction of the incident electromagnetic wave with plasmons confined inside the inclusion (localized plasmon modes). The resonant frequency is lowered considerably allowing the resonance to occur at wavelength of the exciting light much larger than the inclusion size (at microwaves, there would be a half-wavelength requirement for resonance) and the effective parameters are still a valid concept. Near resonance, the currents in the inclusions are enhanced and large magnetic moments are generated. That may either enhance (paramagnetic effect) or oppose (diamagnetic effect) the incident field and the effective permeability exhibits a resonant behavior. Considering a diluted system with a small volume concentration $p\ll 1$ of the current contours and calculating μ_{eff} by summation over independent magnetic moments give the dispersion of the effective permeability with $\mu_{\text{eff}}>1$ below the resonance and μ_{eff} goes to negative values past the resonance. However, the interaction between the inclusions (taken into account within the effective medium theory[21,22]) decreases considerably the values of μ_{eff} near the resonance and for realistic concentrations ($p<0.1$) always $\mu_{\text{eff}}>0$. The considered system has also the effective permittivity ε_{eff}. For ring-inclusions, the value of ε_{eff} is reduced due to geometry. For two-wire contours, the permittivity is essential for the light polarization with the electric field along the wires [see Fig. 1(a)]; however, the resonance frequency for ε_{eff} is shifted towards higher frequencies with respect to that for μ_{eff}, which makes it possible to realize the condition $\mu_{\text{eff}}\approx\varepsilon_{\text{eff}}$ in both cases.

The paper is organized as follows. Section II starts with the description of proposed optical effects due to existence of substantial μ_{eff}. In Sec. III we discuss in more detail the limitations on the concept of permeability at high frequencies. Section IV formulates how to determine the effective parameters in the considered composites. In Sec. V, the mathematical formalism for calculation of the current distri-

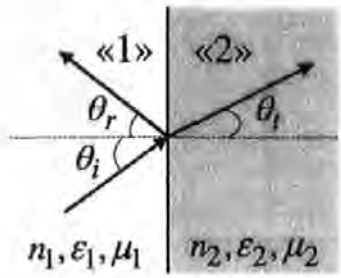

FIG. 2. Geometry of reflection and refraction.

bution in the inclusions is given. Section VI presents the obtained results on μ_{eff} and ε_{eff} and an overall discussion. There are also two mathematical appendixes.

II. BREWSTER'S ANGLE IN THE PRESENCE OF PERMEABILITY

Introducing effective magnetic permeability at optical frequencies may result in some unusual behavior of light propagating in macroscopically heterogeneous composite media (with boundaries). Here we consider the reflection and refraction of a polarized light at an interface between two dielectric media with nontrivial magnetic properties. The results of this section are, in many respects, known (see, for example, Ref. 23), however, it is convenient to reexamine the conditions of reflection/refraction described by Fresnel's equations, since they are customarily analyzed for nonmagnetic materials. In particular, we show that the condition under which there is no a reflected wave from a boundary (Brewster's angle) becomes different in the presence of permeability. The light is incident from medium "1" with the material parameters ε_1, μ_1 towards medium "2" with ε_2, μ_2. The quantities pertaining to the incident, reflected and transmitted waves are distinguished by the suffixes i, r, and t, respectively, as shown in Fig. 2. In the case of the electric field **E** perpendicular to the plane of incidence (s polarization) the Fresnel's relationship between the field in the incident wave and that in the reflected wave is[23]

$$\left(\frac{E_r}{E_i}\right)_{\perp} = \frac{(n_1/\mu_1)\cos\theta_i - (n_2/\mu_2)\cos\theta_t}{(n_1/\mu_1)\cos\theta_i + (n_2/\mu_2)\cos\theta}. \tag{1}$$

Here, $\theta_{i,r,t}$ are the corresponding angles of incidence, reflection and refraction obeying usual Snell's equation

$$\theta_i = \theta_r, \quad n_1 \sin\theta_i = n_2 \sin\theta_t \tag{2}$$

with the index of refraction $n = \sqrt{\varepsilon\mu}$. The condition $E_r = 0$, or

$$n_1\mu_2 \cos\theta_i = n_2\mu_1 \cos\theta_t, \tag{3}$$

gives Brewster's angle θ_b. For nonmagnetic media $\mu_1 = \mu_2 = 1$ Eq. (3) can hold only if $\varepsilon_1 = \varepsilon_2$ (no optical interface). Therefore, Brewster's angle is not observed for s polarization in conventional optics. With $\mu_{1,2} \neq 1$ the absence of reflection and Brewster's angle can happen even for s polarization:

$$\tan\theta_b = \sqrt{\frac{\varepsilon_1\mu_2^2 - \varepsilon_2\mu_1\mu_2}{\varepsilon_2\mu_1\mu_2 - \varepsilon_1\mu_1^2}} \tag{4}$$

when $(\varepsilon_1\mu_2^2 - \varepsilon_2\mu_1\mu_2)/(\varepsilon_2\mu_1\mu_2 - \varepsilon_1\mu_1^2) \geq 0$.

Suppose that the optical properties are due only to the magnetic permeability ($\varepsilon_1 = \varepsilon_2 = 1, n_1 = \sqrt{\mu_1}, n_2 = \sqrt{\mu_2}$), then, the Brewster angle is given by

$$\tan\theta_b = n_2/n_1. \tag{5}$$

Equation (5) formally coincides with a usual equation known for p-polarized light (electrical field is in the plane of incidence). For incidence from air (vacuum) ($\varepsilon_1 = \mu_1 = 1$), Eq. (4) becomes

$$\tan\theta_b = \sqrt{\frac{\mu_2^2 - n_2^2}{n_2^2 - 1}},$$

which can be satisfied either by $\mu_2^2 \geq n_2^2 > 1$ ($|\mu_2| \geq |\varepsilon_2|$ and $|n_2| > 1$) or by $\mu_2^2 \leq n_2^2 < 1$ ($|\mu_2| \leq |\varepsilon_2|$ and $|n_2| < 1$).

For the p-polarization case, the Brewster angle can be found from Eq. (4) by interchanging ε and μ. This is because the boundary conditions for the two cases are symmetrical with respect to **E** and **H**. Then, Eq. (4) becomes

$$\tan\theta_b = \sqrt{\frac{\mu_1\varepsilon_2^2 - \mu_2\varepsilon_1\varepsilon_2}{\mu_2\varepsilon_1\varepsilon_2 - \mu_1\varepsilon_1^2}} \tag{6}$$

and Brewster's angle exists for p polarization when $(\mu_1\varepsilon_2^2 - \mu_2\varepsilon_1\varepsilon_2)/(\mu_2\varepsilon_1\varepsilon_2 - \mu_1\varepsilon_1^2) \geq 0$. For $\mu_1 = \mu_2 = 1$ Eq. (6) gives a standard form for the Brewster angle $\tan\theta_b = n_2/n_1$ [compare with Eq. (5)]. In the case of incidence from air ($\varepsilon_1 = 1$ and $\mu_1 = 1$) Eq. (6) reduces to

$$\tan\theta_b = \sqrt{\frac{\varepsilon_2^2 - n_2^2}{n_2^2 - 1}}. \tag{7}$$

From Eq. (7) it is clear that Brewster's angle in this polarization is realized either under the condition $\varepsilon_2^2 \geq n_2^2 > 1$ ($|\varepsilon_2| \geq |\mu_2|$ and $|n_2| > 1$) or $\varepsilon_2^2 \leq n_2^2 < 1$ ($|\varepsilon_2| \leq |\mu_2|$ and $|n_2| < 1$), which are opposite to those for s polarization.

It is worth mentioning that for both polarizations there is no reflection at normal incidence under the condition $\varepsilon_1/\mu_1 = \varepsilon_2/\mu_2$, as follows from Eqs. (4) and (6). This result is well known for microwaves, representing the condition of the impedance matching since the ratio ε/μ is related to the wave impedance.[23] It also means that an arbitrary polarized light will not be reflected from the interface of air (vacuum) and a medium with optical constants $|\varepsilon_2| = |\mu_2|$. Thus, there may be an optical analogy of the impedance matching. In view of these conditions of reflection, optomagnetic materials may demonstrate interesting phenomena at optical frequencies, suitable for applications in optical filters, phase shifters, and isolators.

III. LIMITATIONS IMPOSED ON PERMEABILITY AT HIGH FREQUENCIES

In this section we analyze the restriction conditions for introducing high frequency permeability to the Maxwell

equations. The magnetization $\mathbf{M}=(\mathbf{B}-\mathbf{H})/4\pi$ appears in the Maxwell equations as a result of averaging the microscopic current density $\mathbf{J}_{\text{mic}}$:

$$\text{curl}\mathbf{M}=\frac{\langle \mathbf{J}_{\text{mic}}\rangle}{c}. \tag{8}$$

Here $\langle\cdots\rangle$ stands for a mean value of a microscopic quantity c is the velocity of light (Gaussian units are used throughout the paper). The physical meaning of magnetization is the magnetic moment per unit volume. This comes from the possibility to rewrite the total magnetization of the body in the form

$$\int \mathbf{M}dV=\frac{1}{2c}\int (\mathbf{r}\times\langle \mathbf{J}_{\text{mic}}\rangle)dV, \tag{9}$$

where the integration is carried out inside the body. Equation (8) is correct for a static magnetic field. When the macroscopic fields depend on time, the establishment of the relationship between the mean value $\langle \mathbf{J}_{\text{mic}}\rangle$ and other quantities is not straightforward. A general form of Eq. (8) is[20]

$$\text{curl}\mathbf{M}=\frac{\langle \mathbf{J}_{\text{mic}}\rangle}{c}-\frac{1}{c}\frac{d\mathbf{P}}{dt}, \tag{10}$$

where $\mathbf{P}$ is the polarization vector. However, Eq. (10) is not consistent with Eq. (9). Therefore, the physical meaning of $\mathbf{M}$ at high frequencies depends on the possibility of neglecting the second term in the right part of Eq. (10):

$$c\text{curl}\mathbf{M}\gg\frac{d\mathbf{P}}{dt}. \tag{11}$$

Let us suppose that the fields are induced by an electromagnetic wave of frequency ω. Estimating $\text{curl}\mathbf{M}\sim\chi H/l$, $dP/dt\sim\omega\alpha E$, where χ is the magnetic susceptibility, α is the electric polarizability, l is the characteristic size of the system, and taking $E\sim H$ for the electromagnetic wave, Eq. (11) can be written as

$$\chi\gg\alpha l/\lambda, \tag{12}$$

where λ is the wavelength. It is generally considered that at optical frequencies (and onward) inequality (12) cannot be satisfied and the concept of the permeability is meaningless. This is correct if the magnetic moment is associated with electron motion in the atom. Indeed, the relaxation times for any paramagnetic or ferromagnetic processes are considerably larger than optical periods. Then χ is due to electron movements under the Lorenz force, and can be estimated as $\chi\sim(v/c)^2$, where v is the electron velocity in the atom. On the other hand, the optical frequencies are of the order of v/b where b is the atomic dimension. Then Eq. (12) reads $l\ll b(v/c)$, which is not compatible with the requirement that the characteristic size of the system has to be much greater than the atomic dimension ($l\gg b$).

The situation may be completely different for metal-dielectric composites. If the inclusion size is smaller than the wavelength (but larger than the atomic size) the effective magnetic and dielectric parameters can be introduced as a result of local field averaging. For a composite with metal grains of a few nanometres, the effective parameters including permeability become meaningful even for optical frequencies. In this case, the effective permeability is obtained by averaging the magnetic moments of induced currents in metal inclusions. Our analysis demonstrates that inequality (12) is satisfied in the composites considered over certain frequencies in the optical range.

IV. PROBLEM FORMULATION

In metal-dielectric composites irradiated by high frequency electromagnetic field the magnetic properties are produced by contour currents induced in metallic inclusions. If the spatial scale of the system is smaller than the incident wavelength, the magnetic moments of individual current loops (within a single inclusion or formed by a number of them) give rise to magnetization and the effective permeability.[2,22,24] The interaction between induced currents can be considered within the effective medium approximation. Composite materials with inclusions of a complex form (split rings, chiral and omega particles) are known to have unusual magnetic properties including both giant paramagnetic effect and negative μ_{eff}.[10–12] These properties are related to resonance interaction of the electromagnetic wave with an inclusion and have been reported for microwave frequencies. The complex form of the inclusion is needed to realize the resonant conditions at wavelengths much larger than the inclusion size. For example, in a unit with two coaxial rings having oppositely oriented splits[12] a large capacitance is generated lowering the resonance frequency considerably. When the inclusion dimensions are reduced down to nanoscale, the wavelength can be proportionally decreased down to microns falling in the optical range. Then, the effective permeability of nanocomposites can be substantial at optical frequencies. However, it seems that the fabrication of nanoinclusions of a complex form may not be a realistic task. Fortunately, in the optical region the resonance frequency is lowered due to localized plasmon modes and fairly simple inclusions of a loop shape will create substantial magnetic moments even when the inclusion size is much smaller than the wavelength of the incident light.

Within the effective medium theory, the problem is reduced to considering the scattering of electromagnetic wave by a metallic contour. In general, this process can be very complicated. Here we consider two types of inclusions: ring-shaped inclusions (having some gap large enough to neglect the edge capacitance) and pairs of parallel conducting sticks connected via displacement currents (see Fig. 1), which permit a fairly simple analysis at certain approximations. For the chosen geometry, the resonance of localized plasmons confined within the inclusion is realized, which leads to the resonant current distributions and eventually, to large induced magnetic moments. The latter is responsible for the effective permeability having a resonancelike dispersion law with the resonant frequency coinciding with that for the current distribution.

Let us formulate the basic assumptions under which the problem is treated. We consider the composite medium irra-

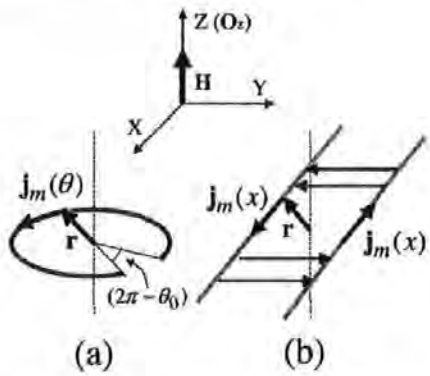

FIG. 3. Geometry of metallic inclusions, principle directions, and quantities used.

diated by a plane-polarized electromagnetic wave of a single frequency ω, so that the time dependence is of the form $\exp(-i\omega t)$. The contour length (l) is much larger than the cross-section size ($2a$). Then, when calculating fields in the surrounding space, the thickness of the contour can be neglected and the induced currents can be replaced by the effective linear currents $\mathbf{j}$. The current distribution inside the inclusion affects the scattered fields only via the boundary conditions imposed at the inclusion surface. The wavelength is also much larger than the cross section $\lambda \gg 2a$, but there is no restrictions on l with respect to λ. The magnetic moments in the composite are induced when the incident light has the magnetic field directed perpendicular to the plane of a metallic contour as shown in Fig. 3. In the case of a circular contour [Fig. 3(a)], the field $\mathbf{H}$ induces a circumferential current $j_m(\theta)$ depending on the azimuthal angle θ. Then, the magnetic moment $\mathbf{m}$ associated with this current is

$$\mathbf{m}=\frac{1}{2c}\int [\mathbf{r}\times\mathbf{J}_m(\mathbf{r})]dV=\mathbf{o}_z\frac{R_0^2}{2c}\int_0^{\theta_0} j_m(\theta)d\theta, \quad (13)$$

where $\mathbf{J}_m=\mathbf{j}_m(\theta)\delta_s$, δ_s is the two-dimensional Dirac delta-function which peaks at the axis of the wire, R_0 is the radius of the contour, $(2\pi-\theta_0)$ is the angle of the gap, and $\mathbf{o}_z$ is the unit vector perpendicular to the contour plane. The currents due to the electric field give no contribution to $\mathbf{m}$. In the case of a pair of conducting sticks [Fig. 3(b)] the current is distributed along their length and can form closed contours via the displacement currents. The metallic sticks as elements to produce the effective permeability were first proposed in Ref. 25. In this work, however, a random assembly of metallic sticks was considered, for which the total magnetic moment vanishes due to symmetry. As a result, the effective permeability for such a system is unity, as was proven by experiments[26] (in Ref. 26 the response from a stick composite is described adequately in terms of the effective permittivity, indicating that the effective permeability is essentially unity). The magnetic properties may appear only in diluted composites containing pairs of parallel sticks as a single element, as shown in Fig. 1(a). The magnetic moment is then found as [from symmetry, the contribution from the displacements currents equals to that from current $j_m(x)$]:

$$\mathbf{m}=\mathbf{o}_z\frac{d}{c}\int_{-l/2}^{l/2} j_m(x)dx, \quad (14)$$

where d is the distance between the sticks. The magnetic polarizability χ_0 of a single inclusion associated with the induced moment can be found from $\mathbf{m}=\chi_0 V\mathbf{H}$, where V is the volume of the metallic inclusion. The effective permeability is calculated from a self-consistent equation of the type[2,22,24]

$$\mu_{\text{eff}}=1+4\pi p\chi_0(\mu_{\text{eff}}), \quad (15)$$

where p is the volume concentration. If the incident electromagnetic wave has the electric field $\mathbf{E}$ parallel to the wires [Fig. 1(a)] a substantial electric dipole moment is generated contributing to the effective permittivity. The currents $\mathbf{j}_e$ induced by this field can be considered separately as shown in the following section. The electric dipole moment $\mathbf{p}$ and the dielectric polarizability α_0 of the inclusion are calculated for stick contour using the continuity equation $\partial j_e/\partial x=i\omega\rho$ and integrating by parts with boundary conditions $j_e(\pm l/2)\equiv 0$ (ρ is the charge density per unit length):

$$\mathbf{p}=\mathbf{o}_x\frac{i}{\omega}\int_{-l/2}^{l/2} j_e(x)dx, \quad \mathbf{p}=\alpha_0 V\mathbf{E}. \quad (16)$$

The effective permittivity can be found from the self-consistent equation similar to Eq. (15).[25]

In our analysis it will be important to consider a resonance distribution of the induced currents. From the microwave antenna theory it is known that a nontrivial current distribution occurs when the wavelength is in the range of l. Then, the use of the effective dielectric and magnetic parameters is doubtful. However, in our case the situation is different. In optical and infrared spectral ranges, metal conductivity σ can be approximated by Drude formula

$$\sigma(\omega)=\frac{\sigma_0}{1-i\omega\tau}, \quad (17)$$

where $\sigma_0=\omega_p^2\tau/4\pi$, ω_p is the plasma frequency, τ is the relaxation time (for silver, $\sigma_0=5.7\times10^{17}\ \text{s}^{-1}$ and $\tau=2.7\times10^{-14}$ s). In the high frequency range considered here ($\omega\sim10^{15}\ \text{s}^{-1}$) losses in metal grains are relatively small $\omega\tau\gg1$. Therefore, the metal conductivity is characterized by the dominant imaginary part. This is very important for our analysis since the current can have a resonance for a considerably larger wavelength $\lambda\gg 2l$. Physically, this is associated with the resonance of localized plasmon modes.

In Eq. (17) the relaxation time τ has a meaning of the mean-free time between electron collisions. The metal inclusions considered here have a length in the range of 100 nm and a cross-section size of 10 nm. The mean-free pass in noble metals such as silver is about 40 nm. It implies that the parameter τ used in Eq. (17) differs from that in bulk materials. However, in the frequency range $\omega\tau\gg1$, electrons oscillate many times between collisions and the collisions are of little importance. The conductivity has a dominant imaginary part independent of τ:

$$\sigma(\omega)=\frac{\omega_p^2}{4\pi\omega^2\tau}+i\frac{\omega_p^2}{4\pi\omega}.$$

The resistive losses, which are determined by the real part, are typically smaller or in the range of the radiation losses and will only slightly change the values of currents at resonance. However, the resonance frequency will shift considerably towards higher frequencies if $\omega\tau\sim 1$. This imposes limitations on the minimum cross section.

V. MATHEMATICAL BACKGROUND

A. Basic equations

Let us consider the current distribution in a thin metallic conductor irradiated by an electromagnetic field. The approximations used are $2a\ll l$, $\lambda\gg 2a$. This is a standard problem of the antenna theory (see, for example, Refs. 27 and 28), which can be treated in terms of retarded scalar φ and vector $\mathbf{A}$ potentials. The total electric field $\mathbf{E}_t=\mathbf{e}_0+\mathbf{e}$ is represented by the sum of the external field $\mathbf{e}_0$ and the scattered field $\mathbf{e}$. In the Lorenz gauge $\varepsilon\partial\varphi/\partial t+4\pi\,\mathrm{div}\,\mathbf{A}=0$, the equation for $\mathbf{e}$ is written as

$$\mathbf{e}=\frac{4\pi i\omega\mu}{c^2}\mathbf{A}-\frac{4\pi}{i\omega\varepsilon}\,\mathrm{grad}\,\mathrm{div}\,\mathbf{A}. \tag{18}$$

The vector potential $\mathbf{A}$ taken at arbitrary point $\mathbf{r}_0$ is obtained in the form of a convolution with the total current density $\mathbf{J}(\mathbf{r})$:

$$\mathbf{A}(\mathbf{r}_0)=(G^*\mathbf{J})=\int_V\mathbf{J}(\mathbf{r}')G(r)dV_{\mathbf{r}'},\quad G(r)=\frac{\exp(ikr)}{4\pi r}, \tag{19}$$

where $\mathbf{r}=\mathbf{r}_0-\mathbf{r}'$, $r=|\mathbf{r}|$, integration is taken over the volume containing current, $k=(\omega/c)\sqrt{\varepsilon\mu}$ is the wave number, $G(r)$ is the Green function satisfying the Helmholtz equation. Customarily, Eq. (19) is solved under the zero boundary condition

$$\bar{\mathbf{E}}_t\equiv 0, \tag{20}$$

where $\bar{\mathbf{E}}_t$ is the tangential component of the total electric field taken at the surface of the conductor. Then, the current distribution is found from an integrodifferential equation. The condition (20) corresponds to the case of an ideal conductor with infinite conductivity. Being used as an approximation, Eq. (20) works reasonably well when the radiation losses are considerably larger than the resistive ones or the system is out of resonance. However, in certain cases (including ours), the current distribution may have a zero (or greatly reduced) dipole moment. This implies that the radiation losses are comparable with the resistive ones and the condition (20) is no longer valid. The processes related to a finite conductivity may change the resonance condition for the current distribution: reduce the current amplitude and shift of the resonance wavelength. Here the problem is solved imposing impedance boundary conditions, which is valid at any frequency including the optical range

$$\bar{\mathbf{E}}_t=\hat{\varsigma}(\bar{\mathbf{H}}_t\times\mathbf{n}), \tag{21}$$

where $\hat{\varsigma}$ is the surface impedance matrix, $\mathbf{n}$ is the unit vector normal to the surface and directed inside the conductor, $\bar{\mathbf{H}}_t$ is the tangential component of the total magnetic field taken at the surface (hereafter, overbar is used to denote tangential fields at the inclusion surface). For the geometry considered here (see Figs. 1 and 3), the external magnetic field is normal to the contour plane and gives no contribution to Eq. (21). The scattered field $\mathbf{h}$ is determined as

$$\mathbf{h}=\frac{4\pi}{c}\,\mathrm{curl}\;\mathbf{A}$$

or

$$\mathbf{h}(\mathbf{r}_0)=\frac{1}{c}\int_V\frac{(1-ikr)\exp(ikr)}{r^3}[\mathbf{J}(\mathbf{r}')\times\mathbf{r}]dV_{\mathbf{r}'}. \tag{22}$$

When the skin effect is strong, Eq. (21) does not depend upon geometry and for a nonmagnetic conductor (permeability of metal is always unity at optical frequencies) is represented by a scalar (normal skin effect):

$$\varsigma=(1-i)\sqrt{\frac{\omega}{8\pi\sigma}}. \tag{23}$$

The case of a thin arbitrarily shaped conductor having a circular cross section allows the surface impedance to be determined for any frequencies. The electromagnetic field inside such a conductor can be taken to be the same as that inside a straight cylinder. Then, in the local cylindrical coordinate system (r,φ,x) with the axis x in the axial direction the impedance boundary conditions (21) become

$$\bar{E}_{tx}=\varsigma_{xx}\bar{h}_\varphi,$$

$$\bar{E}_{t\varphi}=-\varsigma_{\varphi\varphi}\bar{h}_x, \tag{24}$$

with[29]

$$\varsigma_{xx}=\frac{k_0c}{4\pi\sigma}\frac{J_0(k_0a)}{J_1(k_0a)},\quad \varsigma_{\varphi\varphi}=-\frac{k_0c}{4\pi\sigma}\frac{J_1(k_0a)}{J_0(k_0a)}, \tag{25}$$

where $k_0^2=4\pi i\sigma\omega/c^2$ and J_0, J_1 are the Bessel functions of the zero and first order, respectively. Equations (25) are valid for normal skin-effect. For the dimensions considered, the skin depth is in the range of the mean-free pass, and both these parameters are larger than a. Then, the skin effect is week, and using Eq. (25) is still reasonable.

Since we are interested only in fields in the surrounding space, the current inside a thin conductor can be replaced by an effective linear one $j(x)$ that flows along the axis of the wire: $\mathbf{J}(\mathbf{r})=\mathbf{j}(x)\delta_S$. The volume integration in Eq. (19) is then replaced by the integration along the current contour. Thus, the current distribution in a thin conductor irradiated by the electromagnetic field is found from Eqs. (18), (19) with boundary condition (24) that binds scattered fields $\mathbf{e}$ (18) and $\mathbf{h}$ (22) taken on the surface of the conductor.

B. Current equation in a straight wire with circular cross section

First, the current equation is obtained for a straight wire with a circular cross section placed in the electrical field $\mathbf{e}_0$ (of any origin) parallel to the wire axis x. The scattered field $\mathbf{e}$ is determined by the x component of the vector potential. The value of the longitudinal electric field $\bar{e}_x(x)$ taken at the wire surface is represented in terms of the integrodifferential operator with respect to x, as it follows from Eqs. (18), (19):

$$\bar{e}_x(x) = -\frac{4\pi}{i\omega\varepsilon}\left[\frac{\partial^2}{\partial x^2}(G^*j) + k^2(G^*j)\right],$$

$$(G^*j) = \int_{-l/2}^{l/2} j(s)G(r)ds, \quad r = \sqrt{(x-s)^2 + a^2}. \tag{26}$$

For this geometry, the scattered magnetic field $\bar{h}_\varphi$ taken at the surface is circumferential. In Eq. (22), considering that the effective linear current $j(x')$ is flowing along the wire axis and $\mathbf{r}_0$ points at the wire surface yields $[\mathbf{J}(x')\times\mathbf{r}]|_\varphi = j(x')a$. Then, the equation for $\bar{h}_\varphi$ obtains the form

$$\bar{h}_\varphi(x) = \frac{2}{ac}(G_\varphi^* j) = \frac{2}{ac}\int_{-l/2}^{l/2} j(s)G_\varphi(r)ds, \tag{27}$$

where $G_\varphi(r) = a^2(1-ikr)\exp(ikr)/2r^3$.

Finally, substituting Eqs. (26) and (27) into boundary condition (24) yields the integrodifferential equation for the linear current $j(x)$:

$$\frac{\partial^2}{\partial x^2}(G^*j) + k^2(G^*j) = \frac{i\omega\varepsilon}{4\pi}\bar{e}_{0x}(x) - \frac{i\omega\varepsilon\varsigma_{xx}}{2\pi ac}(G_\varphi^* j). \tag{28}$$

Equation (28) is solved imposing zero boundary conditions at the wire ends: $j(-l/2) = j(l/2) = 0$ (the end surfaces are assumed small and associated capacitance is neglected).

Real parts of the Green functions $\mathrm{Re}(G)$ and $\mathrm{Re}(G_\varphi)$ have sharp peaks at $s = x$, which makes it possible to use the following approximations for calculating the convolutions[30]

$$[\mathrm{Re}(G)^* j] \approx j(x)\int_{-l/2}^{l/2} \mathrm{Re}[G(r)]ds = j(x)Q,$$

$$Q = \int_{-l/2}^{l/2} \mathrm{Re}[G(r)]ds \propto \frac{1}{4\pi}\int_{-l/2}^{l/2}\frac{ds}{\sqrt{s^2+a^2}} \sim \frac{\ln(l/a)}{2\pi},$$

$$[\mathrm{Re}(G_\varphi)^* j] \approx j(x)\int_{-l/2}^{l/2} \mathrm{Re}[G_\varphi(r)]ds = j(x)Q_\varphi,$$

$$Q_\varphi = \int_{-l/2}^{l/2} \mathrm{Re}[G_\varphi(r)]ds \propto \frac{a^2}{2}\int_{-l/2}^{l/2}\frac{ds}{(s^2+a^2)^{3/2}} + \frac{a^2k^2}{2}\int_{-l/2}^{l/2}\frac{ds}{\sqrt{s^2+a^2}} \propto [1 + a^2k^2\ln(l/a)] \sim 1, \tag{29}$$

where Q and Q_φ are positive form factors. The logarithmic term in Q_φ is neglected since $ak \ll 1$ in our case.

The convolutions $j(x)$ with $\mathrm{Re}(G)$ and $\mathrm{Re}(G_\varphi)$ give the main contribution to Eq. (28): $|[\mathrm{Im}(G)^* j]| \ll |[\mathrm{Re}(G)^* j]|$ and $|[\mathrm{Im}(G_\varphi)^* j]| \ll |[\mathrm{Re}(G_\varphi)^* j]|$. On the other hand, convolutions $j(x)$ with imaginary parts $\mathrm{Im}(G)$ and $\mathrm{Im}(G_\varphi)$ are responsible for radiation losses and become important at resonance. They can be calculated by the iteration method given in Appendix A. Equation (28) is reduced to an ordinary differential equation for the zero approximation $j_0(x)$ where the radiation losses are neglected:

$$\frac{\partial^2}{\partial x^2}j_0(x) + k_1^2 j_0(x) = \frac{i\omega\varepsilon}{4\pi Q}\bar{e}_{0x}(x), \tag{30}$$

$$k_1 = kg, \tag{31}$$

$$g = \left(1 + \frac{ic\varsigma_{xx}}{2\pi a\omega\mu}\frac{Q_\varphi}{Q}\right)^{1/2} \sim \left(1 + \frac{ic\varsigma_{xx}}{a\omega\mu\ln(l/a)}\right)^{1/2}.$$

Equation (31) shows that the impedance boundary condition renormalizes the wave number of the incident radiation. Considering the solution of Eq. (30) with $j(-l/2) = j(l/2) = 0$, the resonance wavelengths are determined via this new wave number from the condition $\cos k_1 l/2 = 0$ or $k_1 l = \pi(2n-1)$:[27,28]

$$\lambda_{\mathrm{res},n} = \frac{2l}{2n-1}\mathrm{Re}(g\sqrt{\varepsilon\mu}), \quad n = 1,2,3,\ldots. \tag{32}$$

A similar renormalization method for the wave number has been used to tackle boundary effects in the microwave scattering from a conducting stick placed in a thin dielectric layer.[31]

C. Current equation for two parallel wires

With the help of Eq. (28), we can now consider the current distribution in two parallel wires. The distance d between them has to be larger than the diameter ($d > 2a$) in order to use the approximation of thin conductors. The equations for currents are of the form

$$\frac{\partial^2}{\partial x^2}(G^* j_1) + k^2(G^* j_1) = \frac{i\omega\varepsilon}{4\pi}[\bar{e}_{01x}(x) + \bar{e}_{21x}(x)] - \frac{i\omega\varepsilon\varsigma_{xx}}{2\pi ac}(G_\varphi^* j_1),$$

$$\frac{\partial^2}{\partial x^2}(G^* j_2) + k^2(G^* j_2) = \frac{i\omega\varepsilon}{4\pi}[\bar{e}_{02x}(x) + \bar{e}_{12x}(x)] - \frac{i\omega\varepsilon\varsigma_{xx}}{2\pi ac}(G_\varphi^* j_2). \tag{33}$$

Here $\bar{e}_{12x}$ and $\bar{e}_{21x}$ are the longitudinal electric fields induced by each conductor at the surface of other, $\bar{e}_{01x}$ and $\bar{e}_{02x}$ are the external fields, $j_1(x)$ and $j_2(x)$ are the linear currents

inside the conductors. The fields $\bar{e}_{12x}$ and $\bar{e}_{21x}$ are determined from Eq. (26) with $r=r_d=\sqrt{(x-s)^2+d^2}$.

Equations (33) are reduced to two independent equations by introducing $j_e=(j_1+j_2)/2$ and $j_m=(j_1-j_2)/2$:

$$\frac{\partial^2}{\partial x^2}[(G-G_d)^* j_m]+k^2[(G-G_d)^* j_m] = \frac{i\omega\varepsilon}{8\pi}(\bar{e}_{01x}-\bar{e}_{02x})-\frac{i\omega\varepsilon\varsigma_{xx}}{2\pi ac}(G_\varphi^* j_m), \quad (34)$$

$$\frac{\partial^2}{\partial x^2}[(G+G_d)^* j_e]+k^2[(G+G_d)^* j_e] = \frac{i\omega\varepsilon}{8\pi}(\bar{e}_{01x}+\bar{e}_{02x})-\frac{i\omega\varepsilon\varsigma_{xx}}{2\pi ac}(G_\varphi^* j_e), \quad (35)$$

$$G_d(r_d)=\exp(ikr_d)/4\pi r_d .$$

It is easy to see that only electric field e_d directed along the wires and magnetic field H perpendicular to the two-wire contour (xy plane) will excite currents inside the inclusion in the discussed geometry. The perpendicular magnetic field produces circulatory electric field $e_m=(i\omega/2c)\mu H l d/(l+d)$ along the wire contour due to Faraday's law of induction. Therefore, the external electric fields are of the form $\bar{e}_{01x}=e_d+e_m$ and $\bar{e}_{02x}=e_d-e_m$. This implies that the current j_m in the first equation is induced by the magnetic field and is responsible for the magnetic moment $\mathbf{m}$. The current j_e entering the second equation is created by the electric field and defines the electric dipole moment $\mathbf{p}$.

For d sufficiently small (strong interaction), the convolution with the Green function $G_d(r_d)$ can be estimated with the help of an approximate formula (29):

$$[\mathrm{Re}(G_d)^* j]\approx j(x)Q_d , \quad (36)$$

$$Q_d=\int_{-l/2}^{l/2}\mathrm{Re}[G_d(r_d)]ds\propto\frac{1}{4\pi}\int_{-l/2}^{l/2}\frac{ds}{\sqrt{s^2+d^2}}\sim\frac{\ln(l/d)}{2\pi}.$$

Similar to Eq. (30), the zero approximation for the current distribution reads

$$\frac{\partial^2}{\partial x^2}j_{m0}(x)+k_m^2 j_{m0}(x)=\frac{i\omega\varepsilon}{4\pi(Q-Q_d)}e_m , \quad (37)$$

$$\frac{\partial^2}{\partial x^2}j_{e0}(x)+k_e^2 j_{e0}(x)=\frac{i\omega\varepsilon}{4\pi(Q+Q_d)}e_d , \quad (38)$$

$$k_m=kg_m, g_m=\left(1+\frac{ic\varsigma_{xx}}{2\pi a\omega\mu}\frac{Q_\varphi}{(Q-Q_d)}\right)^{1/2} \sim\left(1+\frac{ic\varsigma_{xx}}{a\omega\mu\ln(d/a)}\right)^{1/2}. \quad (39)$$

$$k_e=kg_e, g_e=\left(1+\frac{ic\varsigma_{xx}}{2\pi a\omega\mu}\frac{Q_\varphi}{(Q+Q_d)}\right)^{1/2} \sim\left(1+\frac{ic\varsigma_{xx}}{a\omega\mu\ln(l^2/da)}\right)^{1/2}. \quad (40)$$

The general solution of Eqs. (37), (38) is of the form

$$j_{m,e0}(x)=A\sin(k_{m,e}x)+B\cos(k_{m,e}x)+\frac{i\omega\varepsilon e_{m,d}}{4\pi(Q\mp Q_d)k_{m,e}^2}. \quad (41)$$

In Eq. (41), the first set of subscripts corresponds to the magnetic excitation for which sign "minus" in the last term is taken, and the second set corresponds to the electric excitation with sign "plus." Imposing zero boundary condition $[j_{m,e0}(-l/2)=j_{m,e0}(l/2)\equiv 0]$ yields

$$j_{m,e0}(x)=\frac{i\omega\varepsilon e_{m,d}}{4\pi(Q\mp Q_d)k_{m,e}^2}\frac{[\cos(k_{m,e}l/2)-\cos(k_{m,e}x)]}{\cos(k_{m,e}l/2)}. \quad (42)$$

The resonance wavelengths λ_m, λ_e for the two excitations are different and can be found from the condition $k_{m,e}l=\pi(2n-1)$:[27,28]

$$\lambda_{m,e}=\frac{2l}{2n-1}\mathrm{Re}(\sqrt{\varepsilon\mu}g_{m,e}), \quad n=1,2,3,.... \quad (43)$$

The amplitude of the current at resonance is restricted by losses related to conductivity and relaxation properties of the surrounding medium. However, solution (41) does not contain such an important factor as radiation losses since the imaginary parts of convolutions were neglected. To find the effect of radiation, original Eq. (33) can be solved by iterations. For this purpose, it is converted to an integral form in the Appendix A. The nth iteration can be represented as

$$j_n(x)=j_0(x)+\int_{-l/2}^{l/2}S(x,q)j_{n-1}(q)dq, \quad (44)$$

where the zero iteration j_0 has to be taken in the form of Eq. (41) since the boundary condition is imposed for j_n and $S(x,q)$ is the integral kernel. The iteration method is proven to converge very rapidly. The first iteration j_1 is sufficient to take account of the radiation effects. Its explicit form and the form of the kernel $S(x,q)$ are calculated in Appendix A.

The scattering at a ring inclusion gives similar results for the current distribution and magnetic polarizability. This case is considered in Appendix B.

VI. RESULTS AND DISCUSSION

We are now in a position to proceed with the analysis of the effective magnetic and electric properties associated with the currents induced in the metallic contours. The characteristic size l is taken to be in the range of 100 nm and the cross-sectional size of 10 nm. These scales can be achieved in practice. The conductivity obeying the Drude equation (17) with parameters typical of such noble metals as silver and copper are used in all the calculations. The effect of a

smaller relaxation time (in comparison with that of a bulk metal) due to electron scattering at the inclusion surface results in shifting the dispersion region to higher frequencies.

Two-wire contour. First, we consider two-wire contour composites irradiated by light having the magnetic field H perpendicular to the contour plane and the electric field E perpendicular to the wires. For this polarization, the circulatory currents j_m are induced leading to the effective permeability. The effective permittivity can be considered to be unity. The dimensions used are as follows: $l=100$ nm, $a=6$ nm, $d=30$ nm. It is useful to investigate the forms of the current distribution for different frequencies along with the dispersion law of the magnetic polarizability of the inclusion $\chi_0=\chi'+i\chi''$. Figure 4 shows plots of $j(x)=j'(x)+ij''(x)$ as a function of a distance x along the wire for three frequencies $f<f_{res}$, $f\sim f_{res}$, and $f>f_{res}$, where $f_{res}=c/\lambda_{res}$ is the resonance frequency. The current distribution is calculated using formulas (37) and (A7) obtained in the zero approximation and using first iteration, respectively. In this case, the resonance wavelength is found to be $\lambda_{res}=730$ nm, which is several times larger than it could be expected from half-wavelength resonance condition ($\lambda_{res}=2l$) known for microwave antennas.[27,28] The skin effect is weak for the chosen wire radius and the contribution from the surface impedance causes this remarkable shift of the resonance wavelength since the conductivity is dominantly imaginary for these frequencies. Physically, this result corresponds to localized plasmon modes inside the wire.

On the other hand, the current distribution exhibits all the features typical of those in microwave antennas. The real part j' changes phase at f_{res}. For frequencies below the resonance [Fig. 4(a)] j' is positive and magnetic polarizability of the inclusion χ_0 exhibits a paramagnetic response, as it is seen in Fig. 5. For $f>f_{res}$ [Fig. 4(b)], j' is negative and χ_0 is of a diamagnetic character, showing quite large negative values. Closer to the resonance, j' undergoes rapid transformations [Fig. 4(c)]. In this frequency range small factors such as radiation may introduce essential changes in $j'(x)$ plots, but the integral parameter $\chi_0(\omega)$ does not change much showing only a small shift of the resonance frequency and a slight decrease in the resonance peaks. For the considered geometry, the dielectric dipole moment is zero and the radiation is strongly reduced.

Figure 6 shows the effective permeability $\mu_{eff}=\mu'+i\mu''$ calculated for the volume concentration of inclusions $p=6\%$ by considering the current contours as independent magnetic moments (dipole sum) and within the effective medium theory (EMT) [see Eq. (15)]. In this case, the wire radius was chosen to be 10 nm to demonstrate that the resonance shifts to higher frequencies since the skin effect is stronger for a larger cross section. For noninteracting moments, the resonance peaks in permeability are large reaching negative values past the resonance and the dispersion region is narrow, whereas the interaction broadens the permeability behavior and reduces the peaks of μ' and μ'' greatly, so that the real part is always positive. An important characteristic is that μ' peaks at lower frequency when μ'' is very small. Thus, there exists a range of frequencies where the light propagation is affected by magnetic properties but

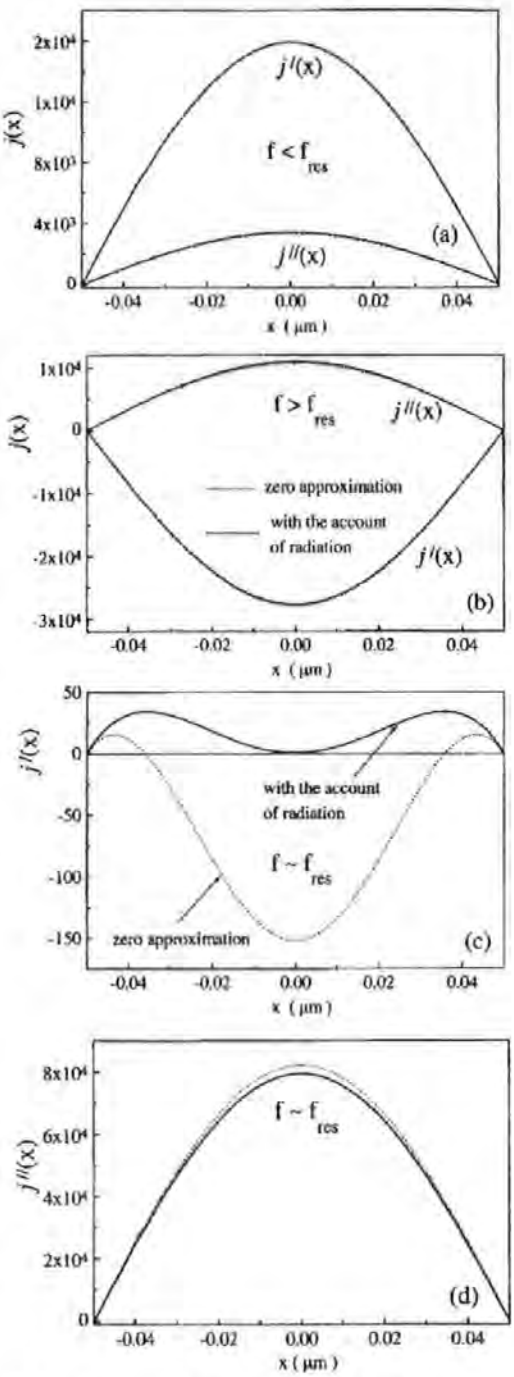

FIG. 4. Typical current distribution (including real j' and imaginary j'' parts) along the wire length for different frequencies (a) $f<f_{res}$, (b) $f>f_{res}$, and (c) and (d) $f\sim f_{res}$.

the light absorption is still negligible. It may happen that EMT is a rather rough approximation for the considered system. A periodic array of two-wire contours may exhibit a stronger magnetic activity as suggested by the dipole sum result, which does show negative μ'. In any way, the actual behavior is somewhere in between the considered cases and the least range of μ' variation is 1.5–0.5 for this concentra-

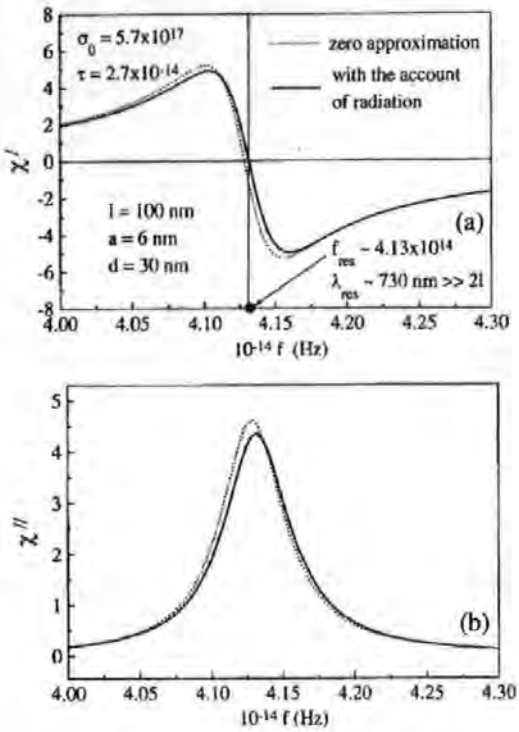

FIG. 5. Magnetic polarizability $\chi_0=\chi'+i\chi''$ of two-wire contour vs frequency. The zero (dashed curve) and first (solid curve) approximations are given.

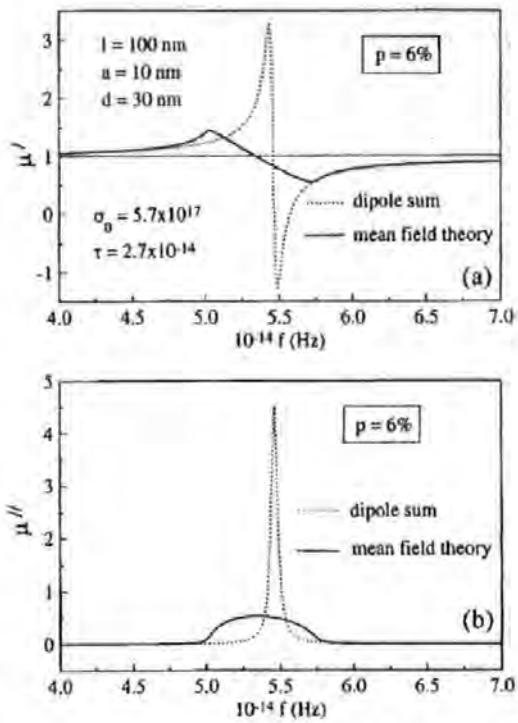

FIG. 6. Effective permeability $\mu_{\text{eff}}=\mu'+i\mu''$ of composite containing wire pairs vs frequency for the volume concentration of 6%, calculated for two cases: independent inclusions (dashed curve) and inclusions in effective medium (solid curve).

tion, which is quite big. It has to be noted that the magnetic properties in two-wire contour system cannot be enhanced by simply increasing the concentration. If the distance between the pairs is in the range of d, then the induced magnetic properties disappear as it is clear from symmetry. The system of randomly placed wires has no magnetic properties (neglecting those due to circumferential currents inside the wires), as already discussed in Sec. IV.

We now consider the polarization of the incident light for which H is still perpendicular to the contour plane but E is along the wires. For this case, both μ_{eff} and ε_{eff} are essential. The result for μ_{eff} is the same as considered previously since the currents j_m and j_e due to H and E contribute independently to the magnetic and electric polarisabilities, respectively. The current j_e, which determines the electric polarizability of the inclusion α_0, is calculated in zero approximation (38) and taking first iteration (A7). In this case, the results for $\alpha_0=\alpha'+i\alpha''$ differ greatly for the zero and first approximations, as shown in Fig. 7, because of a substantial radiation effect. The polarizability has resonant dispersion behavior. The radiation losses make the resonance wider, shift the resonance frequency and reduce the resonant peaks. Comparing plots $\alpha_0(\omega)$ and $\chi_0(\omega)$ (Fig. 5) it is seen that the resonance frequency for α_0 is higher, since the resonance for j_e happens at higher frequency than for j_m. The effective permittivity $\varepsilon_{\text{eff}}=\varepsilon'+i\varepsilon''$ calculated for $p=3\%$ within EMT [see Eq. (15)] shows a very broad dispersion region as seen in Fig. 8. In terms of ε_{eff}, the effect of radiation is not pronounced since the interaction itself has a similar effect of smoothing the resonance characteristics. The real part of the permittivity is negative near the high-frequency side of the resonance. Figure 9 compares the dispersion behavior for ε_{eff} and μ_{eff} ($p=3\%$) for the aforementioned polarization. The resonance region for ε_{eff} is shifted towards higher frequencies. In the area of magnetic resonance, $\mu_{\text{eff}}\sim\varepsilon_{\text{eff}}$ with very small losses $\varepsilon''\ll 1$, $\mu''\ll 1$. It means that inequality (12) is satisfied since $l/\lambda\ll 1$ and the concept of permeability is meaningful at optical frequencies. Therefore, this system can be useful for designing materials with effective parameters suitable for new optical effects described in Sec. II.

Ring contour

A similar magnetic behavior is obtained for ring-composite materials irradiated by light having the magnetic field perpendicular to the plane of the ring (see Appendix B). The electric field of the incident light is in the plane of the ring and always induces some effective permittivity. In this case, the magnetic and electric resonance frequencies coincide. The value of ε_{eff} is reduced in comparison with that of the two-wire case since the average exciting electric field for the electric dipole moment is smaller. Then, $\mu_{\text{eff}}\sim\varepsilon_{\text{eff}}$ at resonance in this system.

Figure 10 shows the dispersion behavior of the magnetic polarizability of the ring inclusion. The calculations are made with $R_0=50$ nm, $a=5$ nm, and $\theta_0=320°$. The gap in the ring is sufficiently large to avoid any effects from the

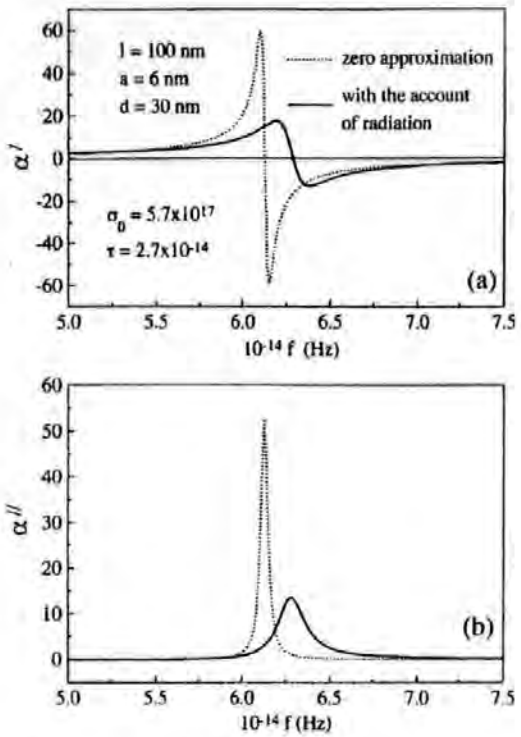

FIG. 7. Electric polarizability $\alpha_0 = \alpha' + i\alpha''$ of two-wire contour vs frequency. The zero (dashed curve) and first (solid curve) approximations are given.

edge capacitance, which could be difficult to control at nanoscales. For these dimensions, the resonance wavelength is about 2 μm (infrared part of the spectrum). The radiation losses are essential because of the existence of the electric dipole moment. They strongly reduce the resonance peaks. In order to move the dispersion region to the visible spectral range, the ring diameter has to be decreased. However, we do not have much flexibility since for our analysis the condition $R_0 \gg a$ is important. Further decrease in a may be not realistic and will bring about complex behavior of the conductivity in low-dimensional systems. Taken $R_0 = 30$ nm, the resonance wavelength decreases down to 1.30 μm, which is still

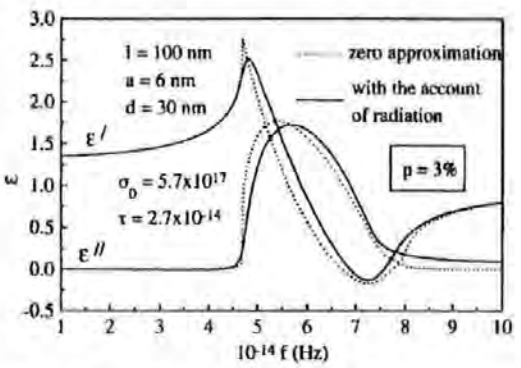

FIG. 8. Effective permittivity of composite containing wire pairs vs frequency for the volume concentration of 3%. The zero (dashed curve) and first (solid curve) approximations are given.

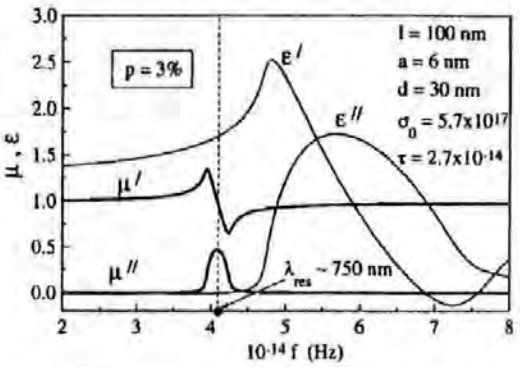

FIG. 9. Effective permeability and permittivity of composite containing wire pairs vs frequency for the volume concentration of 3%.

in the infrared. Surprisingly, the magnetic polarizability of a ring for these higher frequencies is substantially decreased due to strong radiation losses, which will result in much smaller values of the effective permeability. It appears that the dispersion region of μ_{eff} in ring composites is essentially limited by infrared spectral range. The effective permeability for $R_0 = 30$ nm and two concentrations $p = 6\%$ and $p = 30\%$ is presented in Fig. 11. Similar to the two-wire composite, at frequencies where the real part has peaks, the imaginary part is small, which is important for possible applications. For ring composites, the concentration can be increased, which allows the negative permeability to be realized, as demonstrated in Fig. 11(b).

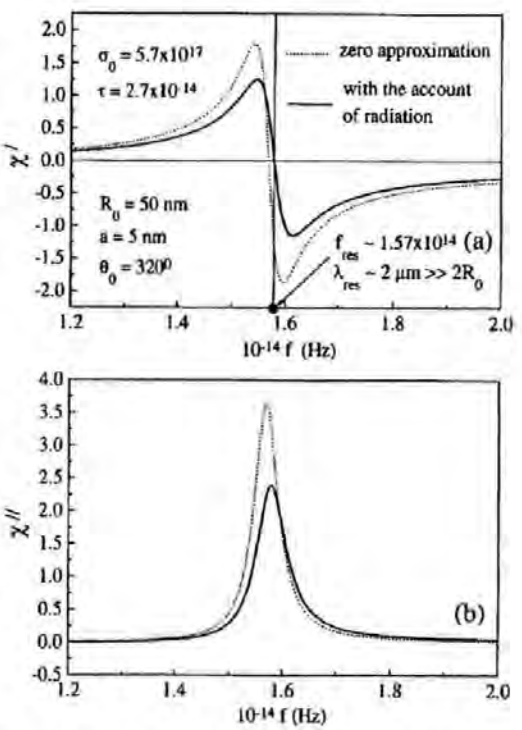

FIG. 10. Magnetic polarizability $\chi_0 = \chi' + i\chi''$ of open-ring contour vs frequency. The zero (dashed curve) and first (solid curve) approximations are given.

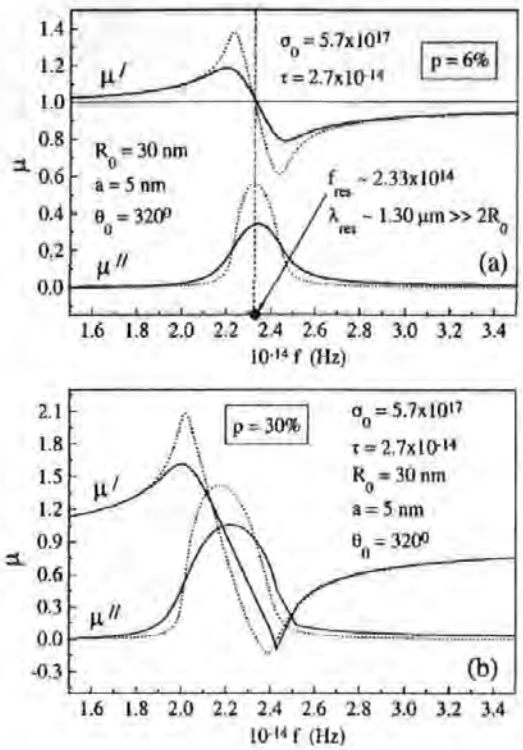

FIG. 11. Effective permeability of composite containing open rings vs frequency for the volume concentration of 6% [in (a)] and 30% [in (b)]. The zero (dashed curve) and first (solid curve) approximations are given.

IV. CONCLUSION

We have shown that a metal-dielectric composite having loop-shape nanoscale inclusions responds to optical radiation as if it has effective magnetic properties. Such material can be named as optomagnetic. It is known that the macroscopic magnetic properties originated by localized electrons in atom have no physical meaning from optical frequencies onward. In contrast, the effective permeability of the proposed composite is proven to be consistent with the macroscopic Maxwell equations even at optical frequencies, having values that can differ substantially from unity within a dispersion band. Optical effects are predicted which are related to specific conditions of reflection and refraction at interface with such a medium. They are likely to find applications in optical filters, sensors, polarizes, and other optoelectronics devices. An interesting example is the reflectionless normal incidence from vacuum when the permeability and permittivity are the same. This condition is an optical analogy of the impedance matching known for microwaves and is quite realistic in the considered optomagnetic materials for a certain narrow frequency range. In addition, the losses (imaginary parts of these parameters) can be small at those frequencies.

The analytical approach developed is based on solving the scattering problem for metallic inclusions of two types: a ring with a relatively large gap and a pair of parallel wires. The method allows us to find the current and charge distributions within the inclusion, which constitute the effective permeability and permittivity. The localized plasmon modes are proven to play an important role as they make the microstructure to be resonant at frequencies much lower than those following from the half-wavelength requirement for microwave antennas. For example, the effective permeability of composites having two-wire inclusions of 100 nm long shows resonance behavior with a characteristic frequency of 4×10^{14} Hz (750 nm). The parameters determining the optical conductivity such as relaxation time (mean-free time between collisions) are also important to realize favorable resonance conditions. The use of noble metals as Au, Ag, and Cu is preferable to increase the relaxation time. However, because the composite structure has nanodimensions, the bulk parameters may need to be modified. This factor requires further investigation.

For composite with volume fraction more than 1% the interactions between inclusions become important. They are considered in a self-consistent manner using the effective medium theory. It turns out that the interactions broaden the dispersion region and strongly reduce the permeability peaks near the resonance, preventing it from having negative values. It may be that the effective medium theory for the considered system is a rough approximation. Then, the analysis of the effective permeability in a periodic array of loop-shaped inclusions allowing an exact solution would be of a considerable interest.

The analysis predicts that inherent metallic microstructure properties will limit magnetic activity of the type considered here by visible spectral range. More specifically, magnetic properties of the composites containing ring-shape inclusions will not be essential past the infrared as radiation effects become very strong. The radiation factor is reduced for a contour formed by two parallel wires. With this structural element the effective magnetism can exist in visible spectral range.

Finally, the resonant properties of the proposed optomagnetic medium strongly depend on conductivity. It is known that the conductivity of nanoinclusions can be changed considerably by external parameters such as bias magnetic or electric fields.[34,35] This opens up a possibility to create adaptive optics: modulators, tuneable lenses, and filters having small energy losses.

APPENDIX A

Here we describe the iteration method of solving Eqs. (34) and (35). The convolutions of the current $j_{m,e}(x)$ with the Green functions are considered separately for the real and imaginary parts. Approximates (29) and (36) are used for the real parts. Equations (34), (35) with $j(x)=j_{m,e}(x)$ and $e_0(x)=\bar{e}_{01x}\mp\bar{e}_{02x}$ can be rewritten in the form

$$\left[\frac{\partial^2}{\partial x^2}+\bar{k}^2\right]\left[j(x)+\frac{i}{(Q\mp Q_d)}[\mathrm{Im}(G\mp G_d)^*j]\right]$$
$$=\frac{i\omega\varepsilon}{8\pi(Q\mp Q_d)}e_0(x)+\frac{l(\bar{k}^2-k^2)}{(Q\mp Q_d)}[\mathrm{Im}(G\mp G_d)^*j]$$
$$+\frac{\omega\varepsilon\zeta_{xx}}{2\pi ac(Q\mp Q_d)}[\mathrm{Im}(G_\varphi)^*j], \qquad \text{(A1)}$$

where

$$\tilde{k}^2=k_{m,e}^2=\frac{\omega^2}{c^2}\varepsilon\mu\left(1+\frac{ic\zeta_{xx}Q_\varphi}{2\pi a\omega\mu(Q\mp Q_d)}\right).$$

The members of Eq. (A1) are grouped in a way to separate a renormalized wave number $\tilde{k}$. Equation (A1) can be treated as an inhomogeneous differential equation with respect to $\partial^2/\partial x^2+\tilde{k}^2$. The general solution of this equation is represented by

$$\begin{aligned}j(x)=&A\sin(\tilde{k}x)+B\cos(\tilde{k}x)+\frac{i\omega\varepsilon}{8\pi(Q\mp Q_d)\tilde{k}}\\&\times\int_{-l/2}^{x}\sin[\tilde{k}(x-s)]e_0(s)ds+\frac{i(\tilde{k}^2-k^2)}{(Q\mp Q_d)\tilde{k}}\\&\times\int_{-l/2}^{x}\sin[\tilde{k}(x-s)][\mathrm{Im}(G\mp G_d)^*j]ds\\&+\frac{\omega\varepsilon\zeta_{xx}}{2\pi ac(Q\mp Q_d)\tilde{k}}\int_{-l/2}^{x}\sin[\tilde{k}(x-s)]\\&\times[\mathrm{Im}(G_\varphi)^*j]ds-\frac{i}{(Q\mp Q_d)}[\mathrm{Im}(G\mp G_d)^*j].\end{aligned}\tag{A2}$$

The parameters A and B are found from the boundary condition

$$j(-l/2)=j(l/2)\equiv 0.\tag{A3}$$

Equation (A2) is the Fredholm equation of the second kind, which allows the iteration method to be successfully used with a rapid convergence. The zero iteration is constructed as follows:

$$\begin{aligned}j_0(x)=&A\sin(\tilde{k}x)+B\cos(\tilde{k}x)\\&+\frac{i\omega\varepsilon}{8\pi(Q\mp Q_d)\tilde{k}}\int_{-l/2}^{x}\sin[\tilde{k}(x-s)]e_0(s)ds.\end{aligned}\tag{A4}$$

The nth iteration can be written as

$$\begin{aligned}j_n(x)=&j_0(x)+\frac{i(\tilde{k}^2-k^2)}{(Q\mp Q_d)\tilde{k}}\int_{-l/2}^{x}\sin[\tilde{k}(x-s)]\\&\times[\mathrm{Im}(G\mp G_d)^*j_{n-1}]ds+\frac{\omega\varepsilon\zeta_{xx}}{2\pi ac(Q\mp Q_d)\tilde{k}}\\&\times\int_{-l/2}^{x}\sin[\tilde{k}(x-s)][\mathrm{Im}(G_\varphi)^*j_{n-1}]ds\\&-\frac{i}{(Q\mp Q_d)}[\mathrm{Im}(G\mp G_d)^*j_{n-1}].\end{aligned}\tag{A5}$$

The parameters A and B have to be calculated at the final stage of the iteration method. In the case of the zero approximation, Eq. (A4) together with Eq. (A3) yield expression (42) of the main text ($e_m=\mathrm{const}$). When the next iteration is considered, the parameters A and B are needed to be calculated again to satisfy Eq. (A3).

Introducing the integral kernel S for Eq. (A5) give

$$j_n(x)=j_0(x)+\int_{-l/2}^{l/2}S(x,q)j_{n-1}(q)dq.\tag{A6}$$

Here

$$j_0(x)=A\sin(\tilde{k}x)+B\cos(\tilde{k}x)+\frac{i\omega\varepsilon e_0}{8\pi(Q\mp Q_d)\tilde{k}^2},$$

$$S(x,q)=S_1(x,q)+S_2(x,q)+S_3(x,q),$$

$$S_1(x,q)=-\frac{i}{(Q\mp Q_d)}\mathrm{Im}[G(r)\mp G_d(r_d)],$$

$$r=\sqrt{(x-q)^2+a^2},\quad r_d=\sqrt{(x-q)^2+d^2},$$

$$\begin{aligned}S_2(x,q)=&\frac{i(\tilde{k}^2-k^2)}{(Q\mp Q_d)\tilde{k}}\int_{-l/2}^{x}\sin[\tilde{k}(x-s)]\\&\times\mathrm{Im}[G(r)\mp G_d(r_d)]ds,\\&r=\sqrt{(s-q)^2+a^2},\\&r_d=\sqrt{(s-q)^2+d^2},\end{aligned}$$

$$\begin{aligned}S_3(x,q)=&\frac{\omega\varepsilon\zeta_{xx}}{2\pi ac(Q\mp Q_d)\tilde{k}}\int_{-l/2}^{x}\sin[\tilde{k}(x-s)]\\&\times\mathrm{Im}[G_\varphi(r)]ds,\quad r=\sqrt{(s-q)^2+a^2}.\end{aligned}$$

The kernel S is written as the sum of three terms that represent three different sources of radiation. S_1 is a local kernel depending only on the wave number k in free space. This contribution corresponds to that of the wire with infinite conductivity. The next two terms are nonlocal. S_2 is responsible for the radiation into free space partly penetrating back to the wires. Points in space are electrically bound via the conductors, which is represented by the convolutions with function $\sin[\tilde{k}(x-s)]$. S_3 accounts for retarding effects related to impedance boundary condition. All three members of kernel S contain a small factor $1/4\pi(Q\mp Q_d)$ resulting in a rapid convergence of the iteration sequence.

The first iteration gives

$$j_1(x)=A\left(\sin(\tilde{k}x)+\int_{-l/2}^{l/2}S(x,q)\sin(\tilde{k}q)dq\right)+B\left(\cos(\tilde{k}x)+\int_{-l/2}^{l/2}S(x,q)\cos(\tilde{k}q)dq\right)+\frac{i\omega\varepsilon e_0}{8\pi(Q\mp Q_d)\tilde{k}^2}\left(1+\int_{-l/2}^{l/2}S(x,q)dq\right). \quad \text{(A7)}$$

The parameters A and B are found by solving two linear equations $[j_1(\pm l/2)\equiv 0]$

$$\begin{pmatrix}\sin(\tilde{k}l/2)+a_{11} & \cos(\tilde{k}l/2)+a_{12}\\ -\sin(\tilde{k}l/2)+a_{21} & \cos(\tilde{k}l/2)+a_{22}\end{pmatrix}\otimes\begin{pmatrix}A\\B\end{pmatrix}=\begin{pmatrix}C\\D\end{pmatrix}, \quad \text{(A8)}$$

where

$$\begin{pmatrix}a_{11} & a_{12}\\ a_{21} & a_{22}\end{pmatrix}=\begin{pmatrix}\int_{-l/2}^{l/2}S(l/2,q)\sin(\tilde{k}q)dq & \int_{-l/2}^{l/2}S(l/2,q)\cos(\tilde{k}q)dq\\ \int_{-l/2}^{l/2}S_1(-l/2,q)\sin(\tilde{k}q)dq & \int_{-l/2}^{l/2}S_1(-l/2,q)\cos(\tilde{k}q)dq\end{pmatrix}, \quad \text{(A9)}$$

$$\begin{pmatrix}C\\D\end{pmatrix}=-\frac{i\omega\varepsilon e_0}{8\pi(Q\mp Q_d)\tilde{k}^2}\begin{pmatrix}1+\int_{-l/2}^{l/2}S(l/2,q)dq\\ 1+\int_{-l/2}^{l/2}S_1(-l/2,q)dq\end{pmatrix}.$$

In Eq. (A9) the equality $S_{2,3}(-l/2,q)\equiv 0$ is used. Equation (A9) is represented as

$$\begin{pmatrix}a_{11}+a_{21} & 2\cos(\tilde{k}l/2)+a_{12}+a_{22}\\ 2\sin(\tilde{k}l/2)+a_{11}-a_{21} & a_{12}-a_{22}\end{pmatrix}\otimes\begin{pmatrix}A\\B\end{pmatrix}=\begin{pmatrix}C+D\\C-D\end{pmatrix}. \quad \text{(A10)}$$

From Eq. (A10), A and B are given by

$$A=\frac{(C-D)+B(a_{22}-a_{12})}{2\sin(\tilde{k}l/2)+a_{11}-a_{21}}, \quad \text{(A11)}$$

$$B=\left(\frac{C+D}{2}+\frac{(D-C)(a_{11}+a_{21})}{4\sin(\tilde{k}l/2)+2(a_{11}-a_{21})}\right)\Bigg/\left(\cos(\tilde{k}l/2)+\frac{(a_{22}-a_{12})(a_{11}+a_{21})}{4\sin(\tilde{k}l/2)+2(a_{11}-a_{21})}+\frac{a_{12}+a_{22}}{2}\right).$$

The resonance wavelengths are calculated by putting to zero the real part of the denominator in the expression for B. The resonance peaks are determined by its imaginary part taken at the resonance wavelength.

APPENDIX B

The current distribution in a thin conductor of arbitrary form was analyzed by Mei.[32,33] The problem was solved using the Fredholm equation of the first kind, which does not contain the wave operator $\partial^2/\partial x^2+k^2$ explicitly. As a result, the iteration procedure cannot be applied to this equation and the overall analysis is very complicated. Fortunately, for a circular current loop the problem can be formulated using the methods developed here for a straight conductor.

We will use cylindrical coordinates (ρ,θ,z) with the origin in the center of the loop as shown in Fig. 12. The loop has a small gap of a segmental angle. The dihedral angle θ is measured from the gap. The vector potential $\mathbf{A}$ taken at the point $P(\mathbf{r}_0)$ is represented as a contour integral along the current loop

$$A(\mathbf{r}_0)=\int_L \mathbf{j}(\mathbf{r}_s)G(r)ds, \quad \text{(B1)}$$

where $\mathbf{r}_s=(R_0,\theta_s,0)$ is the vector pointing to the current element, $r=|\mathbf{r}_0-\mathbf{r}_s|$, R_0 is the radius of the current loop, and $\mathbf{j}(\mathbf{r}_s)$ is the linear current. Because of symmetry, the scattered fields are described by only one component A_θ of the vector potential

$$A_\theta(\mathbf{r}_0)=\int_L j(s)G(r)\cos(\theta_{r_0}-\theta_s)ds, \quad \text{(B2)}$$

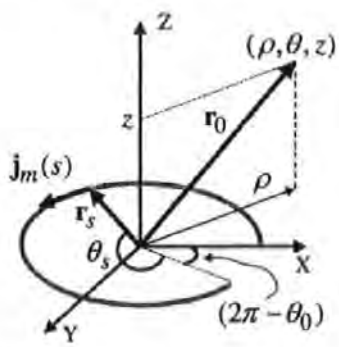

FIG. 12. Principal geometry, directions, and quantities used for the calculation of the current distribution along an open ring.

where the integration is with respect to $s=R_0\theta_s$ and $j(s)=|\mathbf{j}(s)|$. The electric field e_θ is equated as

$$e_\theta(\mathbf{r}_0)=-\frac{4\pi}{i\omega\varepsilon}\left[\frac{1}{\rho^2}\frac{\partial^2}{\partial\theta^2}A_\theta+k^2A_\theta\right]. \tag{B3}$$

Equation (B3) taken at the loop $[\mathbf{r}_0=(R_0,\theta,0)]$ becomes

$$\bar{e}_\theta(\nu)=-\frac{4\pi}{i\omega\varepsilon}\left[\frac{\partial^2}{\partial\nu^2}(G^*j)+k^2(G^*j)\right], \tag{B4}$$

$$(G^*j)=\int_0^l j(s)G(r)\cos(\theta-\theta_s)ds, \tag{B5}$$

$$r=\sqrt{R_0^2+(R_0+a)^2-2R_0(R_0+a)\cos(\theta-\theta_s)}.$$

Here $\nu=R_0\theta$, $l=R_0\theta_0$ is the length of nonclosed loop ($\theta_0<2\pi$). Formally, Eq. (B4) is similar to Eq. (26) for $\bar{e}_x$ in a straight wire. To use the impedance boundary conditions (24) we have to find the circumferential magnetic field $\bar{h}_\varphi$ [in local cylindrical coordinates (a,φ,ν) with ν along the loop axis]. A general form of the scattered magnetic field taken at the loop point ν is

$$\mathbf{h}(\nu)=\frac{1}{c}\int_L\frac{(1-ikr)\exp(ikr)}{r^3}[\mathbf{j}(s)\times\mathbf{r}]ds, \tag{B6}$$

where $r=\sqrt{R_0^2+(R_0+a)^2-2R_0(R_0+a)\cos(\theta-\theta_s)}$. The integration in Eq. (B6) is divided into two parts, one for which $r>\Delta$ and the other for which $r<\Delta$, where Δ is a distance small compared with R_0 but large compared with a. In the first integral, the contribution to $\bar{h}_\varphi(\nu)$ averaged over the wire circumference is estimated to be of the order a/R_0^3, which is small and can be neglected [see expression (29) for Q_φ]. For the integration where $r<\Delta$, we can take $(\mathbf{j}\times\mathbf{r})_\varphi=j(s)a$ and $\bar{h}_\varphi(\nu)$ is equated similar to that for a straight wire

$$\bar{h}_\varphi(\nu)=\frac{a}{c}\int_{\nu1}^{\nu2}\frac{(1-ikr)\exp(ikr)}{r^3}j(s)ds, \tag{B7}$$

where $\Delta=|\nu2-\nu1|$. Although the parameter Δ is chosen arbitrarily, we assume that the integration is bounded in the segment $R_0\psi$ with angle $\psi\approx2\sqrt{2a/R_0}$, between the points $\nu1$ and $\nu2$ as shown in Fig. 13. Then, $\bar{h}_\varphi$ is expressed in terms of the convolution

$$\bar{h}_\varphi(\nu)=\frac{2}{ac}(G_\varphi^*j),(G_\varphi^*j)=\int_{\nu1}^{\nu2}G_\varphi(r)j(s)ds, \tag{B8}$$

where

$$G_\varphi(r)=\frac{a^2(1-ikr)\exp(ikr)}{2r^3},$$

$$\nu1=\max[0,(\nu-\sqrt{2aR_0})],\quad \nu2=\min[\theta_0R_0,(\nu+\sqrt{2aR_0})]. \tag{B9}$$

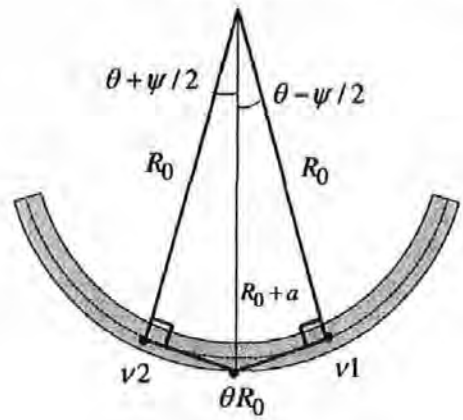

FIG. 13. Principal integration path for Eq. (B7).

Now we are able to formulate the integrodifferential equation for the current distribution in a circular loop. Substituting Eqs. (B4) and (B8) into boundary condition (24) yields

$$\frac{\partial^2}{\partial\nu^2}(G^*j)+k^2(G^*j)=\frac{i\omega\varepsilon}{4\pi}\bar{e}_{\theta0}(\nu)-\frac{i\omega\varepsilon\zeta_{\nu\nu}}{2\pi ac}(G_\varphi{}^*j), \tag{B10}$$

$$j(0)=j(l)\equiv0.$$

Here the convolutions are defined by Eqs. (B5) and (B8). The external electric field $\bar{e}_{\theta0}(\nu)$ is considered to be circular, which is induced by the external magnetic field perpendicular to the loop plane. As in the case of two-wire contour, the external electric field in the plane of the ring does not affect the magnetic moment. The axial component of the surface impedance $\varsigma_{\nu\nu}=\varsigma_{xx}$ is defined by Eq. (25). Equation (B10) formally is similar to Eqs. (28), (33) and can be solved using the method developed. The convolutions are estimated as

$$[\mathrm{Re}(G)^*j]\approx j(\nu)\int_0^l\mathrm{Re}[G(r)]\cos(\theta-\theta_s)ds=j(\nu)Q,$$

$$Q=\int_0^l\mathrm{Re}[G(r)]\cos(\theta-\theta_s)ds\propto\frac{1}{4\pi}\int_0^l\frac{\cos(\theta_0/2-\theta_s)ds}{\sqrt{(s-l/2)^2+a^2}}$$

$$<\frac{\ln(l/a)}{2\pi},$$

$$[\mathrm{Re}(G_\varphi)^*j]\approx j(\nu)\int_{\nu1}^{\nu2}\mathrm{Re}[G_\varphi(r)]ds=j(\nu)Q_\varphi, \tag{B11}$$

$$Q_\varphi=\int_{\nu1}^{\nu2}\mathrm{Re}[G_\varphi(r)]ds\propto\frac{a^2}{2}\int_0^\Delta\frac{ds}{[(s-\Delta/2)^2+a^2]^{3/2}}$$

$$+\frac{a^2k^2}{2}\int_0^\Delta\frac{ds}{\sqrt{(s-\Delta/2)^2+a^2}}\propto[1+a^2k^2\ln(\Delta/a)]\sim1.$$

The iteration method is formulated as follows:

$$j_n(\nu)=j_0(\nu)+\frac{i(\tilde{k}^2-k^2)}{Q\tilde{k}}\int_0^{\nu}\sin[\tilde{k}(\nu-s)][\mathrm{Im}(G)^*j_{n-1}]ds$$

$$+\frac{\omega\varepsilon\varsigma_{\nu\nu}}{2\pi acQ\tilde{k}}\int_0^{\nu}\sin[\tilde{k}(\nu-s)][\mathrm{Im}(G_\varphi)^*j_{n-1}]ds$$

$$-\frac{i}{Q}[\mathrm{Im}(G)^*j_{n-1}], \qquad \text{(B12)}$$

where

$$j_0(\nu)=A\sin(\tilde{k}\nu)+B\cos(\tilde{k}\nu)+\frac{i\omega\varepsilon\tilde{e}_{\varphi 0}}{4\pi Q\tilde{k}^2},$$

$$\tilde{k}=kg,\quad g=\left(1+\frac{ic\varsigma_{\nu\nu}}{2\pi a\omega\mu}\frac{Q_\varphi}{Q}\right)^{1/2}.$$

Introducing a general kernel S gives Eq. (B12) in the form

$$j_n(\nu)=j_0(\nu)+\int_0^l S(\nu,q)j_{n-1}(q)dq, \qquad \text{(B13)}$$

$$S(\nu,q)=S_1(\nu,q)+S_2(\nu,q)+S_3(\nu,q), \qquad \text{(B14)}$$

$$S_1(\nu,q)=-\frac{i}{Q}\mathrm{Im}[G(r)]\cos(\theta-\theta_q),$$

$$r=\sqrt{R_0^2+(R_0+a)^2-2R_0(R_0+a)\cos(\theta-\theta_q)},$$

$$S_2(\nu,q)=\frac{i(\tilde{k}^2-k^2)}{Q\tilde{k}}\int_0^{\nu}\sin[\tilde{k}(\nu-s)]$$

$$\times\cos(\theta_s-\theta_q)\mathrm{Im}[G(r)]ds,$$

$$r=\sqrt{R_0^2+(R_0+a)^2-2R_0(R_0+a)\cos(\theta_s-\theta_q)},$$

$$S_3(\nu,q)=\frac{\omega\varepsilon\varsigma_{\nu\nu}}{2\pi acQ\tilde{k}}\int_0^{\nu}\sin[\tilde{k}(\nu-s)]\mathrm{Im}[G_\varphi(r)]\Theta(s,q)ds,$$

$$r=\sqrt{R_0^2+(R_0+a)^2-2R_0(R_0+a)\cos(\theta_s-\theta_q)}.$$

Here

$$\Theta(s,q)=\begin{cases}1, q\in[s1(s),s2(s)]\\ 0, q\in[s1(s),s2(s)]\end{cases}$$

is the "cutting" function. This function takes into account that the integration with respect to q is made in the interval $[s1,s2]$, where $s1=\max[0,(s-\sqrt{2aR_0})]$ and $s2=\min[\theta_0R_0,(s+\sqrt{2aR_0})]$.

[1] D. Stauffer and A. Aharony, *Introduction to Percolation Theory* (Taylor & Francis, London, 1992), and references therein.

[2] A. N. Lagarkov, L. V. Panina, and A. K. Sarychev, Zh. Eksp. Teor. Fiz **93**, 215 (1987) [Sov. Phys. JETP **66**, 123 (1987)].

[3] V. M. Shalaev and M. Moskovits, Phys. Rev. Lett. **75**, 2451 (1995).

[4] P. M. Duxbury, P. L. Leath, and P. D. Beale, Phys. Rev. B **36**, 367 (1987).

[5] K. K. Bardhan, Physica A **241**, 267 (1997).

[6] V. M. Shalaev, E. Y. Polyakov, and V. A. Markel, Phys. Rev. B **53**, 2425 (1996).

[7] R. J. Gehr, G. L. Fisher, R. W. Boyd, and J. E. Sipe, Phys. Rev. A **53**, 2792 (1996).

[8] A. Fert and L. Piraux, J. Magn. Magn. Mater. **200**, 338 (1999).

[9] J. Rothman, M. Klaui, L. Lopez-Diaz, C. A. F. Vaz, A. Bleloch, J. A. C. Bland, Z. Cui, and R. Speaks, Phys. Rev. Lett. **86**, 1098 (2001).

[10] F. Mariotte, S. A. Tretyakov, and B. Sauviac, IEEE Trans. Antennas Propag. **38**, 22 (1996).

[11] M. M. I. Saadoun and N. Engheta, Microwave Opt. Technol. Lett. **5**, 184 (1992).

[12] J. B. Pendry, A. J. Holden, W. J. Stewart, and I. Youngs, Phys. Rev. Lett. **76**, 4773 (1996).

[13] D. R. Smith, D. C. Vier, W. Padilla, S. C. Nemat-Nasser, and S. Schultz, Appl. Phys. Lett. **75**, 1425 (1999).

[14] J. B. Pendry, A. J. Holden, D. J. Robbins, and W. J. Stewart, IEEE Trans. Microwave Theory Tech. **47**, 2075 (1999).

[15] D. R. Smith, W. J. Padilla, D. C. Vier, S. C. Nemat-Nasser, and S. Schultz, Phys. Rev. Lett. **84**, 4184 (2000).

[16] V. G. Veselago, Sov. Phys. Usp. **10**, 509 (1968).

[17] J. B. Pendry, Phys. Rev. Lett. **85**, 3966 (2000).

[18] R. A. Shelby, D. R. Smith, and S. Schultz, Science **292**, 77 (2001).

[19] M. Notomi, Phys. Rev. B **62**, 10 696 (2000).

[20] L. D. Landau and E. M. Lifshitz, *Electrodynamics of Continuous Media* (Pergamon Press, New York, 1975).

[21] G. A. Niklasson, C. G. Granqvist, and O. Hunderi, Appl. Opt. **20**, 26 (1981).

[22] A. P. Vinogradov, L. V. Panina, and A. K. Sarychev, Dokl. Akad. Nauk SSSR **275**, 590 (1989) [Sov. Phys. Dokl. **34**, 530 (1989)].

[23] R. K. Wangness, *Electromagnetic Field* (Wiley, New York, 1979).

[24] L. V. Panina, A. S. Antonov, A. K. Sarychev, V. P. Paramonov, E. V. Timasheva, and A. N. Lagarkov, J. Appl. Phys. **76**, 6365 (1994).

[25] A. N. Lagarkov and A. K. Sarychev, Phys. Rev. B **53**, 6318 (1996).

[26] A. N. Lagarkov, S. M. Matytsin, K. N. Rozanov, and A. K. Sarychev, J. Appl. Phys. **84**, 3806 (1998).

[27] S. A. Shelkunoff and H. T. Friis, *Antennas. Theory and Practice* (Wiley, New York, 1952).

[28] R. King and G. Smith, *Antennas in Matter. Fundamentals, Theory and Applications* (The MIT Press, Cambridge, MA, 1981).

[29] D. P. Makhnovskiy, L. V. Panina, and D. J. Mapps, Phys. Rev. B **63**, 144424 (2001).
[30] L. Hermander, *The Analysis of Linear Partial Differential Operators I, Distribution Theory and Fourier Analysis* (Springer-Verlag, Berlin, 1983).
[31] D. P. Makhnovskiy, L. V. Panina, D. J. Maps, and A. K. Sarychev, Phys. Rev. B **64**, 134205 (2001).
[32] K. K. Mei, IEEE Trans. Antennas Propag. **AP-13**, 374 (1965).
[33] Y. S. Yeh and K. K. Mei, IEEE Trans. Antennas Propag. **AP-15**, 634 (1967).
[34] K. Liu, C. L. Chien, P. C. Searson, and K. Yu-Zhang, Appl. Phys. Lett. **73**, 1436 (1998).
[35] K. Liu, C. L. Chien, and P. C. Searson, Phys. Rev. B **58**, 14 681 (1998).

Appendix C Thin microwave composites with short wire inclusions

The overwhelming majority of applications using composite materials require that a composite sample be prepared as a thin layer or as an additional surface cover. In this Appendix, the boundary effect of the effective parameters is studied in composite samples that are based on short wire inclusions embedded into a dielectric matrix. When the composite becomes thinner than a certain critical thickness, the depolarisation charges and surface waves induced on the sample surface can significantly change the effective permittivity. Since these effects are not related to wire conductivity, the problem of the boundary effect is dealt with under the assumption of infinite conductivity (ideal conductor). However, on applying the mean field theory for the calculation of the effective permittivity the wire conductivity was taken as finite. These two main factors (the boundary effect and conductivity) can be considered separately. Thus, a generalisation of the "scale mean field theory" has been carried out for a thin composite.

Another issue, which was not clearly considered in this work, is the so-called Sommerfield conditions of radiation. The main method used in the Appendix is the solution of the heterogeneous Helmholtz equation $\Delta u + k^2 u = j(\mathbf{r})$ in the layered structure. To extract an unequal solution of this equation in an infinite region, which is the exterior of a finite region, it is needed to assume the additional limitations on the behaviour of the solution when approaching infinity. These additional limitations are the famous Sommerfield conditions:

$$\frac{\partial u(\mathbf{r})}{\partial |\mathbf{r}|} \pm iku(\mathbf{r}) = o(1/|\mathbf{r}|), \quad |\mathbf{r}| \to \infty, \tag{1}$$

where the signs "$\pm$" correspond to the outgoing and arriving waves. Generally, these conditions are required only if the exterior region does not have any energy losses and both the outgoing and arriving waves decrease as $1/|\mathbf{r}|$ at infinity. Contrary, if the exterior region has the losses, then the amplitude of the outgoing wave (scattered) must decrease at approaching infinity, whereas for the arriving wave it must increase.

However, it is a hardly known fact that the Sommerfield conditions must be generalised in the case of the layered media. Conditions (1) contain the roots $\pm k$ of the simplest dispersion equation $p^2 + k^2 = 0$, which defines the poles of the Fourier transform of the Green function corresponding to the Helmholtz equation in free space. In a layered structure, this equation of poles will be very complicated. These are the dispersion equations of the surface waves $\Delta_1 = 0$ and $\Delta_2 = 0$ considered in the Appendix. Thus, radiation conditions (1) must be formulated for each root of the dispersion equations.

The poles avoidance procedure used in the Appendix, when small losses are introduced in the system, is another method to extract the unequal solution. This method is similar to the Sommerfiled conditions.

It would be very interesting to establish the role of the surface waves in the forming of the effective response of a thin composite layer. The Fourier images of the Green functions used in the Appendix contain the poles, which are found from the dispersion equations $\Delta_1 = 0$ and $\Delta_2 = 0$. As it was mentioned above these poles relate to the spectrum of the surface waves, which lie between two wave numbers k_1 (free space) and k_2 (dielectric layer). With increasing layer thickness this spectrum tends to be everywhere dense covering the interval $[k_1, k_2]$, i.e. it becomes continuous. In this case, the dielectric layer demonstrates "the so-called soft dynamic properties", when it allows the propagation of the surface waves with any wave number between k_1 and k_2. Thus, a thick dielectric layer can be priory characterised by some permittivity, which is obviously closed to the layer permittivity. However, with a decrease in the layer thickness, the spectrum of the allowed surface waves significantly converges. In this case, the effective properties of the layer can not be generally characterised by a single effective permittivity, since then this permittivity should require a certain wave number which may be out of the allowed spectrum. Any way, the system works! How? There is a compromise, when the wire oscillator "opened to the dialog" tries to agree with the layer about a possible surface wave, which can propagate. As a result of this compromise a certain wave number arises, with which the wave leaves the wire. It is obvious that this newborn wave number has to be found from a quite complicated "compromise dispersion equation". At first sight, the existence of such equation appears very doubtful since initially there are several allowed wave numbers in the dielectric layer. Nevertheless, we succeeded in finding this equation, which is the non-linear dispersion equation of the resonance wave lengths (see main text in the Appendix). By means of an approximate calculation we carried out, as it were, an averaging over all excitation spectrum of the dielectric layer. Though this comparison is not very clear but enough for intuitive understanding.

Now we can formulate the basic principle which can be applied to a thin composite system:

Effective response of a thin composite system is formed by the spectrum of elementary excitations allowed by the host layer containing the composite inclusions.

Applying this principle to an opened system, it can be formulated as:

The eigen frequencies (or resonance frequency) of an opened system are defined by the internal parameters (which include its geometry and internal material parameters) as well as by the spectrum of eigen wavenumbers of the ambient space.

In our case the opened system is the wire inclusion, which exhibits an opened resonator radiating inside the dielectric layer. Repeat again: *the spectrum of eigen wavenumbers of the ambient space defines the eigen frequencies of the system and not the material parameters of the ambient space.* In the simplest case of free space, these conditions are equal, since there is an unequal wavenumber, which is unambiguously defined by the material parameters of the space (at a fixed frequency, of course) But in the case of a layered system, this statement is not true, as it was explained above.

The principle formulated states that the wave number selected by "the compromise dispersion equation" sets the effective parameters (permittivity and permeability) which allow the propagation of this wave and not the reverse! The barred wave can not form the effective response.

This point of view is very unusual for the quasistatic insight, which has got into the habit of located parameters (capacitance, resistance and inductance). But we insist that the wave processes are determinative for thin composite systems. The concept language formulated in this introduction also may be of interest for future applications of nanocomposites, where the column (wire) structure may be embedded into the host or formed on the surface of a thin dielectric slab.

PHYSICAL REVIEW B, VOLUME 64, 0942XX

Effect of transition layers on the electromagnetic properties of composites containing conducting fibres

D. P. Makhnovskiy, L. V. Panina, and D. J. Mapps
Department of Electronic, Communication and Electrical Engineering, Plymouth University, Drake Circus, Plymouth, Devon PL4 8AA, United Kingdom

A. K. Sarychev
Physics Department, New Mexico State University, Box 30001, Las Cruces, New Mexico 88003-8001

(Received 29 January 2001)

The approach to calculating the effective dielectric and magnetic response in bounded composite materials is developed. The method is essentially based on the renormalization of the dielectric matrix parameters to account for the surface polarization and the displacement currents at the interfaces. This makes possible the use of the effective-medium theory developed for unbounded materials, where the spatially dependent local dielectric constant and magnetic permeability are introduced. A detailed mathematical analysis is given for a dielectric layer having conducting fibres with in-plane positions. The surface effects are most essential at microwave frequencies in correspondence to the resonance excitation of fibres. In thin layers (having a thickness of the transition layer), the effective dielectric constant has a dispersion region at much higher frequencies compared to those for unbounded materials, exhibiting a strong dependence on the layer thickness. For the geometry considered, the effective magnetic permeability differs slightly from unity and corresponds to the renormalized matrix parameter. The magnetic effect is due entirely to the existence of the surface displacement currents.

DOI: 10.1103/PhysRevB.64.0942XX PACS number(s): 77.84.Lf, 41.20.Jb, 42.25.Bs, 81.05.Qk

I. INTRODUCTION

Metal-dielectric composite materials have received much attention because of their importance in modern technology.[1] Metallic inclusions, in particular metallic fibres, can reinforce the dielectric and magnetic properties of ceramics and plastic materials. Electromagnetic properties of the composite materials are analyzed customarily in terms of the effective macroscopic parameters: dielectric constant ε_{ef} and magnetic permeability μ_{ef}, which are calculated by averaging the responses from material constituents.[2–6] The effective-medium theory offers quick insight into linear problems, which are difficult to analyze by other means. However, it has disadvantages typical to all mean-field theories since it ignores the fluctuations in a system. It assumes that the local electric and magnetic fields are the same in the volume occupied by each component of a composite. In some cases the local-field fluctuations by no means can be ignored, as in the case of a percolation composite in the frequency range corresponding to the plasmon resonances in metal grains.[7] Then, the application of effective-medium theory (EMT) is rather questionable and adequate modifications are needed. Another example is bounded composites or composites containing interfaces. The microscopic local fields near the surfaces (or interfaces) differ considerably from those in the internal regions, due to the existence of the scattering fields from boundaries. In the approach developed here a specific surface polarization is introduced into the EMT approach. The effect of the surface polarization can be strong in thin materials, the characteristic size of which is smaller than the correlation length.[8] For elongated inclusions in the form of a fibre, their length $l \gg r_0$, where r_0 is the fibre radius, corresponds to the correlation length. For many engineering materials l is of the order of few mm, whereas the composite layer thickness is in the range of fractions of mm. In this case, the boundary effects must be taken into account when considering the effective response from a thin system. This is the purpose of the present paper.

A general approach to systems containing interfaces is solving the Maxwell equations in the regions, which are regarded as homogeneous and imposing the boundary conditions at the interfaces. The system is then characterized by ε_{ef} and μ_{ef} having a stepwise variation. However, since the microscopic fields near the boundaries are different, the effective parameters vary gradually within certain transition regions (known as transition layers) adjacent to the interfaces. They also depend on properties and geometry of the media near both sides of the interface. In certain cases, the transition layers can change the response from the entire system even if the system is thick.[9,10] For example, the concept of a transition layer is used to explain the elliptical polarization of the light reflected from an isotropic medium.[11,12] In the present work we also discuss the effect of the transition layers on the dielectric response (calculating the reflection and absorption coefficients) from thick composite systems.

The composite materials with elongated conducting inclusions have a number of characteristics specific for this system, which eventually result in strong boundary effects. In such composites, the concentration of the percolation threshold is proportional to the aspect ratio $p_c \propto r_0/l$.[6,13,14] In the limit $r_0/l \ll 1$, p_c is very small, however, the inclusion contribution to the effective dielectric constant becomes large already for very small concentrations $p \ll p_c$. It implies that the interaction between the fibres is strong even for $p \ll p_c$ and the assembly of conducting fibres is a system with a long-range strong interaction having a characteristic dimen-

PROOF COPY [BA8326] 050133PRB

sionless correlation length of $l/2r_0$. Then, the surface effects have to be essential at large distances comparable with the correlation length. On the other hand, the fibre currents induce surface displacement currents resulting in the fibre depolarization, which weakens the interaction in the transition layer, changing the basic property of the system.

Another characteristic feature of composites containing conducting fibres is the existence of a manifold resonance at microwave frequencies ($\lambda_m \sim 2l$, where λ_m is the wavelength in the dielectric matrix). This effect is responsible for the dispersion of the effective dielectric constant, which otherwise at these frequencies appears only in the vicinity of p_c.[6] For $p \ll p_c$, the frequency behavior of ε_{ef} is of the form[15]

$$\varepsilon_{ef}(\omega) = \varepsilon + \sum_n \frac{A_n}{\omega_{res,n}^2 - \omega^2 + i\beta_n \omega}, \tag{1}$$

where ε is the dielectric constant of the matrix and $\omega_{res,n}$ are the resonance frequencies. The interaction with the boundary changes the resonance excitation condition and the system has a different sequence of the resonance frequencies.[8] Therefore the result of interaction with boundaries is the modification of dispersion for ε_{ef} at microwave frequencies. In this analysis, the desperation characteristics are restricted to this frequency range (but $\lambda_m \gg r_0$).

The approach developed in this paper essentially uses a single-particle model within which the boundary effects are considered. First, the current distribution is analyzed in the antenna approximation ($\ln l/2r_0 \gg 1$, $\lambda_m \gg r_0$) at the fibre placed in a dielectric layer of thickness h. This problem was investigated in Ref. 8, however, we need a more detailed analytical analysis which is of great importance for the calculation of ε_{ef}. The equation for current distribution in bounded layers can be transformed to the form valid for an infinite system using a renormalization procedure. In this sense, the boundaries can be eliminated, instead of them new renormalized matrix parameters (dielectric constant ε_h and magnetic permeability μ_h) appear in the equation determining current at the fibre. This approach allows the further use of EMT in its form developed for unbounded materials. There are a number of approximations in the literature for obtaining the effective parameters of the composite materials with elongated inclusions. We use here the theory developed in Ref. 6 as the most complete and consistent with experiment and not restricted to the quasistatic limit. An important feature of this theory is a spatial dependence of the effective dielectric constant near a fibre for scales smaller than the fibre length. The nonlocal property of ε_{ef} is even enhanced by the interaction with the boundary: the environment near the fibre is characterized by ε_h and μ_h which depend on the layer thickness and the fibre position. As a result, the effective dielectric constant exhibits a strong dependence on the layer thickness for thin materials (thinner than the transition layer). In the case of thick materials, however, the role of the transition layers is not essential and boundaries effects can be neglected.

For the geometry considered the magnetic permeability μ_h arising in the renormalization method constitutes the effective magnetic properties. It is originated by the combination of the fibre current and surface displacement current which together form a circulatory current inducing a magnetic moment directed along the magnetic field (real part of μ_h is larger than unity). In the present case, $(\mu_h - 1) \ll 1$ and is not noticeable in the experiments. However, if the composite layer is placed on the metal substrate it may be essential to take account of the magnetic response. The experimental observation of the magnetic response would be a direct confirmation of the boundary effects.

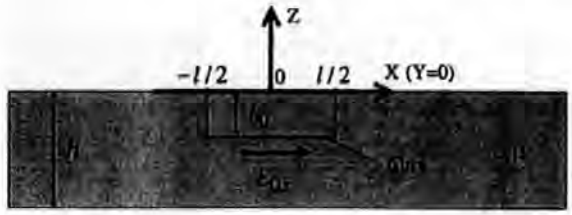

FIG. 1. Geometry of a single-particle problem: a dialectic layer with a conducting fibre.

II. SINGLE-PARTICLE MODEL

This section concerns a single-particle approximation[8] for the response of thin dielectric layer with a conductive fibre excited by an external electric field. This problem allows the effective parameters of layered composite materials to be found taking the boundary effects. The construction of a correct EMT equation uses the differential equation for current density at the fibre, which involves the effect of boundaries.

A model depicted in Fig. 1 is considered. A conducting fibre with a radius r_0 and a length l is placed in a dielectric layer of thickness h parallel to its surface at a depth $h_0[r_0 < h_0 < (h - r_0)]$. The layer is characterized by a dielectric constant ε and magnetic permeability μ. The fibre is assumed to be an ideal conductor. This approximation is reasonable when considering the boundary effects since the current distribution inside a fine fibre does not alter the polarization at the surface. The system is subjected to an ac uniform electrical field directed along the fibre (x direction): $\mathbf{E}_0 = (E_{0x}, 0, 0)\exp(i\omega t)$. The z direction is chosen along the normal to the layer, and the fibre is at $z = -h_0$, $y = 0$. The problem is considered in so-called antenna approximation[16] ($l \gg r_0$, $\lambda_m \gg r_0$ where $\lambda_m = 2\pi c/\omega\sqrt{\varepsilon\mu}$) which allows the distribution of the current density at the fibre to be represented as $j(x)\delta(y)\delta(z + h_0)$ where δ is the Dirac function. The electric and magnetic fields $\mathbf{E}$ and $\mathbf{H}$ scattered by the fibre are convenient to write in terms of a vector potential $\mathbf{A}$ and scalar potential φ (Gaussean units are used),

$$\mathbf{E} = -\frac{4\pi}{c^2} i\omega\mu\mathbf{A} + \frac{4\pi}{i\omega\varepsilon} \operatorname{grad} \operatorname{div} \mathbf{A}, \quad \mathbf{H} = \frac{4\pi}{c} \operatorname{rot} \mathbf{A}. \tag{2}$$

In the present case, only two components of the vector potential A_x and A_z are needed, which are represented in the form of convolutions with current density $j(x)$ (see Appendix A),

$$A_{x1,2,3}(x,y,z)=[G_{x1,2,3}(x,y,z)*f(x)],$$

$$A_{z1,2,3}(x,y,z)=[U_{1,2,3}(x,y,z)*f(x)]. \quad (3)$$

The convolution of two functions $g(x)$ and $f(x)$ is determined as the following integral:

$$(g(x)*f(x))=\int_{-l/2}^{l/2} g(x-s)f(s)ds,$$

where indexes 1, 2, 3 designate areas $z\in[0,\infty+]$, $z\in[-h,0]$, and $z\in[-\infty,-h]$, respectively. Function $G_{x1,2,3}$ satisfies the equation

$$\Delta G_{x1,2,3}+k_{1,2,3}^2 G_{x1,2,3}=\vartheta_{1,2,3} \quad (4)$$

with the boundary conditions

$$\mu G_{x2}|_{z=0}=G_{x1}|_{z=0},$$

$$\mu G_{x2}|_{z=-h}=G_{x3}|_{z=-h},$$

$$\left.\frac{\partial G_{x2}}{\partial z}\right|_{z=0}=\left.\frac{\partial G_{x1}}{\partial z}\right|_{z=0},$$

$$\left.\frac{\partial G_{x2}}{\partial z}\right|_{z=-h}=\left.\frac{\partial G_{x3}}{\partial z}\right|_{z=-h}.$$

Here $k_{1,3}=\omega/c$ and $k_2=(\omega/c)\sqrt{\varepsilon\mu}$ are the wave numbers in free space and dielectric layer, respectively, $\vartheta_{1,3}\equiv 0$, $\vartheta_2=-\delta(x)\delta(y)\delta(z+h_0)$, and $\Delta=\partial^2/\partial x^2+\partial^2/\partial y^2+\partial^2/\partial z^2$ is the Laplace operator.

Functions $U_{1,2,3}$ satisfy the equation

$$\Delta U_{1,2,3}+k_{1,2,3}^2 U_{1,2,3}=0 \quad (5)$$

with the boundary conditions

$$\varepsilon U_2|_{z=0}=U_1|_{z=0},$$

$$\varepsilon U_2|_{z=-h}=U_3|_{z=-h},$$

$$\left.\left(\frac{\partial U_1}{\partial z}-\frac{\partial U_2}{\partial z}\right)\right|_{z=0}=\left(\frac{1}{\varepsilon\mu}-1\right)\left.\frac{\partial G_{x1}}{\partial x}\right|_{z=0},$$

$$\left.\left(\frac{\partial U_3}{\partial z}-\frac{\partial U_2}{\partial z}\right)\right|_{z=-h}=\left(\frac{1}{\varepsilon\mu}-1\right)\left.\frac{\partial G_{x3}}{\partial x}\right|_{z=-h}.$$

Equation (4) together with the boundary conditions is self-sufficient, whereas the boundary conditions for Eq. (5) contain functions G_{x1} and G_{x3} entering the boundary conditions for Eq. (4).

For further analysis, only G_{x2} и $\partial U_2/\partial z$ are needed,

$$G_{x2}(x,y,z)=\frac{\exp(-ik_2 r)}{4\pi r}+\frac{1}{4\pi}\int_0^{+\infty}\frac{a_{x2}(k,h,h_0)\exp(\gamma_2 z)+b_{x2}(k,h,h_0)\exp(-\gamma_2 z)}{\Delta_2(k,h)\gamma_2}J_0(k\rho)k\,dk, \quad (6)$$

$$\left.\frac{\partial U_2(x,y,z)}{\partial z}\right|_{\varepsilon\neq\mu}=\frac{\partial}{\partial x}\left[\frac{1}{2\pi}\int_0^{+\infty}\frac{[a_{z2}(k,h,h_0)\exp(\gamma_2 z)-b_{z2}(k,h,h_0)\exp(-\gamma_2 z)](\varepsilon\mu-1)}{\Delta_1(k,h)\Delta_2(k,h)}\gamma_2 J_0(k\rho)k\,dk\right]\equiv\frac{\partial\tilde{U}}{\partial x}, \quad (7)$$

where $r=\sqrt{x^2+y^2+(z+h_0)^2}$, $\rho=\sqrt{x^2+y^2}$, $\gamma_1(k)=\sqrt{k^2-k_1^2}$, $\gamma_1(k)=\sqrt{k^2-k_2^2}$, and J_0 is the Bessel function. In Eq. (7) a new function $\tilde{U}_2$ is introduced. Integrals in Eqs. (6) and (7) use the following functions:

$$\Delta_1(k,h)=(\gamma_2^2+\gamma_1^2\varepsilon^2)\mathrm{sh}(\gamma_2 h)+2\gamma_1\gamma_2\varepsilon\mathrm{ch}(\gamma_2 h),$$

$$\Delta_2(k,h)=(\gamma_2^2+\gamma_1^2\mu^2)\mathrm{sh}(\gamma_2 h)+2\gamma_1\gamma_2\mu\mathrm{ch}(\gamma_2 h),$$

$$a_{x2}=(\gamma_2-\gamma_1\mu)\{\gamma_1\mu\mathrm{sh}[\gamma_2(h-h_0)]+\gamma_2\mathrm{ch}[\gamma_2(h-h_0)]\},$$

$$b_{x2}=\exp(-\gamma_2 h)(\gamma_2-\gamma_1\mu)[\gamma_1\mu\mathrm{sh}(\gamma_2 h_0)+\gamma_2\mathrm{ch}(\gamma_2 h_0)],$$

$$a_{z2}=\{\gamma_1\mu\mathrm{sh}[\gamma_2(h-h_0)]+\gamma_2\mathrm{ch}[\gamma_2(h-h_0)]\}(\gamma_2+\gamma_1\varepsilon)\times\exp(\gamma_2 h)-[\gamma_1\mu\mathrm{sh}(\gamma_2 h_0)+\gamma_2\mathrm{ch}(\gamma_2 h_0)]\times(\gamma_2-\gamma_1\varepsilon),$$

$$b_{z2}=\{\gamma_1\mu\mathrm{sh}[\gamma_2(h-h_0)]+\gamma_2\mathrm{ch}[\gamma_2(h-h_0)]\}\times(\gamma_2-\gamma_1\varepsilon)\exp(-\gamma_2 h)-[\gamma_1\mu\mathrm{sh}(\gamma_2 h_0)+\gamma_2\mathrm{ch}(\gamma_2 h_0)](\gamma_2+\gamma_1\varepsilon).$$

A special method of calculating the integrals in Eqs. (6) and (7) is given in Appendix B.

The tangential component E_τ of the total electric field at the fibre surface equals zero. In the approximation used the circulatory currents in the fibre are neglected, then this condition is written in the form

$$E_\tau\approx(E_{0x}+E_x)\Big|_{\substack{x\in[-l/2,l/2]\\ y^2+(z+h_0)^2=r_0^2}}=0, \quad (8)$$

where E_x is the longitudinal component of the scattered field. Equations (2) and (8) give

$$-E_{0x}=E_x=\frac{4\pi}{i\omega\varepsilon}\left[k_2^2A_{x2}+\frac{\partial^2A_{x2}}{\partial x^2}+\frac{\partial^2A_{z2}}{\partial x\partial z}\right]_{\substack{x\in[-l/2,l/2]\\ y^2+(z+h_0)^2=r_0^2}}. \tag{9}$$

Using Eqs. (7), (9) and the equality $\partial^2A_{z2}/\partial x\partial z=\partial^2(U_2*j)/\partial x\partial z=\partial^2(\tilde{U}_2*j)/\partial x^2$ the basic integrodifferential equation is obtained:

$$\left[\frac{\partial^2}{\partial x^2}[(G_{x2}+\tilde{U}_2)*j]+k_2^2(G_{x2}*j)\right]_{\substack{x\in[-l/2,l/2]\\ y^2+(z+h_0)^2=r_0^2}}=-E_{0x}\frac{i\omega\varepsilon}{4\pi}. \tag{10}$$

For Eq. (10), the boundary conditions for current density at the fibre ends have to be imposed, $j(-l/2)=j(l/2)=0$. Equation (10) is simplified calculating the convolutions approximately. Using Eqs. (6) and (7), the following approximations for the functions G_{x2} and $\tilde{U}_2$ are obtained in two limiting cases ($h\to 0$ and $h\to\infty$):

$$\lim_{h\to 0}\tilde{U}_2=\frac{(\varepsilon\mu-1)}{\mu}\frac{e^{-ik_1r}}{4\pi r},\quad \lim_{h\to\infty}\tilde{U}_2=0,$$

$$\lim_{h\to 0}G_{x2}=\frac{1}{\mu}\frac{e^{-ik_1r}}{4\pi r},\quad \lim_{h\to\infty}G_{x2}=\frac{e^{-ik_2r}}{4\pi r}. \tag{11}$$

Because the fibre has very small diameter $2r_0$, from Eq. (11) it follows that the real parts $\mathrm{Re}(G_{x2})$ and $\mathrm{Re}(G_{x2}+\tilde{U}_2)$ have sharp positive picks of the order of $1/r_0$ in the vicinity of $x=0$ for any value of h. To the contrary, the imaginary parts $\mathrm{Im}(G_{x2})$ and $\mathrm{Im}(G_{x2}+\tilde{U}_2)$ are limited when both x and r_0 approach zero. Integration of the real parts in the vicinity of the picks (more exactly, within the interval $[-\nu,\nu]$, $\sqrt{lr_0/2}\ll\nu\ll l/2$) gives the main contribution to the integrals. In this case the convolutions are approximated as[17]

$$[\mathrm{Re}(G_{x2}+\tilde{U}_2)*j]\approx j(x)\int_{-\nu}^{+\nu}\mathrm{Re}(G_{x2}+\tilde{U}_2)dx=j(x)Q_1, \tag{12}$$

$$[\mathrm{Re}(G_{x2})*j]\approx j(x)\int_{-\nu}^{+\nu}\mathrm{Re}(G_{x2})dx=j(x)Q_2,$$

where the "form factors" Q_1 and Q_2 are positive and represent the area under the corresponding narrow bell-shaped curves.

Substituting approximations (12) into Eq. (10) yields

$$Q_1\frac{\partial^2}{\partial x^2}\left(j(x)+i\frac{[\mathrm{Im}(G_{x2}+\tilde{U}_2)*j]}{Q_1}\right)+k_2^2Q_2\left(j(x)+i\frac{[\mathrm{Im}(G_{x2})*j]}{Q_2}\right)\approx-\frac{i\omega\varepsilon}{4\pi}E_{0x}. \tag{13}$$

Since the parameters Q_1 and Q_2 involve a large factor $2\ln(l/2r_0)$ (see Appendix C), Eq. (13) can be further simplified when the convolutions with the imaginary parts are neglected in comparison with those with the real parts (see Appendix C),

$$Q_1\frac{\partial^2j(x)}{\partial x^2}+k_2^2Q_2j(x)\approx-\frac{i\omega\varepsilon}{4\pi}E_{0x}, \tag{14}$$

$$j(-l/2)=j(l/2)=0.$$

Equation (14) is a basic differential equation in terms of which the boundary effects are introduced in EMT with the aim to modify the effective parameters.

Equation (14) describes the current distribution in the layered system and allows a generalized expression for the resonance wavelengths λ_{res} to be obtained. In an infinite medium, the value of λ_{res} is given by[18,19]

$$\lambda_{res,n}=\frac{2l\sqrt{\varepsilon\mu}}{2n-1};\quad n=1,2,3\ldots.$$

The effect of the boundaries results in a nonlinear dispersion equation

$$\lambda_{res,n}=\frac{2l\sqrt{\varepsilon\mu}}{2n-1}\sqrt{\frac{Q_2(\lambda_{res,n},h,h_0)}{Q_1(\lambda_{res,n},h,h_0)}};\quad n=1,2,3\ldots. \tag{15}$$

The dependencies on thickness h of the main resonance frequency $f_{res}=c/\lambda_{res,1}$ ($n=1$) obtained from Eq. (15) for different ε ($\mathrm{Im}\,\varepsilon=\mathrm{Im}\,\mu\equiv 0$) are given in Fig. 2(a). The pa-

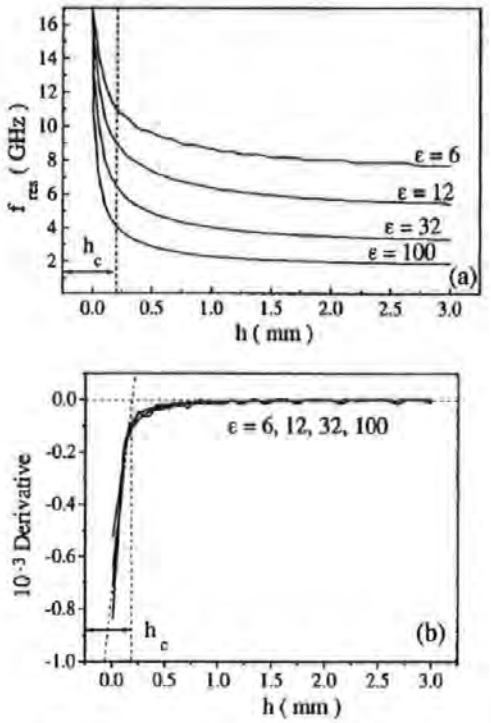

FIG. 2. Resonance characteristics of a dielectric layer with a conducting fibre. In (a), resonance frequency f_{res} as a function of the layer thickness h for different dielectric matrixes, in (b) derivative $\partial f_{res}/\partial h$ versus h, which defines the characteristic transition layer thickness h_c.

rameters used for all the calculations are $h_0/h=0.5$, $r_0=0.004$ mm, $l=8$ mm. The resonance frequency changes from the vacuum value of $c/2l$ (18.75 GHz for $l=8$ mm) at $h\to 0$ to the value of $c/2l\sqrt{\varepsilon}$ at $h\to\infty$ corresponding to that for an infinite medium with the dielectric constant ε. The characteristic feature of all the curves is the existence of two regions defined by the parameter h_c. For $h<h_c$, the resonance frequency rapidly drops with increasing h, and for $h>h_c$ it decreases slowly reaching the saturation limit. The meaning of the introduced parameter h_c can be understood from Fig. 2(b), where the derivatives $\partial f_{res}/\partial h$ as functions of h are given. For small h, this parameter has a constant large gradient, decreasing linearly with h. The value of h_c is defined by continuing this line until it intersects zero derivative level (infinite medium). Then h_c is a characteristic thickness when the system becomes sensitive to its outer boundaries as far as an electromagnetic response is concerned. For the case of Fig. 2, $h_c\approx 0.2$ mm. It is shown that h_c is independent of the material parameter ε, but it depends on geometry of the inclusions being a function of the fibre length l and radius r_0. The numerical analysis shows that this dependence is of a logarithmic type: $h_c\propto\ln(l/2r_0)$, which can be associated with the energy stored in the fibre $L_0 I^2/2$ where $L_0\cong 2\ln(l/2r_0)$ is the inductance per a unit length of a thin wire. The effect of the fibre position inside the layer is not essential for thin layers ($h<h_c$). The change in parameters of thick materials with respect to the fibre position is about 25%, as will be shown below.

To demonstrate the consistency of the model, the results obtained for the resonance frequency are compared with the available experimental data.[8] The experimental method[20–23] is based on measurements of the reflection coefficient from a composite system placed near a metal substrate. As the distance between the sample and substrate is increased the reflection signal exhibits an interference minimum at a frequency corresponding to the resonance frequency. The composite system consisted of a dielectric matrix containing aluminum-coated glass fibres with the volume concentration of about 0.02%. The metal coating is not always continuous and the effective concentration can be even smaller. This concentration is considerably smaller than the percolation threshold $p_c\sim 0.1\%$, allowing the single-particle approximation to be used for analysis. The dielectric matrix comprises a polymer with a metal powder, which makes it possible to reach large ε with a small absorption ($\mathrm{Im}\,\varepsilon\ll\mathrm{Re}\,\varepsilon$). Figure 3 compares the theoretical plots with the experimental data (taken from Ref. 8) for the resonance frequency as a function of thickness h. For $\varepsilon=52$ (obtained for the dielectric matrix from independent measurement), the experimental data can be fitted well by calculations for small h, and there is a large difference between the two curves for $h>h_c$, since the experiment does not come down to the limit corresponding to infinite medium with $\varepsilon=52$. It can be related to the fine dispersed structure of the composite matrix used in Ref. 8 (polymer and metal powder) and the difficulty of determining the effective dielectric constant ε near the fibre in this case. Another reason of this discrepancy can be related to a layered structure of thick samples as they are obtained by

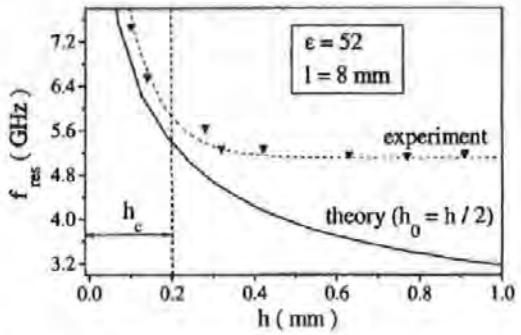

FIG. 3. Plots of f_{res} versus h, comparison of theory (solid curve) and experiment (dashed curve). $\varepsilon=52$, $l=8$ mm, $h_0=h/2$.

combining a number of 0.1–0.2-mm layers. The gaps between very thin layers can apparently decrease the effective value of ε resulting in an increasing resonant frequency $f_{res}=c/2l\sqrt{\varepsilon}$. Further experimental analysis is needed to clarify this case. However, it is more important for our purpose that there is a good agreement for thin layers $h\leq h_c$ which proves that the model describes functionally well the resonance properties of composites containing elongated inclusions in thin layers.

A considerable boundary effect results in the existence of surface layers where the effective dielectric constant is different from that in the inner region. Figure 4 shows the resonance frequency as a function of inclusion position h_0 for a thin layer ($h=0.2$ mm) and thick layer ($h=2$ mm). There is a transition layer h_s ($h_s<h_c$ for $h<h_c$ and $h_s=h_c$ for $h>h_c$) within which the value of f_{res} decreases and approaches that for the case when the inclusion is placed sufficiently inside the sample. It is seen that the variation in f_{res} due to the change in h_0 is considerably smaller than that when h is altered. Thin layers ($h<h_c$) can be considered as resonantly uniform, in which f_{res} is nearly a function of h only and the dependence on h_0 can be neglected. In the case of $h>h_c$, this dependence is essential within the surface transition layers and the sample, generally speaking, can not be treated as uniform. However, as it will be demonstrated

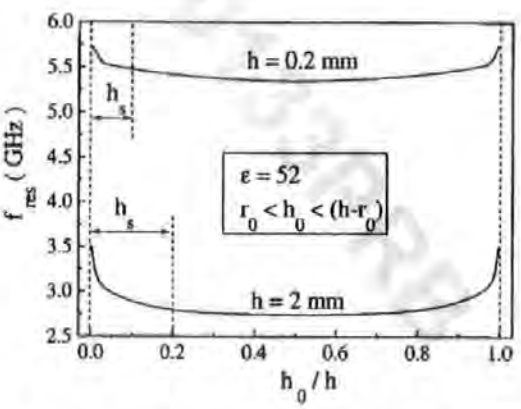

FIG. 4. Resonance frequency f_{res} as a function of the fibre position h_0/h for two layer thicknesses $h=0.2$ mm($\sim h_c$) and $h=2$ mm($\gg h_c$).

later, the existence of the surface transition layers does not alter the resonance frequency in thick samples. This means that they are not important in determining the effective dielectric constant. On the contrary, the effective-medium theory (EMT) in thin composite materials with elongated inclusions has to be essentially modified due to strong boundary effects.

III. EMT FOR THIN COMPOSITE LAYERS BELOW THE PERCOLATION THRESHOLD ($h<h_c$, $p<p_c$)

There are a number of methods developed in the literature to calculate the effective macroscopic parameters of composite materials with nonspherical, in particular, elongated inclusions. However, they are entirely restricted to the case of unbounded materials. Our objective is to obtain an extension to the case of thin composite materials where the boundary effects cannot be ignored. If the layer thickness is comparable with the size of inclusions embedded in it the concept of the dielectric constant seems to lose its direct meaning. Then, there is a question if such a layer can be characterized by the effective parameter ε_{ef}. In the case under consideration, for $h<h_c$, all the fibres are subjected to near-same boundary influence, as was demonstrated in Fig. 4. In this context, such a sample can be treated as a uniform layer characterized by effective parameters, yet these parameters will depend on thickness h and, in general, on properties of the surrounding media.

For our analysis, a modified EMT equation developed in Ref. 6 is used. This approach has been distinguished from other theories since it has a number of advantages: it gives a correct value of the percolation threshold and can be expanded to a nonquasistatic case when the boundary effects are most essential. Along with this, it enables technically to take into account the boundary polarization. For this purpose, it is important that the method combines the Bruggeman EMT (Refs. 2, 24, and 25) and Maxwell-Garnet theory[26,27] with its idea that the local medium near different inclusions may be different. Within this approach it is possible to introduce a renormalized parameters ε_b and μ_b for the medium near fibres as the result of interaction with the boundaries. These parameters will then be involved in EMT equations for ε_{ef} and μ_{ef} and the boundaries can be omitted.

The single-particle approximation considered above can be used for calculating the renormalized parameters. For this purpose, Eq. (14) describing the current distribution at the inclusion is transformed to a certain canonical form. In the antenna approximation ($l \gg r_0$, $\lambda_m \gg r_0$) the current density $j(x)$ at the fibre in the unbounded medium with some material constants ε and μ is determined by Eq. (10) with $\tilde{U}_2 \equiv 0$,

$$\left[\frac{\partial^2}{\partial x^2}(G*j)+k^2(G*j)\right]_{\substack{x\in[-l/2,l/2]\\ y^2+(z+h_0)^2=r_0^2}} = -E_{0x}\frac{i\omega\varepsilon}{4\pi}.$$

This equation can be further simplified in a way similar to that used for obtaining Eq. (14), which requires $\ln(l/2r_0) \gg 1$,

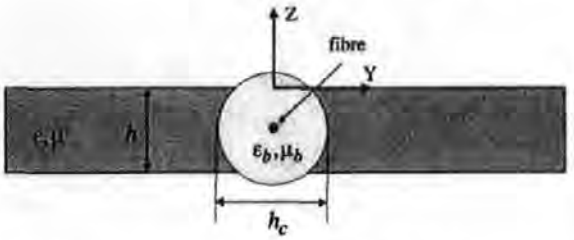

FIG. 5. Structure of a thin layer when the effect of boundaries is replaced by a new medium around the fibre.

$$Q\frac{\partial^2 j(x)}{\partial x^2}+k^2 Q j(x) \approx -\frac{i\omega\varepsilon}{4\pi}E_{0x}. \tag{16}$$

Here $k=(\omega/c)\sqrt{\varepsilon\mu}$ is the wave propagation parameter, the function $G(x,y,z)=\exp(-ikr)/4\pi r$ is related to the solution of Eq. (4) when $h=\infty$, and $Q=\int_{-p}^{+p}\mathrm{Re}(G)dx$. The form of Eq. (16) corresponding to the unbounded medium will be called a canonical form. In the case of bounded materials, Eq. (14) can be reduced to this canonical form by renormalizing material parameters as

$$\varepsilon_b=\varepsilon Q/Q_1, \quad \mu_b=\mu Q_2/Q,$$

$$k_b=(\omega/c)\sqrt{\varepsilon_b\mu_b}=(\omega/c)\sqrt{\varepsilon\mu(Q_2/Q_1)}. \tag{17}$$

This procedure allows the boundaries to be eliminated when determining the current distribution at the inclusion. They are replaced by a "new" medium with ε_b, μ_b, which appears near the inclusion at a characteristic distance h_c, as shown in Fig. 5. For $h<h_c$ the factors Q_1 and Q_2 depend weakly on h_0, then ε_b and μ_b may be considered to be functions of thickness h only. The appearance of the permeability $\mu_b>1$ owes its origin to the magnetic moment related to the current at the fibre and the induced displacement current at the layer surface.

Figure 6 shows the plots of the renormalized parameters ε_b and μ_b as functions of thickness h at the resonance wavelength with $\varepsilon=52$, $\mu=1$. The value of ε_b equals 1 for small $h\to 0$ and increases to its bulk value ε when h tends to infinite. The magnetic permeability μ_b differs slightly from 1 going through a maximum. This is related to the induced magnetic moment as a function of h: it tends to be zero in two limiting cases $h=0$ and $h=\infty$. In the experiment when the metal substrate is placed away from the sample the magnetic response is not noticeable. In the case of the composite placed on the metal substrate the magnetic properties may become noticeable to be measured.

After we have calculated the renormalized parameters characterising the medium near fibres, the EMT equation can be constructed similar to the case of unbounded media. This equation uses the condition that the total polarization averaged over all the inclusions has to be zero.[6,23] For bounded materials, the surface polarization due to surface displacement currents has to be included as well, which gives

$$pP_{\text{fibre}}+(1-p)P_{\text{matrix}}+P_{\text{surface}}=0, \tag{18}$$

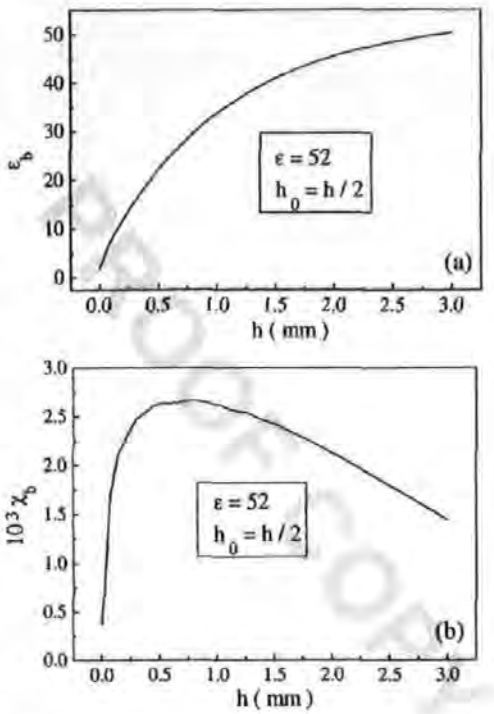

FIG. 6. Renormalized matrix parameters ε_b [in (a)] and $\chi_b = (\mu_b - 1)/4\pi$ [in (b)] as a function of h.

where p is the fibre concentration. The terms in Eq. (18) correspond to averaged polarization of fibres, dielectric matrix, and surface, respectively. Using renormalization procedure (17), the surface contribution can be taken into account by means of the parameters ε_b and μ_b which are used as renormalized matrix constants to determine the fibre polarization P_{fibre}. In this approach $P_{\text{surface}}=0$, however, the regions with parameters ε_b and μ_b appear near fibres; their polarization is different from that of the matrix and has to be included in Eq. (18).

The polarization P_{fibre} can be calculated from the current distribution on a fibre given by Eq. (13). It involves the dielectric constant of the surrounding medium ε. In the effective-medium approach, ε has to be replaced by ε_{ef}. However, the effective medium near elongated inclusions cannot be considered uniform on a characteristic scale of the order of inclusion size l, and the corresponding effective parameter $\tilde{\varepsilon}_{\text{ef}}$ depends on scale s. Since the total electric field on the inclusion is near zero, the interaction between the inclusions has little effect on the dielectric properties of the medium in the vicinity of them. Therefore the value of $\tilde{\varepsilon}_{\text{ef}}(s)$ in this region equals ε_b which differs from ε as the result of boundary effects. Far from the inclusions at distances larger than l, the effective medium can be considered as uniform having the dielectric constant $\tilde{\varepsilon}_{\text{ef}}=\varepsilon_{\text{ef}}$ of a bulk material. It means that Eq. (13) obtained for a fibre in a uniform medium has to be modified. At this stage, it is also important to consider a fibre with a finite conductivity, which influences dispersion of the effective parameter via the skin effect. The equation for the current distribution accounting for the finite conductivity and scale-dependent $\tilde{\varepsilon}_{\text{ef}}(s)$ was developed in Ref. 6 for the case of infinite medium. It turns out that the calculation of fibre polarization involves scaling along the fibre only. Assuming a linear scaling results in

$$\tilde{\varepsilon}_{\text{ef}}(\mathbf{r}-\mathbf{r}') = \varepsilon + 2(\varepsilon_{\text{ef}} - \varepsilon)|\mathbf{r}-\mathbf{r}'|/l, \tag{19}$$

where the points $\mathbf{r}$ and $\mathbf{r}'$ are taken on the fibre surface. In the case of the bounded composite the matrix constant ε must be replaced by the normalized effective constant ε_b. Considering that fibres are placed in the x direction, Eq. (19) becomes

$$\tilde{\varepsilon}_{\text{ef}}(x-x') = \varepsilon_b + 2(\varepsilon_{\text{ef}} - \varepsilon_b)(x-x')/l. \tag{20}$$

Using the scale dependence (20) the fibre polarization can be calculated[6]

$$P_{\text{fibre}} = \frac{4\pi i \sigma_f^*/\varepsilon_{\text{ef}}\omega}{1 + (4\pi i \sigma_f^*/\varepsilon_b\omega)(4r_0^2/l^2)\ln(1 + l\varepsilon_b/2r_0\varepsilon_{\text{ef}})\cos\Omega_b} \times E_0, \tag{21}$$

$$\Omega_b^2 = l^2 k^2 L_b C_b/4, \quad L_b = 2\ln(l/2r_0) + ik_b l,$$

$$c_b = \varepsilon_b/\ln(1 + l\varepsilon_b/2r_0\varepsilon_{\text{ef}}),$$

where Ω_b is the normalized resonance frequency, L_b is the fibre inductance per unit length of fibre, and C_b is the capacitance per unit length calculated after taking the account of the scale dependence (21). The normalized fibre conductivity $\sigma_f^* = f(\Delta)\sigma_f$ takes into account the skin effect in the conducting fibre where σ_f is the fibre conductivity. The function f is obtained from a classical skin effect in a conducting cylinder,[28]

$$f(\Delta) = [(1-i)/\Delta]J_1[(1+i)\Delta]/J_0[(1+i)\Delta],$$

where J_0 and J_1 are the Bessel functions, $\Delta = r_0\sqrt{2\pi\sigma_f\omega/c}$ is the ratio of the fibre radius r_0 to the skin depth $\delta = c/\sqrt{2\pi\sigma_f\omega}$.

The matrix is represented as an assembly of fine spherical particles of dielectric constant ε which are embedded in the effective medium with dielectric constant ε_{ef}. The polarization of the dielectric matrix is given by the standard quasistatic equation[28]

$$P_{\text{matrix}} = \frac{3(\varepsilon - \varepsilon_{\text{ef}})}{2\varepsilon_{\text{ef}} + \varepsilon} E_0, \tag{22}$$

where ε is the initial constant of the matrix (not ε_b). In general, the polarization of the regions with ε_b near fibres has to be considered separately from P_{matrix}. It seems reasonable to assume that they can be represented by ellipsoids with short axes $h_c/2$. The concentration of such new inclusions is enlarged by a factor of $(h_c/2r_0)^2$. With increasing p these areas may change the matrix properties entirely. Here we consider that p is sufficiently small to omit their contribution.

Substituting Eqs. (21) and (22) into Eq. (18) yields

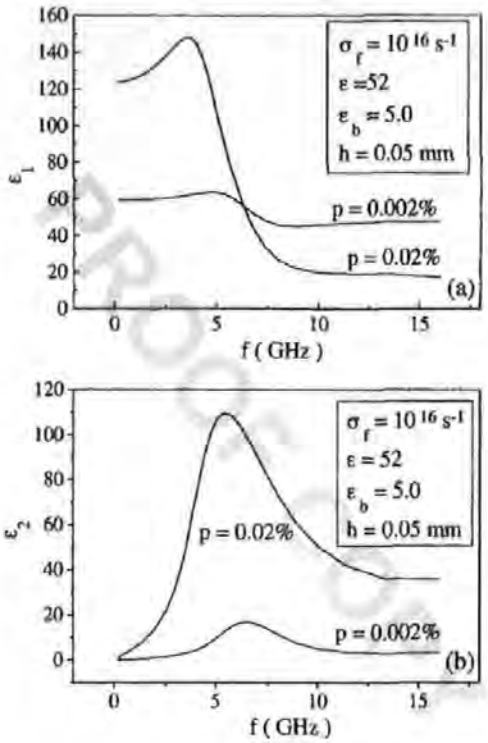

FIG. 7. Effective dielectric constant $\varepsilon_{ef}=\varepsilon_1+i\varepsilon_2$ as a function of frequency for two concentrations 0.002% and 0.02%, $\varepsilon=52$, $\varepsilon_b=5$, $h=0.05$ mm. Real part ε_1 is (a) and imaginary part ε_2 is in (b). The aluminum coating had the semicontinuous structure since the effective fibre conductivity σ_f was less than in the case of the all-metal inclusions and it is taken to be equal to $10^{16}\,s^{-1}$.

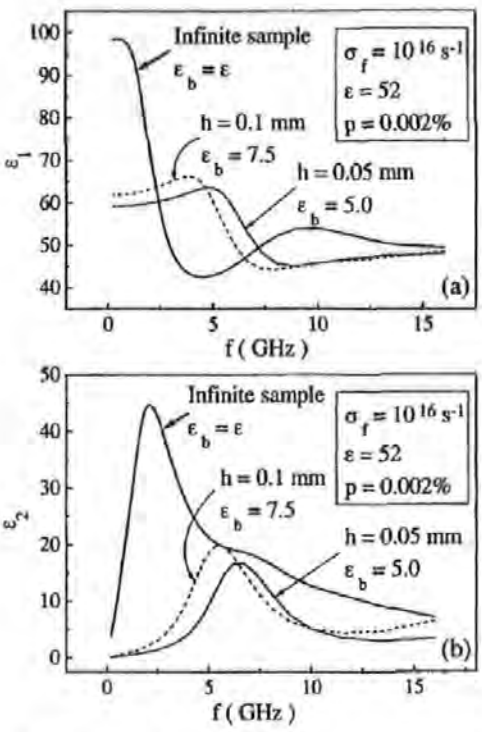

FIG. 8. Effective dielectric constant $\varepsilon_{ef}=\varepsilon_1+i\varepsilon_2$ as a function of frequency for different thickness h. ε_1 is (a) and ε_2 is in (b), $p=0.002\%$.

$$\frac{p}{2}\frac{4\pi i\sigma_f^*/\varepsilon_{ef}\omega}{1+(4\pi i\sigma_f^*/\varepsilon_b\omega)(4r_0^2/l^2)\ln(1+l\varepsilon_b/2r_0\varepsilon_{ef})\cos\Omega_b}+(1-p)\frac{3(\varepsilon-\varepsilon_{ef})}{2\varepsilon_{ef}+\varepsilon}=0. \tag{23}$$

Here the factor $\frac{1}{2}$ in the first term results from averaging by directions in the plane.

Equation (23) describes the effective response from a thin composite sample ($h<h_c$) below the percolation threshold ($p<p_c$).

IV. ANALYSIS OF THE EFFECTIVE RESPONSE NEAR RESONANCE FREQUENCY

In this part the dispersion of the effective response near the main resonance frequency is analyzed. The constant ε_{ef} is calculated from nonlinear Eq. (23) for two concentrations $p=2\times10^{-4}$ and $p=2\times10^{-5}$. These small values of p correspond to the composite materials used for the experimental investigation of ε_{ef} in Ref. 8. Figure 7 shows the dispersion of the real (ε_1) and imaginary (ε_2) parts of $\varepsilon_{ef}=\varepsilon_1+i\varepsilon_2$ for a very thin sample with $h=0.05\,\text{mm}\ll h_c$. The frequency behavior is of a resonance type with the resonance frequency corresponding to a maximum of imaginary part. In the case $p\ll p_c$, this frequency depends weakly on the inclusion concentration [see Fig. 7(b)]. Figure 8 compares the dispersion characteristics of ε_{ef} for layers of different thickness h. The case of an infinite system is also given. The main resonance frequency $f_{res}=c/2l\sqrt{\varepsilon_b}$ ($\mu_b\approx1$) is considerably shifted to the high-frequency region since the renormalized effective constant ε_b is several times smaller than the matrix constant $\varepsilon=52$ for $h<h_c$. Besides, the next resonance which is clearly seen in the case of $\varepsilon_b=52$ (infinite system) is not observed for thin layers. We can conclude that the boundary effects may change very strongly the dispersion characteristics $\varepsilon_{ef}(f)$ near the resonance frequencies.

In the case of thin composite layers $h<h_c$, the renormalized parameter ε_b used to construct EMT is nearly uniform having almost no dependence on the fibre position h_0. Contrary, for thicker materials there are transition layers where ε_b changes significantly, as shown in Fig. 9. Then, the effective dielectric constant is not uniform either and the existence of the transition layers in thick composites seems as if it may affect the wave propagation changing such measured parameters as transmission, reflection, and absorption coefficients. Then, there is a question if this can be a cause in shifting the measured resonance frequency in thick layers, as discussed in Fig. 3. To answer this question, the response from a thick layer ($h\gg h_c$) is calculated, dividing it into a number of layers where ε_b is considered to be uniform. The calculation is done by the matrix method (Abele's method[15,29]). Figure 10 compares the dispersion of the absorption coefficient for a single layer with the matrix constant $\varepsilon=52$ and for a layered system with ε_b distributed as

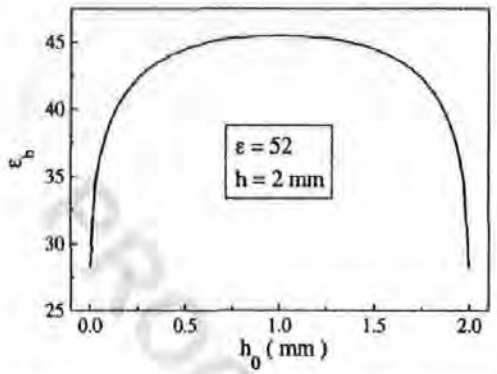

FIG. 9. Renormalized matrix parameters ε_h as a function of the fibre position h_0/h for $h=2$ mm($\gg h_c$).

shown in Fig. 9. The internal part of the sample with $\varepsilon_h \approx \varepsilon$ is considerably larger than the surface transition layers when $h_c \ll h$. Then, the variation in ε_h in these layers is not sufficient to change the total response from the system. It means, that in thick materials with $h \gg h_c$ the EMT approach has no need to be modified.

V. CONCLUSION

The effective-medium theory (EMT) applied to thin composite layers with conducting sticks is developed taking into account the surface displacement currents. The boundary effects are treated within a single-particle approximation, within which it is possible to transform the current distribution at the inclusion to the form similar to that for an infinite system. In this approach, the boundaries can be eliminated considering that the inclusion is embedded in a new matrix with a renormalized dielectric constant. The cross section of this area is of the order of thickness of the transition layer. After this step, the standard procedure to obtain EMT can be used. The dispersion of the effective dielectric constant in thin materials is a function of thickness being significantly different from that for "bulk" materials: the resonance frequency is shifted to higher frequencies and the interval between two resonances is increased.

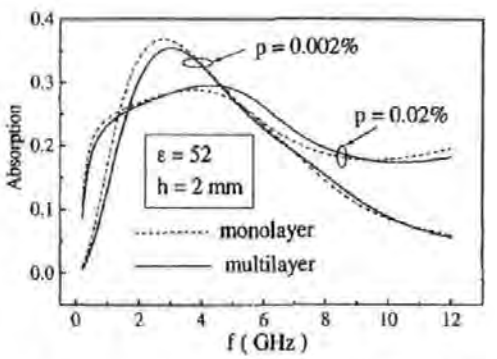

FIG. 10. Effective dielectric response (coefficient of absorption) from a thick composite layer [$h=2$ mm($\gg h_c$)]. Solid curve: multilayer system. Dashed curve: uniform single layer.

APPENDIX A

In this part, the differential equations completed with the boundary conditions for the vector potential **A** in the system shown in Fig. 1 are obtained. If a fibre is placed in an infinite medium, the field scattered by it is described by the vector potential having only A_x component. In the case when the surface effects are essential, using one component of the vector potential is in conflict with the condition of continuity of the fields **E** and **H** at the interface vacuum dielectric. As it follows from Eq. (2), two components A_x and A_z are sufficient to satisfy the continuity condition.[30] The equations for the components A_x and A_z are written as

$$\Delta A_{x1,2,3} + k^2_{1,2,3} A_{x1,2,3} = -j_{1,2,3}, \qquad \text{(A1)}$$

$$\Delta A_{z1,2,3} + k^2_{1,2,3} A_{z1,2,3} = 0.$$

The following boundary conditions are imposed:

$$\mu A_{x2}|_{z=0} = A_{x1}|_{z=0}, \quad \mu A_{x2}|_{z=-h} = A_{x3}|_{z=-h},$$

$$\left.\frac{\partial A_{x2}}{\partial z}\right|_{z=0} = \left.\frac{\partial A_{x1}}{\partial z}\right|_{z=0}, \quad \left.\frac{\partial A_{x2}}{\partial z}\right|_{z=-h} = \left.\frac{\partial A_{x3}}{\partial z}\right|_{z=-h}, \qquad \text{(A2)}$$

$$A_{z2}|_{z=0} = A_{z1}|_{z=0}, \quad A_{z2}|_{z=-h} = A_{z3}|_{z=-h},$$

$$\frac{1}{\varepsilon}\left.\left(\frac{\partial A_{x2}}{\partial x} + \frac{\partial A_{z2}}{\partial z}\right)\right|_{z=0} = \left.\left(\frac{\partial A_{x1}}{\partial x} + \frac{\partial A_{z1}}{\partial z}\right)\right|_{z=0},$$

$$\frac{1}{\varepsilon}\left.\left(\frac{\partial A_{x2}}{\partial x} + \frac{\partial A_{z2}}{\partial z}\right)\right|_{z=-h} = \left.\left(\frac{\partial A_{x3}}{\partial x} + \frac{\partial A_{z3}}{\partial z}\right)\right|_{z=-h},$$

where indexes 1, 2, 3 designates areas $z \in [0,\infty+]$, $z \in [-h,0]$, and $z \in [-\infty,-h]$, respectively, $j_{1,3} \equiv 0$, $j_2 = -j(x)\delta(y)\delta(z+h_0)$, $k_1 = \omega/c$, $k_2 = (\omega/c)\sqrt{\varepsilon\mu}$.

The solution of Eq. (A1) can be presented in the form of convolutions of Green's functions and current density $j(x)$, as it is shown in Eq. (3). The coupled Eqs. (4) and (5) are solved using the double Fourier's transformation with respect to variables x and y, which yields the differential equations with respect to z for the obtained Fourier's transformations. The integrals in Eqs. (6) and (7) are inverse Fourier's transformations written in the cylindrical coordinates with $\rho = \sqrt{x^2+y^2}$ (known as Sommerfield's integrals[30]).

APPENDIX B

The theory developed here requires two types of integrals to be calculated. They are [see Eqs. (6) and (7)]

$$\int_0^{+\infty} \frac{f(k,h,h_0,z)}{\Delta_2(k,h)} J_0(k\rho)\,dk$$

$$\text{or} \quad \int_0^{+\infty} \frac{g(k,h,h_0,z)}{\Delta_1(k,h)\Delta_2(k,h)} J_0(k\rho)\,dk, \qquad \text{(B1)}$$

where f and g are analytical functions with respect to variable k, $\rho = \sqrt{x^2+y^2}$, functions Δ_1, Δ_2 are determined in Eqs. (6)

and (7). The difficulty in calculating Eq. (B1) occurs since in the absence of the dissipation in the medium ($\mathrm{Im}\varepsilon = \mathrm{Im}\,\mu \equiv 0$) the functions $\Delta_1(k,h)$ and $\Delta_2(k,h)$ have real zeros, which are located symmetrically in the regions $-k_2 \leqslant k \leqslant -k_1$ and $k_1 \leqslant k \leqslant k_2$.

The equations $\Delta_1(k,h)=0$ and $\Delta_2(k,h)=0$ are called dispersion equations of the layered media, which determine the propagation numbers of those waves penetrating inside the medium at sufficient distance. The roots obey the following properties (which are given here without proof): (i) they are positioned symmetrically about $k=0$ (then, only positive k will be considered); (ii) in the absence of dissipation there are $N=(2+[\sqrt{k_2^2-k_1^2}h/\pi])$ different roots in the region $k_1 \leqslant k \leqslant k_2$, where the square brackets designate the integer part; (iii) for $h\to\infty$ this number increases to infinite and the roots tend to occupy the region $k_1 \leqslant k \leqslant k_2$ continuously; (iv) for $h < \pi/\sqrt{k_2^2-k_1^2}$ there is the only root which at $h\to 0$ approaches k_1; (v) for $h=\pi n/\sqrt{k_2^2-k_1^2}$, where $n \geqslant 1$ is any integer number, one of the roots equals k_1.

To find real positive roots in the region $k_1 \leqslant k \leqslant k_2$, it is convenient to represent the dispersion equations in the form

$$\Delta_1(k,h)=(-\tilde{\gamma}_2^2+\gamma_1^2\varepsilon^2)\sin(\tilde{\gamma}_2 h)+2\gamma_1\tilde{\gamma}_2\varepsilon\cos(\tilde{\gamma}_2 h)=0$$

which is equivalent to

$$(\gamma_1^2\varepsilon^2+\tilde{\gamma}_2^2)\sin\{\tilde{\gamma}_2 h+\mathrm{arctg}[2\gamma_1\tilde{\gamma}_2\varepsilon/(\gamma_1^2\varepsilon^2-\tilde{\gamma}_2^2)]\}=0, \tag{B2}$$

where $\tilde{\gamma}_2=\sqrt{k_2^2-k^2}$, $\gamma_1(k)$ and $\tilde{\gamma}_2(k)$ are real functions of variable k in the considered region. A similar form can be written for $\Delta_2=0$. From Eq. (B2) the condition of root existence is obtained

$$\tilde{\gamma}_2 h+\mathrm{arctg}[2\gamma_1\tilde{\gamma}_2\varepsilon/(\gamma_1^2\varepsilon^2-\tilde{\gamma}_2^2)]=\pi m, \tag{B3}$$

where m is integer number including zero. For any m there is only one root and the maximum value of m equals $N=(2+[\sqrt{k_2^2-k_1^2}h/\pi])$ as mentioned above. Equation (B3) can be solved by a graphical method finding the intersection of lines: $f_1(k)=-\tilde{\gamma}_2 h+\pi m$ and $f_2(k)=\mathrm{arctg}[2\gamma_1\tilde{\gamma}_2\varepsilon/(\gamma_1^2\varepsilon^2-\tilde{\gamma}_2^2)]$, which is easily realized numerically.

In a standard method,[30] the integrals containing functions with real poles are calculated by integrating along the vertical cuts made from the poles. If the number of poles is large this method becomes impractical and is of no use. The integration of Eq. (B1) can be made by introducing a small dissipation in the system: a small imaginary part appears in ε (and μ). For example, if the medium has a small conductivity σ, then $\mathrm{Im}\,\varepsilon=-i\omega\sigma/4\pi$ [the sign "-" corresponds to time dependence of $\exp(+i\omega t)$]. As a result the poles shift in the complex plane below the real axis and the integrals can be calculated in a usual way (as classical). The challenge now is to calculate the limit of the integrals when the dissipation approaches zero. For this purpose, the integrals of Cauchy type are considered,[31]

$$F(q)=\frac{1}{2\pi i}\int_C \frac{\Psi(k)dk}{k-q}, \tag{B4}$$

where $\Psi(k)$ is a continuous complex function, C is an arbitrary path in the complex plain P, and $q \in P$ is a complex number. The limit of $F(q)$ when the point q approaches a point k^* on the path C can be found by means the Plemelj formulas (or, less often, the Sokhotski formulas),

$$F^+(k^*)=F(k^*)+\tfrac{1}{2}\Psi(k^*),$$

$$F^-(k^*)=F(k^*)-\tfrac{1}{2}\Psi(k^*). \tag{B5}$$

Here $F^+(k^*)$ and $F^-(k^*)$ are the "left" and "right" limits when the point q approaches the point k^* from the "left" and "right" with respect to the integral path. The function $F(k^*)$ is defined by the following equation:

$$F(k^*)=\frac{1}{2\pi i}\int_C \frac{\Psi(k)-\Psi(k^*)}{k-k^*}dk+\frac{1}{2}\Psi(k^*)+\frac{\Psi(k^*)}{2\pi i}\ln\frac{b-k^*}{a-k^*}, \tag{B6}$$

where $\ln[(b-k^*)/(a-k^*)]=\ln\|(b-k^*)/(a-k^*)\|+i\arg[(b-k^*)/(a-k^*)]$ is the principal value of a logarithm, and a,b are the ends of the path. In the absence of the dissipation when k^* is a real root of $\Delta_1(k,h)=0$ or $\Delta_2(k,h)=0$, the integrals in Eq. (B1) can be rewritten in the form of the Cauchy integrals,

$$\int_{a_i}^{b_i}\frac{f(k,h,h_0,z)}{\Delta_2(k,h)}J_0(k\rho)dk = \int_{a_i}^{b_i}\frac{f(k,h,h_0,z)(k-k_i^*)/\Delta_2(k,h)}{k-k_i^*}J_0(k\rho)dk. \tag{B7}$$

Here $\Psi(k)=f(k,h,h_0,z)(k-k_i^*)/\Delta_2(k,h)$ is a continuous function of the variable k, the parameter k_i^* is the ith real root of the dispersion equation, and (a_i,b_i) is the subinterval containing k_i^*. The value of $\Psi(k^*)$ is found via residue: $\Psi(k_i^*)=\mathrm{res}[f(k,h,h_0,z)/\Delta_2(k,h)]_{k=k_i^*}$. The integrals in Eq. (B1) can be calculated by dividing the integration path into intervals: $(0,k_1),\ldots,(a_i,b_i),\ldots,(k_2,+\infty)$ where the integration in the intervals (a_i,b_i) is carried out as explained above. In Eq. (B5) the right limit $F^-(k_i^*)$ has to be used since in the case of dissipation the roots shift below the real axis.

APPENDIX C

In this appendix, the approximation used to obtain Eqs. (14) and (16) is discussed. Let us consider Eq. (13) for the current density, which is written as

$$\frac{\partial^2}{\partial x^2}\left(j(x)+\frac{(G_1*j)}{Q_1}\right)+k_b^2\left(j(x)+\frac{(G_2*j)}{Q_2}\right)=-\frac{i\omega\varepsilon}{4\pi Q_1}E_{0x}, \tag{C1}$$

where the following notations are used: $G_1 = i\,\mathrm{Im}(G_{x2} + \tilde{U}_2)$, $G_2 = i\,\mathrm{Im}(G_{x2})$, and the wave number $k_b^2 = k_2^2 Q_2 / Q_1$. As it follows from Eq. (11) the functions G_1 and G_2 are proportional to

$$G_{1,2} \sim i \frac{\sin(k_b x)}{\sqrt{x^2 + r_0^2}}. \tag{C2}$$

The order of Q_1 and Q_2 is estimated from Eqs. (11) and (12),

$$Q_{1,2} \propto \int_{-l/2}^{+l/2} \frac{dx}{\sqrt{x^2 + r_r^0}} \approx 2 \ln(l/2r_0). \tag{C3}$$

Equation (C1) can be represented as a differential equation with respect to the function $j(x) + (G_1 * j)/Q_1$,

$$\frac{\partial^2}{\partial x^2}\left(j(x) + \frac{(G_1 * j)}{Q_1} \right) + k_b^2 \left(j(x) + \frac{(G_1 * j)}{Q_1} \right) = -\frac{i\omega\varepsilon}{4\pi Q_1} E_{0x} + k_b^2 \left(\frac{(G_1 * j)}{Q_1} - \frac{(G_2 * j)}{Q_2} \right). \tag{C4}$$

The general solution of Eq. (C4) can be written in the form of an integral equation,

$$j(x) = -\frac{i\omega\varepsilon}{4\pi Q_1 k_b^2} E_{0x} + A \sin(k_b x) + B \cos(k_b x) + \frac{(G_1 * j)}{Q_1} + k_b \int_{-l/2}^{x} \sin[k_b(x-s)] F(s)\, ds, \tag{C5}$$

where $F(s) = [(G_1 * j)/Q_1 - (G_2 * j)/Q_2]$, A and B are constants which are defined from the boundary conditions $j(-l/2) = j(l/2) = 0$. The first three terms can be used to construct the zero-order solution,

$$j_0(x) = -\frac{i\omega\varepsilon}{4\pi Q_1 k_b^2} E_{0x} + A \sin(k_b x) + B \cos(k_b x). \tag{C6}$$

The next-order terms can be found from a standard iteration procedure,

$$j_n(x) = j_0(x) + \int_{-l/2}^{l/2} \tilde{F}(x,q) j_{n-1}(q)\, dq; n = 1, N, \tag{C7}$$

where $\tilde{F}(x,q)$ is the kernel of the total linear integral operator,

$$\tilde{F}(x,q) = \frac{1}{Q_1} G_1(x-q) + k_b \int_{-l/2}^{x} \sin[k_b(x-s)] \times \left(\frac{G_1(s-q)}{Q_1} - \frac{G_2(s-q)}{Q_2} \right) ds. \tag{C8}$$

The constants A and B are found from the boundary conditions $j_n(-l/2) = j_n(l/2) = 0$ at the final stage of the iteration procedure for a fixed $n = N \geq 1$. Since the integral operator is linear the equation for A and B form a linear system. The solution for j_0 $(N = 0)$ has the form

$$j_0(x) = -\frac{i\omega\varepsilon E_{0x}}{4\pi Q_1 k_b^2} \frac{[\cos(k_b l/2) - \cos(k_b x)]}{\cos(k_b l/2)}. \tag{C9}$$

Equation (C9) gives singularity at the resonance frequency when $\cos(k_b l/2) = 0$, which can be eliminated using the next iterations. Since the kernel $\tilde{F}(x,q)$ involves parameters $1/Q_1$, $1/Q_2 \propto 1/2 \ln(l/2r_0)$, the last term in the Nth iteration series is of the order of $[1/2 \ln(l/2r_0)]^{N+1}$. In the present case, the iteration parameter is sufficiently small: taking $l/2 = 0.4$ cm and $r_0 = 4 \times 10^{-4}$ cm gives $1/2 \ln(l/2r_0) \approx 0.15$. Then, the higher-order iterations will introduce small changes in the effective parameter k_b and the resonance frequency (but can change the current at the resonance considerably, which is not important in this case) and thus the form factors Q_1 and Q_2 properly define the modified effective parameters. The zero-order iteration corresponds to neglecting the imaginary parts in Eq. (13).

[1] See, for example, G. A. Niklasson and C. G. Granqvist, *Contribution to Cluster Physics in Material Science and Technology*, Vol. 104 of *NATO Advanced Study Institute*, Series ■:■, edited by J. Davenans and P. M. Rabette (Nijhoff, Dordrecht, 1986).

[2] D. J. Bergman and D. Stroud, Solid State Phys. **46**, 147 (1992).

[3] G. A. Niklasson and C. G. Granqvist, J. Appl. Phys. **55**, 3382 (1984).

[4] R. G. Barrera, G. Monsivais, W. L. Mochan, and E. Enda, Phys. Rev. B **39**, 9998 (1989).

[5] R. G. Barrera, J. Giraldo, and W. L. Mochan, Phys. Rev. B **47**, 8528 (1993).

[6] A. N. Lagarkov and A. K. Sarychev, Phys. Rev. B **53**, 6318 (1996).

[7] M. I. Stockman, L. N. Pandley, and T. F. George, Phys. Rev. B **53**, 2183 (1996).

[8] A. P. Vinogradov, D. P. Makhnovskiy, and K. N. Rozanov, J. Commun. Technol. Electron. **44**, 317 (1999).

[9] P. Drude, Wied. Ann. **51**, 77 (1894).

[10] M. Born, *Optik* (Springer, Berlin, 1933).

[11] D. M. Sivukhin, Zh. Eksp. Teor. Fiz. **30**, 374 (1956) [Sov. Phys. JETP **3**, 269 (1956)].

[12] O. N. Gadomskii and S. V. Sukhov, Opt. Spectrosc. **89**, 261 (2000).

[13] C. A. Zuev and A. F. Sidorenko, Teor. Mat. Fiz. **62**, 76 (1985).

[14] I. Balberg, Philos. Mag. **56**, 1991 (1987).

[15] M. Born and E. Wolf, *Principles of Optics*, Fourth edition (Pergamon Press, New York, 1968).

[16] R. King and G. Smith, *Antennas in Matter. Fundamentals, Theory and Applications* (MIT Press, Cambridge, MA, and London, England, 1981).

[17] L. Hermander, *The Analysis of Linear Partial Differential Operators I, Distribution Theory and Fourier Analysis* (Springer-Verlag, Berlin, 1983).

[18] S. A. Shelkunoff and H. T. Friis, *Antennas. Theory and Practice* (Wiley, New York, 1952).

[19] E. Hallen, *Electromagnetic Theory* (Chapman and Hall, London, 1962).

[20] A. A. Kalachev, T. V. Kukolev, S. M. Matytsin, K. N. Rozanov, and A. K. Sarychev, in *Optical and Electrical Properties of Polymers*, edited by J. A. Emerson and J. M. Torkelson, Mater. Res. Soc. Symp. Proc. No. 214 (Materials Research Society, Pittsburgh, 1991), p. 113.

[21] A. N. Kolesnikov, A. N. Lagarkov, K. N. Novogrudskiy, S. M. Matytsin, K. N. Rozanov, and A. K. Sarychev, in *Optical and Electrical Properties of Polymers* (Ref. 20) p. 119.

[22] A. N. Lagarkov, S. M. Matytsin, K. N. Rozanov, and A. K. Sarychev, J. Appl. Phys. **84**, 3806 (1998).

[23] A. S. Antonov *et al.*, *Electrophysical Properties of the Percolation Systems* (Institute for High Temperatures, Russian Academy of Science, USSR, Moscow 1990).

[24] D. A. G. Bruggeman, Ann. Phys. (Leipzig) **24**, 635 (1935).

[25] R. Landauer, in *Electrical Transport and Optical Properties of Inhomogeneous Media*, edited by J. C. Garland and D. B. Tanner, AIP Conf. Proc. No. 40 (AIP, New York, 1978), p. 2.

[26] P. Sheng, Phys. Rev. Lett. **45**, 60 (1980).

[27] U. J. Gibson and R. A. Buhram, Phys. Rev. B **27**, 5046 (1983).

[28] L. D. Landau and E. M. Lifshits, *Electrodynamics of Continuos Media* (Pergamon, New York, 1960).

[29] H. A. Macleod, *Thin-film Optical Filters* (Adam Hilberg LTD, London, 1969).

[30] A. Sommerfield, *Partial Differential Equations in Physics* (Academic, New York, 1964).

[31] A. I. Markushevich, *Theory on Functions of a Complex Variable* (Chelsea, New York, 1985).